The Dissertation Committee for Dongjie Jiang Certifies that this is the approved version of the following dissertation:

CONSTITUTIVE MODELING OF PSEUDOELASTIC NiTi AND ITS APPLICATION TO STRUCTURAL PROBLEMS

Committee:

Stelios Kyriakides, Supervisor

Chad M. Landis, Co-Supervisor

Desiderio Kovar

Kenneth M. Liechti

Krishnaswamy Ravi-Chandar

CONSTITUTIVE MODELING OF PSEUDOELASTIC NiTi AND ITS APPLICATION TO STRUCTURAL PROBLEMS

by

Dongjie Jiang, B.E.; M.E.

Dissertation

Presented to the Faculty of the Graduate School of

The University of Texas at Austin

in Partial Fulfillment

of the Requirements

for the Degree of

Doctor of Philosophy

The University of Texas at Austin

August 2017

Dedication

To my parents.

Acknowledgements

Many thanks are owed to a lot of people for the completion of this dissertation. First of all, I would like to express my sincere gratitude to my advisor, Prof. Stelios Kyriakides, whose academic guidance and moral support have been encouraging me all the time since I joined his group. Also, his stringent attitude and tireless devotion to scientific excellence influence me deeply, not only during the six years that we worked together but also in the future.

I am also grateful to the co-advisor of my research, Prof. Chad M. Landis, for his helpful guidance on the constitutive modeling and the pleasant discussions between us that inspired me significantly. Many thanks are due to other members of my dissertation committee: Profs. Desiderio Kovar, Kenneth M. Liechti and Krishnaswamy Ravi-Chandar for reviewing my dissertation and for their constructive comments.

The work in this dissertation was conducted with financial support from the National Science Foundation under grant no. CMMI-12000465. I would also like to acknowledge the partial support of my studies by The University of Texas at Austin, and the Research Center for Mechanics of Solids, Structures and Materials for the 2011-12 Recruiting Fellowship and the 2015-16 Max L. Williams Endowed Graduate Fellowship.

It was my pleasure to collaborate with Dr. Nathan J. Bechle who performed the experiments on NiTi tubes and Karlos Kazinakis who conducted the tension test on NiTi strip. I feel fortunate to have interacted with a number of excellent fellow students in the doctoral program of Engineering Mechanics, who always inspired me and consoled me during difficult times, including Dr. Liang-Hai Lee, Dr. Rong Jiao, Dr. Julian Hallai, Dr. Seung Ryul Na, Dr. Wei Gao, Dr. Lin Yuan, Dr. Zhiyi Cao, Dr. Shixuan Yang, Dr.

Chenglin Wu, Sundeep Palvadi, Yafei Liu, Chenglin Yang, Kelin Chen, Martin F. Scales, Shutao Qiao, Liu Wang.

I also thank Scott Messec for his help with technical problems associated with the use of computational facilities.

Last, I am sincerely grateful to my parents, whose unconditional love and encouragement has always helped me during difficult times

.

Constitutive Modeling of Pseudoelastic NiTi and its Application to Structural Problems

Dongjie Jiang, Ph.D.

The University of Texas at Austin, 2017

Supervisor: Stelios Kyriakides

Co-Supervisor: Chad M. Landis

Nearly equiatomic NiTi exhibits the unique characteristic of pseudoelasticity, i.e. it can be deformed to strain levels of several percent that is fully recoverable on unloading. Under tension, the phase transformation results in strain of nearly 7% and inhomogeneous deformation while the stress remains essentially constant. By contrast, under compression, transformation occurs at a much higher stress, the induced strain is nearly one-half and deformation is essentially homogeneous. These material nonlinearities interact with structural instabilities to produce hitherto unknown intriguing structural responses.

A constitutive modeling framework based on J_2-type kinematic hardening is developed to address the tension/compression asymmetry of pseudoelastic NiTi, including inhomogeneous versus homogeneous deformations. Its performance is then evaluated in the numerical studies of four nonlinear NiTi structures that were previously investigated experimentally.

The first problem considered is the buckling and recovery of an axially compressed NiTi tube. The modeling efforts reproduce the major events observed, including onset of axisymmetric wrinkling, collapse by progressive development of

buckling lobes with three circumferential waves, erasure of the lobes and recovery of deformation upon unloading. The study shows that the tension/compression asymmetry plays the key role in bringing the calculated response close to the experimental one and addition of plastic deformation further improves the results. The second problem involves a NiTi strip under tension. The constitutive model properly accounting for softening in the tensile response reproduces the closed hysteresis with two stress plateaus with correct levels and extents, as well as localization of deformation into inclined bands that propagate in the specimen. In the third problem, the constitutive model is used to analyze the tension test of a NiTi tube. The simulation reproduces a closed hysteretic response with two stress plateaus close to the measured one. The tubular geometry of the specimen imposes helical and multi-pronged localization patterns. The last problem studied is the bending of a NiTi tube. The simulation reproduces the major features of the experimental results: the hysteretic moment-end rotation response with two plateaus; localization of curvatures; progressive development of diamond patterns of higher strain on the tensioned side and the nearly homogeneous deformation on the compressed side.

Table of Contents

Chapter 1: INTRODUCTION

1.1 SHAPE MEMORY ALLOYS-PROPERTIES

NiTi, also named as *nitinol*, is perhaps the most widely used and extensively studied *Shape Memory Alloy* (SMA). Shape memory alloys are a unique class of materials that are increasingly attractive in a variety of applications because of two special characteristics: the *Shape Memory Effect* and *Pseudoelasticity*. Shape memory effect refers to the property of a material, which seemingly is "plastically" deformed to recover the deformation with a modest increase in temperature. In other words, it "remembers" its original shape. Pseudoelasticity refers to the property of SMAs to be strained well beyond the elastic limit and fully recover the inelastic deformation upon unloading (e.g., see Shaw and Kyriakides [1995]).

These intriguing material properties are attributed to the diffusionless transformations between the microstructural phases: *austenite* (*A*), *martensite* (*M*) and *R-phase* (*R*). Austenite has a B2 lattice with a high degree of symmetry, which can exist stably at high temperatures and low stresses (Philip and Beck [1957], Huang et al. [2003]). By contrast, martensite is stable at low temperatures and high stresses as it has a B19' monoclinic lattice with lower degree of symmetry (Wang, et al. [1965], Otsuka [1971], Wagner and Windl [2008]). The intermediate R-phase is a distortion of B2 austenite (see Ling and Kaplow [1981]) and does not contribute to the main properties of NiTi mentioned. The diffusionless transformation between *A* and *M* is the primary mechanism responsible for the shape memory effect and pseudoelasticity.

The transformation between the phases can be monitored through differential scanning calorimetry (DSC). Figure 1.1 shows the DSC thermogram for one of the NiTi tube stocks used in the experiments referenced in following chapters, together with

schematic drawings for the corresponding crystallographic lattices. The specimen undergoes a thermal heating/cooling cycle and the curve in Fig. 1.1 records the history of heat flux versus temperature. The material starts in the *M* phase, which is stable at low temperatures—marked in red color. As heating progresses and temperature rises, it transforms into *A*. The spike of heat flux between the two phases indicates that the $M \to A$ transformation absorbs heat. The temperature boundaries of the heat flux spike, denoted as A_s and A_f, represent the intersection of constructing tangent lines to the spike and the remaining parts of the curves, as shown in the figure. For this specific specimen, $A_s = -9.6\,^{o}\text{C}$ and $A_f = 12.1^{o}\text{C}$, which represent the austenite start and finish temperatures, respectively. Upon cooling, *A* gradually becomes unstable and transforms back to *M*. A downward spike is observed as the $A \to M$ transformation occurs, which is associated with release of heat. Two temperatures M_s and M_f representing the martensite start and finish can be defined in a similar way to A_s and A_f.

We now consider a NiTi specimen, which is initially in the *M*-phase, i.e., at a temperature below M_f, and loaded in uniaxial tension. With low degrees of symmetry, the B19' monoclinic lattice of *M* has several energetically equivalent configurations, or variants, which are either rigid body rotations and/or mirror images of each other. In the stress-free state, the *M* variants must twin to accommodate their different orientations. As the specimen starts being loaded, some variants alter their orientations to be preferable to the applied loading and finally the orientations of most *M* variants will be aligned with the external load. The reorientation of variants leads to a macroscopic deformation. This process is called detwinning (see Perkins [1981], Shaw and Kyriakides [1995], Bhattacharya [2003]). We terminate loading when the whole specimen has detwinned and unload it completely. Since unloading does not change the orientations of the detwinned *M* variants, most of the macroscopic deformation induced by detwinning remains (e.g.,

see Fig. 3 of Shaw and Kyriakides [1995]). It the specimen is heated, the *M* phase transforms to *A* because *M* is unstable at high temperatures. Thus, the specimen recovers its original shape because *A* and twinned *M* share the same macroscopic geometry. This is the mechanism of shape memory effect.

Figure 1.2 shows the nominal stress-average strain response recorded in a uniaxial tension test on NiTi that is characteristic of pseudoelastic behavior. The test is performed above the A_f temperature and thus the material is initially in the *A* phase. The *A* phase initially deforms along a stiff branch up to ①. At a stress level of about 455 MPa, *A* becomes unstable and starts transforming into *M*. As the transformation progresses, the stress in the specimen traces a plateau, during which the two phases coexist and the deformation is inhomogeneous. The stress-induced martensite deforms to a strain that corresponds to that at the end of the stress plateau, ②, and the strain in the untransformed *A* phase remains at that at the beginning of the plateau, ①. When most of the material transforms to *M*, the stress plateau terminates at ②, and the stress takes an upswing as the *M* phase deforms homogeneously.

If the specimen is loaded to much higher stress levels, the stress-induced detwinned martensite may incur microstructural slipping and permanent unrecoverable deformation (see Shaw and Kyriakides [1995], Jiang et al. [2016b], Reedlunn et al. [2014]). The upper stress plateau indicates that the forward phase transformation resulted in a strain of approximately 6%. The microscopic source of this strain is the difference between the lattice structures of the two phases (see Bhattacharya [2003]). Upon unloading, the *M* phase unloads elastically with homogeneous deformation until ③, where the stress starts to trace a lower plateau and the transformation back to *A* initiates. Similar to the forward transformation, the deformation in the specimen is again inhomogeneous and the two phases coexist during the lower stress plateau. At point ④,

most of the material has reverted to *A*, which unloads along the initial elastic trajectory until the stress is totally removed at ⑤. Pseudoelasticity refers to this fully reversible nature of the phase transformations between *A* and *M* in this temperature regime.

The mechanical behavior of pseudoelastic NiTi exhibits significant asymmetry between tension and compression (see Wasilewski [1971], Vacher and Lexellent [1992], Jacobus et al. [1996], Gall and Sehitoglu [1999], Gall et al. [1999], Mao et al. [2010], etc.). The asymmetry is attributed to differences in the critical resolved shear stresses (Schmid factor) caused by crystallographic textures (Orgeas and Favier [1998]; differences in Schmid factors between tension and compression have been confirmed by Mao et al. [2010].)

The asymmetry adds to the complexity of modeling of the material behavior and in the analysis of NiTi structures. Figure 1.3 shows the tensile and compressive nominal stress-elongation responses of the NiTi tube studied in the experiments of Bechle and Kyriakides [2014]. Included are representative DIC configurations extracted during loading and unloading with color contours of axial strain superimposed. The tensile response is similar to that in Fig. 1.2. As the upper stress plateau is traced, the deformation in the tube localizes and propagates via the multi-helical band shown in Fig. 1.3b. The strain in the *M* phase has reached about 7% while the untransformed *A* remains at nearly 1%. The multi-prong front propagates until the whole specimen has transformed to M, when the upper stress plateau terminates (see also Feng and Sun [2006]). Further loading of the *M* phase leads to a stiff homogeneous response. Deformation remains homogeneous during unloading also until the stress drops below a critical level which can cannot sustain M, and starts to transform back to *A*. The deformation in the tube localizes into a spiral band of relatively low deformation of the *A* phase, which lengthens and

widens as the lower stress plateau is traced until most of the specimen has transformed back to A.

By contrast, the compression is significantly different. As Fig. 1.3a shows, the $A \rightarrow M$ transformation under compression initiates at a much higher stress and induces a transformation strain that is nearly half that of the tensile one. The reverse transformation also starts at a stress that is higher than the lower plateau in tension and the response also forms a closed hysteresis. More importantly, however, during the whole loading/unloading cycle under compression the response of the tube shows a positive tangent stiffness and the associated deformation is essentially homogeneous as illustrated in the DIC strain contours in Fig. 1.3c (see Fig. 5 and related text in Bechle and Kyriakides [2014]).

In summary, the diffusionless transformations between highly symmetric A phase and monoclinic M phase induced by thermal and/or mechanical loads are responsible for the shape memory effect and pseudoelasticity of NiTi. An important characteristic of NiTi in pseudoelastic regime is the significant asymmetry between tension and compression, and the difference between the homogenous versus inhomogeneous deformations.

1.2 Applications of SMAs

The unique properties of SMAs like NiTi have been utilized in various practical applications during the last 30 years. The relatively large recoverable inelastic strain associated with twinning/detwinning of M (shape memory effect) or reversible $A \leftrightarrow M$ transformations (pseudoelasticity) makes SMAs a candidate material for actuation, but also other purposes. One of the earliest known uses of NiTi is in the form of hydraulic tube couplings used to join titanium tubing on the U.S. Navy/Grumman F-14A developed

by Raychem Corporation in 1971 (see Fig. 1.4a from [http://intrinsicdevices.com/history.html]; see also Kauffman and Mayo [1997], Van Humbeeck [1999]).

Strelec et al. [2003] proposed a design of a reconfigurable airfoil (Fig. 1.4b) using SMA wires as actuators attached on the inside of an airfoil, which can alter the shape of the airfoil. Consequently, the wing is capable to actively change its geometry and efficiently accommodate the flows experienced in different flight regimes.

Up to 1984, shocks induced by pyrotechnic release mechanisms were responsible for nearly 14% of failures, more than half of which lead to abortion of space missions, as shown by a 1985 study (Godard et al. [2003]). One option to resolve the shock problem caused by pyrotechnic release mechanisms is to replace them with non-explosive low-shock release mechanism based on SMAs that provides large strains in a reasonably timely manner. For example, in the non-explosive separation device proposed by Johnson [1992], the actuating element comprised of a shape memory alloy recovers from an armed shape to a memory shape when it is heated through the phase transformation temperature.

The shape memory effect was also exploited in the development of the hinge and deployment system (Fig. 1.4c) in the Lightweight Flexible Solar Array (LFSA) program, as reported by Carpenter and Lyons [2001] and other sources. The SMA hinge can deploy the folded solar panels upon heating in approximately 30s.

The actuation function of SMAs is also employed to actively modulate shapes in order to create structures with variable geometries. Mani et al. [2003] developed a micro-electromechanical systems (MEMS) based design for activating the surface of aerial and underwater vehicles for the purpose of reducing drag. The MEMS incorporate thin film SMA actuators, which generate a transversely acting traveling waveform like force on the

surface which changes the viscous sub-layer of the flow, resulting in significant reduction of turbulent drag.

A method for reducing the noise of jet engines during take-off and landing involves the installation of chevrons along the trailing edges of a jet engine's primary and secondary exhaust nozzle as shown in Fig. 1.4d (e.g., Calkins et al. [2006]). The chevrons are thermally actuated by NiTi shape memory alloy beams attached to them, which actively drive the motion of the chevrons to accommodate with the change of air flow under different flight conditions (take off, cruise, etc.).

NiTi is also broadly used in medical applications due to its biocompatibility and bio-functionality (Shabalovskaya [1995]). In addition, NiTi shows higher corrosion resistance and better stability than most alloys used in medicine and dentistry (Speck and Fraker [1980]). These characteristics, in addition to the large strain associated with pseudoelastic behavior, have popularized NiTi orthodontic archwires (see Fig. 1.5a extracted from Fernandes et al. [2011]; see also Andreasen and Hilleman [1971]). Another dental medicine application is the adoption of NiTi to make rotary PathFiles that are used to create the glide path in root canals (see Fig. 1.5b from Berutti et al. [2009]).

In addition to dental orthodontics, NiTi is also widely used in the cardiovascular field. A well-known class of products is the self-expandable vascular stents (see Petrini and Migliavacca [2011]). Such stents inserted in stenotic vessels blocked by atherosclerotic deposits, allow recovery of the blood flow to peripheral tissues. Three examples of SMA stents are shown in Fig. 1.5c.

Another application of SMAs that exploits their hysteretic energy dissipation of the pseudoelastic regime as dampers. For example, in seismic applications, they are used to dissipate ground vibration energy (Dolce et al. [2000], Dolce and Cardone [2000]). The recovery of deformation upon unloading (recentering) saves the cost of replacement

after seismic events if conventional metallic dampers were used. The stress plateaus during phase transformations make it feasible to control the forces transmitted to the structure. Strain hardening at large strain levels (> 6%) as phase transformation completes restore the stiffness of the damper. Sharabash and Andrawes [2009] reported a design of SMA-based passive seismic control dampers implemented at the deck-pier and deck-tower connections in cable-stayed bridges. It was demonstrated that the SMA dampers can reduce the maximum bridge displacement, tower base shear and tower base moment by nearly 70% compared to the same bridge structures that use shock-transmission devices. Asgarian and Moradi [2011] showed that using pseudoelastic SMA braces in steel frames effectively reduces residual roof displacement and peak inter-story drift in nonlinear time history analyses, compared to the same frames equipped with buckling restrained braces.

The latent heat absorbed or released during the forward/reverse transformations in SMAs is also exploited to develop cooling systems. Elastocaloric cooling (eC) is a solid-state cooling mechanism that harnesses the latent heat of reversible martensitic transformation. Cui et al. [2012] have shown that eC can have the coefficient of performance (the ratio between the latent heat and the external mechanical work to induce the phase transformation) as high as about 11 with a directly measured temperature change of 17^{o}C. Moya et al. [2014] report that among the major eC materials prototypical shape memory alloys of NiTi show the largest eC effect with temperature change of 20-40 K and chemical doping can suppress mechanical fatigue and both hysteresis and thermal fatigue. The application of solid-state cryogenic mechanisms using SMAs or other caloric materials can eliminate the global warming of refrigerants such as HCFCs/HFCs, which have been found to be a significant source of greenhouse gas emissions.

This wide use of SMAs in devices and structures points to the need for more effective constitutive models that capture all aspects of their thermomechanical behavior.

1.3 A Brief Review on Constitutive Models for SMAs

Driven by the need to model and analyze SMA structures, a number of phenomenological constitutive models for SMAs have been developed during the last 20 years. Abeyaratne and Knowles [1993, 2006] introduced a double-well potential function to account for the material instability but its use is limited to one-dimensional problems. Lubliner and Auricchio [1996] proposed a 1-D constitutive model for SMAs in which the single-variant martensite volume fraction is taken as the internal variable and its evolution follows a flow rule confined by the transformation surfaces defined in the stress-temperature space. This model was later extended by Auricchio et al. [1997] to 3-D with the addition of the reorientation of martensite and further generalized to finite strain cases by Auricchio and Taylor [1997]. The model proposed for SMAs by Boyd and Lagoudas [1996] decomposes the free energy density into the sum of free energy densities of the two phases weighted by the martensite volume fraction in addition to a contribution from the mix of the two phases. Raniecki and Lexcellent [1998] and Qidwai and Lagoudas [2000] introduced several transformation functions expressed in terms of the three invariants of the stress tensor in order to enable tension/compression asymmetry and volumetric transformation strain. Aleong et al. [2002] adopted a Drucker-Prager criterion that involves the second and third invariants of the stress tensor to address the measured tension/compression asymmetry in the critical stresses of SMAs. Auricchio and Petrini [2004] developed a three-dimensional model for stress-temperature induced solid phase transformation with the transformation strain as the internal variable, which

includes a Prager-Lode type limit surface to induce different critical stresses under tension and compression. Panico and Brinson [2007] and Popov and Lagoudas [2007] took the stress-induced martensite fraction and the temperature-induced martensite fraction as separate internal variables and described martensite reorientation independently from austenite to martensite transformation. Hartl and Lagoudas [2009] extended this idea to include plastic yielding into the constitutive model by adding a back stress term that governs the flow rule of plastic strain. Arghavani et al. [2010] presented a model in which the amount and orientation of the transformation strain evolve separately and the two mechanisms inducing inelastic strains, i.e., transformation and reorientation, are decoupled. Sedlak et al. [2012] presents a thermomechanical model for polycrystalline NiTi-based SMAs that also separates the transformation and reorientation. What makes this model distinct from others is that it introduces the second and third invariants of the transformation strain tensor, rather than those of the stress tensor, to represent the tension/compression asymmetry. Based on the micro-plane modeling approach, Karamooz Ravari et al. [2015] incorporated the tension/compression asymmetry exhibited in SMAs by adopting an equivalent stress based on the second and third invariants of the deviatoric stress tensor.

The asymmetry between the stress and strain levels under tension and those under compression has been reported and investigated over the last 20 years. However, the vital difference between inhomogeneous deformation under tension versus homogenous deformation under compression has not drawn sufficient attention. Recent experiments have shown this asymmetry to play a major role in structural behavior in NiTi. This need and the way we incorporate all aspects of asymmetry in at least the pseudoelastic temperature regime are addressed in this dissertation.

1.4 OUTLINE

This dissertation presents a constitutive model framework for pseudoelastic NiTi, which features the reversible hysteretic behavior of the material. The model addresses the tension/compression asymmetry, including the inhomogeneous deformation observed under primarily tensile stress states. The performance of the constitutive model is then evaluated in numerical simulations of the response and stability of four nonlinear NiTi structures that were previously studied experimentally. Chapter 2 describes the formulation of the J_2-type kinematic hardening constitutive model framework developed. This is followed by the associated algorithm for numerical implementation based on backward Euler integration scheme, and derivation of the tangent stiffness tensor.

Chapter 3 first reviews experimental results that demonstrate the buckling and recovery of a thin-walled pseudoelastic NiTi tube under axial compression. The constitutive model is implemented in a finite element model used to numerical simulate the buckling experiment. Comparison of the predictions with the measurements leads to a progressive improvement of the constitutive model bringing into the fold features like plastic effects that follow the of transformation of martensite, and the tension compression asymmetry, each resulting in improvement of the predictions.

In Chapter 4, the constitutive model framework is incorporated in the numerical analysis on a uniaxial tension test of a long, thin NiTi strip. The problem is dominated by inhomogeneous deformations induced by the phase transformations. Chapter 5 uses the constitutive model in numerical simulations of a second tensile test this time on a NiTi tube, where the tubular geometry imposes helical and multi-pronged localization patterns.

In Chapter 6, uses the model to simulate the highly inhomogeneous deformation observed in bending experiments on NiTi tubes. The constitutive model, calibrated to both the very asymmetric tensile and compressive uniaxial responses of NiTi, is

incorporated in a FE model of the pure bending of NiTi tubes. The numerical model is then used to study the problem in detail, and the strong effect of the material asymmetry on the results. Finally, Chapter 7 summarizes the overall conclusions derived from this study.

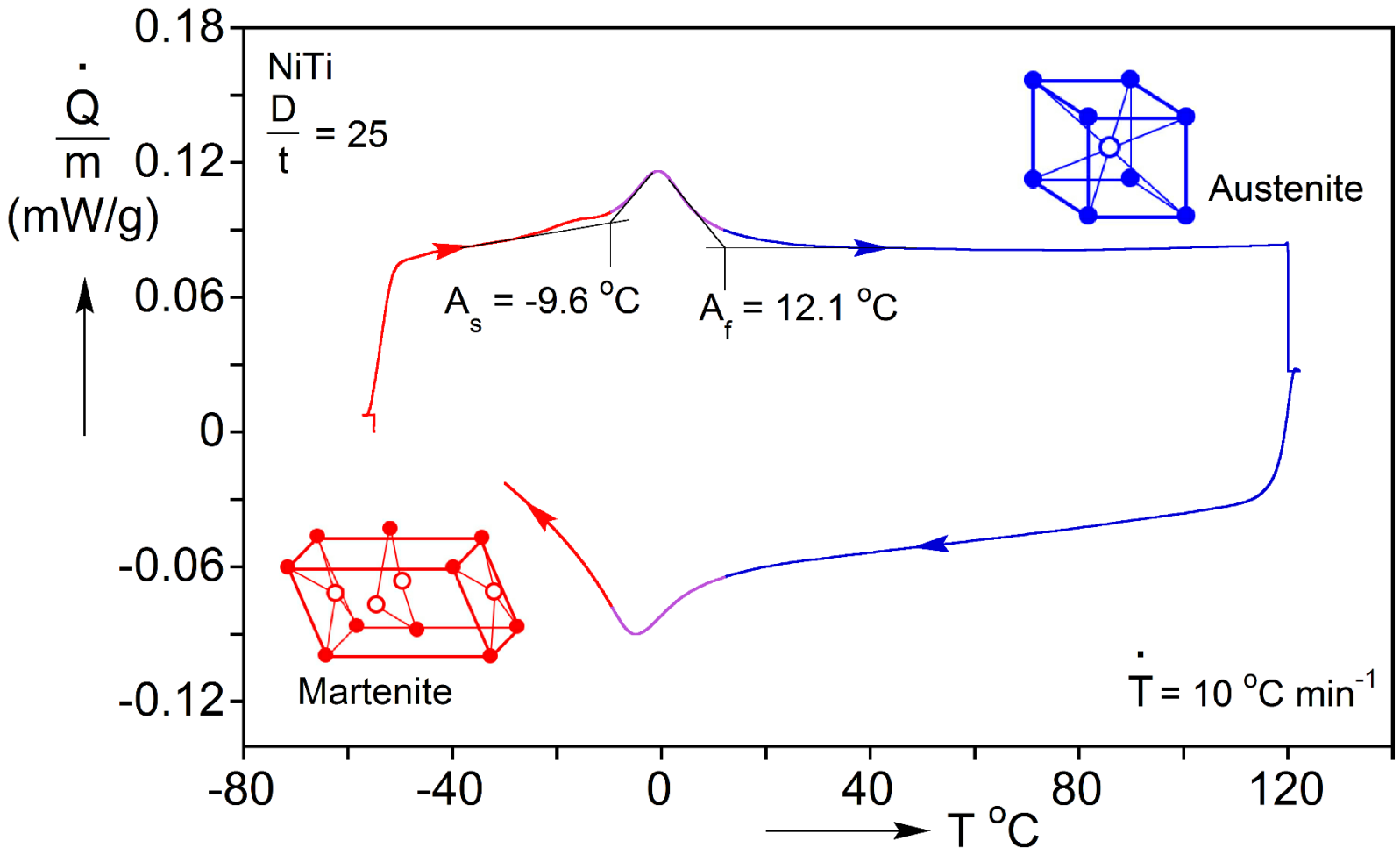

Fig. 1.1 The differential scanning calorimetry (DSC) thermogram of NiTi tube stock (from Bechle [2016]) with schematics of the corresponding crystallographic lattices.

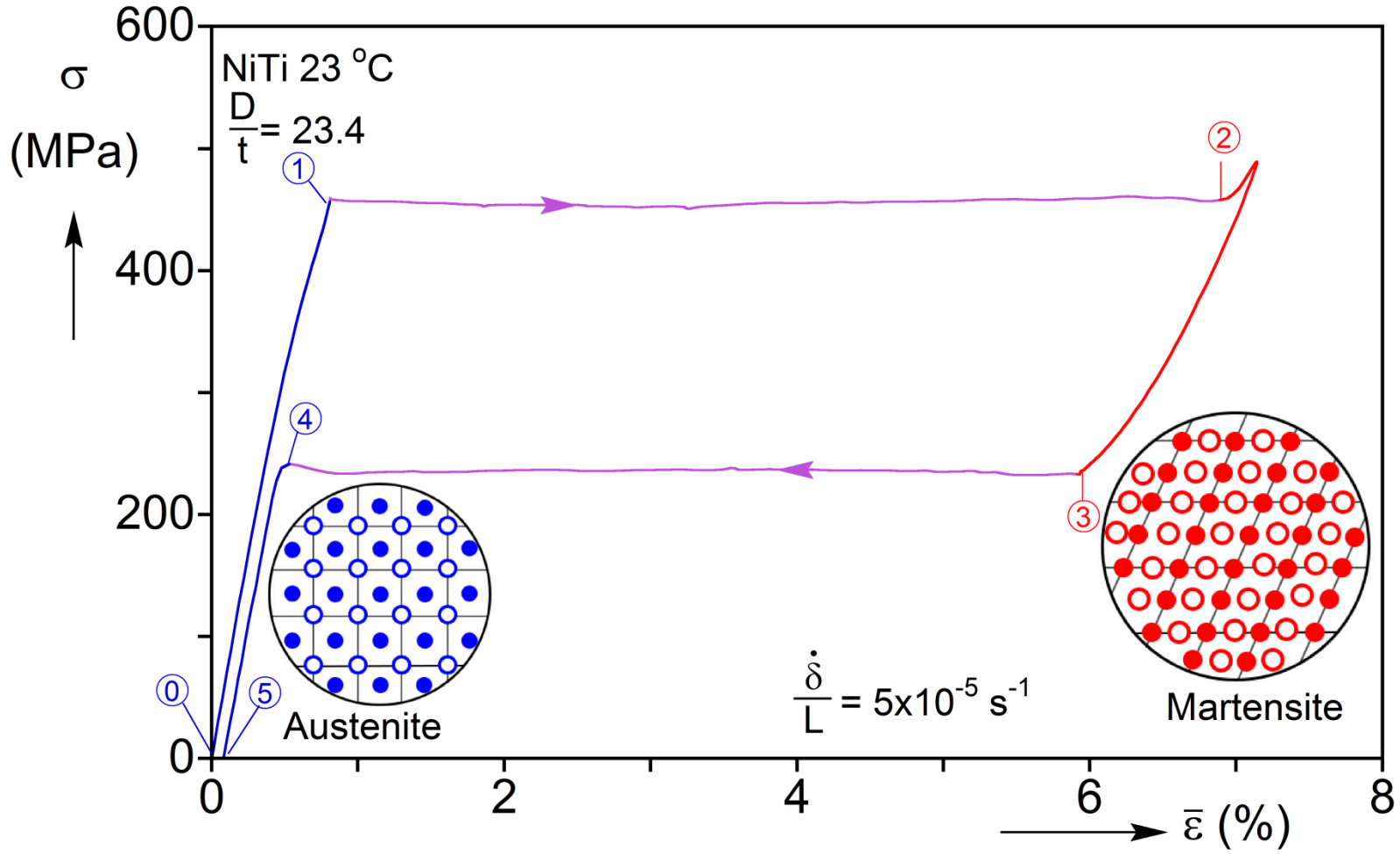

Fig. 1.2 The digital scanning calorimetry (DSC) thermogram of NiTi tube stock (from Bechle [2016]) with schematics of the corresponding crystallographic lattices.

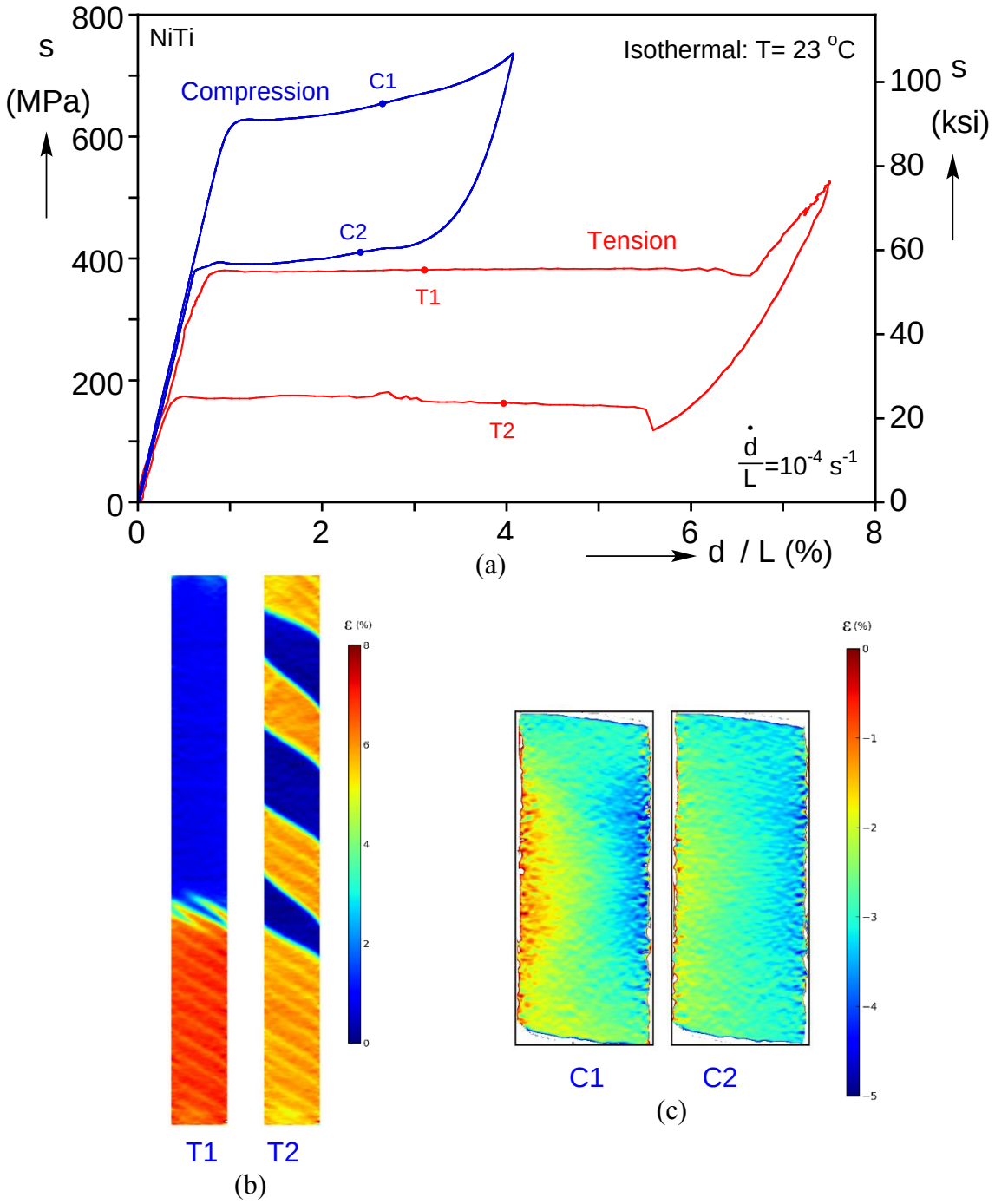

Fig. 1.3 Tension-compression asymmetry in uniaxial loading of pseudoelastic NiTi tubes. (a) Axial stress-elongation/shortening responses. (b) Representative DIC deformation contours during tensile loading and unloading exhibiting helical localization patterns and (c) nearly homogeneous deformation during compressive loading and unloading.

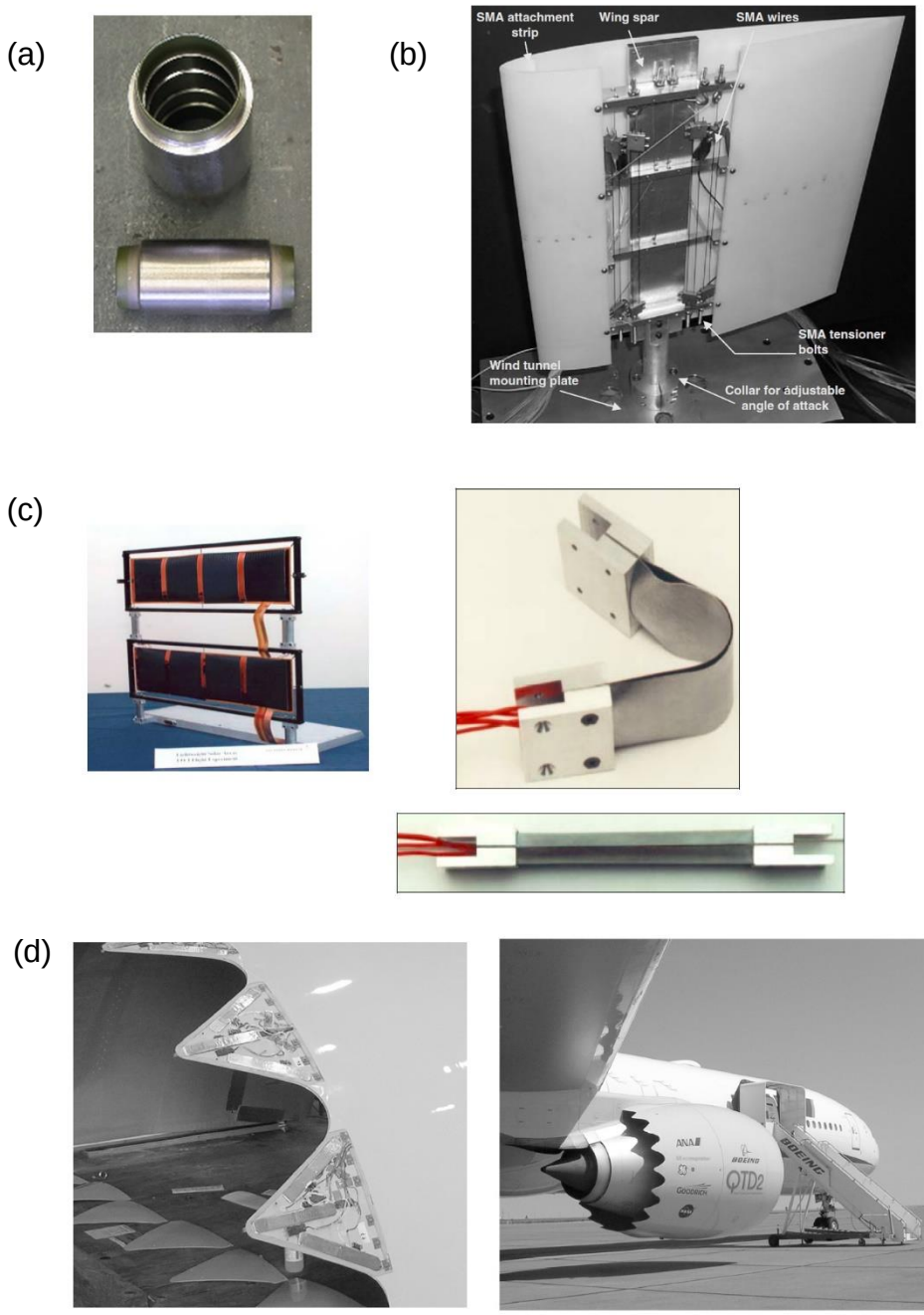

Fig. 1.4 Applications of SMAs in aerospace: (a) CryoFit ® hydraulic tube coupling; (b) Reconfigurable airfoil; (c) Solar panel (left) connected by SMA hinges and the hinge in stowed (right top) and deployed (right bottom) states in LFSA program. (d) A Variable Geometry Chevron (VGC) with covers off showing 3 NiTi actuators per VGC (left) and mounted on GE-115B ready for flight. (Citations in the text)

(a)

(b)

(c)

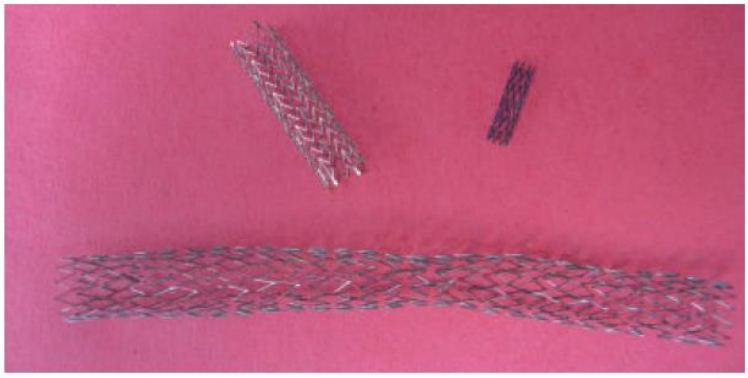

Fig. 1.5 Applications of SMAs in medicine: (a) NiTi orthodontic archwires; (b) NiTi rotary PathFile; (c) Examples of SMA stents (top right) coronary stent, (top left) carotid stent and (bottom left) femoral stent. (Citations in the text.)

Chapter 2: CONSTITUTIVE MODELING FRAMEWORK

2.1 BASIC FORMULATION

Let σ_{ij} and s_{ij} be the stress tensor components and the deviatoric counterparts. The strain tensor is decomposed into elastic, transformation and plastic strains, i.e. $\varepsilon_{ij} = \varepsilon_{ij}^e + \varepsilon_{ij}^t + \varepsilon_{ij}^p$. The transformation strain is governed by a J_2-type kinematic hardening mechanism and the plastic strain evolves according to J_2 isotropic hardening. In this dissertation, plasticity is only used in Chapter 3 and turned off for the work reported in remaining chapters.

The following Helmholtz free energy density is introduced:

$$\psi = \frac{1}{2} C_{ijkl}(\varepsilon_{ij} - \varepsilon_{ij}^t - \varepsilon_{ij}^p)(\varepsilon_{kl} - \varepsilon_{kl}^t - \varepsilon_{kl}^p) + \psi^t(\varepsilon_{ij}^t), \tag{2.1}$$

in which the first term is the elastic strain energy stored per unit volume and the second term represents the part of the free energy attributed to martensitic transformation. C_{ijkl} are the components of the linear elastic stiffness tensor, which may depend on the transformation strain, i.e. $C_{ijkl} = C_{ijkl}(\varepsilon_{mn}^t)$.

The isothermal form of the second law of thermodynamics requires that the dissipation rate for any possible process must be non-negative, i.e.

$$\dot{\Delta} = \sigma_{ij}\dot{\varepsilon}_{ij} - \dot{\psi} \geq 0. \tag{2.2}$$

Together with the following definitions,

$$\bar{\sigma}_{ij} = \frac{1}{2}\frac{\partial S_{pqrs}}{\partial \varepsilon_{ij}^t}\sigma_{pq}\sigma_{rs} \tag{2.3a}$$

$$\sigma_{ij} = \frac{\partial \psi}{\partial \varepsilon_{ij}} = C_{ijkl}(\varepsilon_{kl} - \varepsilon_{kl}^t) \tag{2.3b}$$

$$\sigma_{ij}^B = \frac{\partial \psi^t}{\partial \varepsilon_{ij}^t} \tag{2.3c}$$

$$\hat{\sigma}_{ij} = \sigma_{ij} - \sigma_{ij}^B + \bar{\sigma}_{ij} \tag{2.3d}$$

the second law expressed in (2.2) may be re-organized as

$$\dot{\Delta} = \hat{\sigma}_{ij}\dot{\varepsilon}^t_{ij} + \sigma_{ij}\dot{\varepsilon}^p_{ij} \geq 0 \tag{2.4}$$

Note that S_{ijkl} are the components of the elastic compliance tensor, which is the inverse of the elastic stiffness tensor, i.e., $S_{ijkl} = (C^{-1})_{ijkl}$.

It is assumed that elastic deformation is enclosed by both a transformation surface $\Phi^t(\hat{\sigma}_{ij}, \varepsilon^t_{ij}) = 0$ and a yield surface $\Phi^p(\sigma_{ij}, \varepsilon^p_e) = 0$, and transformation (plastic yielding) may occur if $\hat{\sigma}_{ij}(\sigma_{ij})$ lies on the transformation (yield) surface. The variable ε^p_e is the accumulated plastic strain defined as

$$\varepsilon^p_e = \int_0^t (2\dot{\varepsilon}^p_{ij}\dot{\varepsilon}^p_{ij}/3)^{1/2} dt\,. \tag{2.5}$$

Stress states outside the transformation or yield surfaces are forbidden. It is assumed that both transformation and plastic straining abide by the maximum dissipation postulate, and hence both surfaces must be convex and the transformation and plastic strain increments follow associated flow rules:

$$\dot{\varepsilon}^t_{ij} = \lambda^t \frac{\partial \Phi^t}{\partial \hat{\sigma}_{ij}}. \tag{2.6}$$

$$\dot{\varepsilon}^p_{ij} = \lambda^p \frac{\partial \Phi^p}{\partial \sigma_{ij}}. \tag{2.7}$$

Equations (2.6-7) indicate that the transformation strain increment and the plastic strain increment are normal to the corresponding surfaces. Additionally, λ^t and λ^p are non-negative multipliers that are determined from consistency conditions. Note that along with the maximum dissipation postulate which implies convexity of the surfaces and normality for the flow rules, (2.4) is then satisfied as long as $\Phi^t(\hat{\sigma}_{ij} = 0, \varepsilon^t_{ij}) \leq 0$ and $\Phi^p(\sigma_{ij} = 0, \varepsilon^p_e) \leq 0$. The loading and unloading conditions can also be recast as the Kuhn-Tucker conditions:

$$\lambda^t \geq 0, \Phi^t \leq 0, \lambda^t \Phi^t = 0. \tag{2.8a}$$

$$\lambda^p \geq 0, \Phi^p \leq 0, \lambda^p \Phi^p = 0 \tag{2.8b}$$

To derive the continuum tangent behavior for this model, we define

$$U_{ijkl} = \frac{1}{2} \frac{\partial^2 S_{pqrs}}{\partial \varepsilon^t_{ij} \partial \varepsilon^t_{kl}} \sigma_{pq} \sigma_{rs}, \tag{2.9}$$

$$H_{ijkl} = \frac{\partial^2 \psi^t}{\partial \varepsilon^t_{ij} \partial \varepsilon^t_{kl}}, \tag{2.10}$$

$$\hat{\varepsilon}_{ij} = \frac{\partial \Phi^t}{\partial \hat{\sigma}_{ij}} + \frac{\partial \Phi^t}{\partial \hat{\sigma}_{kl}} \frac{\partial S_{mnij}}{\partial \varepsilon^t_{kl}} \sigma_{mn}, \tag{2.11}$$

in which case the consistency conditions, $\dot{\Phi}^t = 0$ and $\dot{\Phi}^p = 0$, lead to the following equations:

$$\begin{pmatrix} A^{tt} & A^{tp} \\ A^{pt} & A^{pp} \end{pmatrix} \begin{bmatrix} \lambda^t \\ \lambda^p \end{bmatrix} = \begin{bmatrix} b^t \\ b^p \end{bmatrix}, \tag{2.12}$$

where

$$A^{tt} = \hat{\varepsilon}_{ij} C_{ijkl} \hat{\varepsilon}_{kl} + \frac{\partial \Phi^t}{\partial \hat{\sigma}_{ij}} (H_{ijkl} - U_{ijkl}) \frac{\partial \Phi^t}{\partial \hat{\sigma}_{kl}} - \frac{\partial \Phi^t}{\partial \varepsilon^t_{ij}} \frac{\partial \Phi^t}{\partial \varepsilon^t_{ij}}, \tag{2.13}$$

$$A^{tp} = A^{pt} = \hat{\varepsilon}_{ij} C_{ijkl} \frac{\partial \Phi^p}{\partial \sigma_{kl}}, \tag{2.14}$$

$$A^{pp} = \frac{\partial \Phi^p}{\partial \sigma_{ij}} C_{ijkl} \frac{\partial \Phi^p}{\partial \sigma_{kl}} - \frac{\partial \Phi^p}{\partial \bar{\varepsilon}^p} \sqrt{\frac{2}{3} \frac{\partial \Phi^p}{\partial \sigma_{ij}} \frac{\partial \Phi^p}{\partial \sigma_{ij}}}, \tag{2.15}$$

$$b^t = \hat{\varepsilon}_{ij} C_{ijkl} \dot{\varepsilon}_{kl}, \text{ and} \tag{2.16}$$

$$b^p = \frac{\partial \Phi^p}{\partial \sigma_{ij}} c_{ijkl} \dot{\varepsilon}_{kl}. \tag{2.17}$$

The multipliers λ^t and λ^p are solved from (2.12), given the variables at the current state and the stain increment $\dot{\varepsilon}_{ij}$. Note that if both $\Phi^t < 0$ and $\Phi^p < 0$, then both $\lambda^t = 0$ and $\lambda^p = 0$, hence this increment exhibits elastic behavior. If $\Phi^t = 0$ and $\Phi^p < 0$, then λ^t is solved from (2.12) using $\lambda^p = 0$. The solution to the multipliers is

then used in (2.6) and (2.7), which are in turn applied within the rate form of (2.3b) to obtain the continuum stress increment versus strain increment behavior. The solution to (2.12) can be written in the following form:

$$\lambda^t = L^t_{mn}\dot{\varepsilon}_{mn}\,. \tag{2.18a}$$

$$\lambda^p = L^p_{mn}\dot{\varepsilon}_{mn}\,. \tag{2.18b}$$

Then the incremental stress-strain relationships are

$$\dot{\sigma}_{ij} = \left(C_{ijkl} - C_{ijmn}\frac{\partial \Phi^t}{\partial \hat{\sigma}_{mn}} L^t_{kl} - C_{ijmn}\frac{\partial \Phi^p}{\partial \sigma_{mn}} L^p_{kl} \right)\dot{\varepsilon}_{kl} \tag{2.19}$$

The terms within the parentheses are the components of the continuum tangent modulus.

The material properties that need to be specified for the constitutive model include the dependence of the elastic properties on the transformation strain, the transformation function Φ^t, the yield function Φ^p and the back stress potential ψ^t.

For the sake of simplicity, we assumed that the elastic properties are independent of the transformation strain and represented by a constant Young's modulus E and Poisson's ratio ν. As a result, $\bar{\sigma}_{ij}$ and U_{ijkl} vanish. The following J_2-type transformation function Φ^t and yield function Φ^p are adopted,

$$\Phi^t = 3(s_{ij} - s^B_{ij})(s_{ij} - s^B_{ij})/2 - \sigma_o^2 = 0 \tag{2.20}$$

$$\Phi^p = 3s_{ij}s_{ij}/2 - \sigma_e^2 = 0 \tag{2.21}$$

where σ_o represents the size of the transformation surface, which may be dependent on transformation strain, and $\sigma^p_e(\varepsilon^p_e)$ is the yield strength that hardens as plastic deformation accumulates.

Recall that the back stress is related to the transformation strain through a potential ψ^t, as shown in Eq. (2.3c). The tension/compression asymmetry in the stress-strain behavior is introduced through the following representation of the potential

$$\psi^t = \xi\psi^t_c(\varepsilon^t_e) + (1-\xi)\psi^t_t(\varepsilon^t_e)\,, \tag{2.22}$$

where ψ_c^t and ψ_t^t are potentials that are calibrated to the measured uniaxial compressive and tensile stress-transformation strain responses, and ε_e^t is an equivalent transformation strain that governs the strain asymmetry. The following definition of equivalent transformation strain is adopted

$$\varepsilon_e^t = J'_2 \, f(J_r), J_r = J'_3 / J'_2 \tag{2.23a}$$

with

$$f = \cos\{\cos^{-1}[1 - a(J_r^3 + 1)] / 3\}, \tag{2.23b}$$

where the following definitions of the deviatoric strain invariants hold

$$J'_2 = (2e_{ij}^t e_{ij}^t / 3)^{1/2}, J'_3 = (4e_{ij}^t e_{jk}^t e_{ki}^t / 3)^{1/3} \text{ and } e_{ij}^t = \varepsilon_{ij}^t - \varepsilon_{kk}^t \delta_{ij} / 3. \tag{2.23c}$$

The function f scales the uniaxial compressive transformation strain to the tensile one.

The weight function χ, chosen to be a function of the ratio of the deviatoric strain invariants, J_r, facilitates the generalization of these results to arbitrary strain states. $J_r = 1$ represents uniaxial extension and $J_r = -1$ represents uniaxial contraction. Thus, $\chi(J_r)$ with

$$\chi(-1) = 1 \text{ and } \chi(1) = 0, \tag{2.24a}$$

interpolates between the tensile and compressive responses. In addition, to ensure that the hardening moduli remain finite as $J_r \to 0$

$$\chi'(0) = 0, \ \chi''(0) = 0, \ \chi^{iv}(0) = 0 \text{ and } \chi^{v}(0) = 0. \tag{2.24b}$$

The back stress then becomes

$$\sigma_{ij}^B = \xi \frac{d\psi_c^t}{d\varepsilon_e^t} \frac{\partial \varepsilon_e^t}{\partial \varepsilon_{ij}^t} + (1 - \xi) \frac{d\psi_t^t}{d\varepsilon_e^t} \frac{\partial \varepsilon_e^t}{\partial \varepsilon_{ij}^t} + \xi'(J_r)(\psi_c^t - \psi_t^t) \frac{\partial J_r}{\partial \varepsilon_{ij}^t}. \tag{2.25}$$

It can be shown that reduction of Eq. (2.25) to uniaxial stress states (see Appendix A) results in

$$\sigma_{11c}^B = \frac{d\psi_c^t}{d\varepsilon_e^t} \frac{\partial \varepsilon_e^t}{\partial \varepsilon_{11}^t} \quad \text{and} \quad \sigma_{11t}^B = \frac{d\psi_t^t}{d\varepsilon_e^t} \frac{\partial \varepsilon_e^t}{\partial \varepsilon_{11}^t} \tag{2.26}$$

for compression and tension respectively. In view of the kinematic hardening model adopted, and the reductions in Appendix A, Eqs. (2.26) imply:

$$|\sigma_{11c}| - f(-1)\frac{d\psi_c^t}{d\varepsilon_e^t} = \sigma_{oc} \quad \text{and} \quad \sigma_{11t} - f(1)\frac{d\psi_t^t}{d\varepsilon_e^t} = \sigma_{ot} \tag{2.27}$$

for loading, where s_{oc} and s_{ot} represent the sizes of the compressive and tensile transformation surfaces (the LHS becomes negative for unloading).

The function ξ extends the model to general strain states and ultimately should be calibrated to experimental results. Without such results, the following expression is adopted for the calculations presented in subsequent chapters which satisfies the conditions (2.24),

$$\xi(J_r) = \frac{f(J_r) - f(1)}{f(-1) - f(1)}. \tag{2.28}$$

The constitutive model outlined above is implemented into a user-defined material subroutine (UMAT) in ABAQUS. In the UMAT, the constitutive equations are discretized according to a backward Euler routine and are solved by Newton's method. In each of the following chapters, the model is customized to the specific problem and calibrated accordingly.

The major challenge of the model calibration is the selection of the two potentials ψ_c^t and ψ_t^t. As shown in Eq. (2.25), the expression of the back stress includes a term related to the difference between these two potentials. Experience from the numerical studies on the structural problems presented in the following chapters indicates that the difference between the two potentials should be as small as possible, e.g., the derivatives of the two potentials shown in Fig. 2.1, in order to circumvent potential numerical difficulties that would terminate the finite element calculations. This requirement is similar to the condition described in Landis [2003a] that the remanent strain along

various loading paths should saturate at the same equivalent value for polycrystalline ferroelastic materials.

2.2 NUMERICAL IMPLEMENTATION WITHOUT PLASTICITY

For most of the work presented in this dissertation, plasticity is excluded in the model by enforcing $\varepsilon_{ij}^{p} = 0$ in Section 2.1. This section presents the numerical implementation of the constitutive model with the plastic part deactivated.

2.2.1 Backward Euler Integration Routine

A UMAT is a type of user-defined subroutine that allows users to implement constitutive models that are not included in the intrinsic material library of ABAQUS in finite element calculations. Each time a UMAT is called at a quadrature point, the stress, strain and state variables at the beginning of the time increment t_n are passed in together with a strain increment tensor estimated by the finite element solver. The UMAT should be programmed such that stress, strain and state variables at the end of the time increment t_{n+1} and the tangent stiffness for this time increment are correctly calculated.

Assume that $(\sigma_{ij}^{n}, \varepsilon_{ij}^{n}, \varepsilon_{ij}^{t,n})$ represent the stress, strain and transformation strain (state variables for this constitutive model) at time t_n and $\Delta\varepsilon_{ij}$ is the strain increment for this quadrature point, all variables at time t_{n+1} are solved through the following time-discrete system (superscripts n+1 for variables at time t_{n+1} are dropped for simplicity):

$$\varepsilon_{ij} = \varepsilon_{ij}^{n} + \Delta\varepsilon_{ij} \tag{2.29a}$$

$$\sigma_{ij} = C_{ijkl}(\varepsilon_{kl} - \varepsilon_{kl}^{t,n} - \Delta\varepsilon_{kl}^{t}) \tag{2.29b}$$

$$\Delta\varepsilon_{ij}^{t} = 3\lambda^{t}(s_{ij} - s_{ij}^{B}) \tag{2.29c}$$

$$\Phi^{t} = 3(s_{ij} - s_{ij}^{B})(s_{ij} - s_{ij}^{B})/2 - \sigma_{o}^{2} \tag{2.29d}$$

supplemented by Kuhn-Tucker conditions:

$$\lambda^t \geq 0, \Phi^t \leq 0, \Lambda^t \Phi^t = 0 \tag{2.29e}$$

where $\Delta\varepsilon_{ij}^t$ are the increments of the transformation strain components and the deviatoric back stress components s_{ij}^B are calculated based on the updated transformation strain $\varepsilon_{ij}^{t,n} + \Delta\varepsilon_{ij}^t$.

Note that the transformation strain is volume preserving in this model, i.e. $\varepsilon_{kk}^t = 0$, and the volumetric deformation is purely elastic as indicated by the transformation function (2.29d). Hence, the integration routine can focus on the deviatoric part of the stress and strain tensors. Consequently, Eq. (2.29b) is replaced by

$$s_{ij} = 2\mu(e_{ij} - \varepsilon_{ij}^{t,n} - \Delta\varepsilon_{ij}^t) \tag{2.29f}$$

where μ is the shear modulus and e_{ij} are the components of the deviatoric strain tensor at time t_{n+1}.

The integration routine is called backward Euler because Eq. (2.29e) is required to be numerically satisfied at time t_{n+1}. A classical elastic prediction-transformation correction return mapping algorithm is adopted to solve the above system of equations. First, an elastic trial state is evaluated by freezing the passed-in transformation strain:

$$s_{ij}^{trial} = 2\mu(e_{ij} - \varepsilon_{ij}^{t,n}) \tag{2.30a}$$

$$\Phi^{t,trial} = 3[s_{ij}^{trial} - s_{ij}^B(\varepsilon_{kl}^{t,n})][s_{ij}^{trial} - s_{ij}^B(\varepsilon_{kl}^{t,n})]/2 - [\sigma_o(\varepsilon_{kl}^{t,n})]^2 \tag{2.30b}$$

If $\Phi^{t,trial} \leq 0$, this elastic prediction is accepted as the state at time t_{n+1}. Otherwise, a Newton-Raphson iteration scheme must be performed to obtain a new state such that the above system of equations (2.29a-f) is satisfied to within some tolerance.

For numerical convenience, we reorganize the above system of equations as follows.

Since $\Phi^t = 0$ holds for any inelastic increment, the combination of Eqs. (2.29c) and (2.29d) leads to

$$\Phi^t = \frac{3}{2}\frac{\Delta\varepsilon_{ij}^t \Delta\varepsilon_{ij}^t}{(3\lambda^t)^2} - \sigma_o^2 = 0 \tag{2.31a}$$

Thus

$$3\lambda^t = \frac{3}{2\sigma_o}\sqrt{\frac{2}{3}\Delta\varepsilon_{ij}^t \Delta\varepsilon_{ij}^t} := \frac{3\Delta\varepsilon_e^t}{2\sigma_o} \tag{2.31b}$$

where $\Delta\varepsilon_e^t = \sqrt{2\Delta\varepsilon_{ij}^t \Delta\varepsilon_{ij}^t / 3}$.

Combined with Eqs. (2.29f) and (2.31b), the flow rule (2.29c) can be rewritten as

$$\Delta\varepsilon_{ij}^t - \frac{3\Delta\varepsilon_e^t}{2\sigma_o}[2\mu(e_{ij} - \varepsilon_{ij}^{t,n} - \Delta\varepsilon_{ij}^t) - s_{ij}^B(\varepsilon_{kl}^{t,n} + \Delta\varepsilon_{kl}^t)] = 0, \tag{2.32}$$

which is a nonlinear system of equations for the $\Delta\varepsilon_{ij}^t$ components. Once the $\Delta\varepsilon_{ij}^t$ are solved, all variables at time t_{n+1} can be determined. As a result, the integration routine is reduced to finding the solution to Eq. (2.32).

In order to remove the $\Delta\varepsilon_{ij}^t = 0$ root, we modify (2.32) and define the following residual:

$$r_{ij} = \Delta\varepsilon_{ij}^t / \Delta\varepsilon_e^t - \frac{3}{2\sigma_o}[2\mu(e_{ij} - \varepsilon_{ij}^{t,n} - \Delta\varepsilon_{ij}^t) - s_{ij}^B(\varepsilon_{kl}^{t,n} + \Delta\varepsilon_{kl}^t)] = 0, \tag{2.33}$$

which is of order one and precludes the trivial solution $\Delta\varepsilon_{ij}^t = 0$ for (2.32).

The Newton-Raphson scheme requires the Jacobian of the residual,

$$\begin{aligned} J_{ijkl} &= \frac{\partial r_{ij}}{\partial\Delta\varepsilon_{kl}^t} = \frac{I_{ijkl}}{\Delta\varepsilon_e^t} - \frac{2\Delta\varepsilon_{ij}^t\Delta\varepsilon_{kl}^t}{3(\Delta\varepsilon_e^t)^3} + \frac{3}{2\sigma_o}(2\mu I_{ijkl} + H_{ijkl}) \\ &+ \frac{3}{2\sigma_o^2}[2\mu(e_{ij} - \varepsilon_{ij}^{t,n} - \Delta\varepsilon_{ij}^t) - s_{ij}^B]\frac{\partial\sigma_o}{\partial\varepsilon_{kl}^t} \end{aligned} \tag{2.34}$$

where $I_{ijkl} = (\delta_{ik}\delta_{jl} + \delta_{il}\delta_{jk})/2$ are components of the fourth order identity tensor and $H_{ijkl} = \partial s_{ij}^B / \partial\varepsilon_{kl}^t$ are hardening moduli of the back stress. Note $J_{ijkl} = J_{jikl} = J_{ijlk}$ and $H_{ijkl} = H_{jikl} = H_{ijlk} = H_{klij}$, the last equal sign of which results from the definition of back stress through a potential function.

The process of the Newton-Raphson scheme starts from an initial guess of $\Delta\varepsilon_{ij}^{t}$, designated as $\Delta\varepsilon_{ij}^{t(0)}$. For the ith iteration (i = 0, 1, 2 …), calculate the residual $r_{ij}^{(i)}$ from Eq. (2.33) and check if $\left\|r^{(i)}\right\| \le TOL$, where TOL is the tolerance for convergence, e.g. 1.0×10^{-8}. If yes, $\Delta\varepsilon_{ij}^{t(i)}$ is accepted as the solution. Otherwise, assemble the Jacobian $J_{ijkl}^{(i)}$ and calculate the increment of the unknowns $d\varepsilon_{kl}^{t(i)}$ by solving

$$r_{ij}^{(i)} = -J_{ijkl}^{(i)} d\varepsilon_{kl}^{t(i)}, \tag{2.35a}$$

and update the unkonwns $\Delta\varepsilon_{kl}^{t(i+1)} = \Delta\varepsilon_{kl}^{t(i)} + d\varepsilon_{kl}^{t(i)}$ and the index $i \leftarrow i+1$. The tensorial equation (2.35a) is numerically solved by means of expressing it in the following matrix form:

$$\begin{bmatrix} r_{11}^{(i)} \\ r_{22}^{(i)} \\ r_{33}^{(i)} \\ r_{12}^{(i)} \\ r_{13}^{(i)} \\ r_{23}^{(i)} \end{bmatrix} = -\begin{bmatrix} J_{1111}^{(i)} & J_{1122}^{(i)} & J_{1133}^{(i)} & 2J_{1112}^{(i)} & 2J_{1113}^{(i)} & 2J_{1123}^{(i)} \\ J_{2211}^{(i)} & J_{2222}^{(i)} & J_{2233}^{(i)} & 2J_{2212}^{(i)} & 2J_{2213}^{(i)} & 2J_{2223}^{(i)} \\ J_{3311}^{(i)} & J_{3322}^{(i)} & J_{3333}^{(i)} & 2J_{3312}^{(i)} & 2J_{3313}^{(i)} & 2J_{3323}^{(i)} \\ J_{1211}^{(i)} & J_{1222}^{(i)} & J_{1233}^{(i)} & 2J_{1212}^{(i)} & 2J_{1213}^{(i)} & 2J_{1223}^{(i)} \\ J_{1311}^{(i)} & J_{1322}^{(i)} & J_{1333}^{(i)} & 2J_{1312}^{(i)} & 2J_{1313}^{(i)} & 2J_{1323}^{(i)} \\ J_{2311}^{(i)} & J_{2322}^{(i)} & J_{2333}^{(i)} & 2J_{2312}^{(i)} & 2J_{2313}^{(i)} & 2J_{2323}^{(i)} \end{bmatrix} \begin{bmatrix} d\varepsilon_{11}^{t(i)} \\ d\varepsilon_{22}^{t(i)} \\ d\varepsilon_{33}^{t(i)} \\ d\varepsilon_{12}^{t(i)} \\ d\varepsilon_{13}^{t(i)} \\ d\varepsilon_{23}^{t(i)} \end{bmatrix} \tag{2.35b}$$

through which the components of $d\varepsilon_{ij}^{t(i)}$ are calculated.

The backward Euler integration routine is also illustrated by the flow chart shown in Fig. 2.2.

2.2.2 Tangent Stiffness

Once the solution is obtained, we need to determine the algorithmically consistent tangent stiffness for this time increment, which is defined in the variational form

$$\delta\sigma_{ij} = C_{ijkl}^{\tan}\delta\varepsilon_{kl} \tag{2.36}$$

The variation of the elasticity relation (2.29b) leads to

$$\delta\sigma_{ij} = C_{ijkl}\delta\varepsilon_{kl} - 2\mu\delta\varepsilon_{kl}^{t} \tag{2.37}$$

Comparison between (2.36) and (2.37) suggests that we find the relation between the variation of transformation strain $\delta\varepsilon_{kl}^{t}$ and that of the total strain $\delta\varepsilon_{kl}$. To achieve this, we derive the variation of the residual (2.33) as:

$$0 = \delta r_{ij} = J_{ijkl}\delta\varepsilon_{kl}^{t} + M_{ijkl}\delta\varepsilon_{kl} \tag{2.38}$$

where J_{ijkl} are the Jacobian components and $M_{ijkl} = \partial r_{ij} / \partial\varepsilon_{kl}$,both calculated at the convergence of the Newton-Raphson scheme. Eq. (2.33) indicates that

$$M_{ijkl} = -3\mu(I_{ijkl} - \delta_{ij}\delta_{kl} / 3) / \sigma_o \tag{2.39}$$

Obviously, $M_{ijkl} = M_{jikl} = M_{ijlk} = M_{klij}$.

Eq. (2.38) leads to

$$\delta\varepsilon_{ij}^{t} = P_{ijkl}\delta\varepsilon_{kl} \tag{2.40}$$

where P_{ijkl} satisfy

$$J_{ijmn}P_{mnkl} = -M_{ijkl} \tag{2.41}$$

and are solved by rearranging Eq. (2.41) into the following matrix equation:

$$[J][P] = -[M] \tag{2.42}$$

where

$$[J] = \begin{bmatrix} J_{1111} & J_{1122} & J_{1133} & 2J_{1112} & 2J_{1113} & 2J_{1123} \\ J_{2211} & J_{2222} & J_{2233} & 2J_{2212} & 2J_{2213} & 2J_{2223} \\ J_{3311} & J_{3322} & J_{3322} & 2J_{3312} & 2J_{3313} & 2J_{3323} \\ J_{1211} & J_{1222} & J_{1233} & 2J_{1212} & 2J_{1213} & 2J_{1223} \\ J_{1311} & J_{1322} & J_{1333} & 2J_{1312} & 2J_{1313} & 2J_{1323} \\ J_{2311} & J_{2322} & J_{2333} & 2J_{2312} & 2J_{2313} & 2J_{2323} \end{bmatrix} \tag{2.43a}$$

$$[P] = \begin{bmatrix} P_{1111} & P_{1122} & P_{1133} & P_{1112} & P_{1113} & P_{1123} \\ P_{2211} & P_{2222} & P_{2233} & P_{2212} & P_{2213} & P_{2223} \\ P_{3311} & P_{3322} & P_{3333} & P_{3312} & P_{3313} & P_{3323} \\ P_{1211} & P_{1222} & P_{1233} & P_{1212} & P_{1213} & P_{1223} \\ P_{1311} & P_{1322} & P_{1333} & P_{1312} & P_{1313} & P_{1323} \\ P_{2311} & P_{2322} & P_{2333} & P_{2312} & P_{2313} & P_{2323} \end{bmatrix} \tag{2.43b}$$

$$[M] = \begin{bmatrix} M_{1111} & M_{1122} & M_{1133} & M_{1112} & M_{1113} & M_{1123} \\ M_{2211} & M_{2222} & M_{2233} & M_{2212} & M_{2213} & M_{2223} \\ M_{3311} & M_{3322} & M_{3333} & M_{3312} & M_{3313} & M_{3323} \\ M_{1211} & M_{1222} & M_{1233} & M_{1212} & M_{1213} & M_{1223} \\ M_{1311} & M_{1322} & M_{1333} & M_{1312} & M_{1313} & M_{1323} \\ M_{2311} & M_{2322} & M_{2333} & M_{2312} & M_{2313} & M_{2323} \end{bmatrix} \tag{2.43c}$$

Substitution of (2.40) into (2.37) results in

$$\delta\sigma_{ij} = C_{ijkl}\delta\varepsilon_{kl} - 2\mu P_{ijkl}\delta\varepsilon_{kl} = (C_{ijkl} - 2\mu P_{ijkl})\delta\varepsilon_{kl} \tag{2.44}$$

Finally, the tangent stiffness can be obtained by comparing (2.44) and (2.36), i.e.

$$C^{\tan}_{ijkl} = C_{ijkl} - 2\mu P_{ijkl} \tag{2.45}$$

2.3 Numerical Implementation with Plasticity

This section describes the numerical implementation of the constitutive model with plasticity.

2.3.1 Backward Euler Integration Routine

Similar to 2.2.1, assume that $(\sigma^n_{ij}, \varepsilon^n_{ij}, \varepsilon^{t,n}_{ij}, \varepsilon^{p,n}_{ij}, \varepsilon^{p,n}_{e})$ represent stress, strain, transformation strain, plastic strain and accumulated plastic strain at time t_n and $\Delta\varepsilon_{ij}$ is the strain increment for this time increment at a quadrature point, all variables at time t_{n+1} are solved through the following time-discrete system (superscripts n+1 for variables at time t_{n+1} are dropped for the purpose of simplicity):

$$\varepsilon_{ij} = \varepsilon^n_{ij} + \Delta\varepsilon_{ij} \tag{2.46a}$$

$$\sigma_{ij} = C_{ijkl}(\varepsilon_{kl} - \varepsilon^{t,n}_{kl} - \varepsilon^{p,n}_{kl} - \Delta\varepsilon^t_{kl} - \Delta\varepsilon^p_{kl}) \tag{2.46b}$$

$$\Delta\varepsilon^t_{ij} = 3\lambda^t(s_{ij} - s^B_{ij}) \tag{2.46c}$$

$$\Delta\varepsilon^p_{ij} = 3\lambda^p s_{ij} \tag{2.46d}$$

$$\Phi^t = 3(s_{ij} - s^B_{ij})(s_{ij} - s^B_{ij})/2 - \sigma^2_o \tag{2.46e}$$

$$\Phi^p = 3s_{ij}s_{ij}/2 - \sigma_e^2 \tag{2.46f}$$

supplemented by Kuhn-Tucker conditions:

$$\lambda^t \geq 0, \Phi^t \leq 0, \Lambda^t \Phi^t = 0 \tag{2.46g}$$

$$\lambda^p \geq 0, \Phi^p \leq 0, \Lambda^p \Phi^p = 0 \tag{2.46h}$$

Note that since both $\varepsilon_{kk}^t = 0$ and $\varepsilon_{kk}^p = 0$, the integration routine can focus on the deviatoric part of the tensors. Consequently, Eq. (2.46b) is replaced by

$$s_{ij} = 2\mu(\tilde{e}_{ij} - \Delta\varepsilon_{ij}^t - \Delta\varepsilon_{ij}^p) \tag{2.47}$$

where $\tilde{e}_{ij}$ is the deviator of $\tilde{\varepsilon}_{ij} = \varepsilon_{ij} - \varepsilon_{ij}^{t,n} - \varepsilon_{ij}^{p,n}$ and μ is the shear modulus.

Combining $\Phi^t = 0$ and $\Phi^p = 0$ and the time-discrete flow rules (2.46c, d), we can express the multipliers as follows:

$$3\lambda^t = \frac{3\Delta\varepsilon_e^t}{2\sigma_o} \tag{2.48a}$$

$$3\lambda^p = \frac{3\Delta\varepsilon_e^p}{2\sigma_o} \tag{2.48b}$$

where $\Delta\varepsilon_e^t = \sqrt{2\Delta\varepsilon_{ij}^t \Delta\varepsilon_{ij}^t / 3}$ and $\Delta\varepsilon_e^p = \sqrt{2\Delta\varepsilon_{ij}^p \Delta\varepsilon_{ij}^p / 3}$.

Thus, substitution of (2.48a, b) into the incremental inelastic strains (2.46c, d) results in the following

$$\Delta\varepsilon_{ij}^t = \frac{3\Delta\varepsilon_e^t}{2\sigma_0}[2\mu(\tilde{e}_{ij} - \Delta\varepsilon_{ij}^t - \Delta\varepsilon_{ij}^p) - s_{ij}^B] \tag{2.49a}$$

$$\Delta\varepsilon_{ij}^p = \frac{3\Delta\varepsilon_e^p}{2\sigma_e} 2\mu(\tilde{e}_{ij} - \Delta\varepsilon_{ij}^t - \Delta\varepsilon_{ij}^p) \tag{2.49b}$$

Note that Eq. (2.49b) can be reorganized into

$$\Delta\varepsilon_{ij}^p = \frac{3\mu\Delta\varepsilon_e^p}{\sigma_e + 3\mu\Delta\varepsilon_e^p}(\tilde{e}_{ij} - \Delta\varepsilon_{ij}^t) \tag{2.50}$$

Equation (2.50) means that solving $\Delta\varepsilon_{ij}^p$ is reduced to finding $\Delta\varepsilon_e^p$. Combining Eqs. (2.49) and (2.50) leads to the following residuals that are similar to those defined in (2.33):

$$r_{ij} = \frac{\Delta\varepsilon_{ij}^t}{\Delta\varepsilon_e^t} - \frac{3}{2\sigma_o}\left[\frac{2\mu\sigma_e}{\sigma_e + 3\mu\Delta\varepsilon_e^p}(\tilde{e}_{ij} - \Delta\varepsilon_{ij}^t) - s_{ij}^B\right] = 0, \tag{2.51a}$$

$$r_p = \frac{\sigma_e}{3\mu\Delta\varepsilon_e^p} + 1 - \frac{1}{\Delta\varepsilon_e^p}\sqrt{\frac{2}{3}(\tilde{e}_{ij} - \Delta\varepsilon_{ij}^t)(\tilde{e}_{ij} - \Delta\varepsilon_{ij}^t)} = 0. \tag{2.51b}$$

Note that these residuals are of order one and exclude trivial solutions. Equation (2.51a) is quite similar to (2.33) except that 2μ is replaced by $2\mu\sigma_e/(\sigma_e + 3\mu\Delta\varepsilon_e^p)$. Now the integration scheme is reduced to solving the nonlinear algebraic equations (2.51).

The Newton-Raphson scheme requires the Jacobians of the residuals:

$$J_{ijkl} = \frac{\partial r_{ij}}{\partial\Delta\varepsilon_{kl}^t} = \frac{I_{ijkl}}{\Delta\varepsilon_e^t} - \frac{2\Delta\varepsilon_{ij}^t\Delta\varepsilon_{kl}^t}{3(\Delta\varepsilon_e^t)^3} + \frac{3}{2\sigma_o}\left(\frac{2\mu\sigma_e}{\sigma_e + 3\mu\Delta\varepsilon_e^p} I_{ijkl} + H_{ijkl}\right)$$
$$+ \frac{3}{2\sigma_o^2}\left[\frac{2\mu\sigma_e}{\sigma_e + 3\mu\Delta\varepsilon_e^p}(\tilde{e}_{ij} - \Delta\varepsilon_{ij}^t) - s_{ij}^B\right]\frac{\partial\sigma_o}{\partial\varepsilon_{kl}^t} \tag{2.52a}$$

$$J_{ijp} = \frac{\partial r_{ij}}{\partial\Delta\varepsilon_e^p} = -\frac{3}{2\sigma_o}\frac{6\mu^2(H^p\Delta\varepsilon_e^p - \sigma_e)}{(\sigma_e + 3\mu\Delta\varepsilon_e^p)^2}(\tilde{e}_{ij} - \Delta\varepsilon_{ij}^t) \tag{2.52b}$$

$$J_{pij} = \frac{\partial r_p}{\partial\Delta\varepsilon_{ij}^t} = \frac{2}{3\Delta\varepsilon_e^p}\frac{\tilde{e}_{ij} - \Delta\varepsilon_{ij}^t}{\sqrt{2(\tilde{e}_{mn} - \Delta\varepsilon_{mn}^t)(\tilde{e}_{mn} - \Delta\varepsilon_{mn}^t)/3}} \tag{2.52c}$$

$$J_{pp} = \frac{\partial r_p}{\partial\Delta\varepsilon_e^p} = \frac{H^p\Delta\varepsilon_e^p - \sigma_e}{3\mu(\Delta\varepsilon_e^p)^2} + \frac{1}{(\Delta\varepsilon_e^p)^2}\sqrt{2(\tilde{e}_{ij} - \Delta\varepsilon_{ij}^t)(\tilde{e}_{ij} - \Delta\varepsilon_{ij}^t)/3} \tag{2.52d}$$

where $H^p = d\sigma_e / d\varepsilon_e^p$ is the plastic hardening modulus.

The process of the Newton-Raphson scheme starts from an initial guess of $\Delta\varepsilon_{ij}^t$ and $\Delta\varepsilon_e^p$, designated as $\Delta\varepsilon_{ij}^{t(0)}$ and $\Delta\varepsilon_e^{p(0)}$. For the ith iteration (i = 0, 1, 2…), calculate the residuals $r_{ij}^{(i)}$ and $r_p^{(i)}$ from Eqs. (2.51) and the norm of residual defined as

$$\|r\| = \sqrt{r_{11}^2 + r_{22}^2 + r_{33}^2 + r_{12}^2 + r_{13}^2 + r_{23}^2 + r_p^2} \tag{2.53}$$

Check if $\left\|r^{(i)}\right\| \le TOL$, where TOL is the tolerance for convergence, e.g. 1.0×10^{-8}. If yes, $\Delta\varepsilon_{ij}^{t(i)}$ and $\Delta\varepsilon_e^{p(i)}$ are accepted as the solution. Otherwise, assemble the Jacobians $J_{ijkl}^{(i)}$, $J_{ijp}^{(i)}$, $J_{pij}^{(i)}$, $J_{pp}^{(i)}$ and calculate the increment of the unknowns $d\varepsilon_{kl}^{t(i)}$, $d\varepsilon_e^{p(i)}$ by solving

$$r_{ij}^{(i)} = -J_{ijkl}^{(i)} d\varepsilon_{kl}^{t(i)} - J_{ijp}^{(i)} d\varepsilon_e^{p(i)}, \tag{2.54a}$$

$$r_p^{(i)} = -J_{pkl}^{(i)} d\varepsilon_{kl}^{t(i)} - J_{pp}^{(i)} d\varepsilon_e^{p(i)}, \tag{2.54b}$$

and update the unknowns $\Delta\varepsilon_{kl}^{t(i+1)} = \Delta\varepsilon_{kl}^{t(i)} + d\varepsilon_{kl}^{t(i)}$, $\Delta\varepsilon_e^{p(i+1)} = \Delta\varepsilon_e^{p(i)} + d\varepsilon_e^{p(i)}$ and the index $i \leftarrow i+1$. The tensorial equations (2.54) are numerically solved by re-organizing them into the following matrix form

$$\begin{bmatrix} r_{11}^{(i)} \\ r_{22}^{(i)} \\ r_{33}^{(i)} \\ r_{12}^{(i)} \\ r_{13}^{(i)} \\ r_{23}^{(i)} \\ r_p^{(i)} \end{bmatrix} = - \begin{bmatrix} J_{1111}^{(i)} & J_{1122}^{(i)} & J_{1133}^{(i)} & 2J_{1112}^{(i)} & 2J_{1113}^{(i)} & 2J_{1123}^{(i)} & J_{11p}^{(i)} \\ J_{2211}^{(i)} & J_{2222}^{(i)} & J_{2233}^{(i)} & 2J_{2212}^{(i)} & 2J_{2213}^{(i)} & 2J_{2223}^{(i)} & J_{22p}^{(i)} \\ J_{3311}^{(i)} & J_{3322}^{(i)} & J_{3333}^{(i)} & 2J_{3312}^{(i)} & 2J_{3313}^{(i)} & 2J_{3323}^{(i)} & J_{33p}^{(i)} \\ J_{1211}^{(i)} & J_{1222}^{(i)} & J_{1233}^{(i)} & 2J_{1212}^{(i)} & 2J_{1213}^{(i)} & 2J_{1223}^{(i)} & J_{12p}^{(i)} \\ J_{1311}^{(i)} & J_{1322}^{(i)} & J_{1333}^{(i)} & 2J_{1312}^{(i)} & 2J_{1313}^{(i)} & 2J_{1323}^{(i)} & J_{13p}^{(i)} \\ J_{2311}^{(i)} & J_{2322}^{(i)} & J_{2333}^{(i)} & 2J_{2312}^{(i)} & 2J_{2313}^{(i)} & 2J_{2323}^{(i)} & J_{23p}^{(i)} \\ J_{p11}^{(i)} & J_{p22}^{(i)} & J_{p33}^{(i)} & 2J_{p12}^{(i)} & 2J_{p13}^{(i)} & 2J_{p23}^{(i)} & J_{pp}^{(i)} \end{bmatrix} \begin{bmatrix} d\varepsilon_{11}^{t(i)} \\ d\varepsilon_{22}^{t(i)} \\ d\varepsilon_{33}^{t(i)} \\ d\varepsilon_{12}^{t(i)} \\ d\varepsilon_{13}^{t(i)} \\ d\varepsilon_{23}^{t(i)} \\ d\varepsilon_e^{p(i)} \end{bmatrix} \tag{2.55}$$

through which $d\varepsilon_{ij}^{t(i)}$, $d\varepsilon_e^{p(i)}$ are calculated.

2.3.2 Tangent Stiffness

The variation of the elasticity relation (2.46b) leads to

$$\delta\sigma_{ij} = C_{ijkl}\delta\varepsilon_{kl} - 2\mu(\delta\varepsilon_{ij}^t + \delta\varepsilon_{ij}^p) \tag{2.56}$$

Similar to (2.38), we also need the variation of the residuals (2.51) here:

$$0 = \delta r_{ij} = J_{ijkl}\delta\varepsilon_{kl}^t + J_{ijp}\delta\varepsilon_e^p + M_{ijkl}\delta\varepsilon_{kl} \tag{2.57a}$$

$$0 = \delta r_p = J_{pkl}\delta\varepsilon_{kl}^t + J_{pp}\delta\varepsilon_e^p + M_{pkl}\delta\varepsilon_{kl} \tag{2.57b}$$

where $J_{ijkl}, J_{ijp}, J_{pkl}, J_{pp}$ are the Jacobian components and

$$M_{ijkl} = \partial r_{ij} / \partial \varepsilon_{kl} = -\frac{3}{2\sigma_o} \frac{2\mu\sigma_e}{\sigma_e + 3\mu\Delta\varepsilon_e^p} (I_{ijkl} - \frac{1}{3}\delta_{ij}\delta_{kl}), \tag{2.58a}$$

$$M_{pkl} = \partial r_p / \partial \varepsilon_{kl} = -\frac{2}{3\Delta\varepsilon_e^p} \frac{\tilde{e}_{kl} - \Delta\varepsilon_{kl}^t}{\sqrt{2(\tilde{e}_{mn} - \Delta\varepsilon_{mn}^t)(\tilde{e}_{mn} - \Delta\varepsilon_{mn}^t)/3}}, \tag{2.58b}$$

both of which are calculated at the convergence of the Newton-Raphson scheme.

Equations (2.57) leads to

$$\delta\varepsilon_{ij}^t = P_{ijkl}\delta\varepsilon_{kl}, \tag{2.59a}$$

$$\delta\varepsilon_e^p = P_{pkl}\delta\varepsilon_{kl}, \tag{2.59b}$$

where P_{ijkl} and P_{pkl} satisfy

$$J_{ijmn}P_{mnkl} + J_{ijp}P_{pkl} = -M_{ijkl} \tag{2.60a}$$

$$J_{pij}P_{ijkl} + J_{pp}P_{pkl} = -M_{pkl} \tag{2.60b}$$

and can be solved by rearranging Eqs. (2.60) into the following matrix equation:

$$[J][P] = -[M] \tag{2.61}$$

where

$$[J] = \begin{bmatrix} J_{1111} & J_{1122} & J_{1133} & 2J_{1112} & 2J_{1113} & 2J_{1123} & J_{11p} \\ J_{2211} & J_{2222} & J_{2233} & 2J_{2212} & 2J_{2213} & 2J_{2223} & J_{22p} \\ J_{3311} & J_{3322} & J_{3333} & 2J_{3312} & 2J_{3313} & 2J_{3323} & J_{33p} \\ J_{1211} & J_{1222} & J_{1233} & 2J_{1212} & 2J_{1213} & 2J_{1223} & J_{12p} \\ J_{1311} & J_{1322} & J_{1333} & 2J_{1312} & 2J_{1313} & 2J_{1323} & J_{13p} \\ J_{2311} & J_{2322} & J_{2333} & 2J_{2312} & 2J_{2313} & 2J_{2323} & J_{23p} \\ J_{p11} & J_{p22} & J_{p33} & 2J_{p12} & 2J_{p13} & 2J_{p23} & J_{pp} \end{bmatrix} \tag{2.62a}$$

$$[P] = \begin{bmatrix} P_{1111} & P_{1122} & P_{1133} & P_{1112} & P_{1113} & P_{1123} \\ P_{2211} & P_{2222} & P_{2223} & P_{2212} & P_{2213} & P_{2223} \\ P_{3311} & P_{3322} & P_{3333} & P_{3312} & P_{3313} & P_{3323} \\ P_{1211} & P_{1222} & P_{1233} & P_{1212} & P_{1213} & P_{1223} \\ P_{1311} & P_{1322} & P_{1333} & P_{1312} & P_{1313} & P_{1323} \\ P_{2311} & P_{2322} & P_{2333} & P_{2312} & P_{2313} & P_{2323} \\ P_{p11} & P_{p22} & P_{p33} & P_{p12} & P_{p13} & P_{p23} \end{bmatrix} \tag{2.62b}$$

$$[M] = \begin{bmatrix} M_{1111} & M_{1122} & M_{1133} & M_{1112} & M_{1113} & M_{1123} \\ M_{2211} & M_{2222} & M_{2223} & M_{2212} & M_{2213} & M_{2223} \\ M_{3311} & M_{3322} & M_{3333} & M_{3312} & M_{3313} & M_{3323} \\ M_{1211} & M_{1222} & M_{1233} & M_{1212} & M_{1213} & M_{1223} \\ M_{1311} & M_{1322} & M_{1333} & M_{1312} & M_{1313} & M_{1323} \\ M_{2311} & M_{2322} & M_{2333} & M_{2312} & M_{2313} & M_{2323} \\ M_{p11} & M_{p22} & M_{p33} & M_{p12} & M_{p13} & M_{p23} \end{bmatrix} \tag{2.62c}$$

In addition to (2.59), we need the relation between $\delta\varepsilon_e^p$ and $\delta\varepsilon_{ij}^p$. The variation of (2.50) provides

$$\delta\varepsilon_{ij}^p = \mu^{pp}(\tilde{e}_{ij} - \Delta\varepsilon_{ij}^t)\delta\varepsilon_e^p + \mu^p(\delta e_{ij} - \delta\varepsilon_{ij}^t) \tag{2.63}$$

where

$$\mu^p = \frac{3\mu\Delta\varepsilon_e^p}{\sigma_e + 3\mu\Delta\varepsilon_e^p} \quad \text{and} \quad \mu^{pp} = \frac{3\mu(\sigma_e - H^p\Delta\varepsilon_e^p)}{(\sigma_e + 3\mu\Delta\varepsilon_e^p)^2}. \tag{2.64}$$

Combining (2.59) and (2.63) leads to

$$\begin{aligned} \delta\varepsilon_{ij}^p &= \mu^{pp}(\tilde{e}_{ij} - \Delta\varepsilon_{ij}^t)P_{pkl}\delta\varepsilon_{kl} + \mu^p(I_{ijkl} + \delta_{ij}\delta_{kl}/3 - P_{ijkl})\delta\varepsilon_{kl} \\ &= [\mu^{pp}(\tilde{e}_{ij} - \Delta\varepsilon_{ij}^t)P_{pkl} + \mu^p(I_{ijkl} + \delta_{ij}\delta_{kl}/3 - P_{ijkl})]\delta\varepsilon_{kl} \end{aligned} \tag{2.65}$$

Substitution of (2.59a) and (2.65) into (2.56) results in

$$\begin{aligned} \delta\sigma_{ij} &= C_{ijkl}\delta\varepsilon_{kl} - 2\mu P_{ijkl}\delta\varepsilon_{kl} \\ &- 2\mu[\mu^{pp}(\tilde{e}_{ij} - \Delta\varepsilon_{ij}^t)P_{pkl} + \mu^p(I_{ijkl} - \delta_{ij}\delta_{kl}/3 - P_{ijkl})]\delta\varepsilon_{kl} \end{aligned} \tag{2.66}$$

which leads to the tangent stiffness components

$$C_{ijkl}^{\tan} = C_{ijkl} - 2\mu[\mu^{pp}(\tilde{e}_{ij} - \Delta\varepsilon_{ij}^t)P_{pkl} + \mu^p(I_{ijkl} - \delta_{ij}\delta_{kl}/3) + (1 - \mu^p)P_{ijkl}] \tag{2.67}$$

Note, if the plastic strain does not change in this increment, i.e., $\Delta\varepsilon_e^p = 0$, Eq. (2.64) indicates that $\mu^p = \mu^{pp} = 0$. Consequently, (2.67) degrades to (2.45).

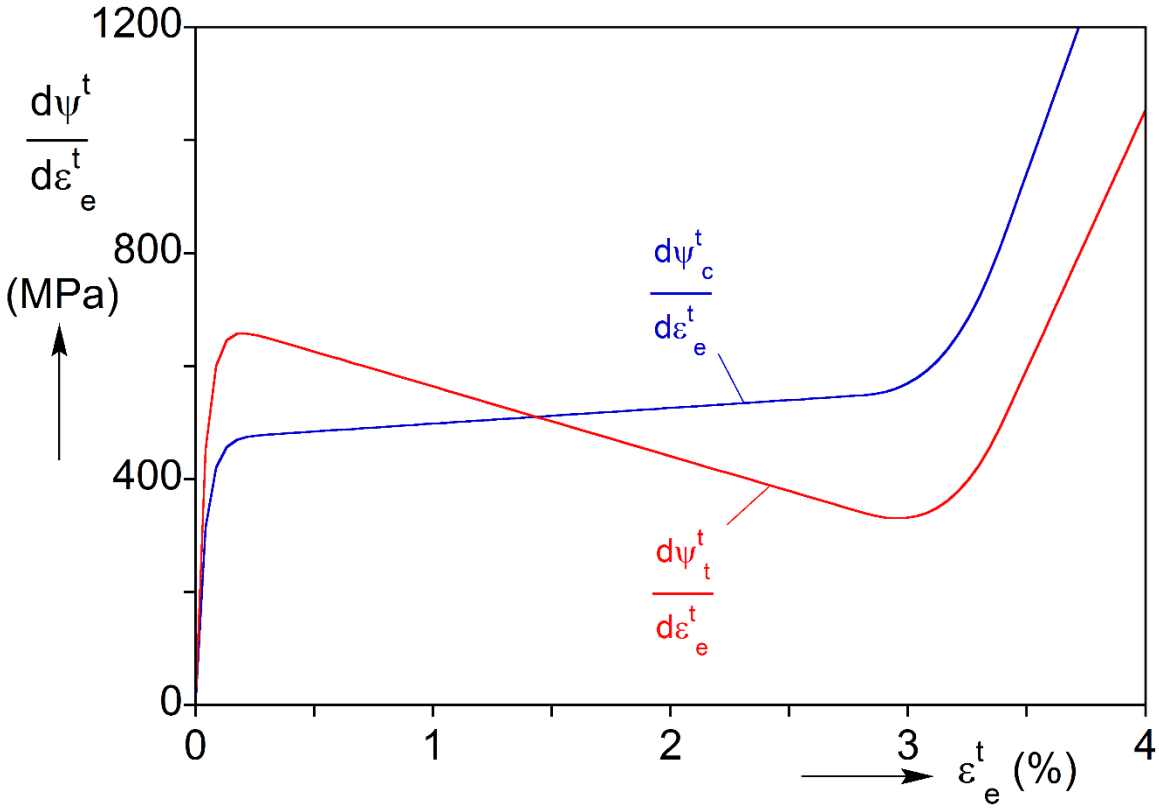

Fig. 2.1 An example calibration of the derivatives of the two back stress potentials.

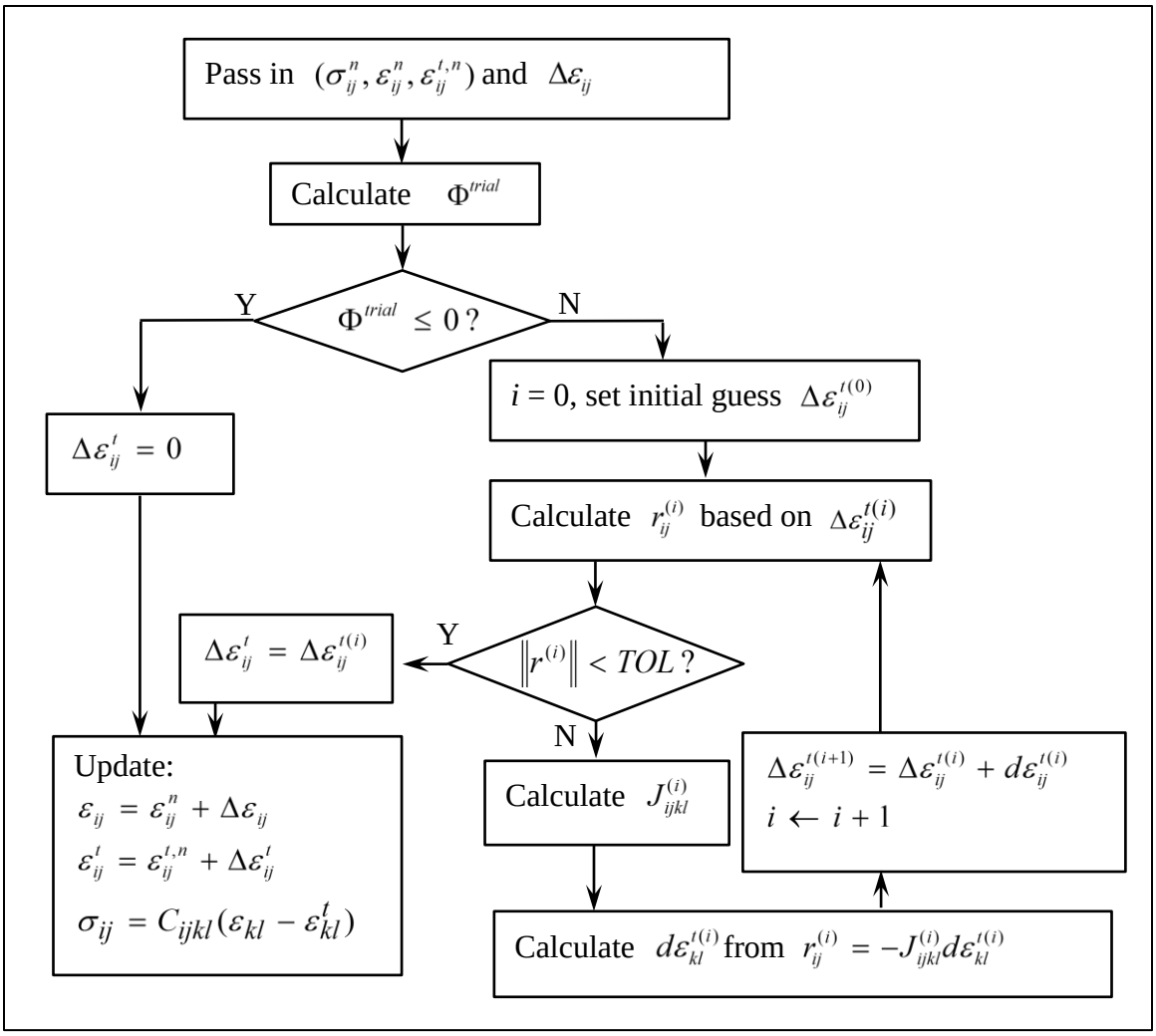

Fig. 2.2 Flow chart for the backward Euler integration routine without plasticity.

Chapter 3: BUCKLING AND RECOVERY OF NiTi TUBES UNDER AXIAL COMPRESSION[1] [2] [3]

3.1 INTRODUCTION

This chapter presents the results of a study of the buckling and recovery of a thin-walled NiTi shell under axial compression. The behavior is governed by a strong interaction of geometric nonlinearities with those of the pseudoelastic NiTi material, including the tension/compression asymmetric behavior described in Chapter 1. Shell buckling and recovery experiments performed for this study used NiTi tubes with nominal diameters of 6.23 mm and $D/t \approx 23.6$ (See Jiang et al., 2016a). Figure 3.1a shows the tensile and compressive responses of this family of tubes. They exhibit the same hysteretic behavior reported in Chapter 1 for a thicker NiTi tube, a similar inhomogeneous deformation in tension (see Fig. 3.1b) and a similar tension/compression asymmetry. These differences placed a high level of demands on the constitutive model framework presented in Chapter 2 and guided the development of additional features of the material behavior shown to be required for accurate prediction of this complex structural behavior. The NiTi shell buckling and recovery experiment is outlined first. It is followed by presentation of a finite element model used to simulate the experiment using first the simplest version of the constitutive model. By comparing the results of the simulation with the experimental response, new features of the material behavior are

[1]Jiang, D., Bechle, N.J., Landis, C.M., Kyriakides, S. (2016a). Buckling and recovery of NiTi tubes under axial compression. *Int'l J. Solids & Structures* **80**, 52-63. (Implemented the constitutive model, conducted the numerical simulations and wrote the analysis section in the paper)

[2]Jiang, D., Landis, C.M., Kyriakides, S. (2016b). Effects of tension/compression asymmetry on the buckling and recovery of NiTi tubes under axial compression. *Int'l J. Solids Struct.* **100-101**, 41-53. (Implemented the constitutive model, conducted the numerical simulations and wrote the paper)

[3]Jiang, D., Landis, C.M. (2016). A constitutive model for isothermal pseudoelasticity coupled with plasticity. *Shape Memory and Superelasticity* **2**, 360-370. (Implemented the constitutive model, conducted the numerical simulations and wrote the paper)

progressively added to the constitutive model leading to a successful prediction of the experiment.

3.2 EXPERIMENT

The axial buckling experiment performed on a NiTi shell is presented in detail in Jiang et al. [2016a]. This section provides a brief review of the experiment. The tube tested had a diameter, D, of 6.23 mm, a wall thickness $t = 0.268$ mm for a $D/t = 23.6$, and a length-to-diameter ratio (L/D) of 3.1. The material is nearly equiatomic NiTi with $A_f = 12$ °C (see Table 3.1). The test was performed at 23 °C so that the material was in the pseudoelastic regime. The tube was compressed at a very the slow displacement rate of 5×10^{-5} s^{-1} between stiff platens and the shell deformation was monitored by high-resolution digital imaging that included digital image correlation (DIC).

Table 3.1 Buckling test specimen parameters.

D mm	t mm	L mm	T °C	$\sigma_{PM} : T$ MPa	$\sigma_{NM} : C$ MPa	A_s °C	A_f °C
6.32	0.268	19.62	23	445	-725	-10	12

Figure 3.2 shows the hysteretic nominal stress-normalized shortening response recorded in the experiment. Included with a dash line is the compressive response of the material. Figure 3.3 presents a select set of photographic images of the specimen that correspond to the numbered bullets on the response in Fig. 3.2. Initially, the tube follows the stiff response corresponding to the elastic modulus of A. The reduction in the stiffness indicated by the knee near ②, is associated with the onset and evolution of M transformation, and causes the compressed tube to buckle into an axisymmetric wrinkling mode. It is well-known that axisymmetric wrinkling is the first instability in inelastic buckling of axially loaded shells (see Bardi and Kyriakides [2006], Bardi et al. [2006]

and references therein). Wrinkles were not visible in the photographic record of the buckling experiment in Fig. 3.3, because of their small amplitude. However, local wrinkles were recorded in a similar experiment. Figure 3.4 shows the early part of the response from such an experiment and a DIC image with contours of the radial displacement superimposed. A clear axisymmetric wrinkle has developed near the top end soon after the onset of transformation as the stress traces a nearly flat plateau. A wrinkle with smaller amplitude developed also at the bottom end but was erased when the mode-3 collapse commenced at the top.

As compression continues, the stress traces a relatively flat response during which the wrinkle amplitude grows. This growth in the wrinkles causes a local maximum (marked by the caret "^") in the early part of the stress plateau. By point ③ wrinkling yields to a diamond-type non-axisymmetric mode with three circumferential waves. This is an unstable mode, leading to localization of deformation initially into one single buckling lobe. In images ④ and ⑤, the amplitude of the mode-3 lobe grows with the axial load decreasing. Transformation is eventually exhausted, the transformed *M* stiffens, and the growth of this lobe is arrested (see similar results in Nemat-Nasser et al. [2006] and Tang and Li [2012]). With the axial load continuing to drop, a second mode-3 lobe develops below the first one, which is apparent in images ⑦ and ⑧. For compatibility, the second lobe is rotated by 60^{o} relative to the first one. The second drop in stress from ⑥ to ⑧ is associated with the growth of the second lobe. At point ⑨, the loading is terminated and the unloading starts. So far, the reported buckling and collapse events are reminiscent of those observed in plastic buckling of conventional metal tubes but, instead of the progressive concertina folding (see Fig. 3c in Bardi and Kyriakides, 2006), the buckling lobes here remain intact.

The unloading of the NiTi tube differs significantly from that of conventional metal tubes. As a pseudoelastic material, NiTi transforms back to A during unloading, deformation is recovered leading to the erasure of the buckling lobes (⑪-⑲) in the reverse order to the one followed during loading. The hysteresis in Fig. 3.2 nearly closes but a small residual deformation is left behind, indicating that some plastic deformation has taken place in the structure.

3.3 FINITE ELEMENT MODEL

The tube buckling experiment is simulated numerically using the FE model shown in Fig. 3.5. A model tube assigned the length (L), outer diameter (D) and wall thickness (t) of the NiTi tube tested (Table 3.1) is compressed between two rigid flat surfaces. As is customary in inelastic buckling, the model is assigned an initial geometric imperfection, $\overline{w}$, that includes an axisymmetric component with a half-wavelength λ, and a non-axisymmetric imperfection with half-wavelength 2λ and m circumferential waves (e.g., see Bardi et al., 2006). The two imperfections have respective amplitudes of ω_o and ω_m, as follows:

$$\overline{w} = t\left[\omega_o \cos\frac{\pi x}{\lambda} + \omega_m \cos\frac{\pi x}{2\lambda}\cos m\theta\right]e^{-\beta(x/L)^4} \qquad (3.1)$$

In concert with the mode-3 buckling mode observed in the experiments, m is assigned the value 3 in Eq. (3.1). The wavelength parameter of the imperfections is assigned the value $\lambda = 0.274D$ that was established through the inelastic bifurcation analysis in Appendix B. The imperfection is modulated by an exponentially decaying term so that buckling localizes at the top end of the model. The axisymmetric mode is depicted in Fig. 3.5b and the non-axisymmetric one with m = 3 in Fig. 3.5c. In both images, β in the modulating function is 20. This value of β reduces the imperfection amplitude by 71% by mid-span.

The structure is discretized in ABAQUS 6.13 using quadratic reduced-integration continuum elements, C3D20R. The lower rigid surface is fixed while the axial displacement of the upper one, δ, is prescribed incrementally. The contact between the rigid surfaces and the tube is modeled using the finite sliding surface-to-surface formulation of ABAQUS with the "hard" pressure-overclosure option. A Coulomb friction coefficient of 0.05 was found to have a stabilizing effect on the solution. The resultant nominal stress acting on the model at $x = L$ is evaluated from the reaction force on the rigid plate.

In the subsequent sections, the tube buckling problem will be simulated using four versions of the constitutive model, each of which captures one or more features of the behavior of pseudoelastic NiTi. These four models were developed chronologically and comparisons between the simulation results exhibit the influence of each aspect of pseudoelastic NiTi. Table 3.2 shows the features of NiTi that each model represents:

Table 3.2 Four models used for the buckling problem.

Model	Feature(s)
SYM	Symmetric pseudoelasticity
SYM+PL	Symmetric pseudoelasticity + Plasticity
ASY	Asymmetric pseudoelasticity
ASY+PL	Asymmetric pseudoelasticity + Plasticity

3.4 Analysis Using the Symmetric Model (SYM)

Motivated by the presumption that this is primarily a compressive stress problem, the simplest version of the constitutive model used at the outset of this study (Jiang et al.,

2016a) neglected the asymmetry between the tensile and compressive responses of this NiTi material and the plastic deformation. The constitutive model was calibrated strictly to the compressive response and is designated as SYM.

3.4.1 Model Calibration

Since the stress state in the tube structure in the buckling problem is primarily compressive, the calibration of SYM is purely based on the measured compressive hysteretic response shown in Fig. 3.1a. Thus, the scaling function f in Eq. (2.23b) and the weight function ξ in Eq. (2.22) are both made to be identically equal to one. Thus, the back stress potential function in Eqs. (2.3c, 2.22) degrades to $\psi^t = \psi^t(\varepsilon_e^t)$, where $e_e^t = J'_2$. In the uniaxial settings, the governing equation (2.27) for loading in compression is reduced to

$$|\sigma_{11c}| - \frac{d\psi^t}{d\varepsilon_e^t} = \sigma_{oc} \tag{3.2}$$

with $\varepsilon_e^t = \left|\varepsilon_{11c}^t\right|$.

The back stress $s^B(e^t)$ is chosen to approximately fit the shape of the measured loading response as shown in Fig. 3.6a. It is established by first constructing a function that appropriately depicts the variation of the inelastic modulus

$$\frac{d\sigma^B}{d\varepsilon^t} = h_0 + (h_1 - h_0)(1 - e^{-b\varepsilon^t}) + (h_2 - h_1)\begin{cases} 0 & 0 \le \varepsilon^t \le \varepsilon_2 \\ (10\zeta^3 - 15\zeta^4 + 6\zeta^5), & \varepsilon_2 \le \varepsilon^t \le \varepsilon_3 \\ 1 & \varepsilon_3 \le \varepsilon^t \end{cases} \tag{3.3}$$

with $\zeta = (\varepsilon^t - \varepsilon_2)/(\varepsilon_3 - \varepsilon_2)$. The modulus starts with a very high value, h_0, decreases quickly to a lower value, h_1, in accordance with the exponential multiplier with constant b, and then transits to h_2 following a polynomial form in the interval

between ε_2 and ε_3. This function is similar to the one used in Landis [2003a] to model the strain saturation phenomenon in polycrystalline ferroelastic materials with h_2 very large. Thus, integration of Eq. (3.3) leads to the fundamental form of the back stress

$$\sigma^B = h_0\varepsilon^t + (h_1 - h_0)\left[\varepsilon^t - \frac{1}{b}(1 - e^{-b\varepsilon^t})\right] + (h_2 - h_1)\begin{cases} 0 & 0 \le \varepsilon^t \le \varepsilon_2 \\ (2.5\zeta^4 - 3\zeta^5 + \zeta^6)(\varepsilon_3 - \varepsilon_2), & \varepsilon_2 \le \varepsilon^t \le \varepsilon_3 \\ (\varepsilon_3 - \varepsilon_2)/2 + (\varepsilon^t - \varepsilon_3) & \varepsilon_3 \le \varepsilon^t \end{cases} \tag{3.4}$$

However, it is well known that at some higher stress level, the transformed martensite exhibits additional, mainly dislocation-plasticity-driven, nonlinearity. This is idealized as a second "stress plateau" as shown in Fig. 3.6a and is introduced by adding an arctangent term in the back stress while giving h_2 a very small value. Thus, $d\psi^t / d\varepsilon_e^t$ is modified as follows:

$$\frac{d\psi^t}{d\varepsilon_e^t} = h_0\varepsilon_e^t + (h_1 - h_0)\left[\varepsilon_e^t - (1 - e^{-b\varepsilon_e^t})/b\right] + \frac{2}{\pi}h_3\left[\tan^{-1}(c\varepsilon_1) + \tan^{-1}(c\varepsilon_e^t - c\varepsilon_1)\right] + (h_2 - h_1)\begin{cases} 0 & 0 \le \varepsilon_e^t \le \varepsilon_2 \\ (\varepsilon_3 - \varepsilon_2)(2.5\zeta^4 - 3\zeta^5 + \zeta^6), & \varepsilon_2 \le \varepsilon_e^t \le \varepsilon_3 \\ (\varepsilon_3 - \varepsilon_2)/2 + (\varepsilon_e^t - \varepsilon_3) & \varepsilon_3 \le \varepsilon_e^t \end{cases} \tag{3.5}$$

with $\zeta = (\varepsilon_e^t - \varepsilon_2)/(\varepsilon_3 - \varepsilon_2)$.

The idealized plasticity-driven nonlinearity results in the "S" shaped trajectories shown in Fig. 3.6a and 3.6b. In the absence of experimental data at the time this model was developed, the level of the higher transformation stress was chosen somewhat arbitrarily.

It must be pointed that the NiTi tubes used in the buckling experiments buckled soon after transformation to *M* commenced (Fig. 3.2). Thus, measurement of the full

compressive response of this tube was not possible. The complete compressive response shown in Fig. 1.3 originated from a much thicker tube of the same alloy (Bechle and Kyriakides, 2014). Because of small differences in the training of the materials, this response has a somewhat lower transformation stress. In order to be adopted in the buckling calculations, the complete hysteresis was shifted upwards by about 100 MPa to match the level of stress that transformation commenced in the thinner tubes used in the buckling experiments. The shifted hysteresis is designated as the "experimental" material in Fig. 3.6b, which is used to calibrate the present model. The parameters for the SYM model are listed in Table 3.3.

Table 3.3 Model parameters for SYM.

E GPa	n	s_o MPa	b	h_0 GPa	h_1 GPa	h_2 MPa	h_3 MPa	e_1 (%)	e_2 (%)	e_3 (%)	c
68.3	0.392	120.7	2500	1509	2.772	0	494.8	3.3	3.1	3.3	1500

3.4.2 Numerical results

The finite element model outlined in Section 3.3, coupled with the calibrated constitutive model SYM, is now used to simulate the buckling experiment presented in Section 3.2. As expected, the calculated response is influenced by the imperfection amplitudes adopted in Eq. (3.1). This sensitivity of the solution was studied through a parametric study the results of which will follow. Here we choose to use the imperfection amplitudes that were found to result in an initial part of the response that is closest to the experimental ones, that is: $\omega_0 = 0.001$ and $\omega_3 = 0.14$. The following mesh density was shown from convergence studies to provide sufficiently accurate solutions. Four elements are used across the wall thickness and 156 elements around the circumference.

In anticipation of the expected localization of deformation, two mesh densities were used in the axial direction: 78 elements in the upper half of the model and 30 in the lower half.

The calculated nominal compressive stress-normalized displacement ($\sigma - \delta / L$) response is shown in Fig. 3.7. To facilitate the discussion that follows, Fig. 3.7a shows the initial loading part of the response together with the uniaxial material response, and Fig. 3.7b the complete load-unload response. The response measured in the experiment is included with a dashed line in Fig. 3.7b for comparison. Figure 3.8 shows two sets of deformed configurations of the shell corresponding to the numbered bullets on the response in Fig. 3.7. Superimposed on the configurations are color contours representing the "equivalent" transformation strain $J_2^{\mathcal{C}}$ (≡ESN). Note that in Fig. 3.8 different color scales are used for contours on the images corresponding to the initial loading part of the response (①-⑥) and for the complete response (⑥-⑭).

Initially, the compressive response follows the nearly linear material response and image ① at a stress of about 625 MPa shows no signs of transformation strain. Starting from point ②, the response deviates from the uniaxial stress-strain response, a sign that the imperfection is being excited. A maximum stress of about 714 MPa is achieved at point ③ beyond which the response starts a gradual descent, an indication that the collapse of the structure has commenced. This growth of non-trivial deformation is reflected in the images in Fig. 3.8 where the m = 3 mode is seen to develop close to the upper end. It appears as a single lobe in image ③, but in images ⑤ and ⑥ a second lobe below it begins to develop. By image ⑥ the maximum strain in the intrados of the first lobe has exceeded 5%. It is worth noting that the amplitude of the mode-3 non-axisymmetric imperfection component (0.14) is unreasonably greater than that of the axisymmetric one (0.001). Consequently, the axisymmetric wrinkling prior to the mode-3 buckling observed in the experiment is not captured in this calculation.

Switching now to Fig. 3.7b, the calculated response is seen to follow the experimental one quite closely up to nearly point ⑥. Between points ⑥ and ⑧ the stress continues its downward trend but at a slower rate than in the experimental one. In this process the amplitude of the first lobe increases significantly as evidenced in image ⑦. It is noteworthy that the shape of the trajectory traced is similar to the experimental one where the near plateau is associated with the growth of the first lobe. However, the stress drop is less abrupt than that in the experiment. A second drop in stress occurs just before point ⑧ at essentially the same displacement as a similar drop recorded in the experiment. This is associated with the growth in the amplitude of the second lobe below the first one. The deformation in this lobe grows while the growth of the first lobe has slowed significantly. By image ⑨ at the end of loading, the amplitudes and strains of the two lobes appear to be at similar levels.

On unloading the induced deformation is fully recovered. The response follows a trajectory that is similar in shape as that of the experiment but tracing a significantly higher stress. Furthermore, unlike the experiment in which the lobes unloaded nearly in reverse order to the loading, in the simulation the two lobes unload nearly simultaneously. The stress reaches a local minimum near point ⑪ and then gradually rises with the two lobes exhibiting the tendency to snap back, which was also observed in the experiments. The stress reaches a local maximum between points ⑫ and ⑬. In image ⑬ the deformation in the two buckle lobes has been reduced very significantly. The material has unloaded back to *A* by image ⑭, beyond which the structure unloads with essentially the elastic modulus. Finally, the calculated hysteresis is fully closed.

Clearly, the analysis captures the onset of instability, the switch to mode-3 and its localization first into a single lobe followed by a second one. It also captures the arrest of deformation in each lobe following a similar amount of deformation as that observed in

the experiment. However, to achieve this, the amplitude for the non-axisymmetric imperfection component $\omega_3 = 14\%$ has to be adopted, which is a value that past experience indicates unnaturally large. In addition, the stress level in the loading part of the response is high. The load drop associated with collapse into mode-3 is smaller than the experimental one. On unloading, although the simulation follows the same recovery trend with that in the experiment, it occurs at a significantly higher stress level than that of the experimental response. These deviations result in significant underprediction of the energy dissipated by the hysteretic response. Also, the calculated hysteresis is fully closed because of the assumptions the constitutive model adopts. These differences between the measured and predicted responses using this model prompt consideration of additional features of the NiTi response, such as plastic deformations that occur when a certain stress is exceeded, the strong asymmetry between tension and compression and the inhomogeneous nature of transformation-induced inelastic deformation associated with material softening. The effects of these aspects of the material behavior on the buckling problem are being discussed in the following sections.

3.4.3 Parametric Study

As in all inelastic buckling problems the compressive response produced by a model is influenced by the imperfections adopted. Here we report selected results from studies of the sensitivity of the calculated response to the amplitudes of the imperfection for the SYM constitutive model.

Figure 3.9a shows a set of responses in which the amplitude of the axisymmetric imperfection, ω_o, is varied with the other two imperfection parameters kept constant (i.e., $\omega_3 = 14\%$, $\beta = 20$). The responses agree up to the knee induced by the onset of

transformation. At higher compressive displacements, increasing ω_o causes an extension of the initial stress plateau and delays collapse by the non-axisymmetric shell mode. Axisymmetric wrinkling is usually a stable buckling mode, so increasing its amplitude has a stabilizing effect.

Figure 3.9b shows a set of responses in which ω_3 was varied with the other two variables kept at the values used in the optimal simulation (i.e., $\omega_o = 0.001, \beta = 20$). Remembering that the value that produced the response closest to the experimental one was $\omega_3 = 0.14$, we observe that decreasing this value again delays collapse. Correspondingly, increasing this value reduces the extent of the initial stress plateau and accelerates the onset of collapse.

The extent of influence of the imperfection over the shell length is governed by the parameter β in the modulating function in Eq. (3.1). Thus increasing β limits its influence to a shorter length of the model shell. Figure 3.10 compares calculated responses for $\beta = 2$ and 40 to that produced for $\beta = 20$ with the two imperfection amplitudes kept at the levels of the optimal simulation. Adoption of $\beta = 2$ causes the shell to collapse earlier. Here the amplitude of the second wave is comparable to that of the first, thus collapse starts in the second lobe with the first one collapsing at a later stage. This order of collapse is the reverse to that observed in the experiment. When β is increased to 40, collapse is delayed but occurs in the correct order.

3.5 Addition of Plastic Deformations into the Constitutive Model

The strain levels that develop as the mode-3 buckling lobes grow are large enough to suspect that plastic deformations may play a role in the postbuckling behavior observed in the experiments. The fact that the hysteresis did not close completely also

supports this conjecture. Thus, in this section, the constitutive model is extended to include plastic deformations and then used to re-evaluate the buckling and postbuckling response of the tube experiment in Section 3.2.

It has been long known from tensile experiments on pseudoelastic NiTi that martensite lattices start to slip once the stress level goes beyond a critical level (e.g., see Fig. 2 in Shaw and Kyriakides [1995]). Less is known about yielding of martensite under compression, primarily because of experimental challenges in compressive loading under high stress levels required. This issue was explored in a compression experiment on a NiTi rod with approximately the same alloy composition and processing characteristics with the tubular stock used in the buckling experiments. The test was performed in the compression test setup of Bechle and Kyriakides [2014], leaving a test section with a length-to-diameter ratio (L/D) of 2.5. The test involved series of load-unload responses that resulted in the nominal stress-shortening results shown in Fig. 3.11 (taken from Jiang et al. [2016b]).

The innermost one exhibits pure pseudoelastic behavior with a closed hysteresis and the saturation response associated with the completion of M transformation. However, when M is compressed to a high enough stress level, the response becomes nonlinear and exhibits permanent deformation on unloading. Unloading from an even higher stress level increases the residual deformation, leaving the hysteresis open.

Within this background, the plastic deformation shown in Chapter 2 is activated in the model so that $\dot{\varepsilon}_{ij} = \dot{\varepsilon}^{e}_{ij} + \dot{\varepsilon}^{t}_{ij} + \dot{\varepsilon}^{p}_{ij}$. With the addition of plastic deformations, the model now is named: SYM+PL.

3.5.1 Model Calibration

The model SYM+PL is generated by adding a plastic component of strain into the symmetric model, as described by the previous section. This additional component is represented by the hardening function $\sigma_e(\varepsilon_e^p)$, for which the following form is adopted:

$$\sigma_e(\varepsilon_e^p) = \sigma_y\left[1+\frac{2}{\pi}h^p \tan^{-1}(b^p\varepsilon_e^p)\right],\ \ \varepsilon_e^p = \int_0^t \dot{\varepsilon}_e^p dt. \qquad (3.6)$$

where σ_y is the initial yield stress and the arc tangent term is intended to represent the "S" shaped trajectory in the response following the saturation of *M* transformation. The transformation strain evolves in the same manner with that in Section 3.4. The back stress potential $\psi^t(\varepsilon_e^t)$ function inherits the form in Eq. (3.5), but the parameters are adjusted such that the model can produce a response, as shown in Fig. 3.12, the loading part of which is nearly identical to that of SYM. The parameters for SYM+PL are listed in Table 3.4.

Table 3.4 Model parameters for SYM+PL.

E GPa	n	s_o MPa	b	h_o GPa	h_1 GPa	h_2 MPa	h_3 MPa
68.3	0.392	120.7	2500	1509	2.772	630.3	543
ε_1 (%)	ε_2 (%)	ε_3 (%)	c	s_y MPa	b^p	h^p	
3.3	3.1	3.3	2000	1240	1650	0.446	

3.6 Analysis Using the Symmetric Model Including Plasticity (SYM+PL)

The finite element simulation of the tube buckling experiment is now repeated using the SYM+PL constitutive model. The same imperfection amplitudes $w_0 = 0.001$ and $w_3 = 0.14$ are adopted. The calculated nominal stress-normalized shortening $(\sigma - \delta / L)$ response is plotted in Fig. 3.13. Figure 3.13a shows the initial loading part

of the response together with the material response and Fig 3.13b the complete load-unload response with the experimental response, as well as the one predicted by SYM for the comparison purpose. Figure 3.14 shows two sets of deformed configurations with superimposed contours of summed "equivalent" transformation and plastic strains (≡ESN+PEEQ). Because the strain levels associated with the two sets of images are different, they are assigned different color scales. The images correspond to the numbered bullets in Fig. 3.13 and represent the same levels of shortening as those in Figs. 3.7 and 3.8 for the SYM model

The response calculated using SYM+PL during loading (①-⑨) is essentially identical to that of SYM. The stress level during collapse is still much higher than that in the experiment. The simulation again reproduces the localization of deformation initially into one buckling lobe and subsequently into a second one, the load drops associated with the development of each lobe and the arrest of deformation in the lobes.

During unloading, the deformation in the tube is recovered and the buckling lobes are erased following the reverse order to that they develop during loading (⑨-⑭ in Fig. 3.14). However, the inclusion of plasticity significantly lowers the stress level of the unloading part of the response, bringing it closer to the experimental one. As a consequence, the energy dissipation, i.e., the area enclosed by the calculated hysteresis, increases and becomes closer to the measured value. Another improvement is that at zero axial stress, a residual net displacement remains that is somewhat smaller than the experimental value, leaving the calculated hysteresis slightly open, as was the case in the experiment. The permanent deformation in the tube is evidenced by the small islands of plastic deformation in the zones that experienced the most severe deformation during loading (e.g., image ⑭).

3.7 Analysis Using the Asymmetric Model (ASY)

In the tube buckling problem that is analyzed here, the structure is under a primarily compressive stress. As pointed out in Section 3.2, the tube collapsed through the progressive development of mode-3 buckling lobes, which means that a significant amount of tension developed on one side of the lobes. Thus, in this section the tension/compression asymmetry of the material is incorporated in the constitutive model. The extended constitutive model is incorporated into the FE model and used to re-calculate the compressive response of our tube. Because the tension induced by bending is limited to narrow zones in the lobes, which limit the extent of localized deformation, the localization associated with tension is not addressed. Furthermore, this version of the model, designated as ASY, precludes plastic deformations.

3.7.1 Model Calibration

The back stress potential functions in ASY are similar to the potential in SYM except that the function f in Eqs. (2.23) must be chosen carefully to correctly represent the difference between the tensile and compressive responses. The parameter a in Eq. (2.23b) is chosen to be 0.99225, implying that $f(1) = 0.55$, that is approximately the ratio between the compressive and tensile transformation strains shown in Fig. 3.1a. In addition, functions $y_c^t(\bar{e}_e^t)$ and $y_t^t(\bar{e}_e^t)$ are chosen to the same as $y^t(\bar{e}_e^t)$ in the SYM model, with the functional form of Eq. (3.5) and the parameters in Table 3.3. Collectively these assumptions produce the same compressive response as the SYM model, and a tensile response that is close to the measured one. A main difference is that the tensile response has a positive tangent modulus, which does not reproduce the inhomogeneous behavior observed in the tension experiment. Figure 3.15a shows the saturating compressive and tensile back stress-transformation responses. As implied by Eq. (2.27), the tensile response is scaled by 0.55 vertically but 1/0.55 horizontally from the

compressive one. The resultant compressive and tensile stress-strain responses of ASY are plotted in Fig. 3.15b.

3.7.2 Numerical Results

The finite element model, coupled with ASY, is now used to simulate the tube buckling experiment. The mesh adopted for ASY contains 6 elements across the wall thickness, 168 elements around the circumference, 91 elements along the length in the upper half and 35 in the lower half. This mesh is denser than that for SYM and SYM+PL, which is dictated by the complexity of the stress distribution across the tube wall thickness in the buckled zones induced by the tension/compression asymmetry. The values of imperfection amplitudes adopted w_o = 0.02% and w_3 = 0.5% are established through a sensitivity study for optimal performance of the solution.

The calculated nominal compressive stress-normalized shortening (s - d/L) response is shown in Fig. 3.16. Figure 3.16a shows the initial part of the loading response in an expanded view with the uniaxial material response, and Fig. 3.16b shows the complete load-unload hysteresis. For comparison, it also includes the measured response and the one calculated using the SYM model. Figure 3.17 shows two sets of deformed configurations of the tube corresponding to the numbered bullets on the response in Fig. 3.16. Like the previous simulation results, two color scales are used in Fig. 3.16 for contours on the images corresponding to the initial loading part of the response (①-⑥) and for the remaining response (⑥-⑭).

The first consequence of the asymmetric material behavior is that the imperfection amplitudes required to match the initial part of the buckling response are significantly smaller ($w_o = 0.02\%$, $w_3 = 0.5\%$) and thus, more realistic. Although the

initial part of the response shown in Fig. 3.16a is apparently similar to the ones predicted using the symmetric models (SYM and SYM+PL), the smaller amplitude of w_3 allows activation of the wrinkling mode observed in the experiment. It becomes discernible at both ends of the model tube in image ② and increasingly more pronounced in images ③ and ④ with the stress remaining approximately constant up to about station ⑤. In contrast, the imperfection amplitudes required for best results vis-a-vis the experiments were significantly larger with $\omega_o = 0.1\%$ and $\omega_3 = 14\%$ in the analysis using the SYM model. We are reminded that the tensile transformation stress of this material is significantly lower than the compressive one (Fig. 3.1). Thus, imposing a tensile transformation stress equal to the compressive value artificially stiffened the structure. Because of this stiffening, the imperfection amplitudes required to match the measured response had to be unnaturally large. As a result, wrinkling did not materialize as the mode-3 imperfection dominated as is evident from the deformed images in Fig. 3.8.

Even more importantly, the introduction of the tension/compression asymmetry significantly lowered the stress level of the loading part of the calculated response and consequently made the entire hysteresis closer to the experimental response as shown in Fig. 3.16b. The deformation for this model is fully recovered on unloading causing the hysteresis traced to close.

3.8 Analysis Using the Asymmetric Model Including Plasticity (ASY+PL)

The results of the simulations using the SYM+PL and ASY models clearly show that inclusion of plastic deformations and the tension/compression asymmetry influence the response. In this section, we consider a constitutive model that encompasses both plasticity and the tension/compression asymmetry.

3.8.1 Model Calibration

The ASY+PL model is generated by adding plasticity into the ASY model. Thus, it still has $y_c^t(e_e^t) = y_t^t(e_e^t)$ with the functional form in Eq. (3.5), and $s_e(e_e^p)$ is represented by Eq. (3.6) and the parameter values listed in Table 3.4. The asymmetry in the transformation behavior is introduced by letting a = 0.99225 in Eq. (2.23b). Figure 3.18a shows the resultant asymmetric compressive and tensile responses in the pseudoelastic regime and Fig. 3.18b shows the responses including plasticity under compression and tension.

3.8.2 Numerical Results

The tube buckling problem is now simulated by adopting ASY+PL in the finite element model with the same mesh density as that used in the ASY simulation. The numerical results presented are obtained based on the same imperfection amplitudes with those for ASY, that is $w_o = 0.02\%$ and $w_3 = 0.5\%$. This choice was based on the results of a parametric study of the sensitivity of the performance of the solution to the imperfections, the results of which will follow.

As expected, the inclusions of both tension/compression asymmetry and plasticity further improves the calculated response and the solution in general. The calculated nominal stress-shortening response (s - d/L) is plotted in Fig. 3.19. Figure 3.19a shows the early part of the response expanded and Fig. 3.19b shows the complete load-unload hysteresis. Figures 3.20 shows two sets of deformed configurations of the model tube that correspond to the numbered bullets on the two depictions of the stress-shortening response in Fig. 3.19. The superimposed color contours now represent the sum of the equivalent transformation and plastic strains (≡ESN+PEEQ). Because of the different levels of strain associated with the two sets of images they are assigned different color

scales. The calculated stress-shortening response follows the nearly linear compressive response of the material up to a stress of about 600 MPa. The nonlinearity that follows and the associated wrinkling, are identical to the results in for the ASY model in Fig. 3.16. The amplitude of the axisymmetric imperfection adopted is so small that the modest friction between the ends of the tube and the rigid plates affects both ends equally. Beyond ② the wrinkles at both ends become more pronounced (see images ③ and ④) with the stress remaining nearly constant up to about station ⑤. In the neighborhood of station ⑤, the mode-3 imperfection gets excited, the first signs of which can be seen in image ⑤ and more prominently in image ⑥. The activation of mode-3 triggers the collapse of the structure that can be seen in Fig. 3.19b to follow point ⑥.

The buckling response is seen to follow the experimental one quite closely. Between stations ⑥ and ⑦, the stress drops rather abruptly as mode-3 localizes into a single lobe at the top. As the amplitude of this lobe increases, the local strain reaches levels as high as 10% (see Fig. 3.20) indicating that the transformation phase has been completed and some local plastic deformation has taken place. The associated local stiffening of the material decelerates further growth of this lobe and a second one starts to develop below it. The growth of the second lobe is seen to take place in images ⑧, ⑨, and ⑩ while the stress continues to drop but at a decreasing rate.

Unloading from ⑩ follows the measured response quite closely. The stress drops up to station ⑫. The deformation initially decreases in both lobes but the lower one recovers faster as evident in images ⑫ and ⑬. Beyond station ⑫, the stress increases once more developing the potential of snap-back as was the case in the experiment. By image ⑭ the radial deformation has essentially fully recovered, but small islands of permanent deformation remain in the zones that experienced the most severe deformation during loading. Beyond ⑭, the material is essentially back to the *A* phase and unloads

with a stiff slope. At zero axial stress at station ⑮, a residual net displacement remains that is somewhat smaller than the experimental value. Interestingly, the residual strain in image ⑮ is larger than that in image ⑭ as the overall unloading has caused local reverse loading at the intrados of the erased top lobe.

3.8.3 Parametric Study

Figure 3.21a shows a set of responses calculated using ASY+PL, in which the amplitude of the axisymmetric imperfection w_o is varied with the other two imperfection parameters kept constant (i.e., $w_3 = 0.5\%, b = 20$). The responses are quite close to each other. Thus, an expanded view of the responses for δ / L between 1.6% and 2.0% is shown to better visualize the differences. As w_o increases, the response moves upwards, which validates again the stabilizing effect of the axisymmetric component of the imperfection. Note that the optimal value for this amplitude, $w_o = 0.02\%$, is so small that the variation near this value affects the calculated response only slightly and the events are not influenced.

Figure 3.21b shows a set of responses in which the mode-3 imperfection amplitude, w_3, was varied with the other two variables kept at the values used in the optimal simulation (i.e., $w_o = 0.02\%$, $b = 20$). Similar to the observations in the sensitivity study on imperfection using model SYM, increasing w_3 reduces the extent of the initial stress plateau and accelerates the onset of collapse. However, the other two values of ω_3 do not change the evolution or events either quantitatively or qualitatively.

Figure 3.22 compares the calculated responses for $\beta = 5$, 20, 40 and 80 with the two imperfection amplitudes kept at the levels for optimal performance (i.e., $\omega_o = 0.02\%$, $\omega_3 = 0.5\%$). As anticipated, the imperfection amplitudes adopted are so

small that these responses are too close to each other and thus an expanded view of the responses is presented to zoom in the differences. Despite this, increasing β delays the onset of collapse slightly, showing the same trend with that observed for the SYM model

The study on the sensitivity of the calculated response on the imperfection parameters for ASY+PL shows that the introduction of tension/compression asymmetry into the constitutive model reduces the imperfection amplitudes required in order to match the experimental response, to levels that are in concert in other inelastic buckling problems. Furthermore, the solution is much less sensitive to imperfections.

3.9 SUMMARY

The pseudoelastic NiTi tube considered, D/t = 23.6, under axial compression initially deforms uniformly following the elastic modulus of the *A* phase. The onset of transformation to *M* causes a reduction in stiffness, which leads to axisymmetric wrinkling close to one end while the stress enters a plateau. Wrinkling grows and yields to a non-axisymmetric buckling mode with three circumferential waves. This mode is unstable, leading to localization of deformation and a drop in stress. The deformation localizes first into a single mode-3 buckling lobe and subsequently a second one. Different from crushing of conventional metal tubes that involves concertina folding, the growth of the lobes is arrested here due to stiffening of the material at the completion of *M* transformation. Upon unloading, the buckling lobes are erased in the reverse order to that followed during loading. Most of the material reverts to *A*, which unloads along the initial elastic trajectory, producing a nearly closed hysteresis. A small residual

displacement remains unrecovered, indicating the development of some plastic deformation in the specimen.

The buckling experiment is simulated using a FE model, in which the constitutive model presented in Chapter 2 is implemented. The instability is initiated by introducing a small geometric imperfection to the FE model, which has an axisymmetric component and a non-axisymmetric one. Guidance about the characteristic wavelength of the imperfection comes from a bifurcation analysis of the perfect tube.

The simplest version of the constitutive model, based on the compressive response of the NiTi that does not allow for plastic deformations to develop in the transformed martensite, was first used to simulate the experiment. Although the model reproduced the correct buckling stress level, the localization that follows and the recovery of buckling, the hysteresis traced did not reproduce the experimental one adequately. Additional features were progressively added to the constitutive model making it more representative of the actual material behavior.

Plasticity was then introduced into the model when the transformed martensite reaches a critical state. This change lowered the stress level of the unloading response and resulted in a small permanent deformation upon unloading. However, the calculated response during loading remained much higher than the experimental one.

The next modification of the constitutive model incorporated the tension/compression asymmetry. It was first implemented in the finite element model without plasticity. The calculated response and most aspects of the evolution of buckling improved significantly by comparison to the experimental results.

The constitutive model was subsequently expanded to include plasticity in addition to the tension/compression asymmetry. This model produced the best prediction of the force-displacement response as well as all aspects of the buckling and recovery of

the model tube. The response became closer to the measured one during both loading and unloading and left behind a small permanent deformation and a slightly open hysteresis. Furthermore, the energy consumed by the load/unload cycle closely approximated the experimental value.

In summary, the incorporation of the tension/compression asymmetry into the constitutive model was found to be necessary in bringing the calculated response of the NiTi tube close to the experimental results. The addition of plastic deformation further improves the predictions.

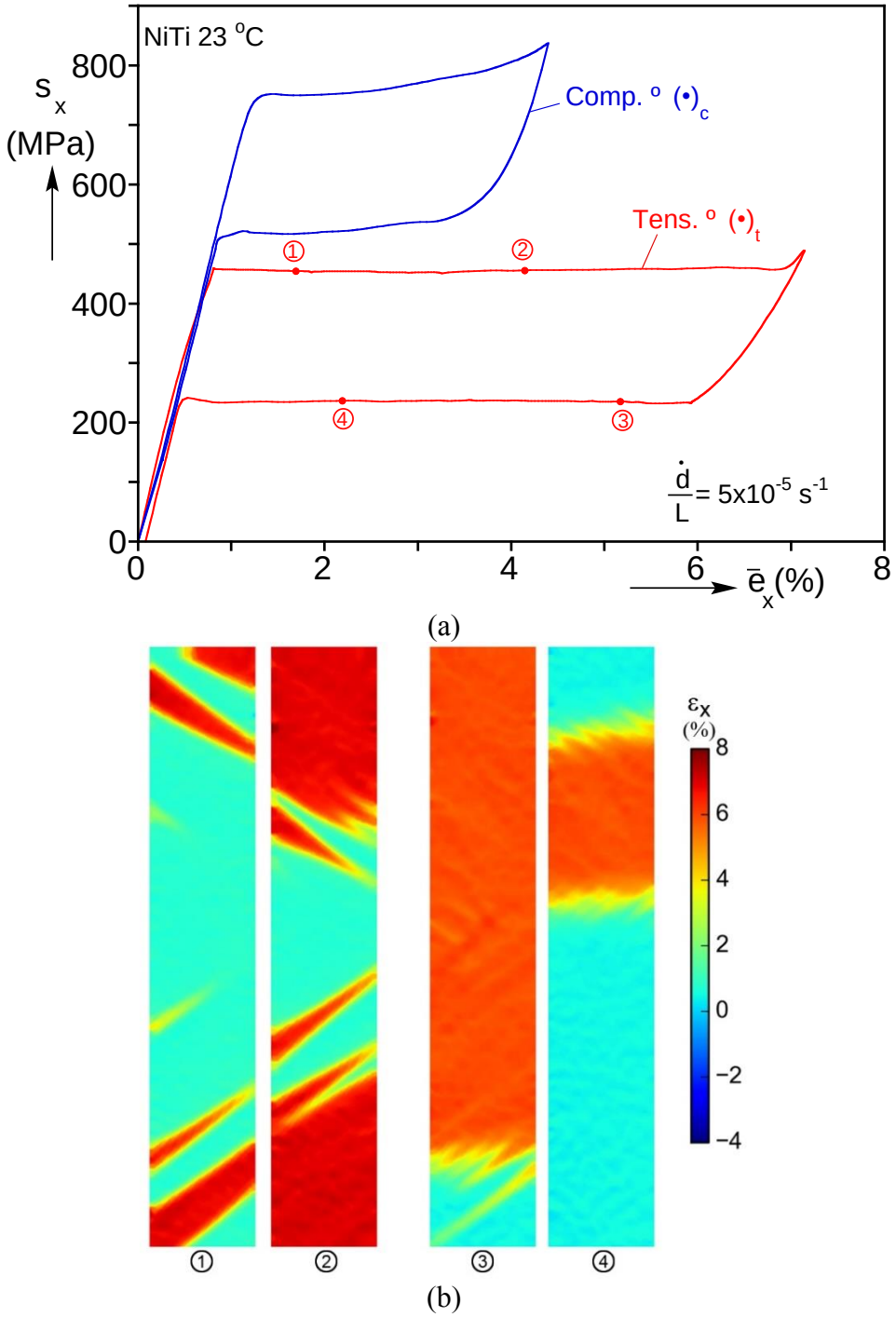

Fig. 3.1 (a) Tensile and compressive axial stress-elongation/shortening responses of NiTi tubes xihibiting significant asymmetry. (b) Select DIC deformation contours during tensile loading and unloading exhibiting spiral localization patterns (from Bechle and Kyriakides, 2016a)

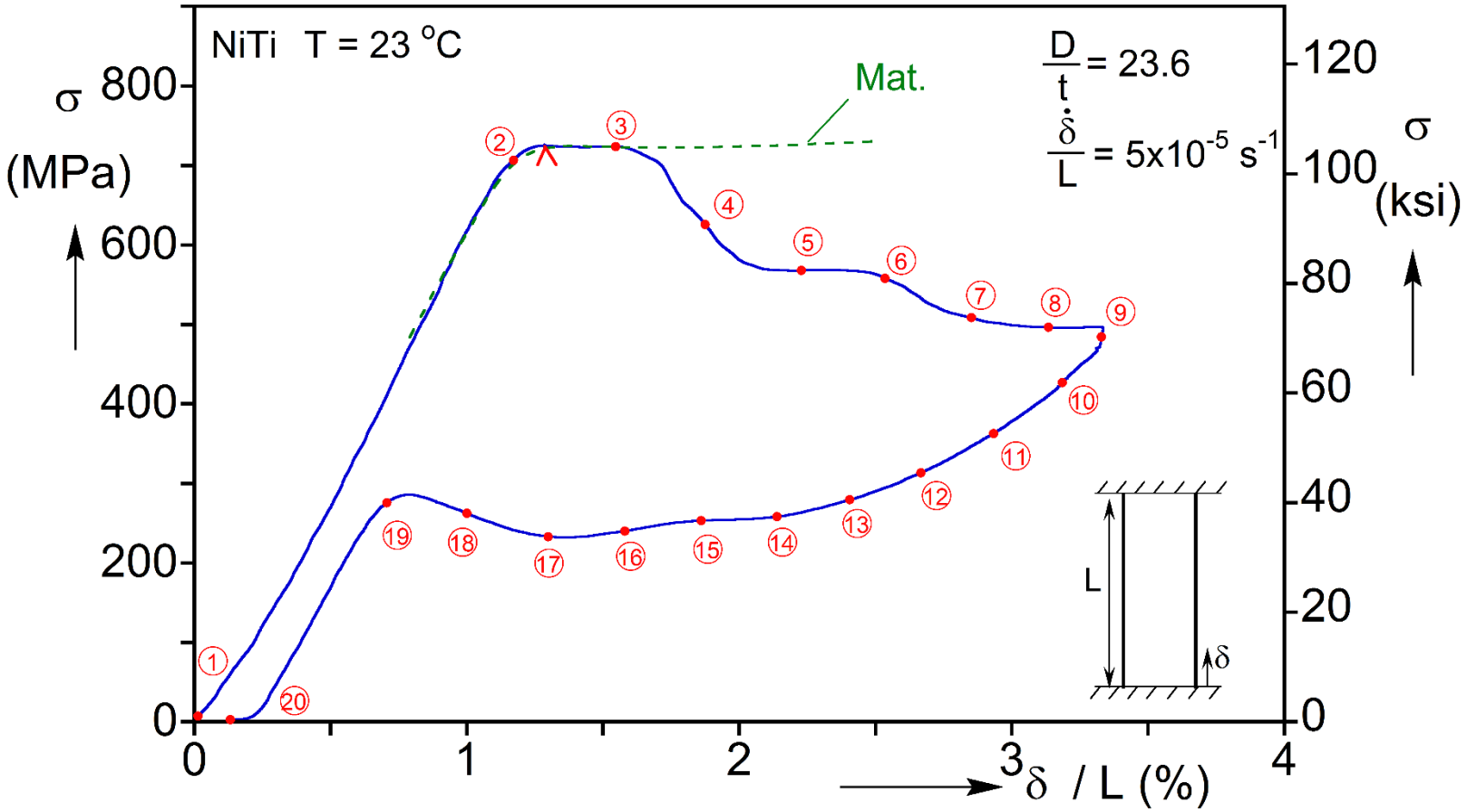

Fig. 3.2 Compressive axial stress-shortening buckling and recovery response recorded in an experiment on a pseudoelastic NiTi tube with $D/t = 23.6$ (from Jiang *et al.* [2016a]).

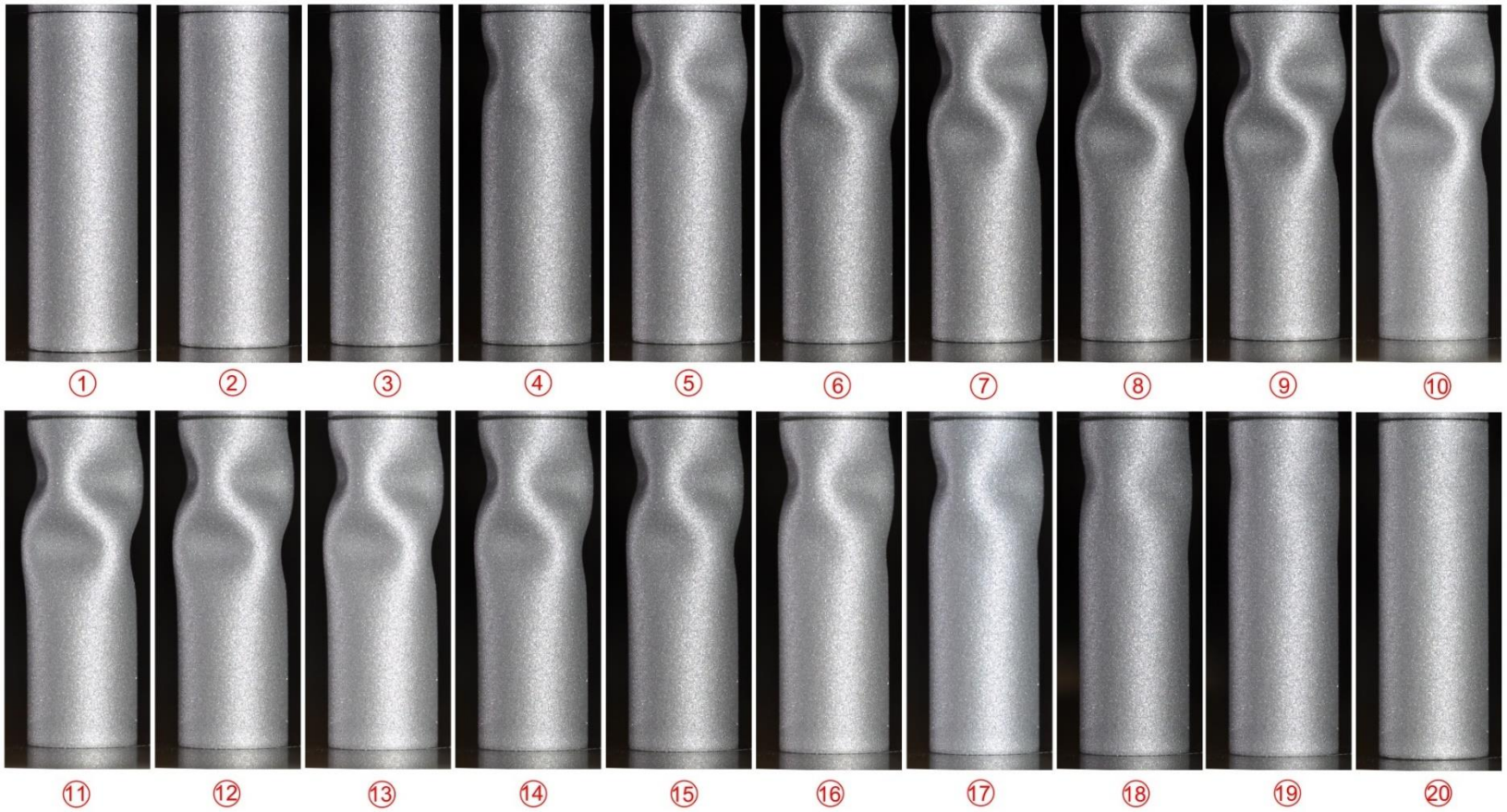

Fig. 3.3 Sequence of photographic images showing the evolution of a mode-3 buckling model during loading (①-⑨) and the recovery of the deformation on unloading (⑩-⑳) (from Jiang, Bechle *et al.* [2016a]).

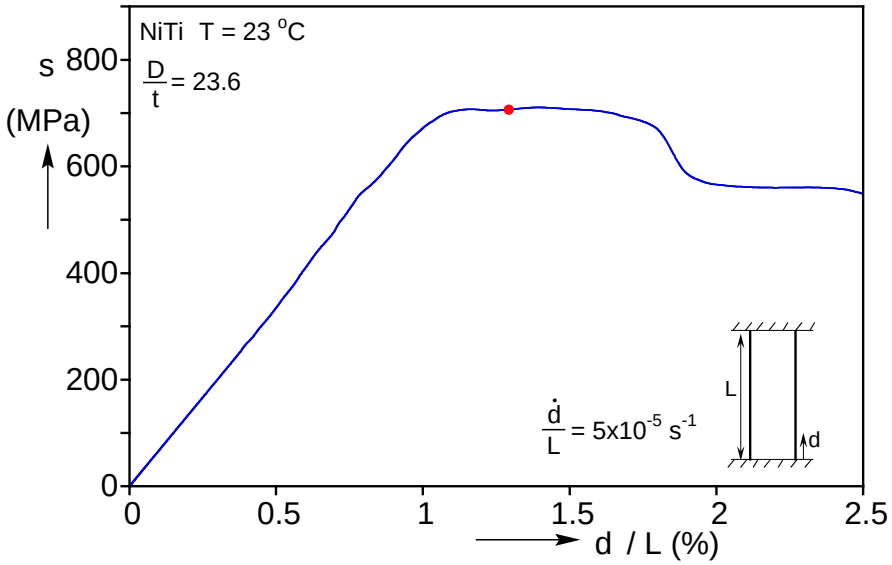

(a)

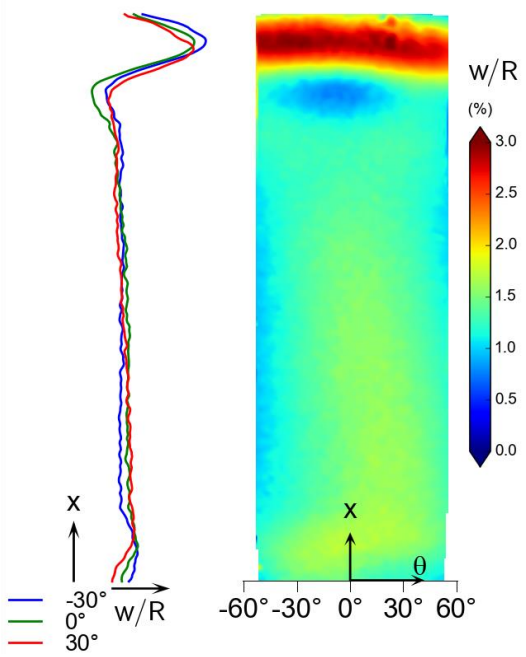

(b)

Fig. 3.4 (a) The early part of the compressive response of a NiTi tube similar to the one studied. (b) DIC image that shows axisymmetric wrinkling at the top of the specimen corresponding to the point marked on the response in (a) with a solid bullet. The color contours correspond to the radial displacement (from Jiang *et al.* [2016b]).

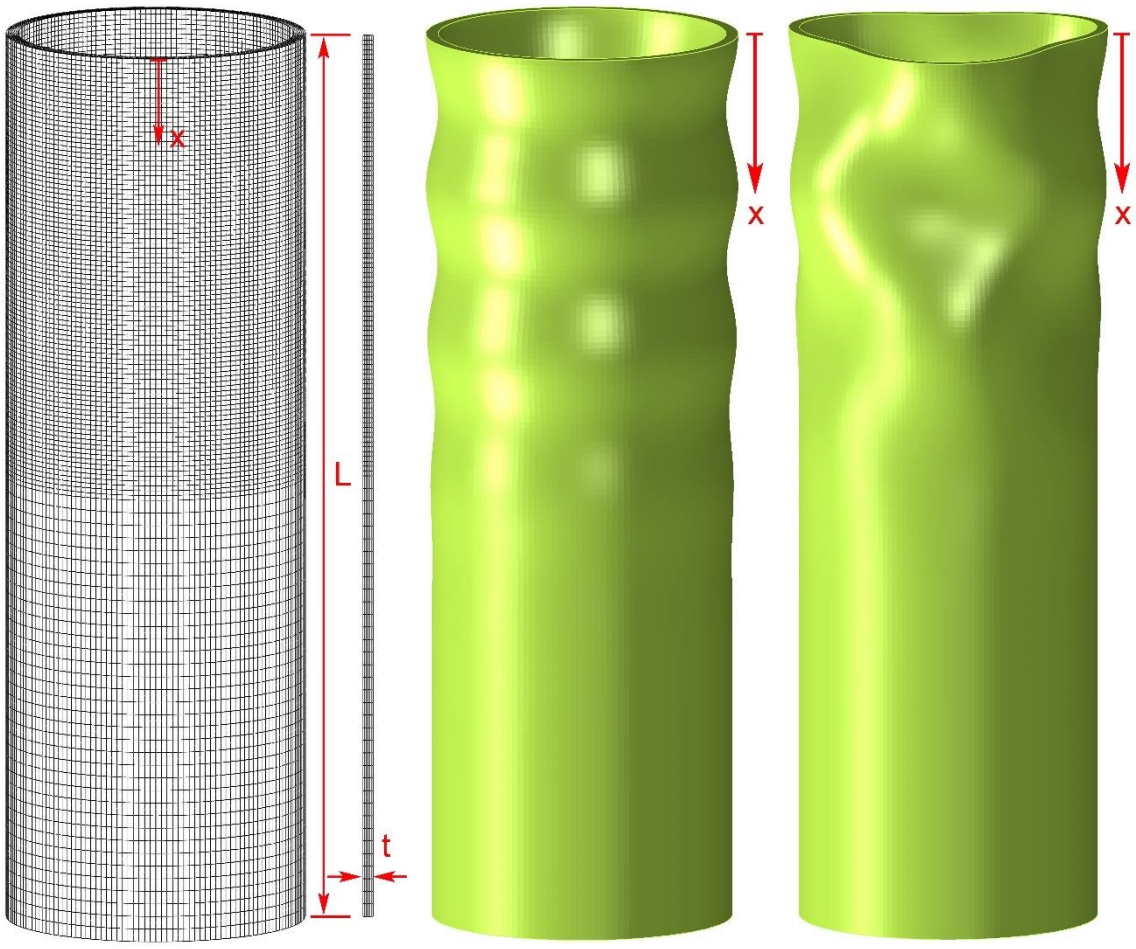

(a) (b) (c)

Fig. 3.5 (a) Schematic of the finite element mesh of the structural model. (b)Axisymmetric and (c) mode-3 geometric imperfections adopted (amplitudes exaggerated).

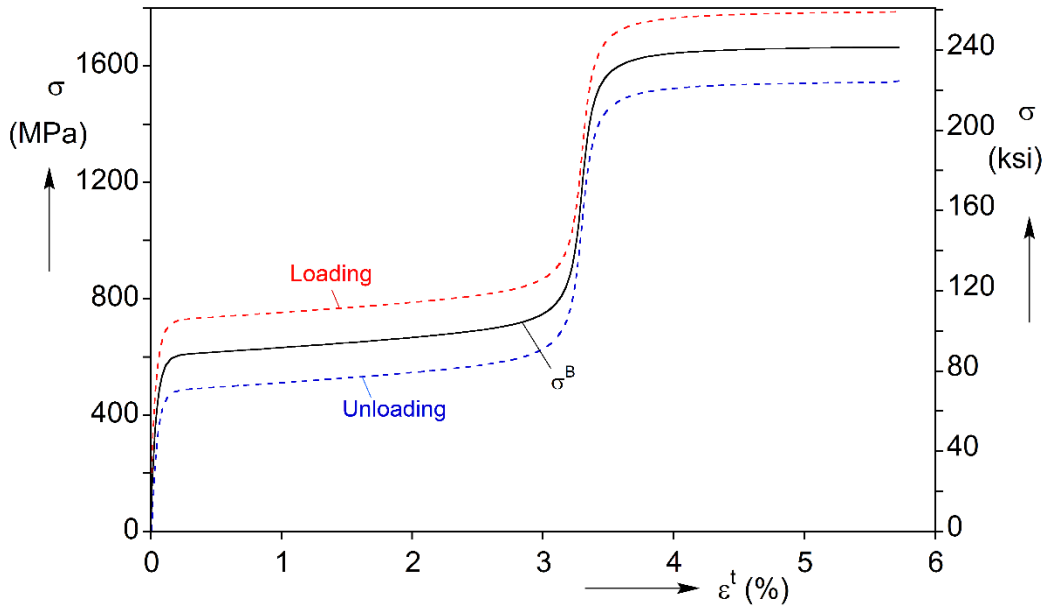

(a)

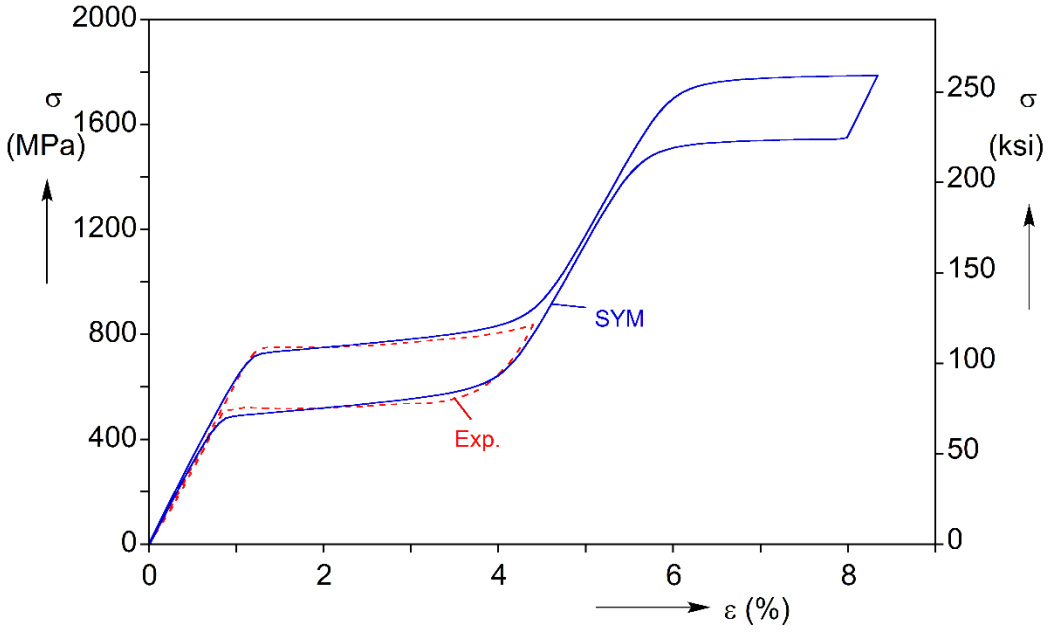

(b)

Fig. 3.6 (a) Uniaxial compressive back stress-transformation strain relation in the model SYM. (b) The resultant stress-strain response of SYM, together with the experimental one.

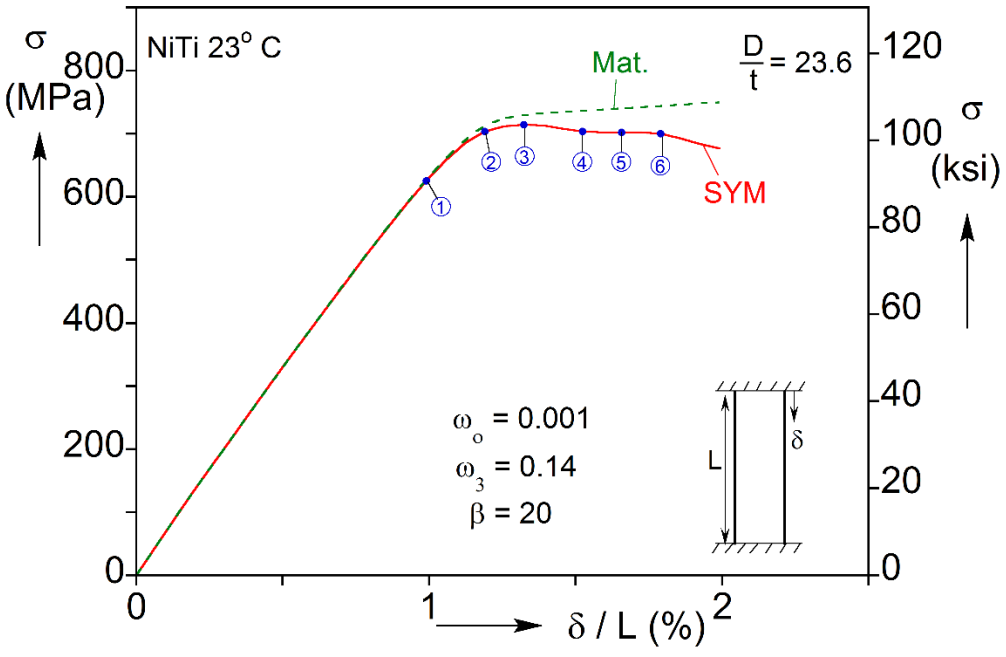

(a)

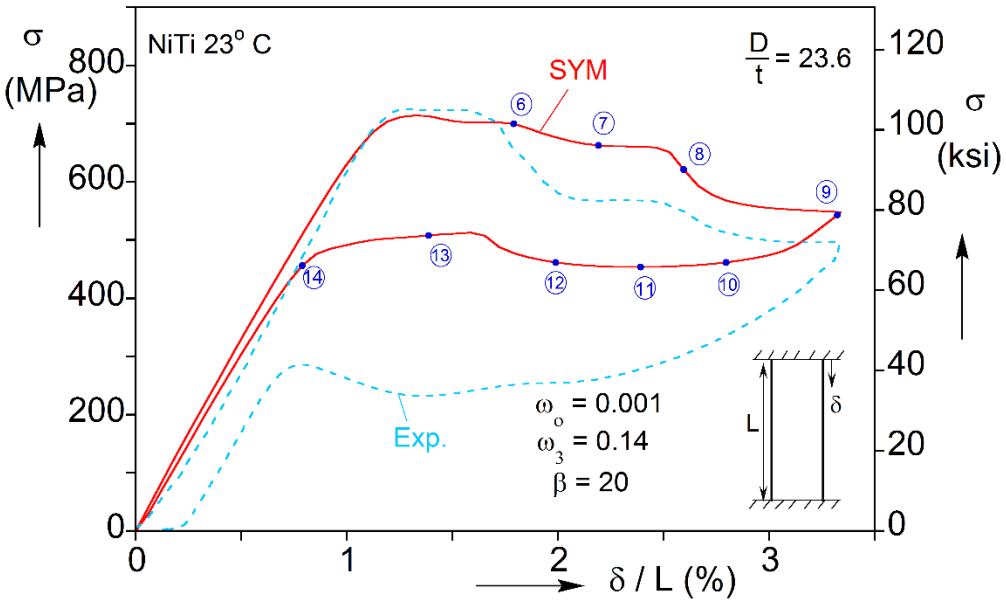

(b)

Fig. 3.7 Calculated compressive axial stress-shortening response using model SYM. (a) Early part of the structural and material responses. (b) Complete load-unload response together with the experimental one.

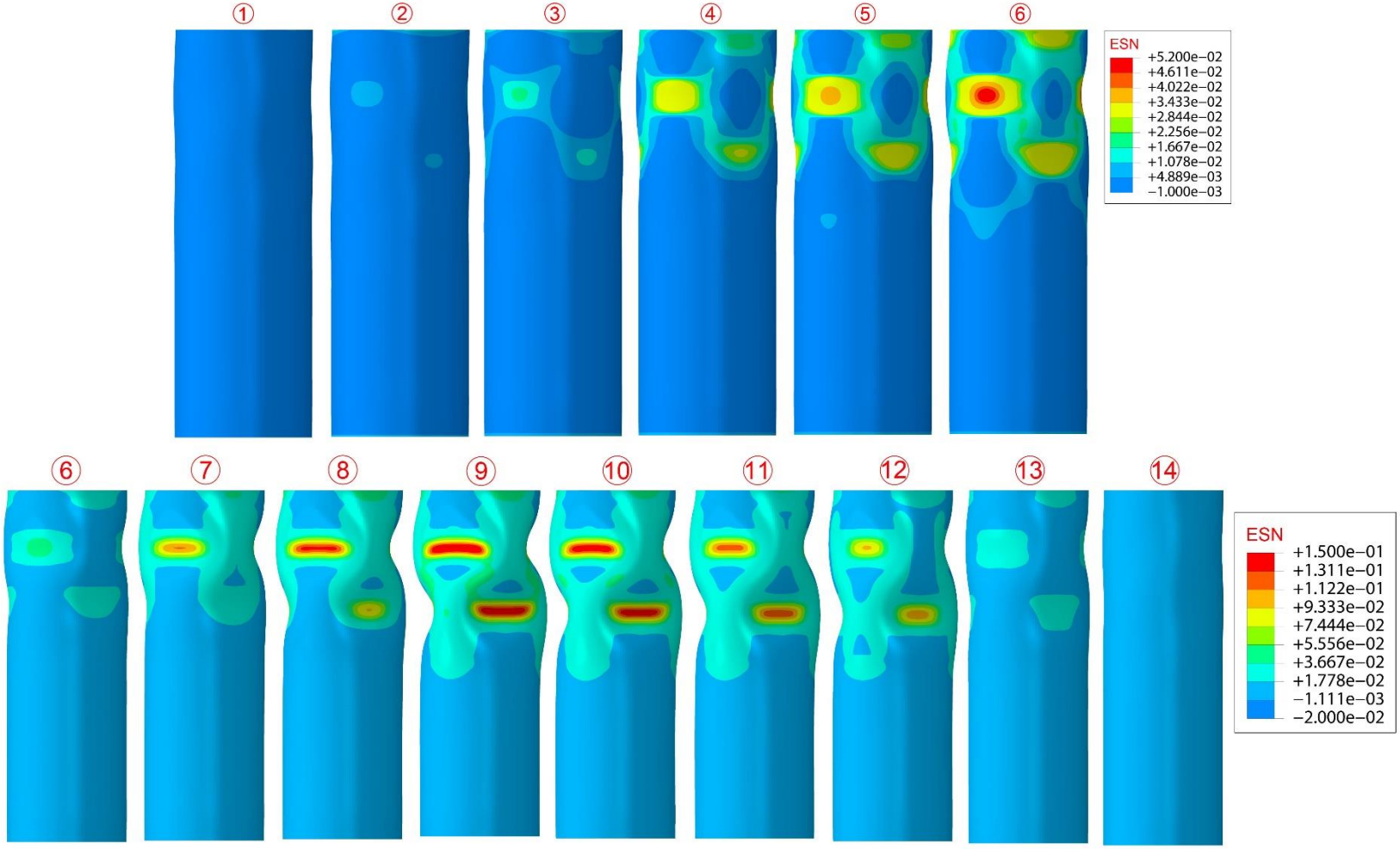

Fig. 3.8 Sequence of deformed configurations with superimposed strain contours showing the predicted buckling and recovery by using SYM. Images correspond to the numbered bullets on the response in Fig. 3.6.

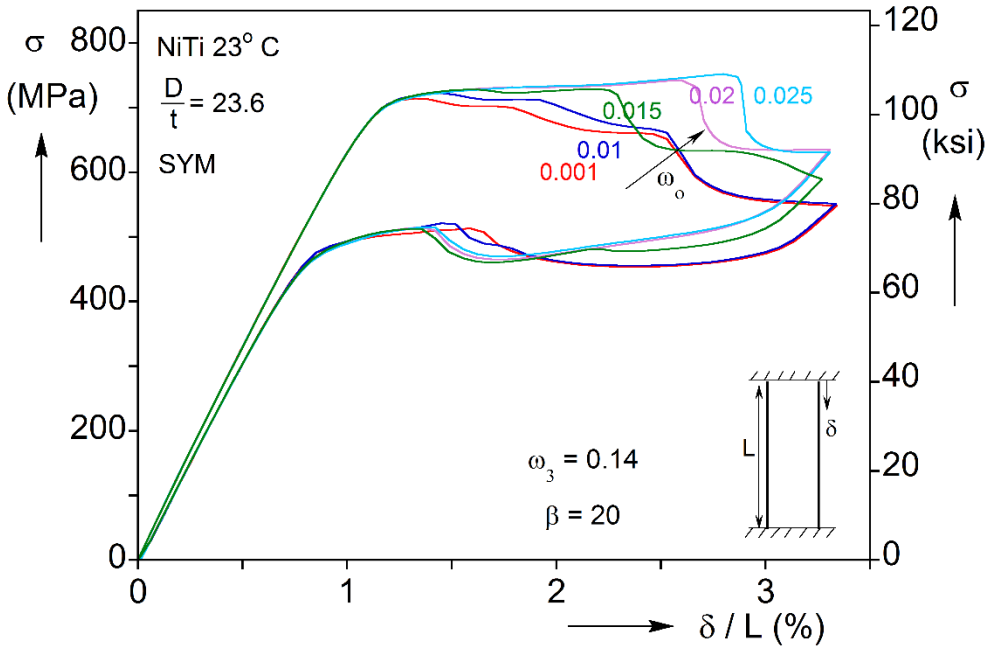

(a)

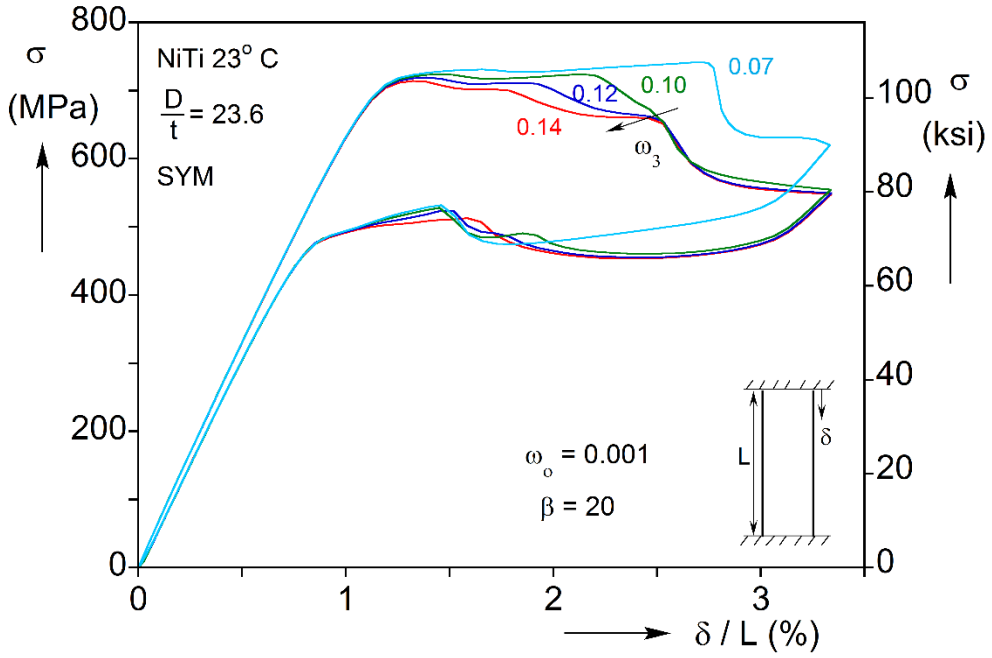

(b)

Fig. 3.9 Effect of imperfection amplitudes on calculated stress-shortening response using SYM. (a) Effect of axisymmetric amplitude ω_o and (b) effect of non-axisymmetric amplitude ω_3.

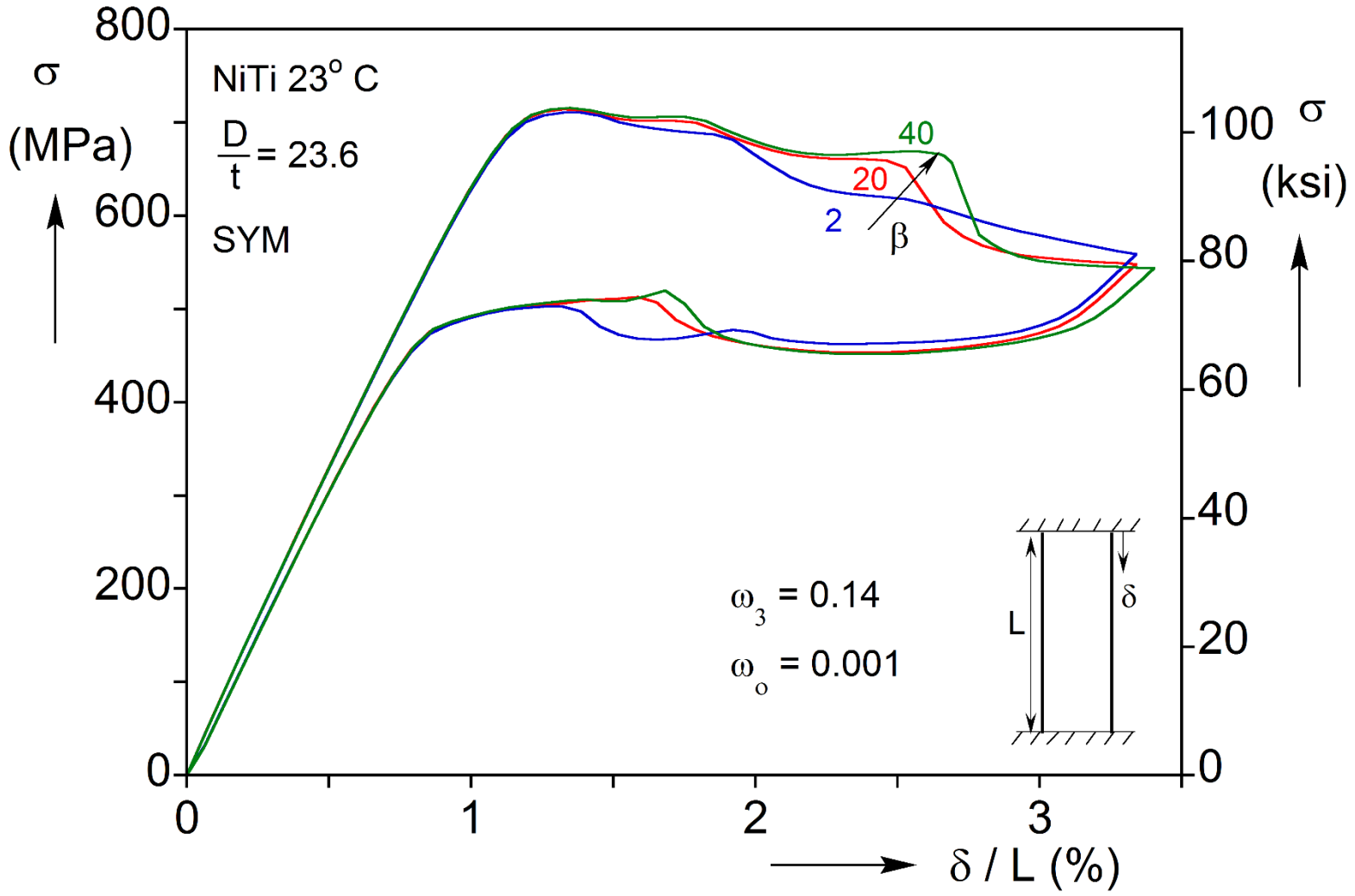

Fig. 3.10 Effect of imperfection extent β on calculated stress-shortening response using SYM.

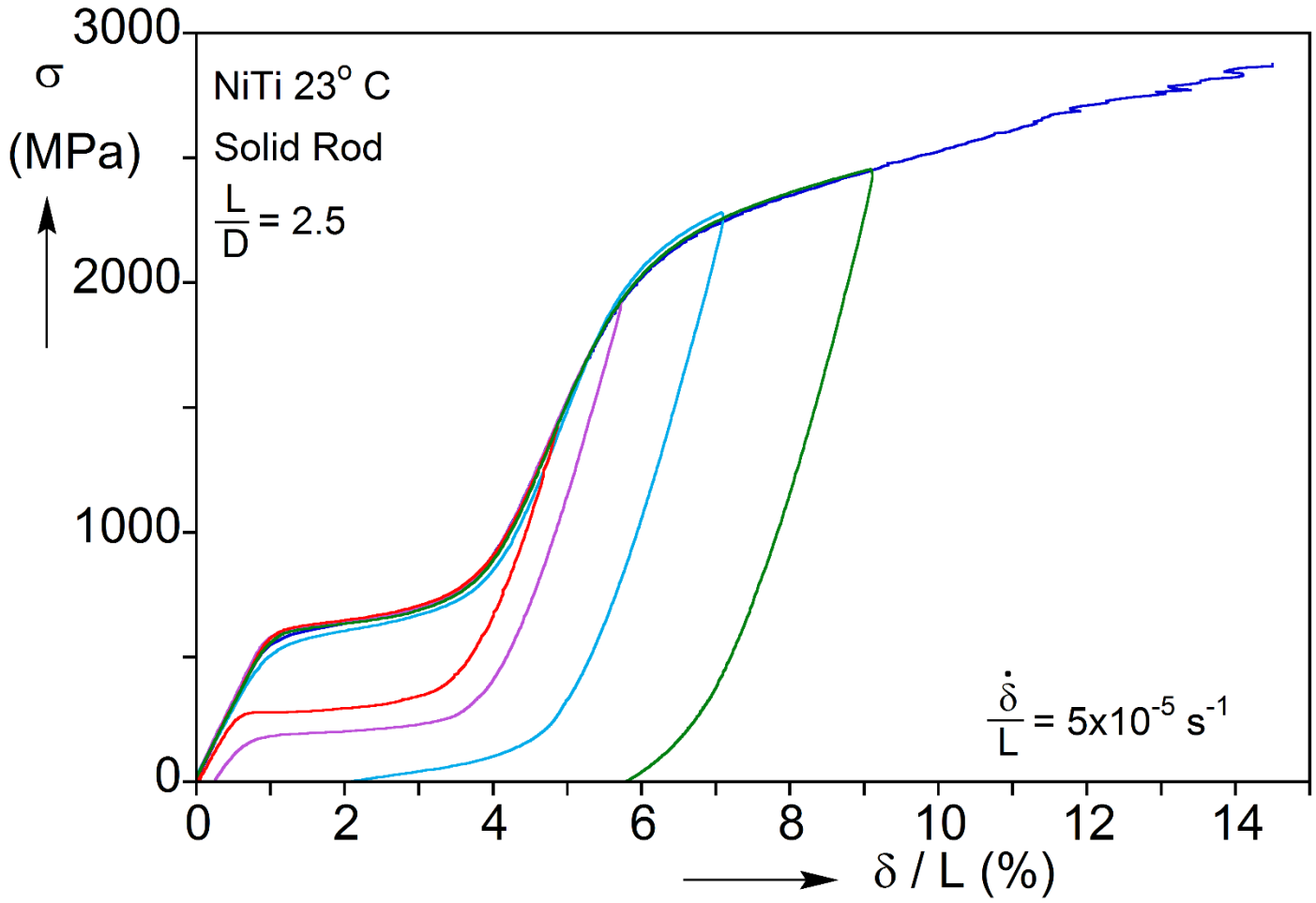

Fig. 3.11 Measured load-unload compressive responses of a NiTi rod that demonstrate permanent deformation due to yielding of transformed martensite (from Jiang *et al.* [2016b]).

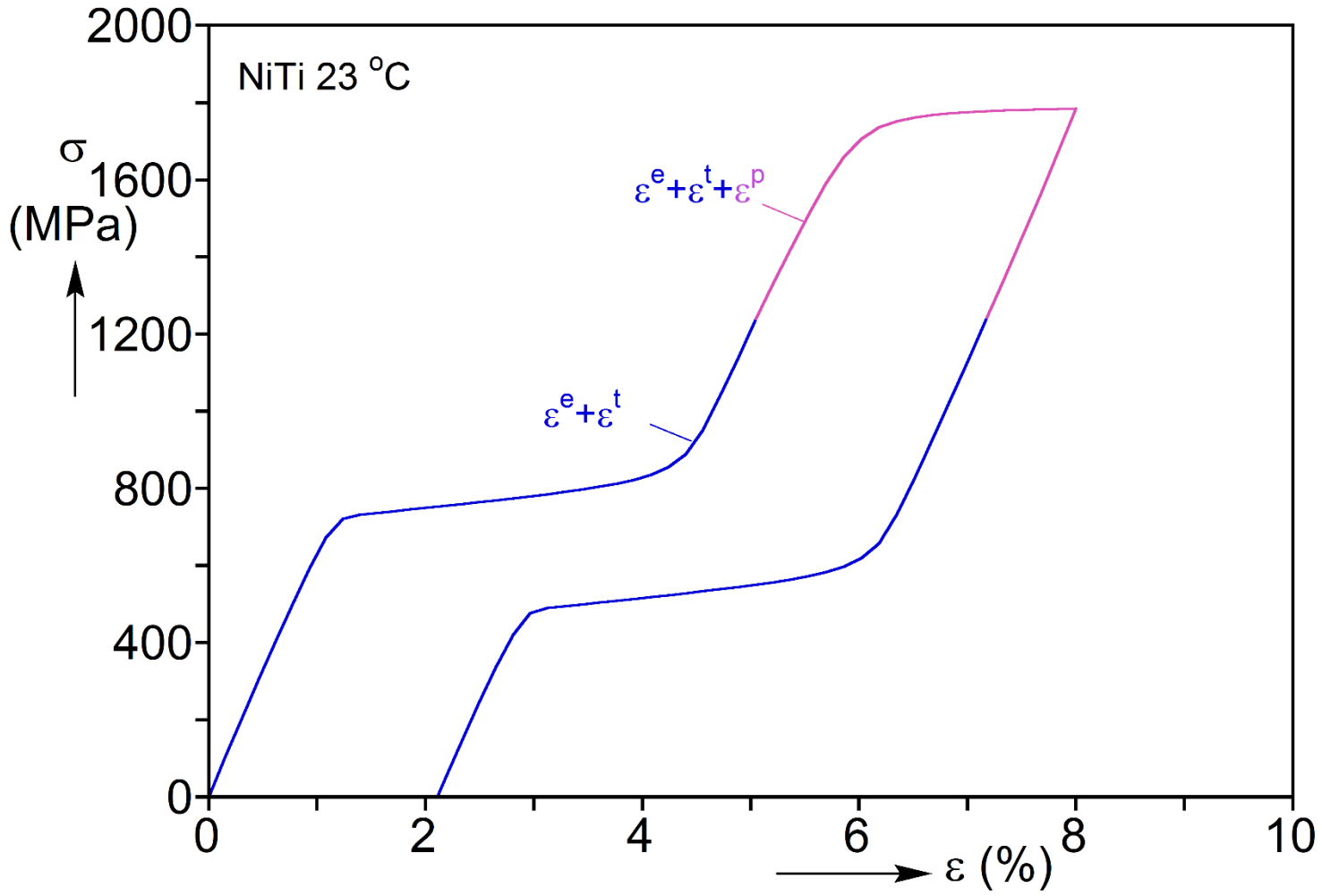

Fig. 3.12 Uniaxial response produced by the model SYM+PL.

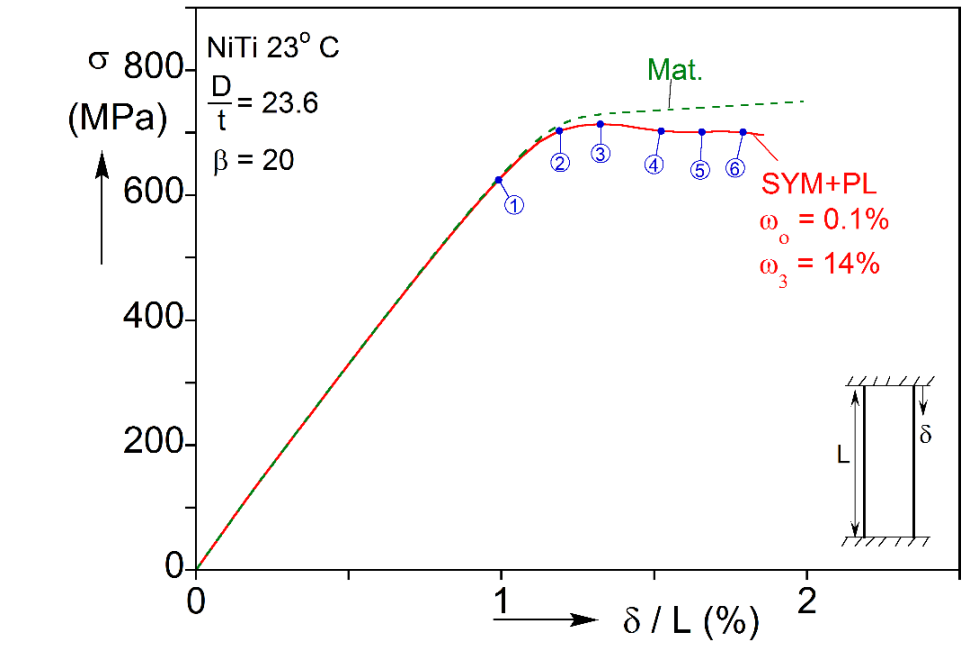

(a)

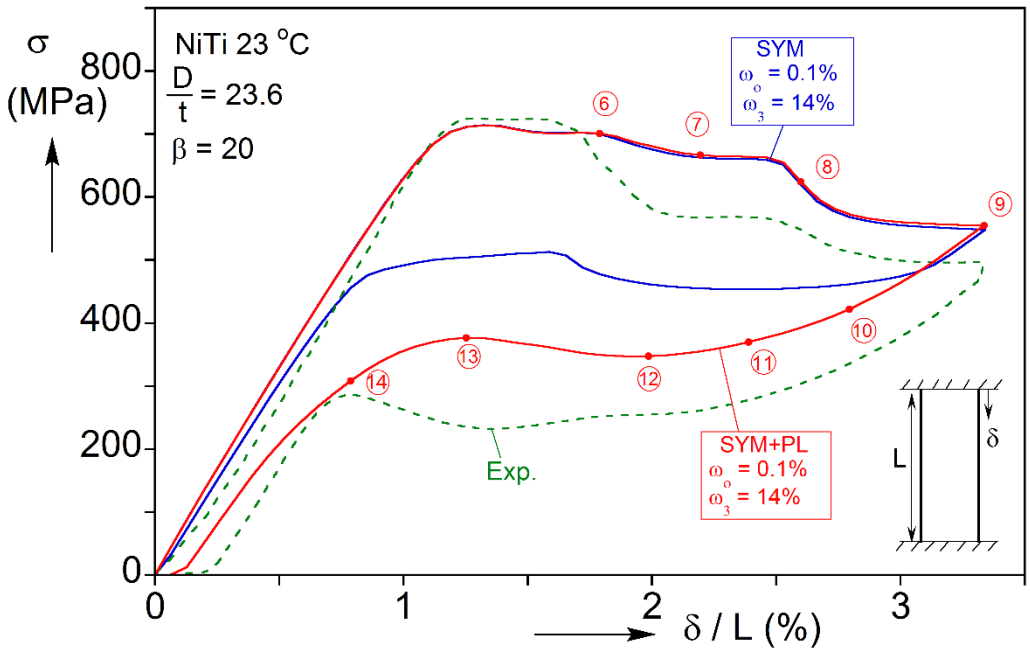

(b)

Fig. 3.13 Calculated compressive stress-shortening response using model SYM+PL. (a) Early part of the structural and material responses. (b) Complete load-unload response together with the experimental one and the one resulting from SYM.

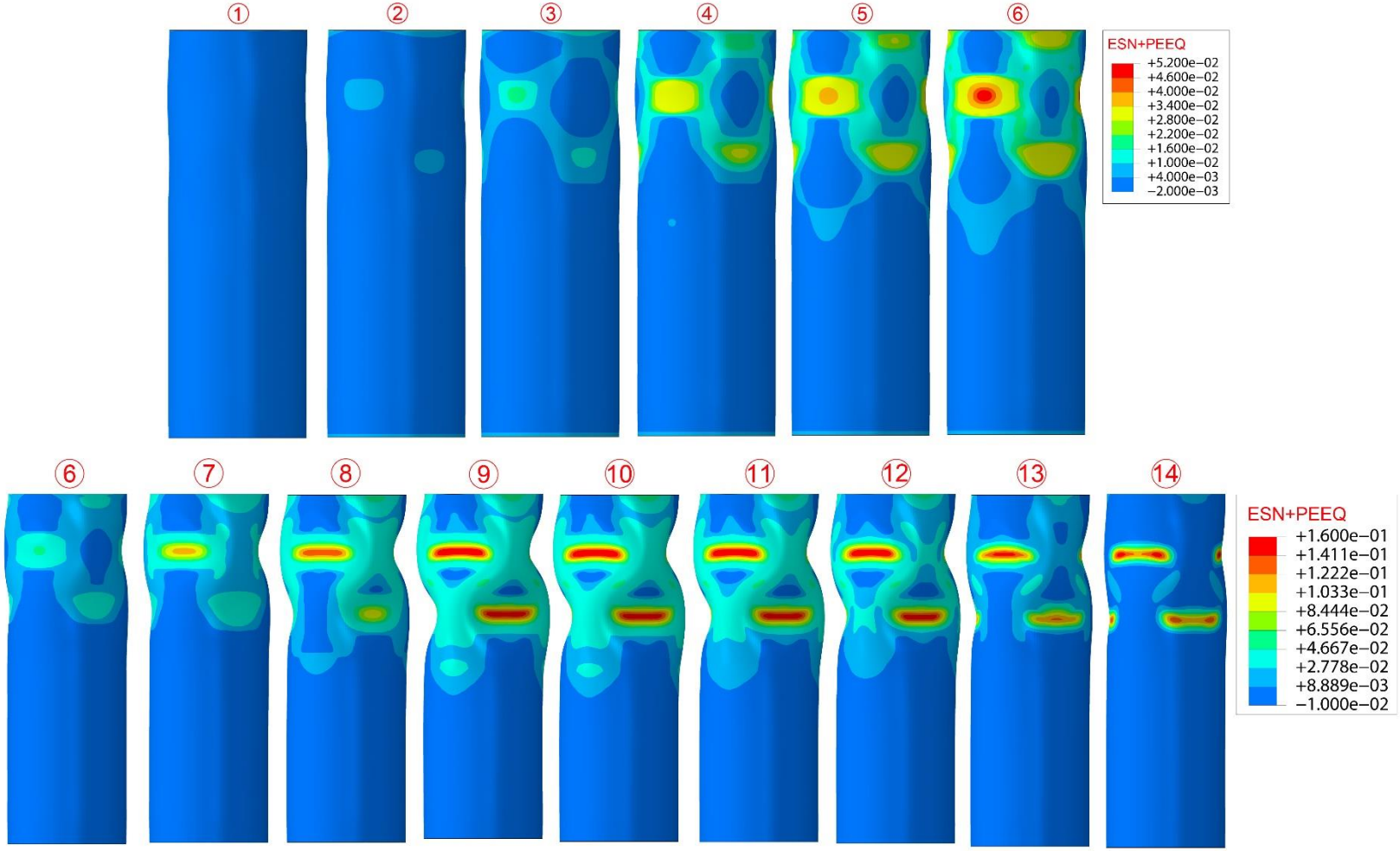

Fig. 3.14 Sequence of deformed configurations with superimposed strain contours predicted by SYM+PL. Images correspond to the numbered bullets on the response in Fig. 3.12.

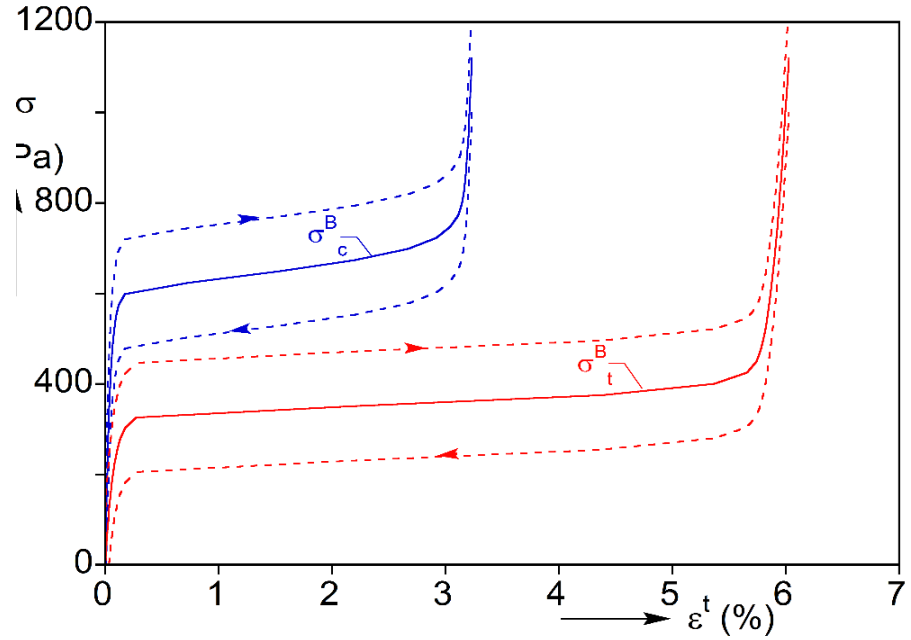

(a)

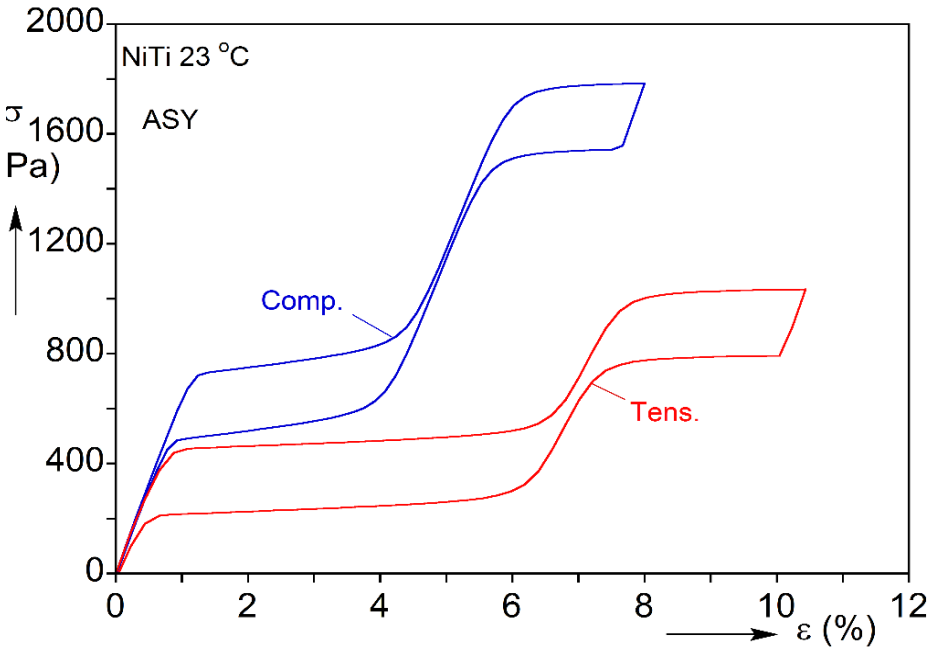

(b)

Fig. 3.15 (a) Uniaxial compressive and tensile stress-transformation strain responses produced by ASY. (b) Uniaxial compressive and tensile responses of ASY.

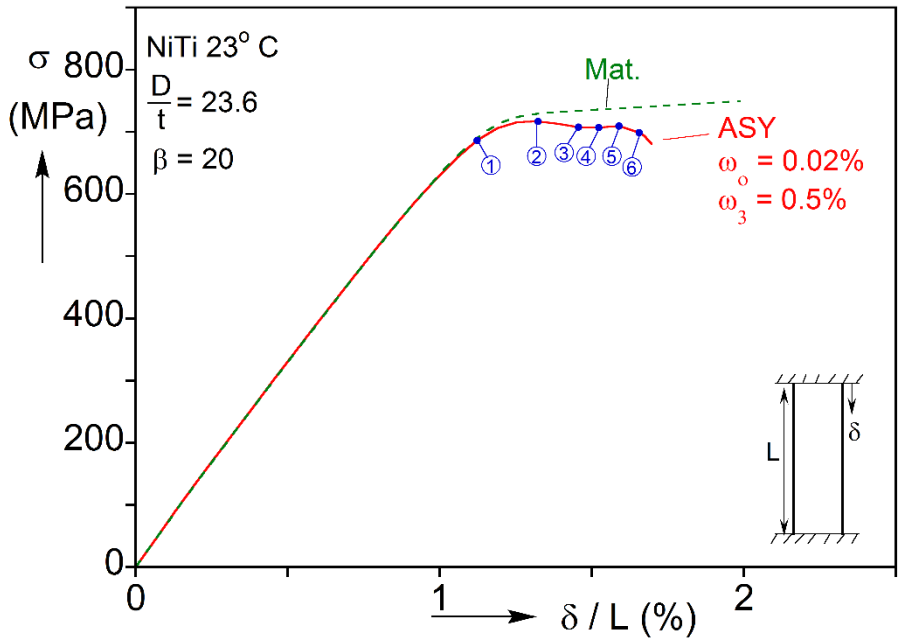

(a)

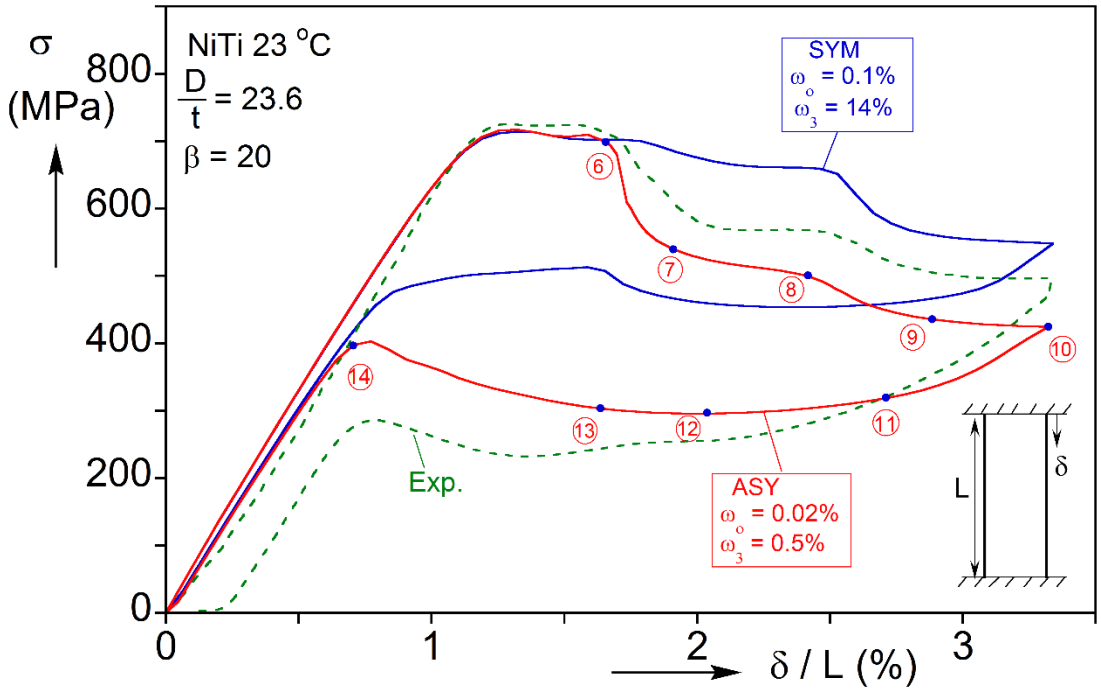

(b)

Fig. 3.16 Calculated compressive stress-shortening response using ASY. (a) Early part of the structural and material responses. (b) Complete load-unload response together with the experimental one and the one resulting from SYM.

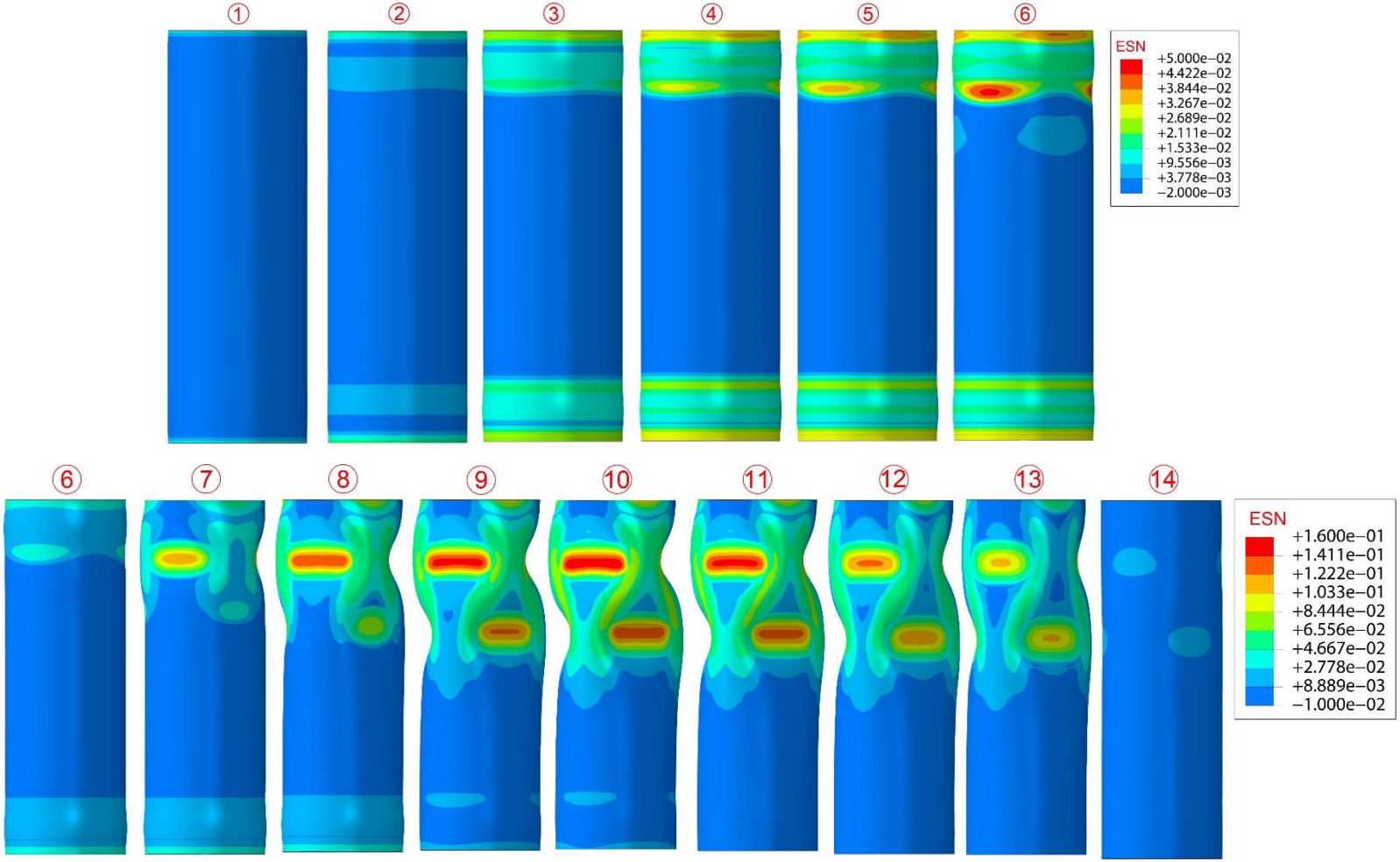

Fig. 3.17 Sequence of deformed configurations with superimposed strain contours showing the predicted buckling and recovery by using ASY. Images correspond to the numbered bullets on the response in Fig. 3.15.

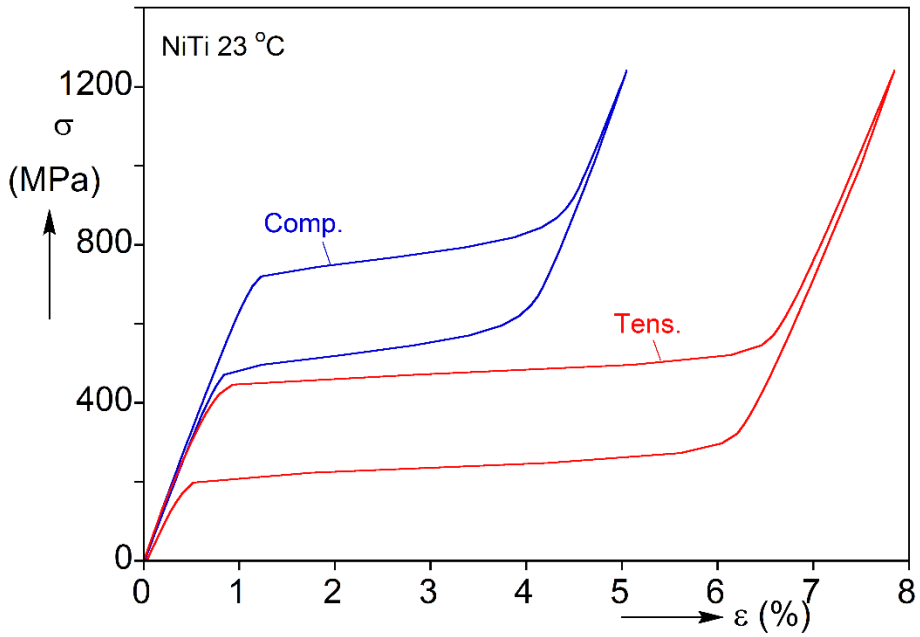

(a)

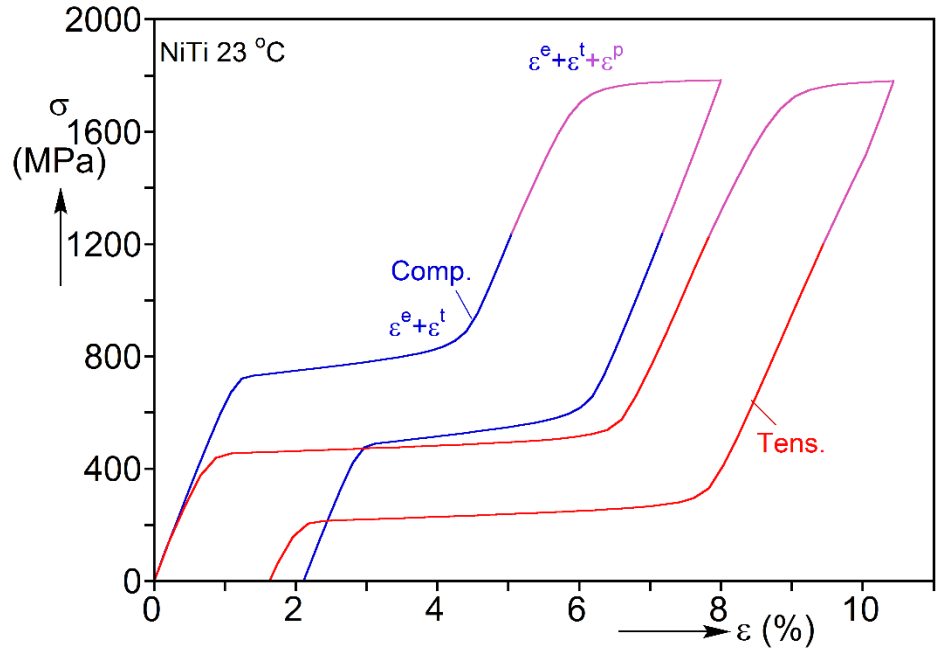

(b)

Fig. 3.18 (a) Pseudoelastic responses of the model ASY+PL under compression and tension. (b) Compressive and tensile responses of ASY+PL including plasticity.

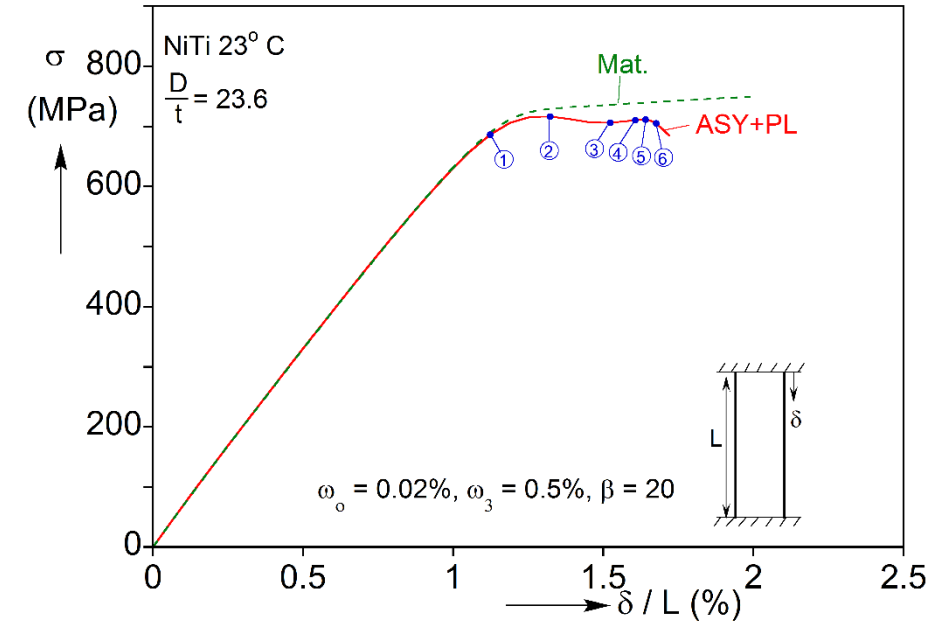

(a)

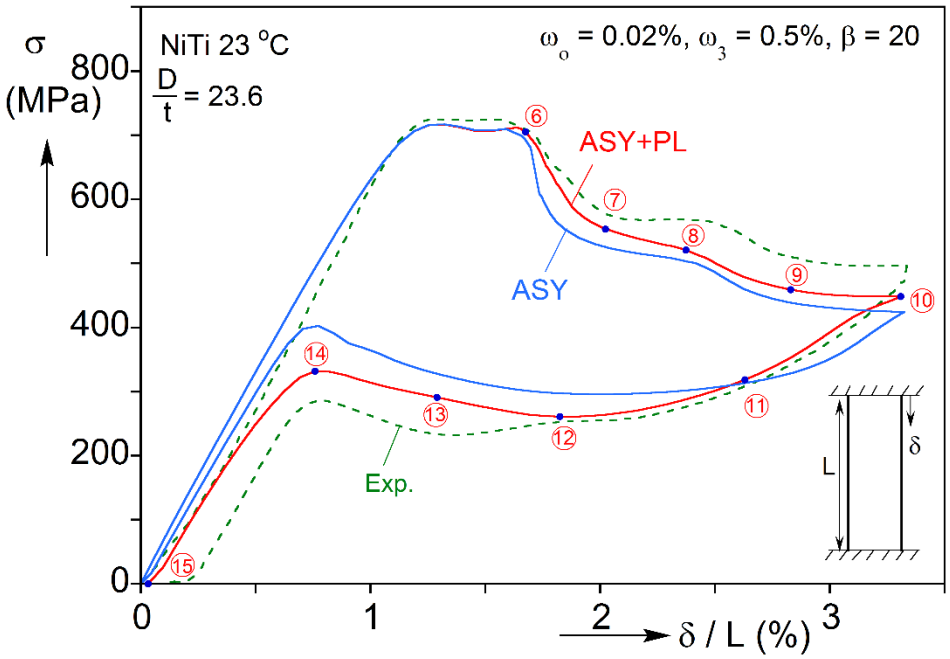

(b)

Fig. 3.19 Calculated compressive stress-shortening response using ASY+PL. (a) Early part of the structural and material responses. (b) Complete load-unload response together with the experimental one and the one from ASY.

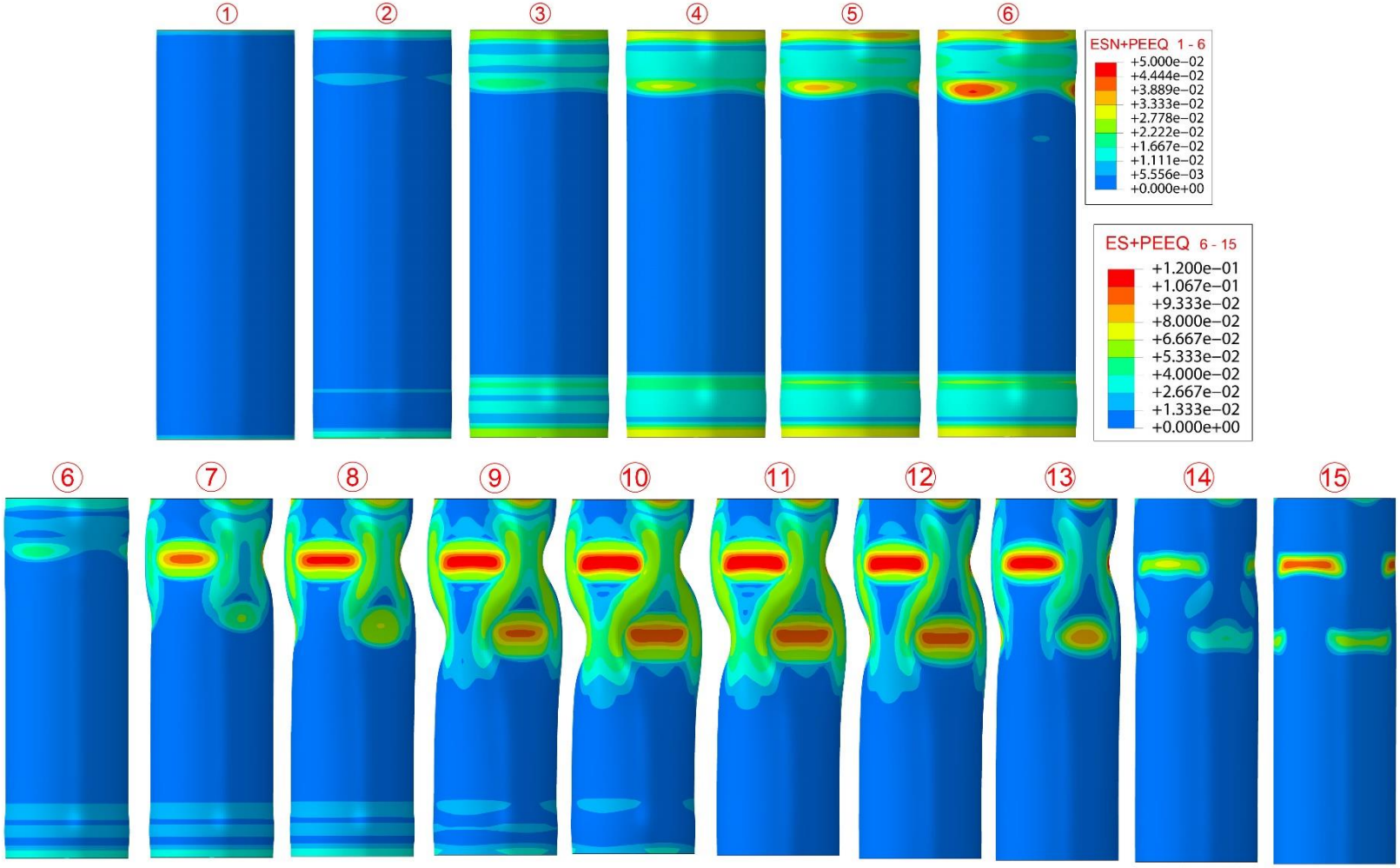

Fig. 3.20 Sequence of deformed configurations with superimposed strain contours showing the predicted buckling and recovery by using ASY+PL. Images correspond to the numbered bullets on the response in Fig. 3.18.

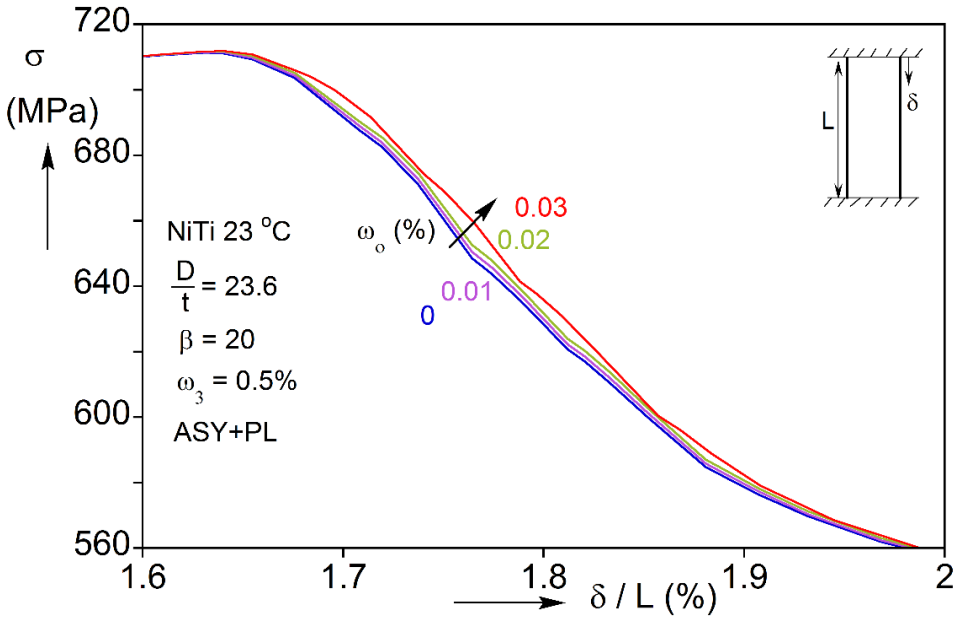

(a)

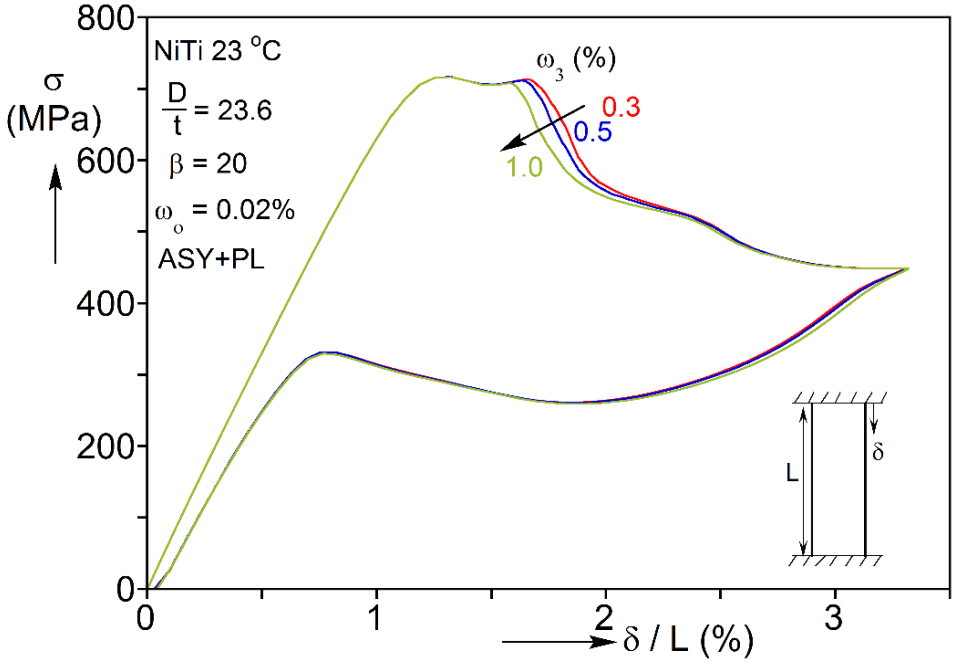

(b)

Fig. 3.21 Effect of imperfection amplitudes on calculated stress-shortening response using ASY+PL. (a) Effect of axisymmetric amplitude ω_o and (b) effect of non-axisymmetric amplitude ω_3.

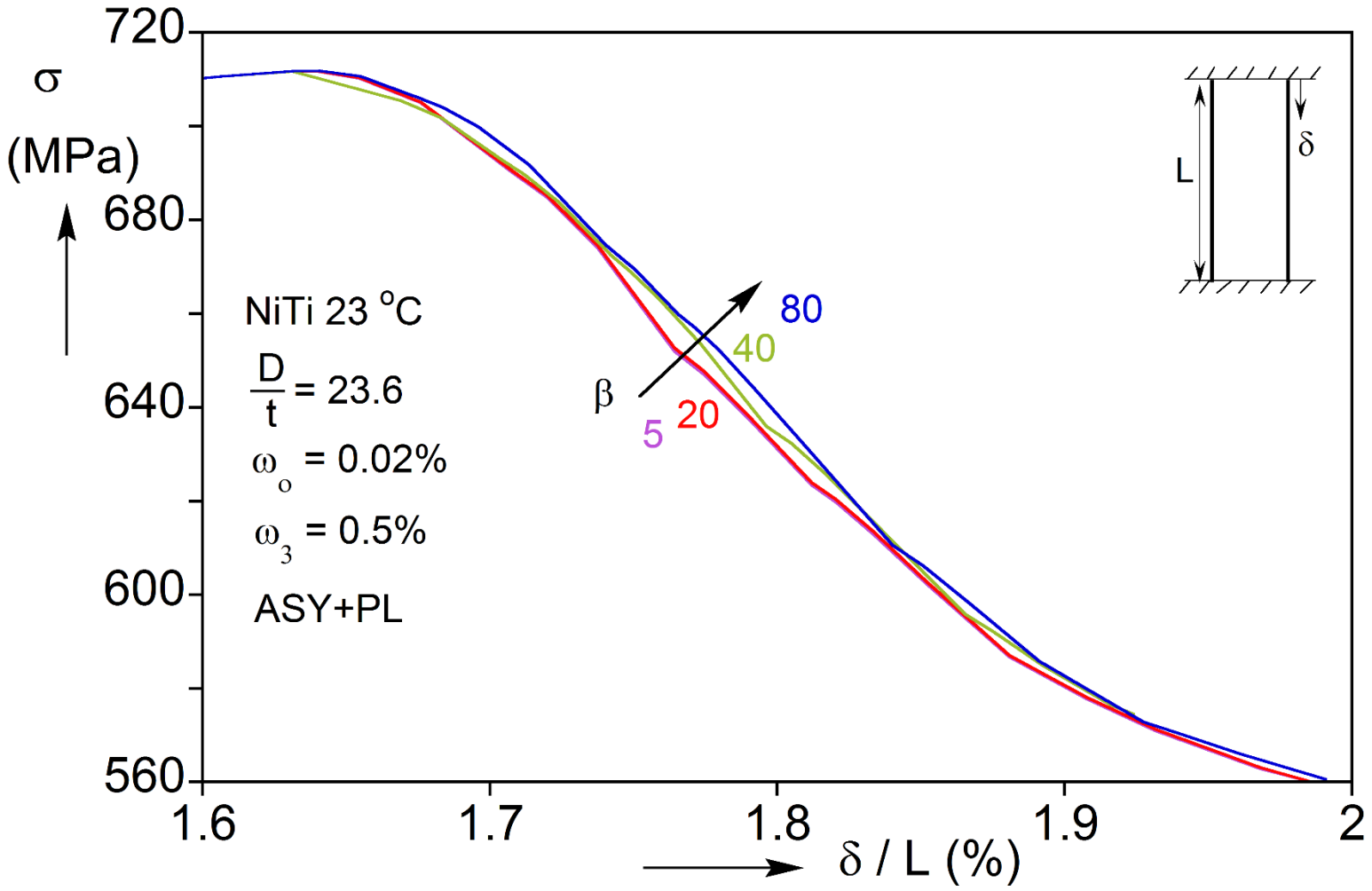

Fig. 3.22 Effect of imperfection extent β on calculated stress-shortening response using ASY+PL.

Chapter 4: Uniaxial Tension of NiTi Strips[4]

4.1 Introduction

This chapter reports the results of a study on the uniaxial tension of a long, thin pseudoelastic NiTi strip. In contrast to the axial buckling and recovery of the NiTi tube studied in Chapter 3, in which the structure is primarily under a compressive stress state, the strip is primarily under tension. Thus, inhomogeneous deformation associated with tension-induced phase transformation dominates the behavior of the structure. This problem is thus used to evaluate the performance of the constitutive model framework in Chapter 2 in a problem dominated by inhomogeneous deformation. The results of a tensile experiment on a NiTi are briefly reviewed. It is followed by the calibration of the constitutive model to the tension test and the numerical simulation of the experiment using a finite element model.

4.2 Experiment

A uniaxial tensile test was performed on a polycrystalline NiTi strip in the pseudoelastic temperature regime. The material has an alloy composition of 50.5 at. % Ni with A_f = 15.5°C (same material used in Shaw and Kyriakides [1997]; Hallai and Kyriakides [2013]). The strip had an overall length of 120 mm, width w = 3.95 mm and wall thickness t = 0.40 mm. Clamping the specimen in the grips left behind a 48.8 mm long (L) gage section. To minimize the thermal effect, the tension test was performed at a slow average strain rate of 0.83×10^{-5} s^{-1}. For more details on the experiment, see Jiang et al. [2017].

[4]Jiang, D., Kyriakides, S., Landis, C.M., Kazinakis, K. (2017a). Modeling of propagation of phase transformation fronts in NiTi under uniaxial tension. *Euro. J. Mech. A/Solids* **64**, 131-142. (Implemented the constitutive model, conducted the numerical simulations and wrote the analysis section in the paper)

Figure 4.1 shows the recorded nominal axial stress (σ) plotted against the average axial strain ($\bar{\varepsilon}$) in the gage section. Figure 4.2 shows a set of 18 full field DIC axial strain contours corresponding to the numbered bullets on the response in Fig. 4.1. The response exhibits the distinctive pseudoelastic closed hysteresis of NiTi. It first rises stiffly to a stress of 374 MPa followed by an extended stress plateau. In the process the initial *A*-phase deforms elastically and homogeneously as depicted by image ①. The first abrupt stress knee is associated with the onset of localized deformation that accompanies transformation to *M*. The clamping of the ends of the strip induces stress concentrations, which are sufficient to suppress the nucleation stress peak. Thus, the onset of transformation here is without the usual initiation stress peak (for more details on initiation see Shaw and Kyriakides, 1997). A single narrow inclined transformation front that separates transformed and untransformed materials has appeared in image ②. The band propagates to the right (see ③ and ④) while the stress remains essentially constant. The strain of the transformed material corresponds to that of the end of the stress plateau while that of the untransformed is at the level of the beginning of the plateau. The band front is initially rather straight with an inclination (ϕ) of 55-60^o and a width of about 5-8 mm (see expanded image ③ in Fig. 4.3). As observed previously, the steep gradient across such inclined bands causes local kinking of the specimen in the plane of the strip (for NiTi strips see Shaw and Kyriakides [1998]; for strips deformed by Lüders banding, see Lomer [1952], Butler [1962], Kyriakides and Miller [2000]). For the present specimen, the kink angle, γ, is of the order of 2^o (Fig. 4.3), which results in the buildup of in-plane moment. Transformation along the second characteristic with an inclination of $-f$ tends to be activated to relieve the moment. This did not materialize during loading but the second characteristic had the effect of making the front curved in this experiment.

At some point during loading, a second front initiated from the clamped end on the right (see image ⑤). It has the same inclination as the first front as this is again a moment relieving mechanism. Subsequently the two fronts propagated simultaneously towards each other meeting in image ⑦, causing the small stress valley just after point ⑦ on the response. The inhomogeneous part of the response has now been completed and the response recovers stiffness associated with the mainly *M*-phase.

Unloading from point ⑧ initially occurs with homogeneous deformation as depicted by image ⑨. At a stress of 152 MPa, the *M*-phase stops being stable and starts transforming back to *A*. It is again in the form of two inclined parallel fronts that propagate away from each other (image ⑩). Transformation returns the material to the strain level at the end of the lower stress plateau while the section remaining in the *M*-phase is at a strain of about 4.6% at the beginning of the lower plateau. By point ⑫ the right front has reached the clamped end and subsequently the specimen transforms with the propagation of a single front towards the left end (images ⑫ and ⑬). Close to point ⑭, transformation nucleates along the second characteristic developing the more symmetric crisscross pattern observed in image ⑭ and quickly switches to a single front with the opposite inclination (see expanded view of image ⑮ in Fig. 4.3). Soon after image ⑯ the whole specimen is back to the *A*-phase. It unloads homogeneously along the same stiff response as that of loading (image ⑰).

4.3 Constitutive Model Calibration

The phenomenological constitutive framework presented in Chapter 2 was shown to successfully reproduce the buckling and recovery behavior of NiTi tubes in compression (see Chapter 3). In that problem, the unstable nature of the material

exhibited under tension did not play a significant role and was not modeled. In the present problem, the state of stress is tensile throughout the load/unload history and consequently the representation of the unstable tensile uniaxial stress-strain response is of paramount importance. Thus, the aim of the present analysis is to test the capabilities of the model in the tensile setting. We start by describing the calibration of the up-down-up responses that will be adopted to model the measured strip hysteresis. Since compression plays no role in the present solution, the fit of the compressive stress-strain response is included here strictly for completeness of the constitutive model. In addition, for simplicity, the size of the transformation surface, σ_0, is assigned the same value as that of the tensile response. Details of the calibration of the tensile response follow:

- The elastic modulus of A used is similar to the value of the Hallai and Kyriakides [2013] strip experiments. It is somewhat higher than the DIC value of the present strip experiment and this difference is reflected in Fig. 4.4a.
- The initial nonlinearity exhibited during the initial homogeneous deformation of A is not fitted and thus the corresponding model response is somewhat stiffer than that of the measured response.
- The softening modulus of the $A \rightarrow M$ transformation is equal to that extracted from the sandwich experiment on this strip material by Hallai and Kyriakides [2013] (see also Zhu et al. [2016]). Its effect will be studied in the parametric study that follows. Lacking a similar experimental support for the $M \rightarrow A$ transformation, the softening modulus was assumed to be the same as that of the forward transformation.
- The two negative slopes are placed approximately at stress levels that correspond to the corresponding Maxwell stress levels, but the exact positions are determined for best reproduction of the two stress plateaus of the experimental response.

- The size of the transformation surface Φ^t (σ_o in Eq. (2.20)) corresponds to the stress difference between the measured loading and unloading stress plateaus.
- The initial hardening modulus following the stress valley is fitted to that of the experiment.
- For simplicity, the elastic modulus of M is assumed to be the same as that of A.
- The stable and unstable branches are connected by functions that provide algebraic convenience and optimal numerical performance.

With these assumptions, the derivatives of back stress potentials ψ_c^t and ψ_t^t in Eq. (2.22) take the following form:

$$\frac{d\psi^t}{d\varepsilon_e^t} = h_0\varepsilon_e^t + (h_1 - h_0)\left[\varepsilon_e^t - \frac{1}{b}(1 - e^{-b\varepsilon_e^t})\right]$$
$$+ (h_2 - h_1)\begin{cases} 0 & 0 \le \varepsilon_e^t \le \varepsilon_1 \\ (\varepsilon_2 - \varepsilon_1)(\zeta^3/4 + \zeta^2/8) & , \varepsilon_1 \le \varepsilon_e^t \le \varepsilon_2 \\ 3(\varepsilon_2 - \varepsilon_1)/8 + (\varepsilon_e^t - \varepsilon_2) & \varepsilon_2 \le \varepsilon_e^t \end{cases} \quad (4.1)$$
$$\text{with} \quad \zeta = (\varepsilon_e^t - \varepsilon_1)/(\varepsilon_2 - \varepsilon_1)$$

with the values for the parameters b, h_0, h_1, h_2, ε_1, ε_2 listed in Table 4.1. The constant a in the function f (see Eq. (2.23b)) is assigned the value of 0.9357, which leads to $f(1) = 0.64$. The resultant back stress responses are shown in Fig. 4.4b.

Table 4.1 Model parameters for tensile and compressive responses

Model	E GPa	n	s_o MPa	b	h_o GPa	h_1 GPa	h_2 MPa	e_1 (%)	e_2 (%)
Comp.	68.3	0.425	93.8	2500	1575	2.772	157.5	2.7	3.3
Tens.	68.3	0.425	93.8	2500	1434	-9.751	78.55	2.7	3.3

4.4 FINITE ELEMENT MODEL

The calibrated constitutive model is used in conjunction with a finite element model of the strip experiment to simulate the tensile test. The model geometry, shown in Fig. 4.5 has the dimensions of the strip tested $\{L \times w \times t\} = \{48.8 \times 3.95 \times 0.399\}$ mm. To accommodate the expected strain jumps, as in past works by this group (e.g., Aguirre et al. [2004]; Hallai and Kyriakides [2011a, 2011b, 2013]), we adopt ABAQUS's 3-D incompatible elements C3D8I (see Wilson et al. [1973], Ortiz et al. [1987], Nacar et al. [1989], Simo and Armero [1992]). In order to avoid any directional bias, the meshes adopted are uniform with cubical elements. The mesh used to generate the main results presented in the following section has 2 elements through the thickness, 20 across the width and 245 along the length for a total of 9800 elements. In the experiment, the strip was clamped between flat grips. This is a difficult boundary condition to reproduce; so instead, in the model the boundary conditions are idealized by fixing the degrees of freedom of the nodes at both ends except that the axial displacement of the nodes on the left end is prescribed incrementally. A small geometric imperfection in the form of a small indentation on the top surface of the strip is introduced in the way of initiating the instability. The imperfection is located a distance w from the left end and is generated by reducing the local width by $0.02t$ over two elements (see Fig. 4.5).

4.5 NUMERICAL RESULTS

The calculated load-unload average nominal stress-elongation $(\sigma - \delta / L)$ response is plotted in Fig. 4.6a together with the experimental one. Figure 4.7 shows a set of 21 full-field deformed configurations of the strip corresponding to the numbered bullets on the response. Superimposed on the configurations with color contours is the calculated axial strain. Initially the strip deforms uniformly with the response following

the uniaxial material response. The stress rises to a local maximum of 439 MPa then it drops sharply down to 362 MPa. Localized deformation has initiated from the imperfection in the form of a narrow band of higher strain. The band can be seen in the expanded view of image ① in Fig. 4.9. It is rather weak, with a width of a couple of elements and an inclination of 53° to the direction of loading, which is very close to that of the Hill [1952] characteristics of 54.7° (see also Bijlaard [1940]). The band can be seen fully developed covering the width of the strip in image ② that corresponds to the bottom of the load drop. It has the same inclination, its width now covers four elements, and the center of the band has reached a strain of about 5.6%, which corresponds to the value at the end of the stress plateau.

Before discussing the rest of the calculated response, it is worthwhile to investigate the load drop between ① and ②, which leads to some unloading in the rest of the strip. For the particular length of strip analyzed, the unloading is large enough such that it cannot be handled by the displacement-controlled loading scheme adopted. A more rigorous arc length incrementation scheme based on Riks' method shows the response to unload along a path that is to the left of the vertical as depicted in Fig. 4.8. Thus, the vertical part of the solution in Fig. 4.6a constitutes a "jump". This particular aspect of the response is not of interest in the rest of the study and thus for simplicity the solutions shown subsequently are based on displacement-controlled loading.

As discussed in the experimental section (see also Shaw and Kyriakides [1998]; Kyriakides and Miller [2000]), inclined zones of higher strain result in the built up of in-plane moment in these strips. The moment acting on the left edge of the strip, M, will be monitored in Fig. 4.6b where it is plotted against the applied end displacement (normalized by $M_o = \sigma_{NM} t w^2 / 6$). It can be observed that the sudden appearance of the band between the stress maximum and point ②, has resulted in a sharp built up of

moment. Beyond point ②, the stress starts to trace a somewhat ragged plateau during which the band of high strain propagates initially toward the right. The shear deformation of the highly-deformed zone causes local kinks in the strip and increases the moment. In image ③ in Fig. 4.9, the kink angle is approximately 1.8^o and the moment reaches a local maximum. At this point, a small band along the second characteristic initiates from the upper left corner of the specimen that can be seen in image ④. The new band has a straightening effect and results in a reduction in the moment of about 30% between image ③ and ④. The small zone of material on the left end is soon fully deformed and the ensuing deformation takes place strictly by the propagation of the right front. As this takes place the moment increases again. This is not sustainable and some deformation along the second characteristic is activated which results in the front developing some curvature that can be seen in image ⑤. The additional increase in the moment observed after image ⑤ again cannot be sustained causing the front to flip its inclination along the second characteristic as observed in image ⑥. Associated with the new front is a kink of about 1.9^o while its inclination is now about 71^o (see Fig. 4.9). This is because the moment remains large and the second characteristic is active. The front propagates with the new inclination for a short distance but because of the large moment the band initiation starts to alternate between the two characteristics producing the crisscross patterns observed in images ⑦ and ⑧ (see also the expanded view in Fig. 4.9). These patterns have a straightening effect on the structure and result in the moment fluctuations and the reducing trend observed in Fig. 4.6b. The alternating initiation of bands leaves behind small islands of undeformed material, each of which is deformed somewhat later. In addition, the multiple initiations and terminations of localized deformation result in the higher amplitude stress undulations between points ⑦ and ⑨ in Fig. 4.6a. By point ⑨ the front has reached the right end. A small island of undeformed material finally

deforms but with a small increase of stress to 399 MPa at point ⑩. At the end of the plateau at point ⑨ the average strain is 5.62% a value that closely corresponds to the end of the stress plateau recorded in the experiment.

The strip unloads from ⑩ tracing a similar nonlinear path to that of the experiment. In images ⑪ and ⑫ the deformation remains essentially homogeneous and the bending moment is reduced to essentially zero. Inhomogeneous deformation initiates from the right end soon after point ⑫. It is in the form of a crisscross pattern that appears similar to those developed during loading (images ⑬-⑮), while the stress traces a plateau that corresponds to that of the experiment. The crisscross pattern of the propagating front maintains the moment at a low level but causes fluctuations in the moment as well as in the recorded axial stress. In the neighborhood of point ⑯, one of the characteristics wins and a single front develops with an inclination that is opposite to that developed during the early parts of loading. The asymmetry associated with a single front results in a significant increase in the moment between points ⑯ and ⑰. In the neighborhood of point ⑰, a second front with the same inclination initiates from the left. In images ⑰-⑲ the two fronts propagate towards each other and in the process the bending moment gradually reduces. In the expanded view in Fig. 4.9, the inclinations of the fronts in image ⑱ have returned to 53^o and 57^o. The last remaining sliver of high strain material in image ⑲ has an inclination of 54^o. Beyond this point the deformation is homogeneous as the strip unloads along the stiff path followed during loading.

Comparison between the numerical and experimental results leads to the following observations:

- In the experiment transformation initiates from one of the clamped ends due to the inherent stress concentration. In the simulation, localized deformation is initiated from an imperfection introduced artificially. The location and type of imperfection

used influences the initial patterns of localized deformation and its subsequent propagation.

- The calculated stress-displacement response closely follows the experimental one. The small difference in the initial modulus is caused by differences between the modulus of the response used in the calibration and that recorded by the DIC system used in the experiment (see Section 4.3).
- In the calculated response, the initial stress peak is governed by the slope of the negative branch and its connection to the initial stable branch, which determines the initial stress maximum of the stress-strain response. It is also influenced to some degree by the type and amplitude of the imperfection used.
- The stress valley in the "reverse transformation" is partly masked by the residual untransformed material at the two ends.
- In the experiment, the transformation propagated mainly through a single band during loading. Reverse transformation propagated also via an inclined front but a crisscross pattern developed towards the end of the transformation. In the simulation, deformation also propagated initially via an inclined band but switched to a crisscross pattern in the second half of the test. During unloading, the front propagation followed the reverse order to that of loading. Band and kink angles produced in the model matched those of the experiment. The differences in the propagating fronts between experiment and simulation are influenced by the idealized boundary conditions adopted in the model and by the strength of the instability implied by the stress peaks/valleys and the negative slopes assumed. Support for this will be given in the parametric studies that follow.
- The model is an idealization of the experiment, with simpler/cleaner boundary conditions. The islands at the two ends left untransformed in image ⑩ are a

consequence of this idealized boundary conditions adopted in the model. They require a higher stress to be transformed.

4.6 Parametric Study

4.6.1 Mesh Sensitivity of the Solution

The softening branches introduced in the stress-strain response imply some degree of mesh sensitivity of the solution. As in our treatment of Lüders banding in structures, our approach has been to choose a uniform mesh that is fine enough to reproduce the finer features of the localized deformation observed in the experiments. Once this is decided, the addition of mild rate dependence to the constitutive model regularizes the solution removing the sensitivity to the mesh (Needleman, 1988). The alternative approach is to introduce higher order gradients in the formulation with an intrinsic length scale. To date, this length parameter is chosen for best performance of the model—e.g., see He and Sun, 2010; Duval et al., 2011 for SMA applications, Maziere et al., 2017 for Lüders banding. The SMA phenomenological constitutive model outlined in Chapter 2 is rate independent. Consequently, the mesh sensitivity of the strip tension solution presented in the previous section must be examined. To this end, two additional mesh densities were used to simulate the tension test in which the number of cube-shaped elements through the thickness (N_t) was increased to 3 and 4. This respectively increases the number of elements across the width to 30 and 40 and to 33,300 and 78,400 total elements.

The solutions from the two finer meshes are very similar to the one depicted in Figs. 4.6 and 4.7 and will be simply outlined here. Figure 4.10 shows the stress-elongation responses calculated using the two finer meshes together with the original one.

Figures 4.11 and 4.12 display sequences of deformed configurations of the NiTi strip for N_t = 3 and 4, respectively. The configurations correspond approximately to the same values of normalized elongations with the bullet numbers in Fig. 4.6a. As these figures indicate, the mesh refinement had next to no visible effects on the calculated stress-elongation response or on the front initiation and propagation patterns. The main effect of mesh refinement is in the width of the front transition zone. Figure 4.13a shows expanded views of the banded localized deformation produced by the three mesh densities. They correspond to point ③ on the calculated response shown in Fig. 4.6a, the location of which is also marked by the arrow "↓" in Fig. 4.10. The inclinations of the two band fronts, the kink angles, and the secondary band that has initiated at the upper corner of the left end of the strip are essentially the same in the three solutions. However, the front transition zones occupy approximately two elements in each mesh. Consequently, the front is getting narrower as N_t increases. Another illustration of the effect of the mesh on the width of the band is shown in Fig. 4.13b, where the axial strain along the centerline of the strip in the neighborhood of the right hand front is plotted for the three meshes. All three cases show the strain ahead of the front to be 0.77% and behind it 5.6%. They are connected through transition zones the widths of which decrease as N_t increases.

In summary the present problem the width of this transition zone does not affect the solution if the mesh is fine enough to capture the finer features of localized deformation. This is to be contrasted with other problems where localization bands result in failure and must be modeled more accurately

4.6.2 Effect of Strain Rate

The present constitutive model does not incorporate material rate dependence. Here we will demonstrate the effect of rate on the solution using J_2 plasticity with a mild power-law rate dependence calibrated to the same up-down-up stress-strain response as that used in the present model (Fig. 4.4a). The mild power-law rate dependence adopts the same form with that used in Hallai and Kyriakides, 2013. The comparison is limited to loading only, because J_2 isotropic hardening model is unable to represent the hysteretic behavior of NiTi. The strip is discretized with the same elements using the three uniform meshes used in the previous section (i.e., $N_t = 2$, 3 and 4). Each case is analyzed first with rate independent plasticity and then using the power law rate model; the solutions are then compared. Figure 4.14 shows the calculated stress-elongation responses using rate-independent and rate dependent plasticity models based on mesh $N_t = 2$ while Figure 4.15 shows the sequences of deformed configurations produced by the two models. Similarly, Figs. 4.16/4.17 and 4.18/4.19 show the responses and corresponding configurations using refined meshes $N_t = 3$ and $N_t = 4$.

Summarized below are the main observations from these comparisons.

- The *loading response* and the evolution of fronts produced using J_2 plasticity models, either rate independent or rate dependent, are very similar to those of the present constitutive model in Section 4.5.
- For each mesh density, the rate independent and rate dependent solutions produced front evolutions that are very similar (e.g., see comparison of rate independent and rate dependent responses in Figs 4.14, 4.16 and 4.18, and configurations in Figs. 4.15, 4.17 and 4.19).
- The mesh was not found to affect the evolution of fronts for the rate independent plasticity and, of course, the same was true for the rate dependent case.

- As pointed out in Section 4.6.1, in the hysteretic model the main effect of the mesh is in the width of the transition zone. The solutions using the rate independent plasticity model exhibit a similar slight narrowing of the transition zone as the mesh is refined. The addition of rate eliminates this difference.

4.6.3 Effect of Softening Modulus

The softening slope adopted in the model used to simulate the strip experiment was based on the one measured in the sandwich tensile test performed by Hallai and Kyriakides, 2013 on the same strip as that used in the present experiment. In order to assess the effect of the strength of softening on the solution to the strip problem, here we will vary the slope of the negative branches, while keeping other characteristics of the up-down-up responses similar. The tensile stress-strain responses considered are shown in Fig. 4.20a. The response used thus far is designated as 0 and two cases with stronger softening are designated as +1 and +2 and those with weaker softening as -1 and -2.

Fig. 4.20b shows the calculated stress-displacement responses using the mesh of the base case (Fig. 4.5). The corresponding sets of deformed configurations of the strips are included as Figs. 4.21-4.24, in which the images correspond to approximately the same displacement as that of the bullets on response 0 included in Fig. 4.20b. All responses exhibit a local stress maximum that of course is higher for the two stronger cases and lower for the two weaker ones. The stress maxima are followed by the usual stress plateaus and stress undulations. The same is repeated for the unloading plateaus. The major observations from the comparisons are summarized as follows:

- All cases develop localized deformation that propagates as the stress plateaus are traced.

- The strength of softening does influence the patterns and the events as follows: During loading, as the softening becomes stronger, the single front propagation persists further into the displacement history, while the crisscross front propagation is less prominent. As the softening gets weaker, the single front propagation terminates earlier and the crisscross pattern becomes dominant.
- During unloading, for +2 and -2 the front propagates from left to right, in other words it does not follow the reverse order to that of loading. For +1, 0 and -1 the front propagated from right to left. For +2 the propagation was dominated by a single front whereas for +1, 0 and -1, the crisscross pattern covered nearly half of the unloading history and in the rest a single front dominated. In the case of -2, the front propagated with both characteristics active, resulting in the butterfly shaped of the front observed in Confs-2.

4.7 SUMMARY

This chapter dealt with the calibration and use of the NiTi pseudoelastic constitutive model in a primarily tensile stress state problem: the tension test on a NiTi strip. Experimental results from such a test exhibit the usual tensile pseudoelastic response tracing a closed hysteresis consisting of an upper and a lower stress plateaus as the $A \rightarrow M$ and the $M \rightarrow A$ transformations take place. The transformations lead to inhomogeneous deformation with transformed and untransformed materials co-existing and being separated by an inclined front that propagates in the specimen.

The constitutive model is calibrated to the tensile response of the material. To reproduce the inhomogeneous deformation, softening moduli are introduced over the extents of the plateaus of the response at approximately the Maxwell stress levels. A

uniform mesh consisting of cubical 3-D solid incompatible elements is chosen fine enough for good reproduction of the finer features of the fronts observed in the experiment. A parametric study demonstrated that the main effect of the mesh is on the width of the transition zones separating the relatively deformed and undeformed materials.

The numerical simulation of the test reproduces the closed hysteresis with the correct stress plateau levels and extents. The numerical solution exhibits the usual initiation stress peak, whereas in the experiment the initiation peak was suppressed by the stress concentrations at the clamped ends. Localized deformation is initiated from a small geometric imperfection introduced on one side of the strip model. It takes the form of a single narrow band of higher strain inclined to the length of the strip along one of the Hill characteristics (~55^{o}). As in the experiment, as the end of the strip is pulled, the high strain zone propagates initially with an inclined front with the stress remaining nearly constant. The shear in the inclined deformed zones causes in-plane local kinking of the strip similar to that observed in the experiment. Kinking causes a build-up of in-plane moment, which is relieved by the front first flipping to the alternate characteristic, and subsequently propagating in a crisscross pattern.

The lower stress plateau starts without the usual stress valley recorded in the experiment as localization initiates at one of the ends from a small island of material that was left undeformed during loading. In the experiment the front propagated mostly with a single inclination, developing a crisscross pattern and switching to the alternate characteristic close to the end. In the model, the band propagates with the crisscross front for half the length and then switches to a single inclined front.

Overall, the simulation captured the main features of the response and the associated deformation patterns. Differences with the experimental patterns and their

evolution are caused by differences in the idealized boundary conditions used in the model, the manner in which the localization is initiated from a local imperfection and by its location, and by the strengths of the two softening branches adopted.

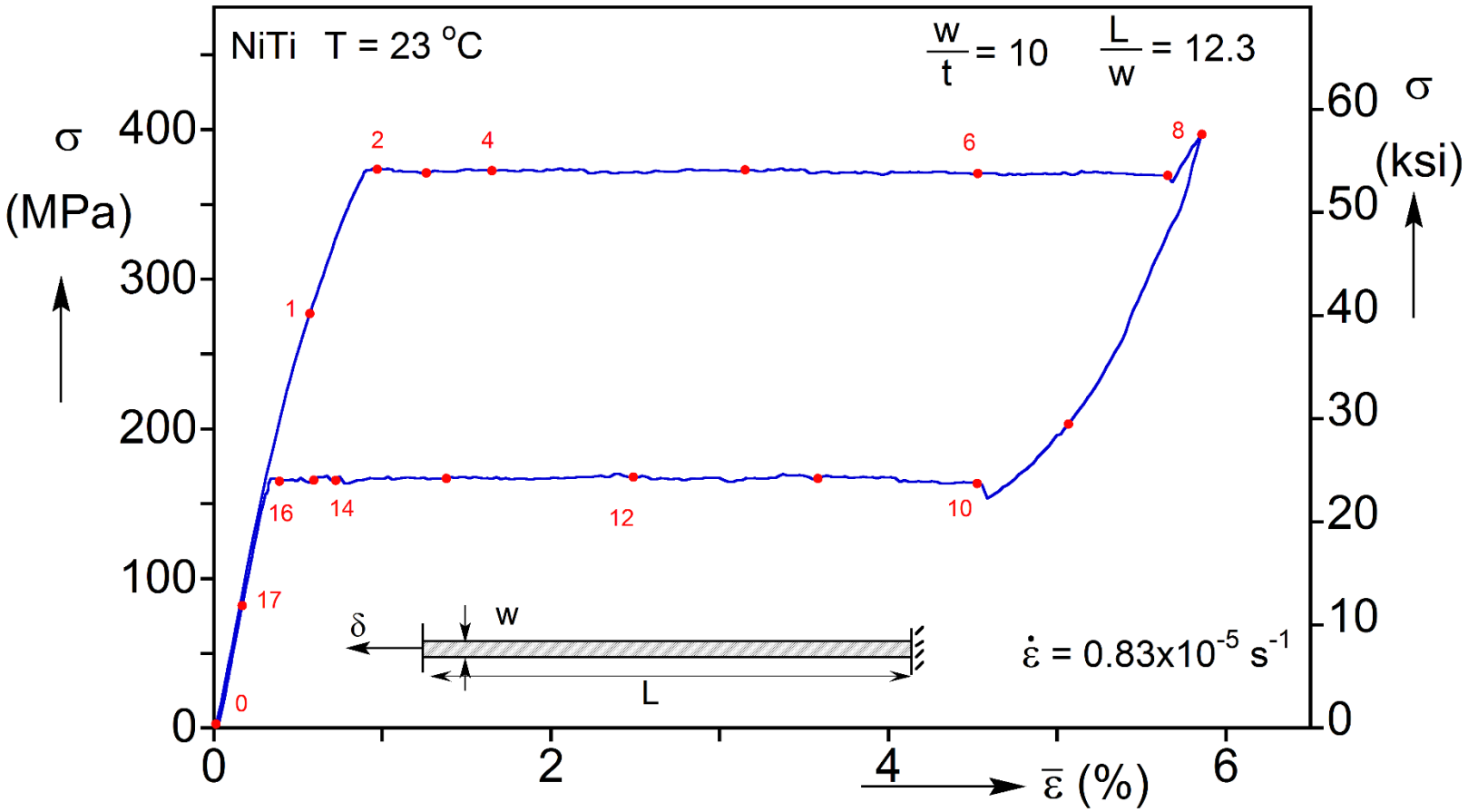

Fig. 4.1 Pseudoelastic tensile stress-elongation response of the NiTi strip.

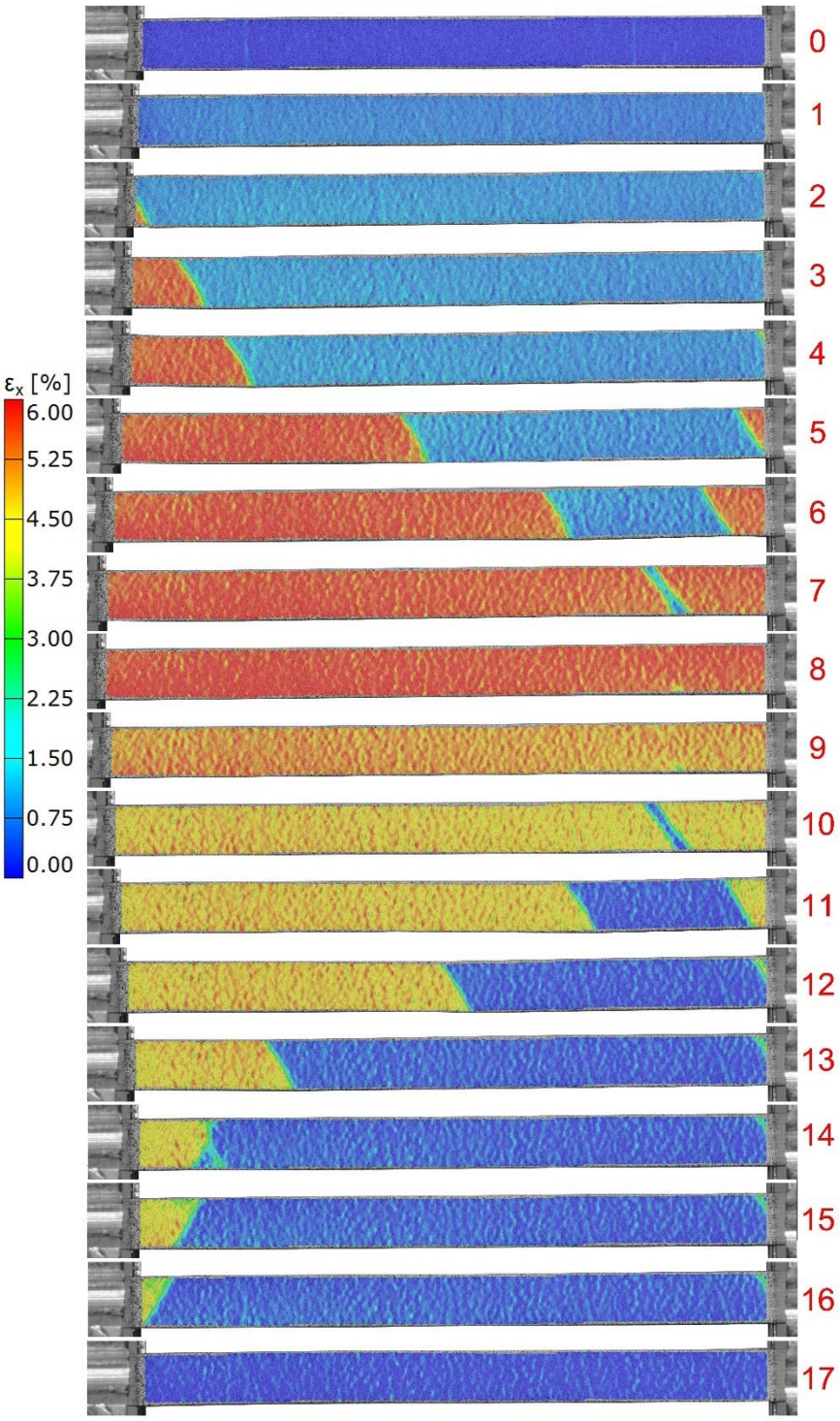

Fig. 4.2 Set of deformed configurations with DIC axial strain contours superimposed; images correspond to numbered bullets on the response in Fig. 4.1.

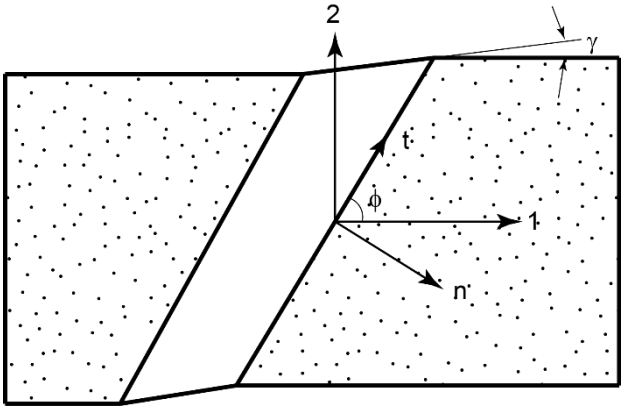

(a)

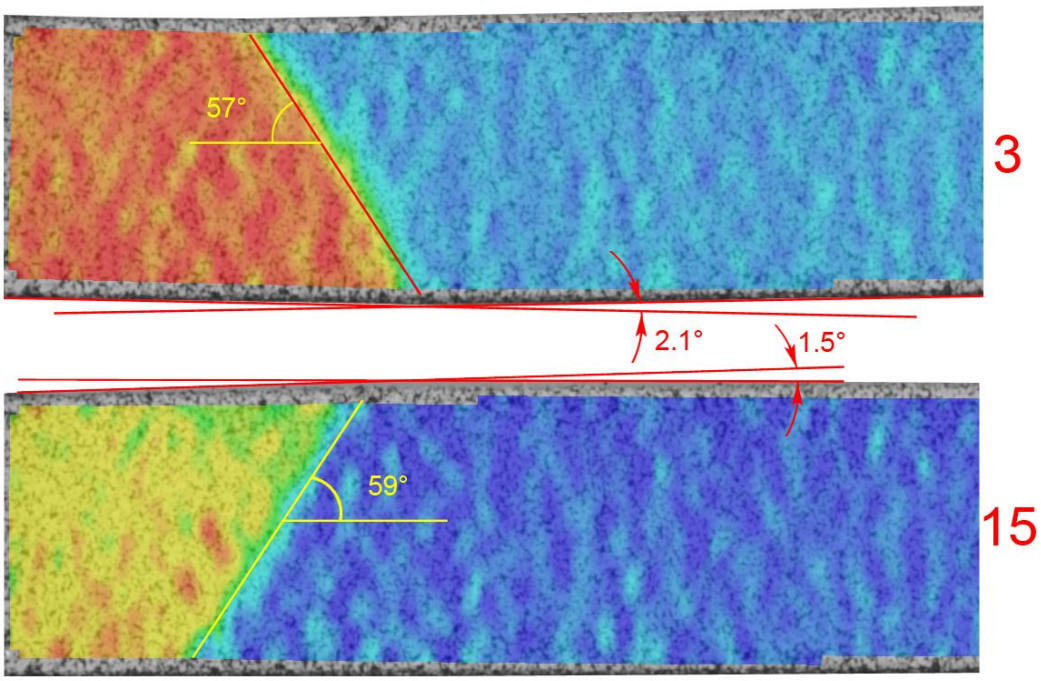

(b)

Fig. 4.3 (a) Geometric variables of inclined bands. (b) Expanded views of inclined transformation bands from configurations ③ (loading) and ⑮ (unloading).

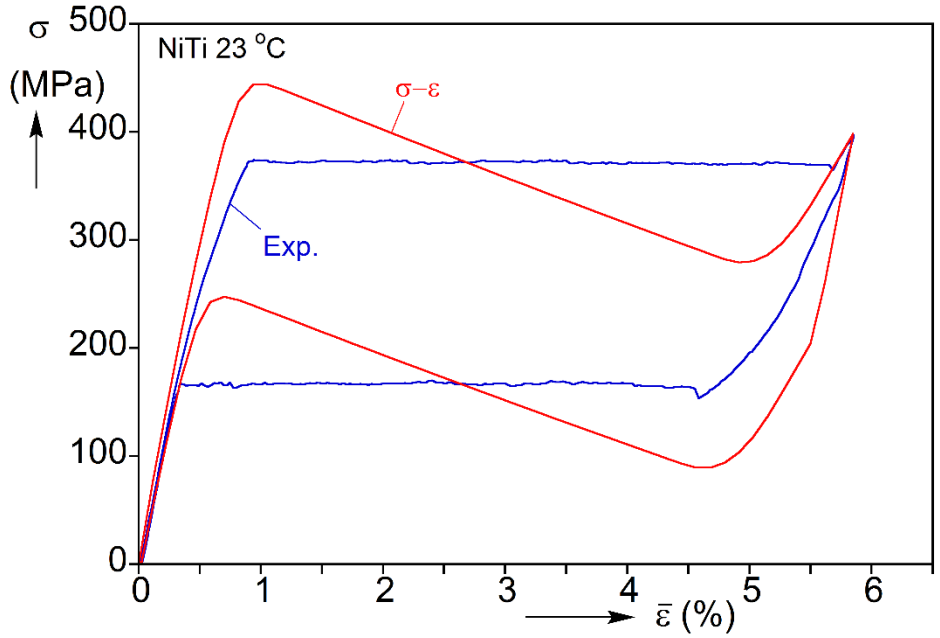

(a)

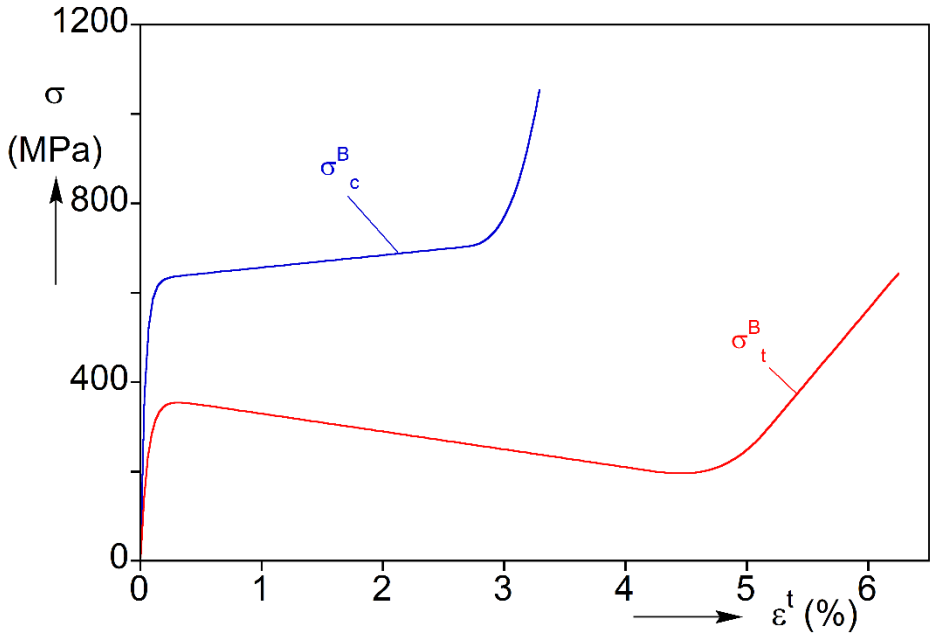

(b)

Fig. 4.4 (a) The assumed softening tensile stress-strain response (red) together with the measured structural response of the strip. (b) The back stress-transformation strain responses for tension and compression used in the model.

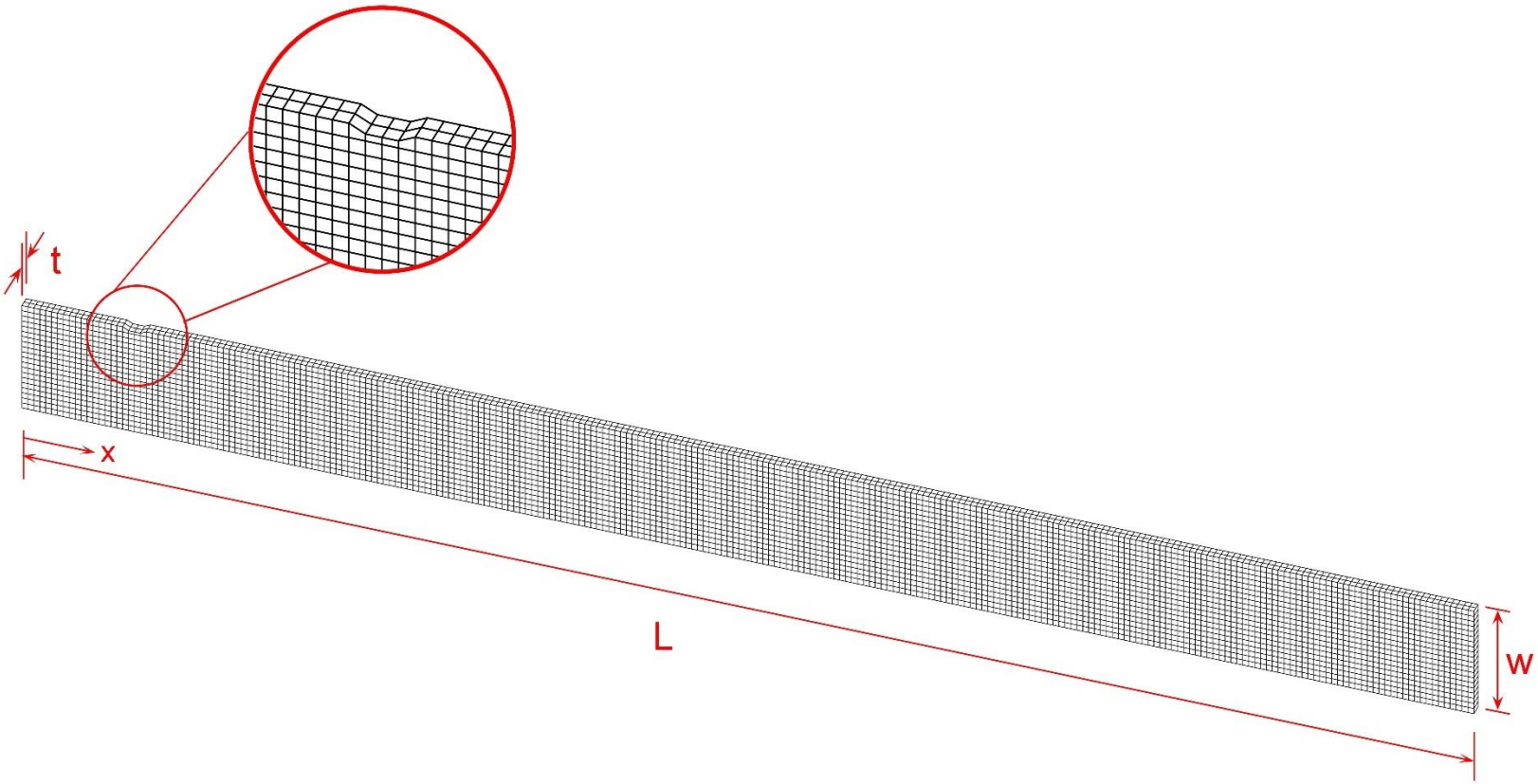

Fig. 4.5 Geometry of the model strip and the finite element mesh used.

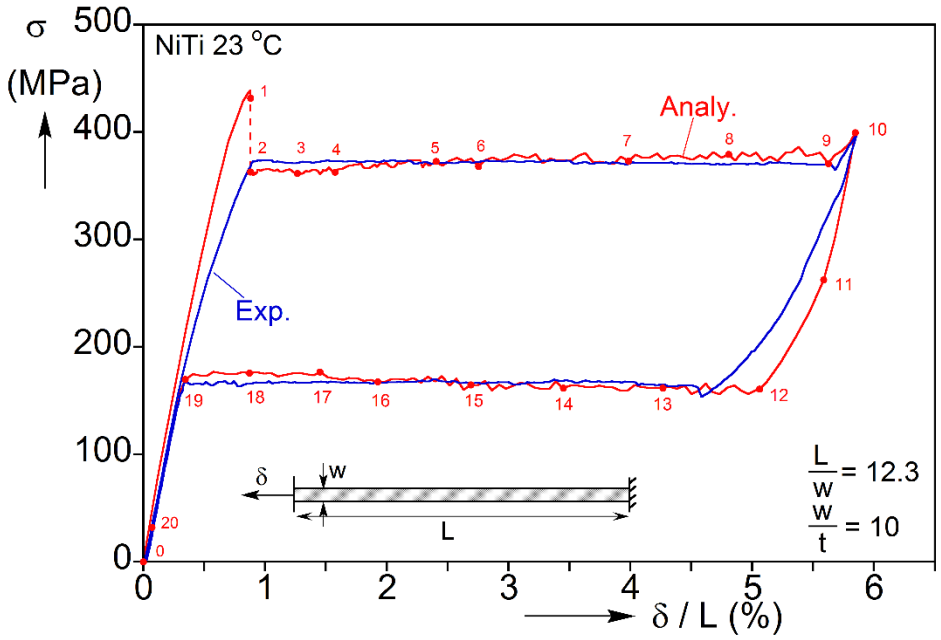

(a)

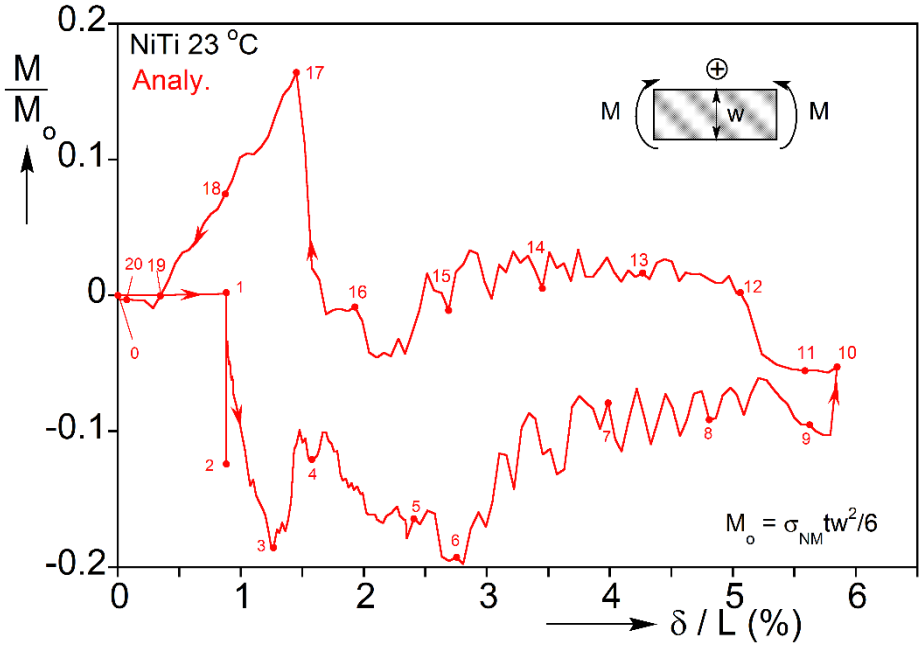

(b)

Fig. 4.6 (a) Comparison of calculated and measured stress-elongation responses for the NiTi strip. (b) Moment induced by the inhomogeneous deformation at the end of the strip versus the applied end displacement.

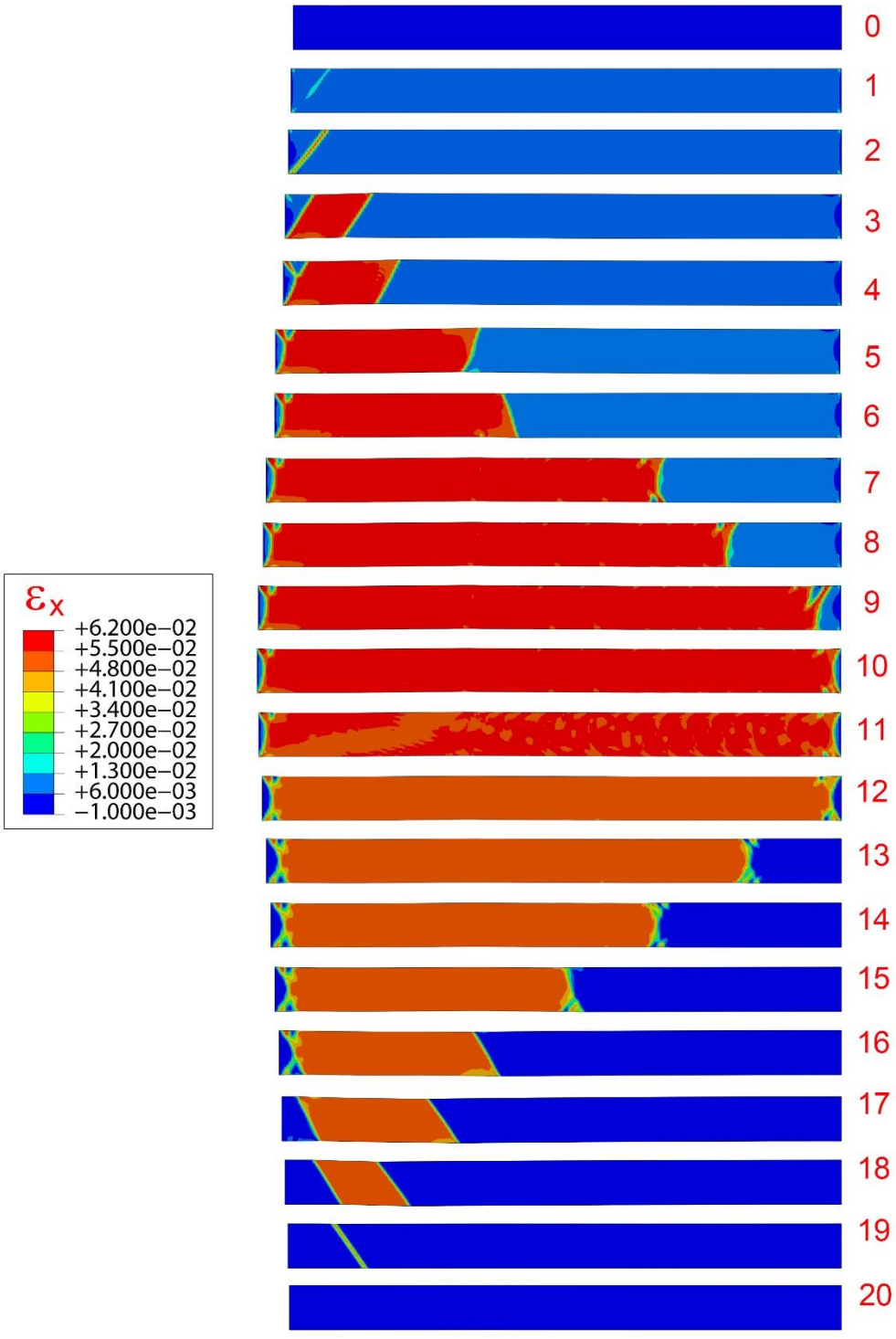

Fig. 4.7 Sequence of calculated strip deformed configurations with axial strain contours superimposed corresponding to numbered bullets on the response in Fig. 4.6.

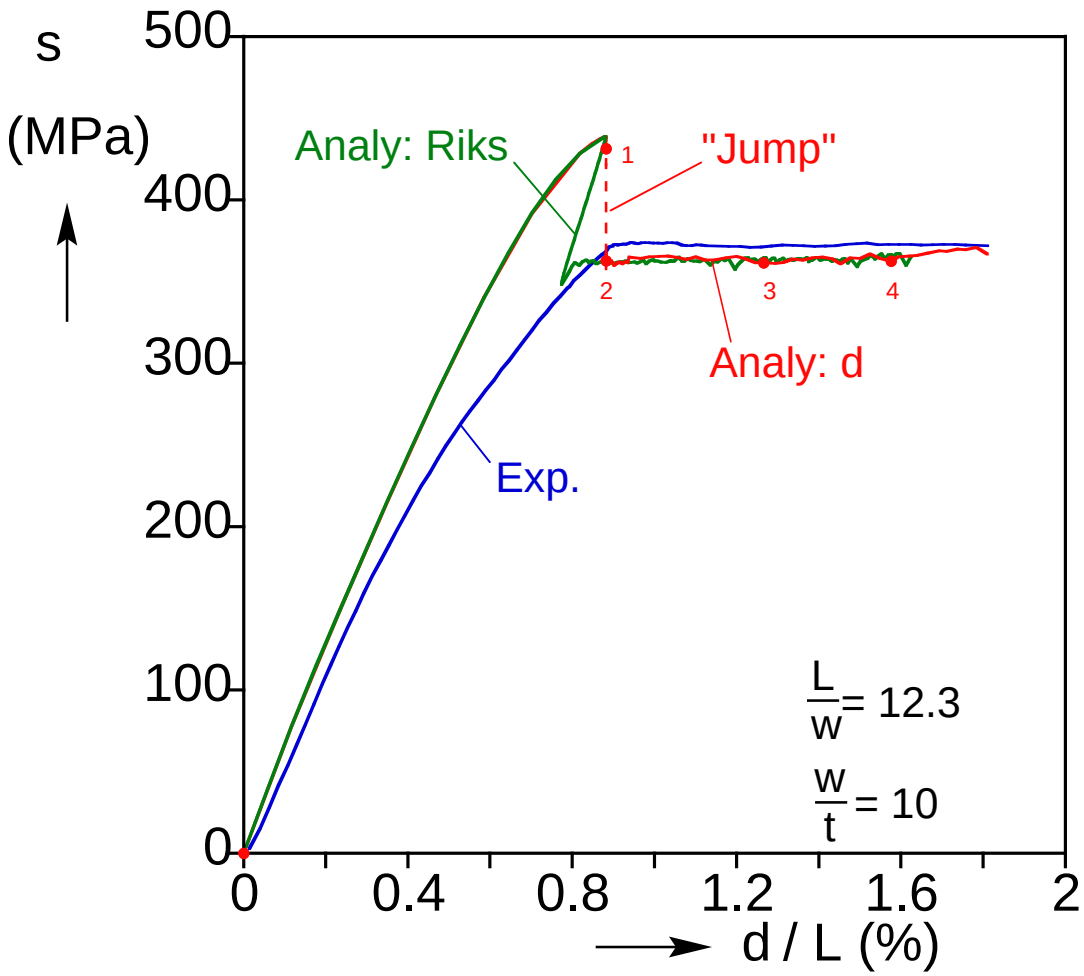

Fig. 4.8 Initial parts of the stress-deformation response calculated using “displacement controlled” loading and the Riks arc length incrementation method.

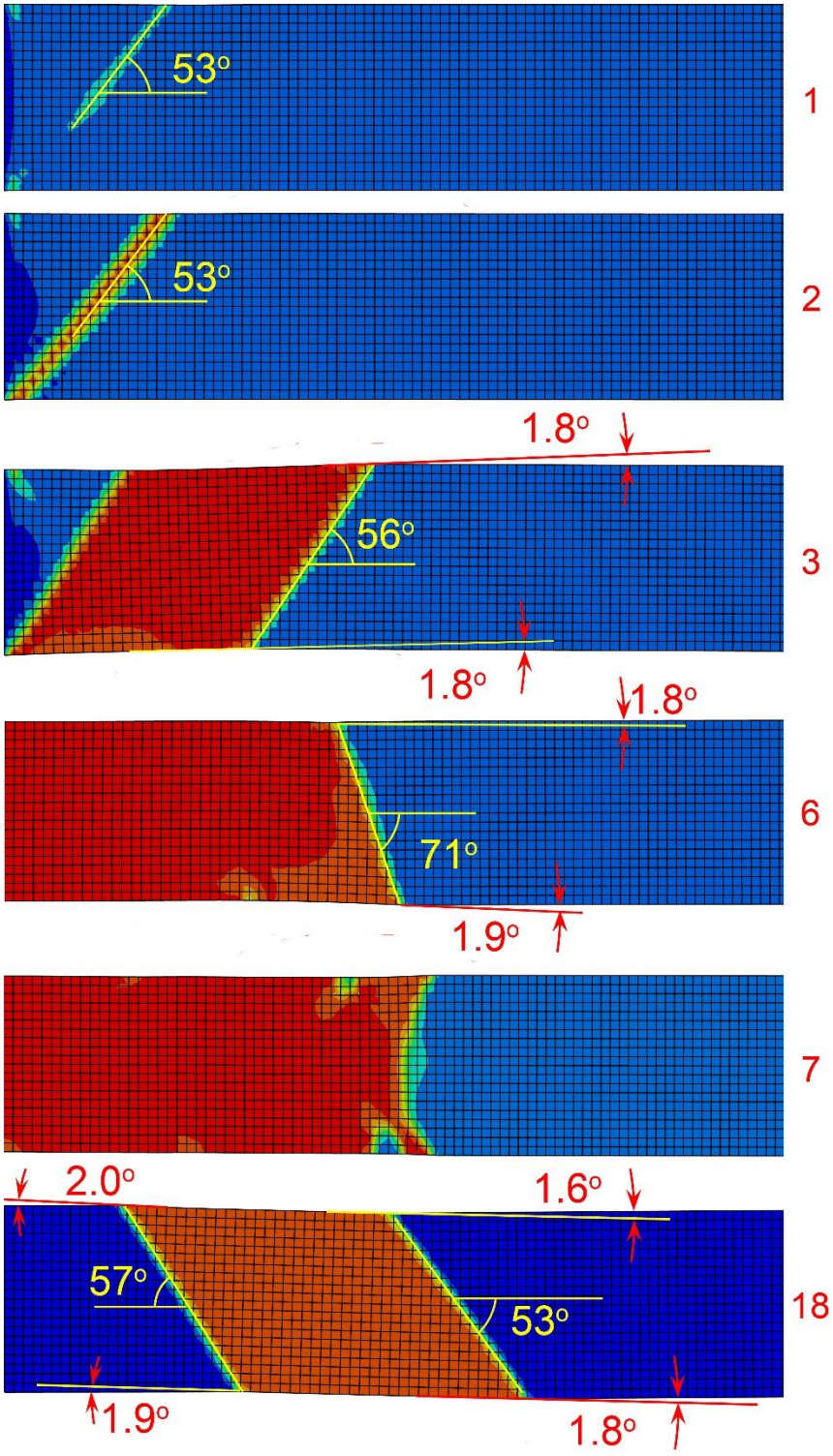

Fig. 4.9 Expanded views of the transformation bands from six configurations in Fig. 4.7.

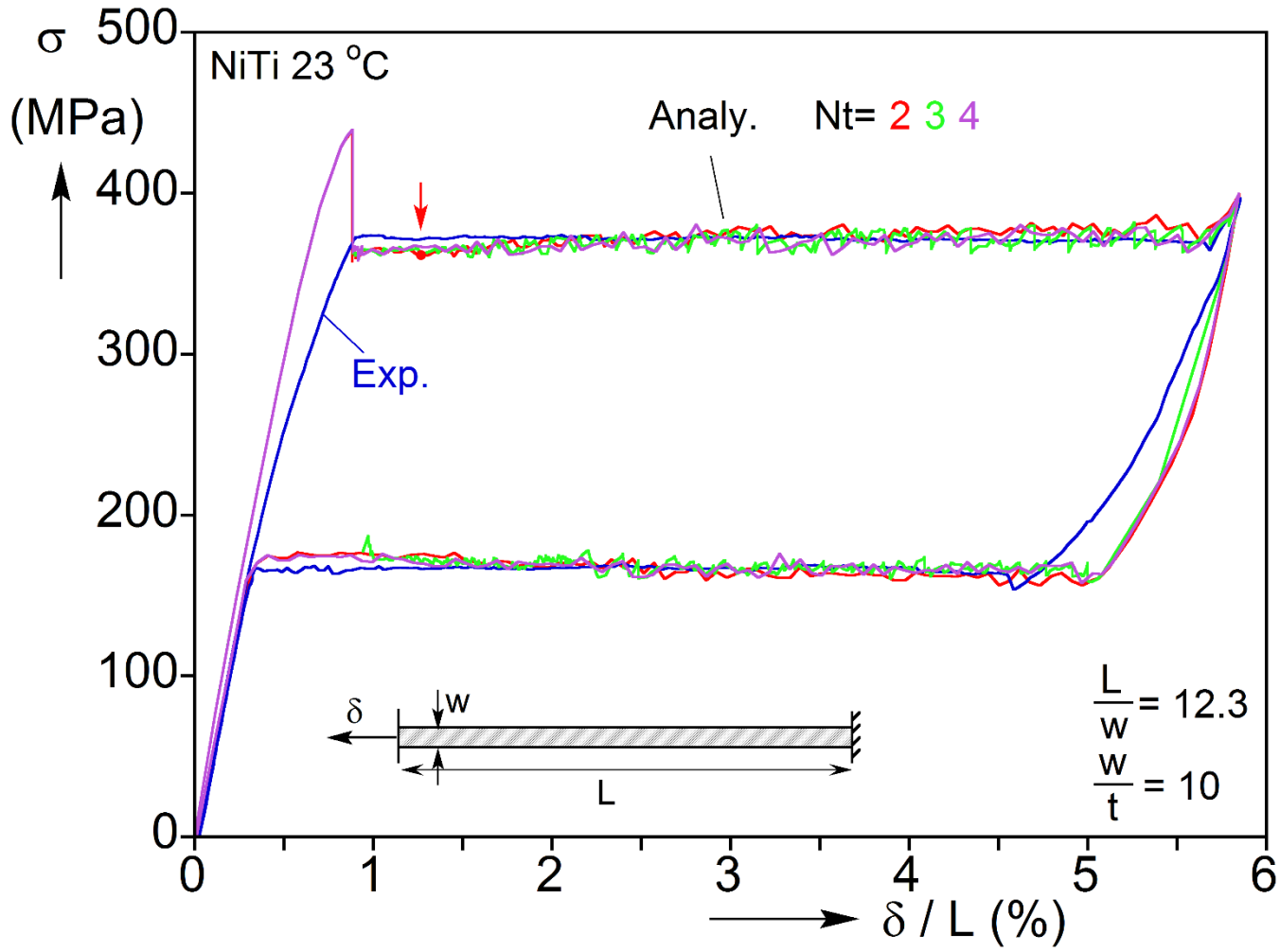

Fig. 4.10 Stress-elongation responses of the strip calculated using meshes with N_t = 2, 3 and 4.

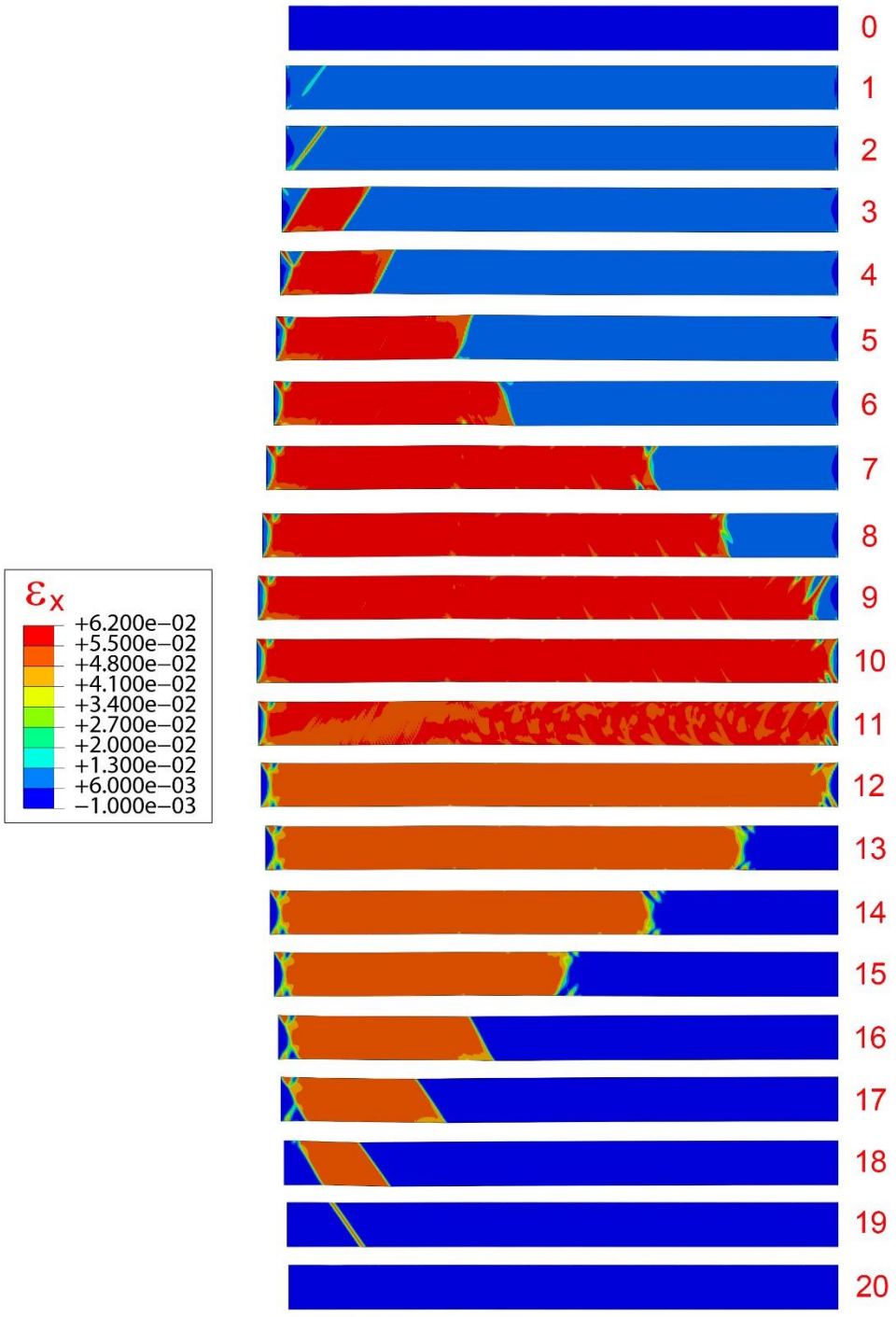

Fig. 4.11 Sequence of calculated strip deformed configurations using mesh with $N_t = 3$ superimposed with axial strain contours (numbers correspond to the numbered bullets on the response in Fig. 4.6).

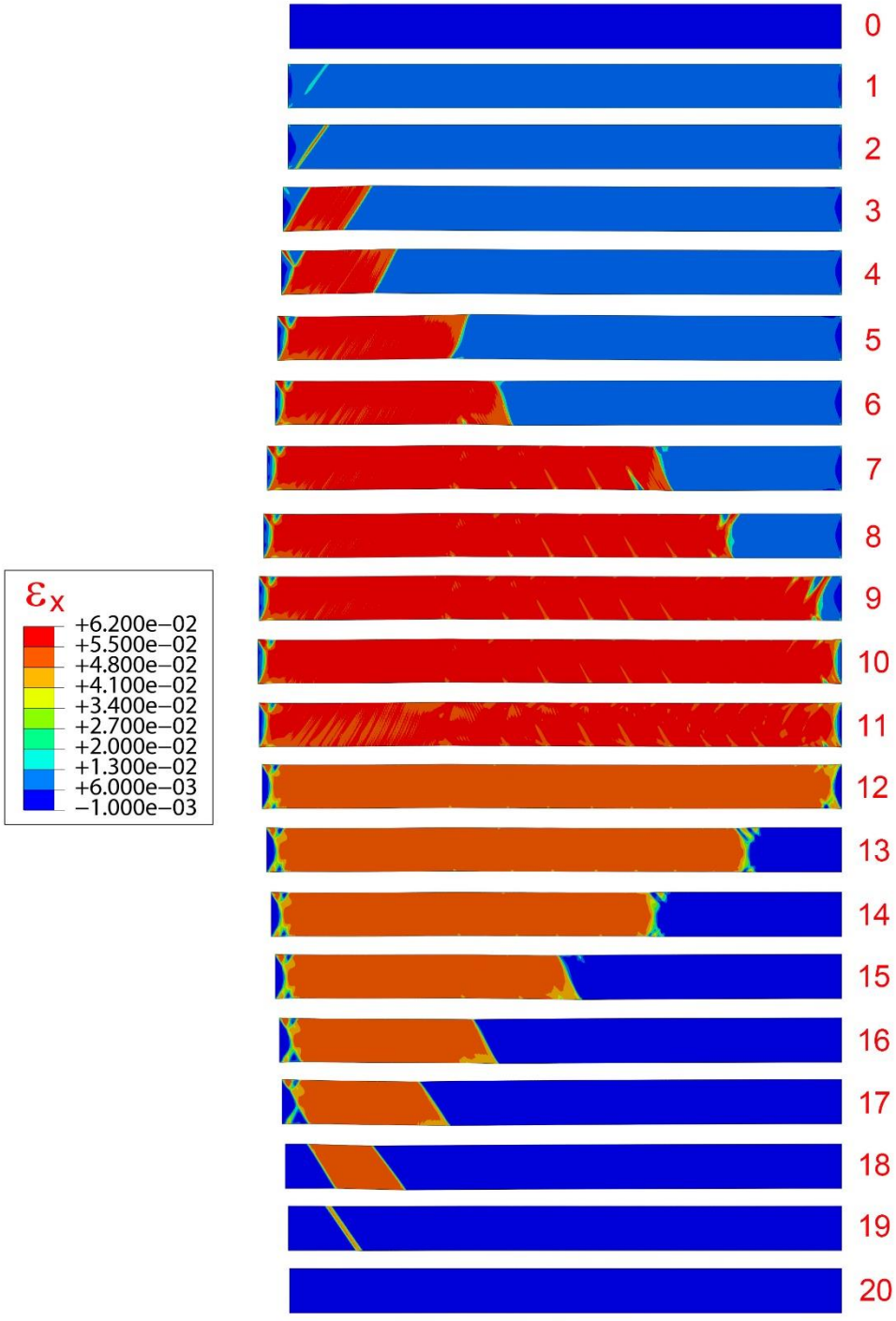

Fig. 4.12 Sequence of calculated strip deformed configurations using mesh with $N_t = 4$ superimposed with axial strain contours (numbers correspond to the numbered bullets on the response in Fig. 4.6).

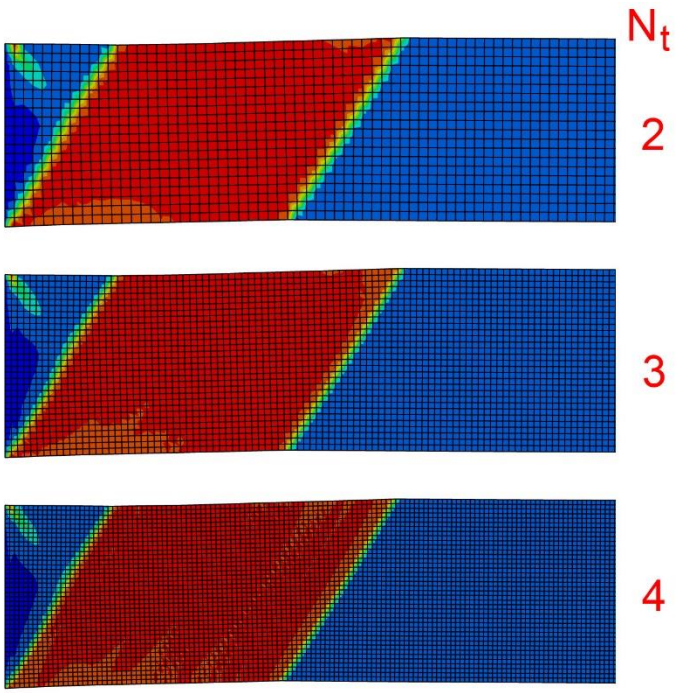

(a)

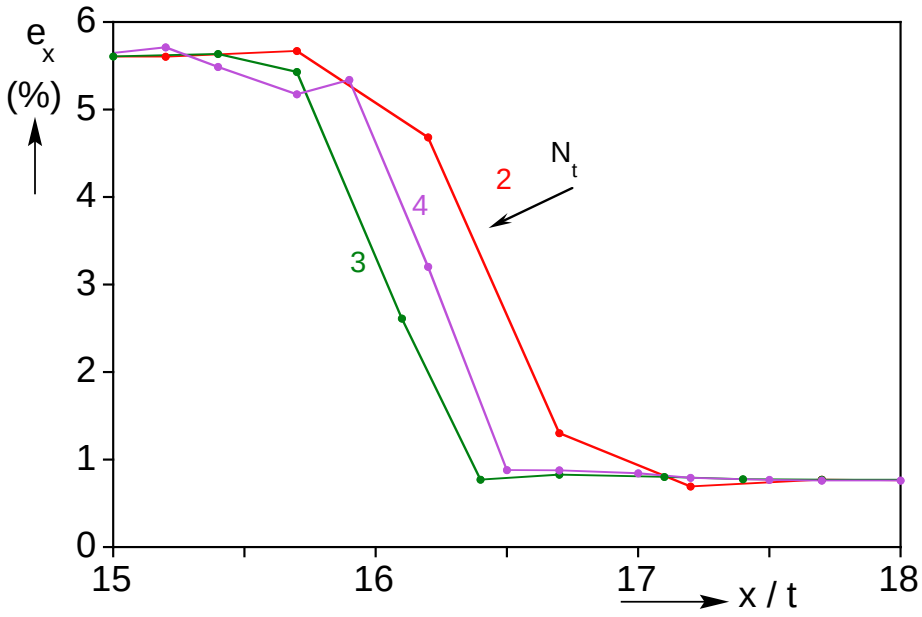

(b)

Fig. 4.13 (a) Comparison of the expanded views of the banded deformation in image 3 calculated with FE meshes with $N_t = 2$, 3 and 4. (b) The axial strain profiles of the right front from the three meshes.

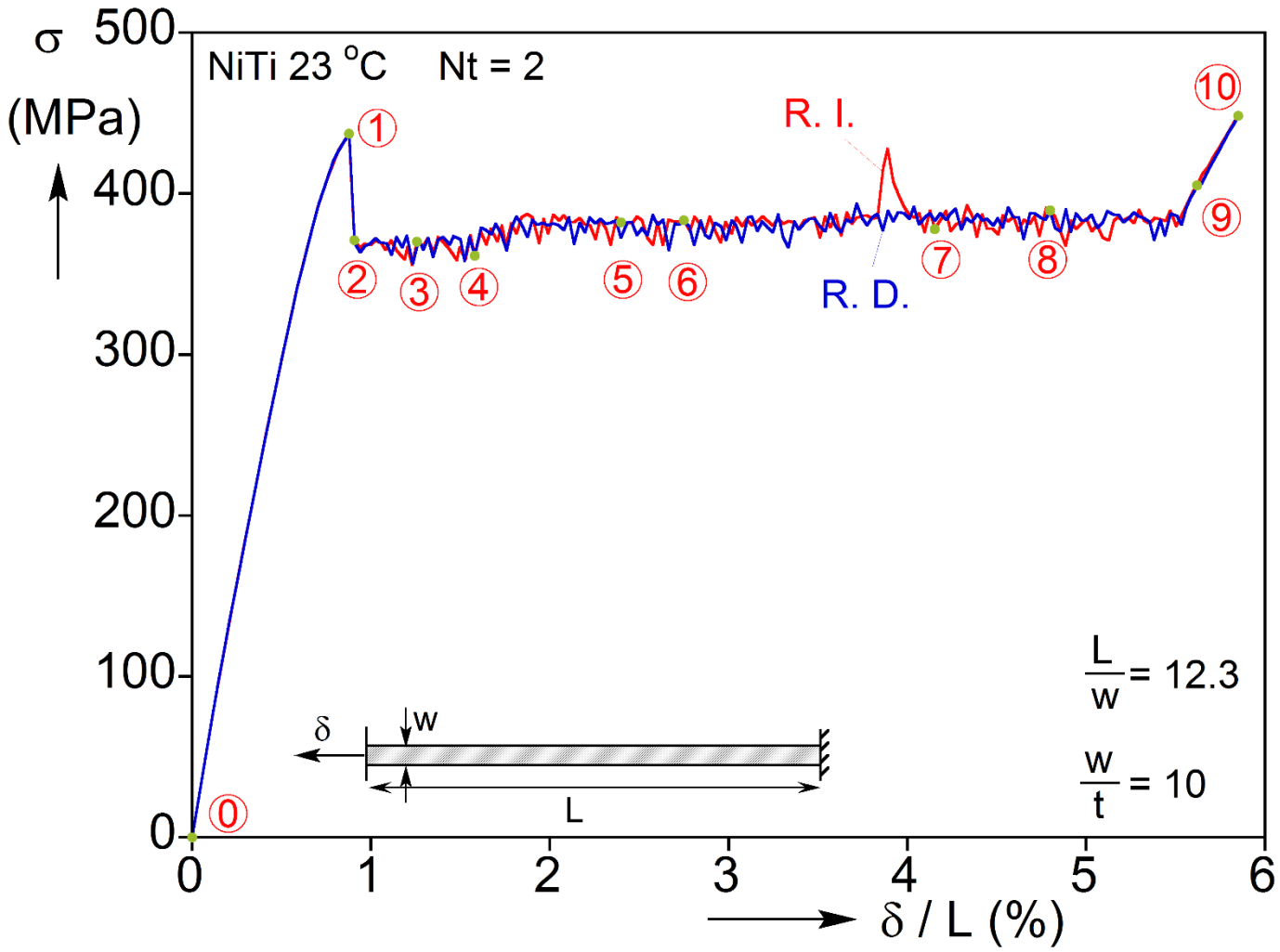

Fig. 4.14 Calculated stress-elongation responses ($N_t = 2$) with rate independent vs. rate dependent J_2 plasticity models.

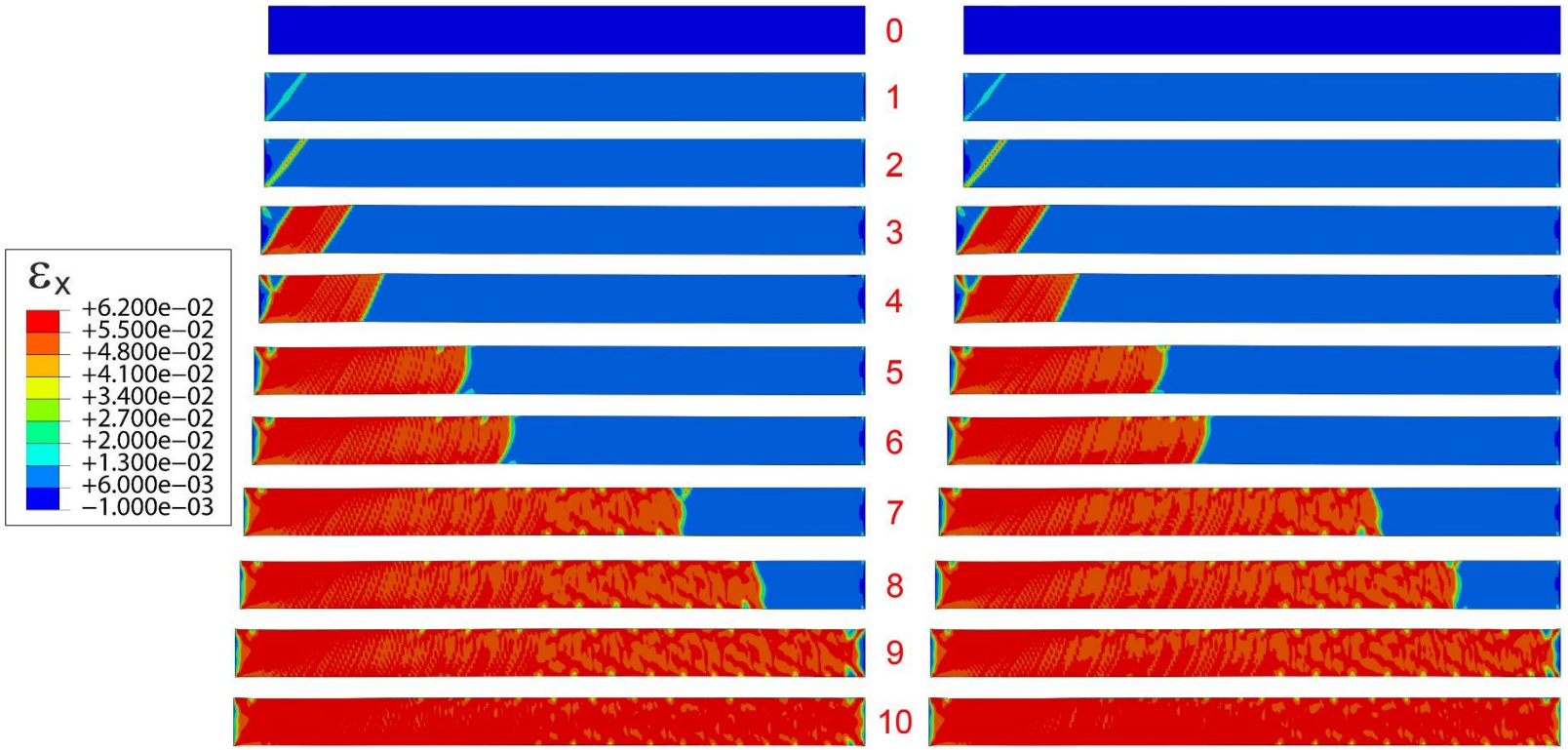

Fig. 4.15 Comparison of the model strip loading deformed configurations produced by rate independent (left) and rate dependent (right) plasticity models ($N_t = 2$), corresponding to the numbered bullets in Fig. 4.14.

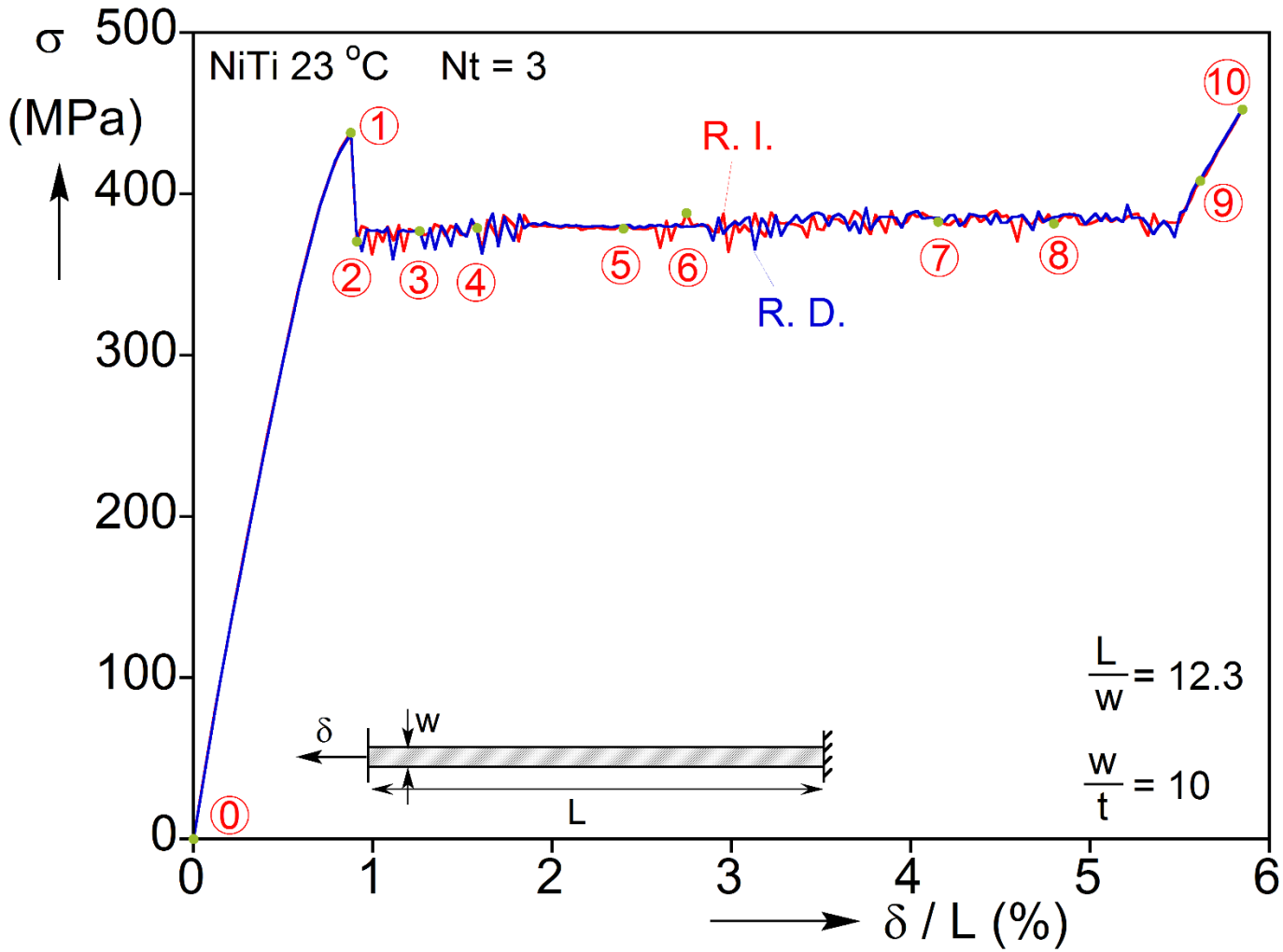

Fig. 4.16 Calculated stress-elongation responses ($N_t = 3$) with rate independent vs. rate dependent J_2 plasticity models.

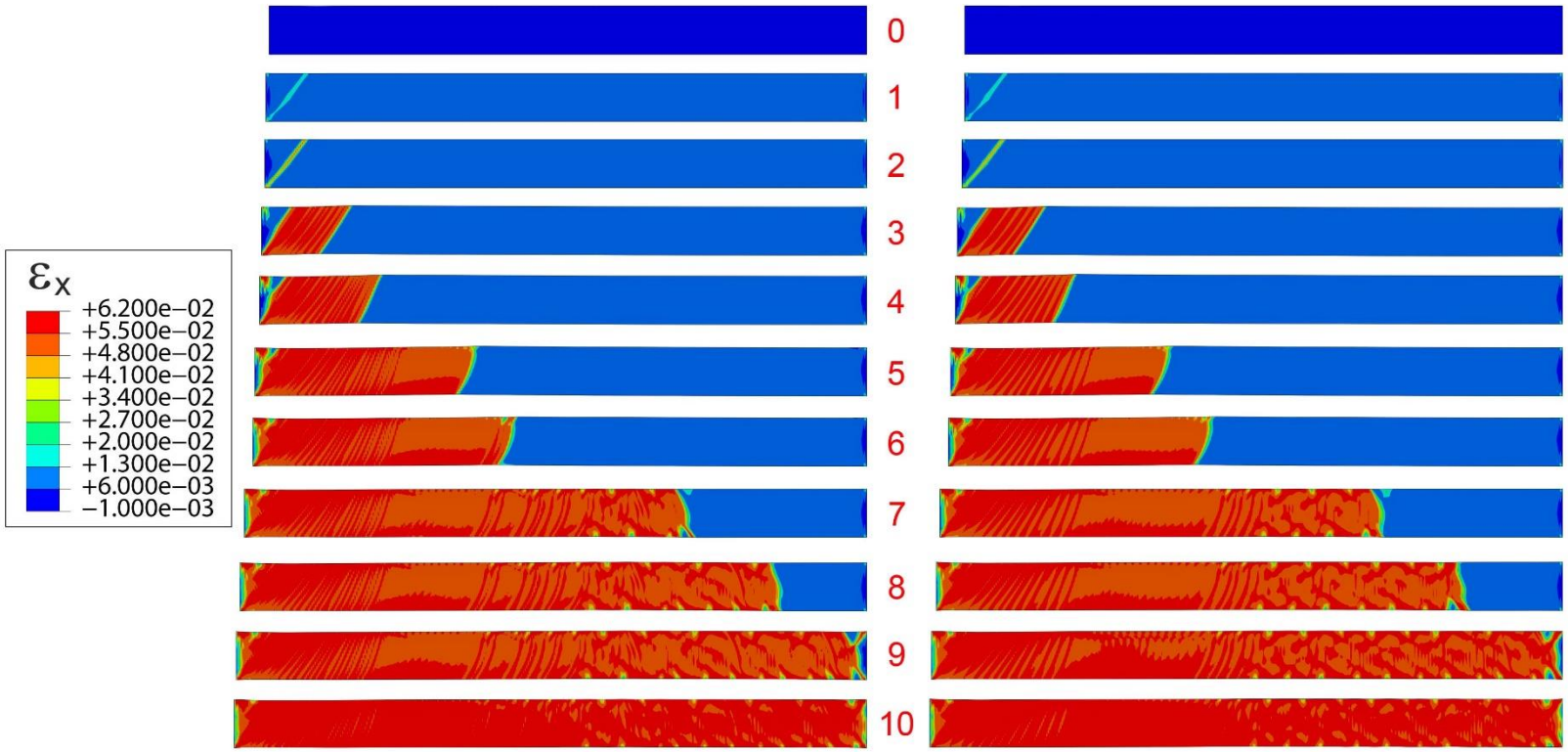

Fig. 4.17 Comparison of the model strip loading deformed configurations produced by rate independent (left) and rate dependent (right) plasticity models ($N_t = 3$), corresponding to the numbered bullets in Fig. 4.16.

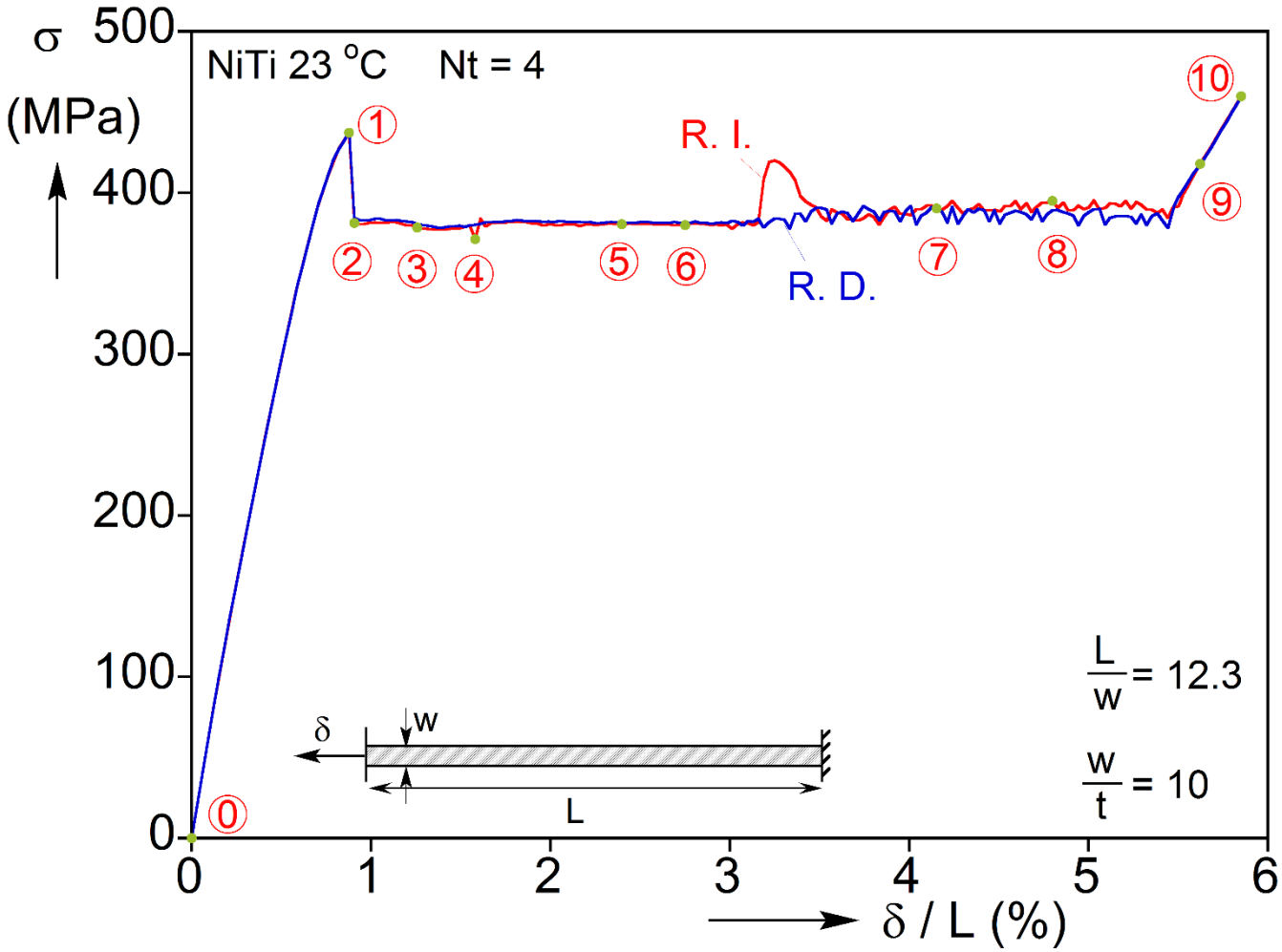

Fig. 4.18 Calculated stress-elongation responses ($N_t = 4$) with rate independent vs. rate dependent J_2 plasticity models.

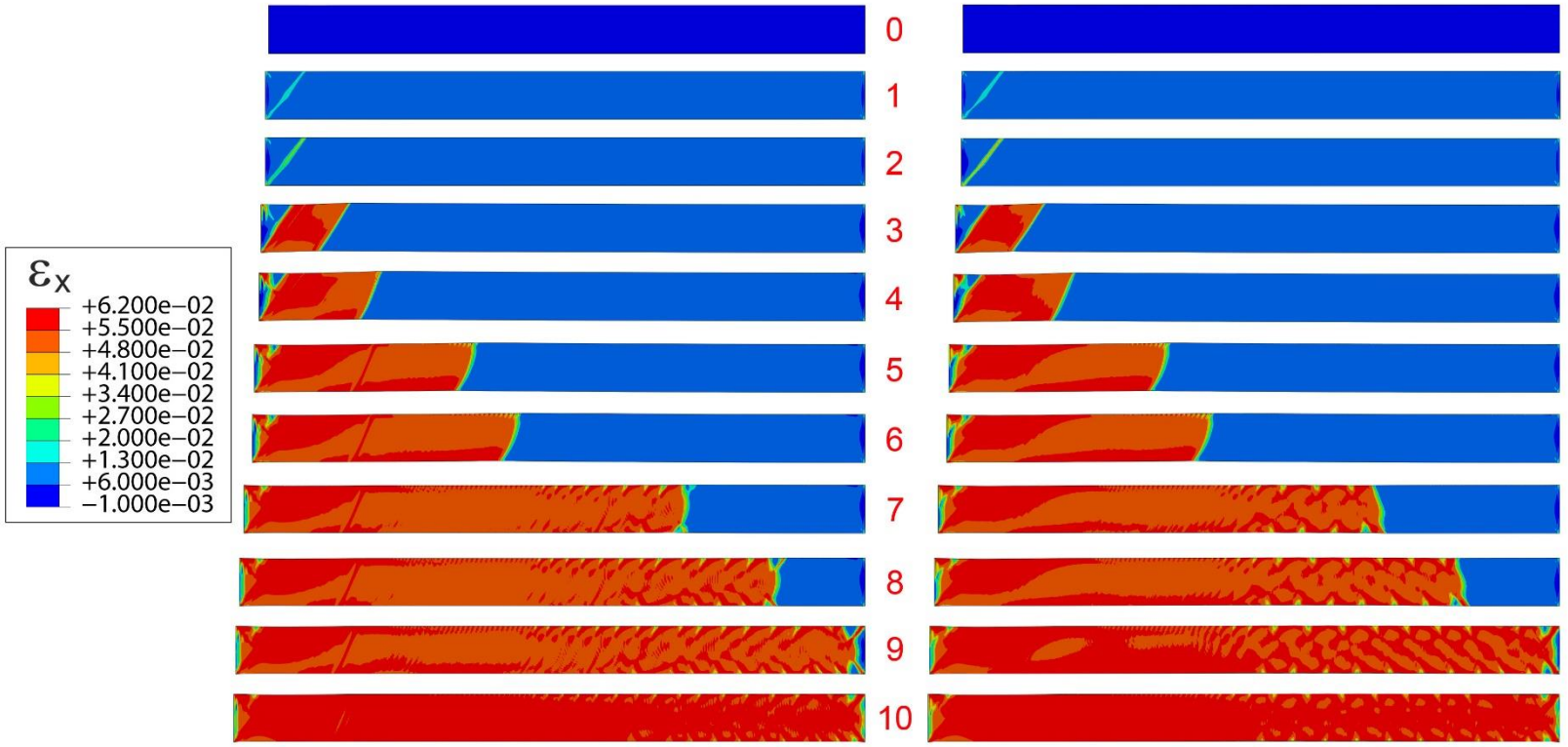

Fig. 4.19 Comparison of the model strip loading deformed configurations produced by rate independent (left) and rate dependent (right) plasticity models ($N_t = 4$), corresponding to the numbered bullets in Fig. 4.18.

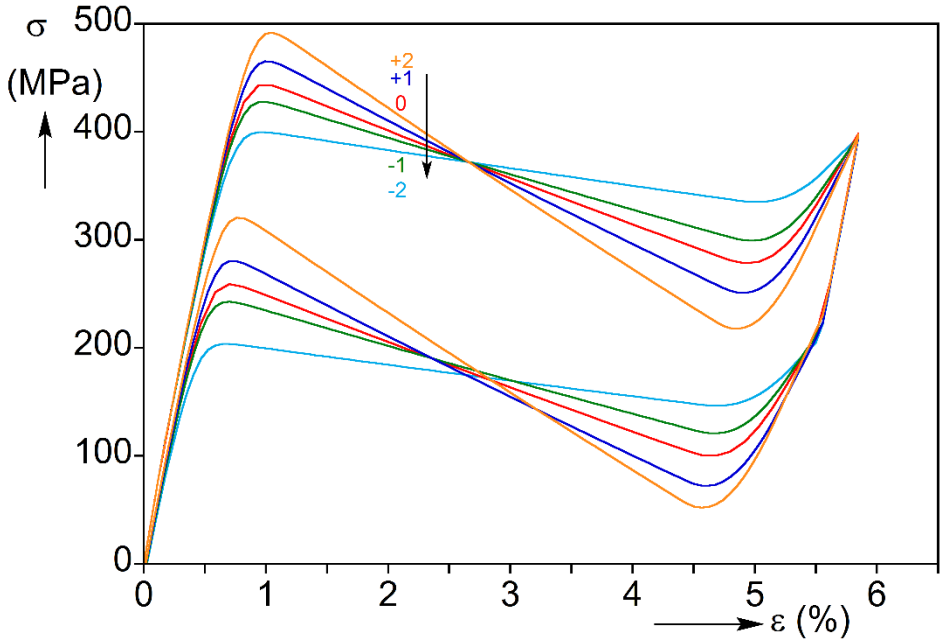

(a)

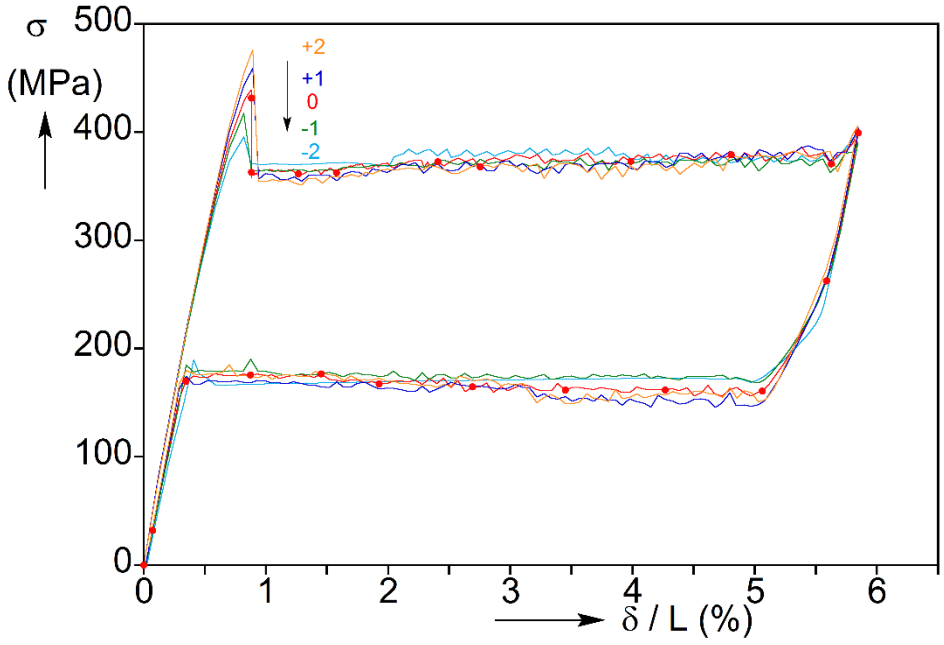

(b)

Fig. 4.20 (a) A set of assumed stress-strain responses with variable softening slopes ("0" corresponds to that in Fig. 4.4a. (b) The corresponding strip stress-displacement responses.

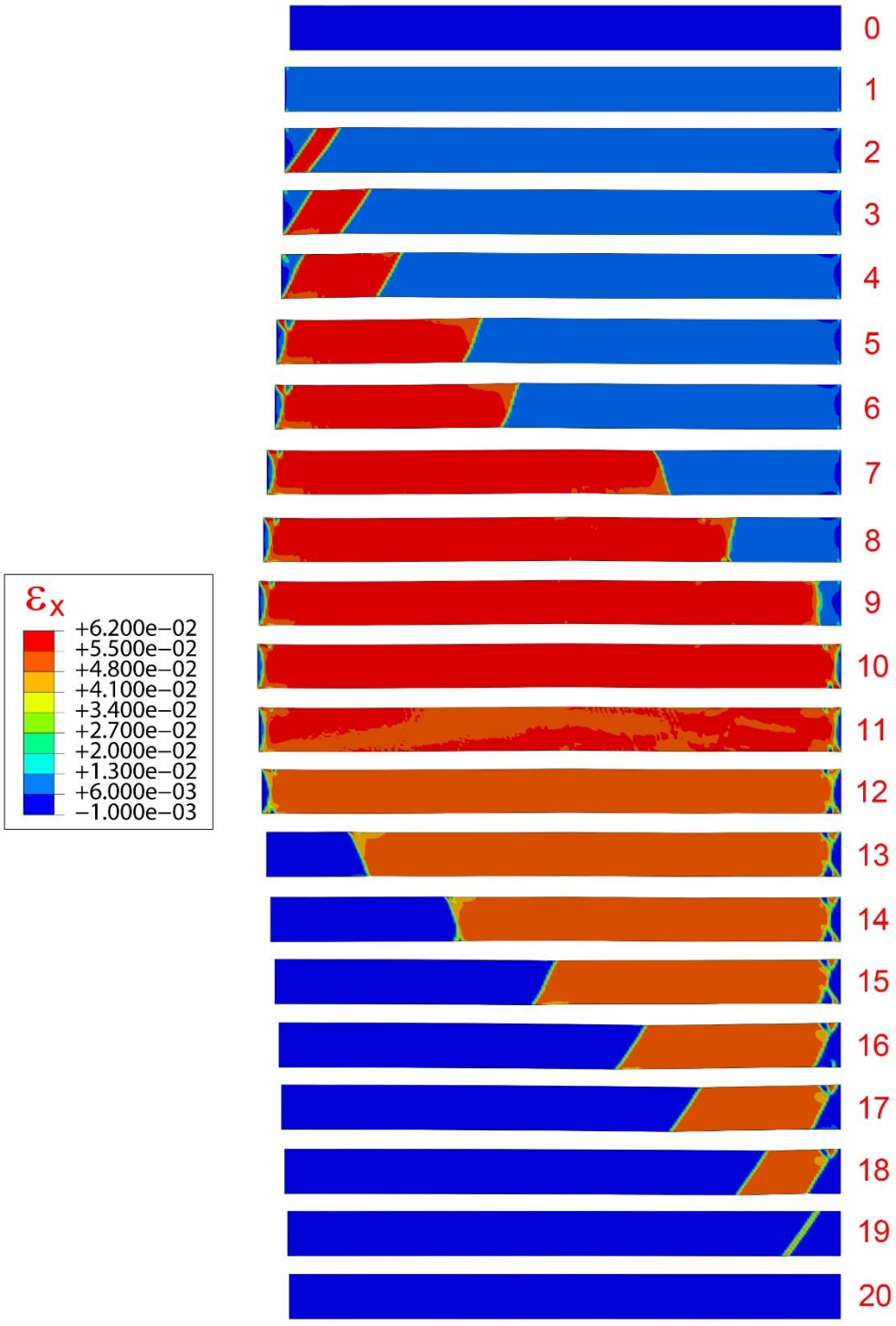

Fig. 4.21 Sequence of strip deformed configurations calculated using the +2 tensile stress-strain response in Fig. 4.20a.

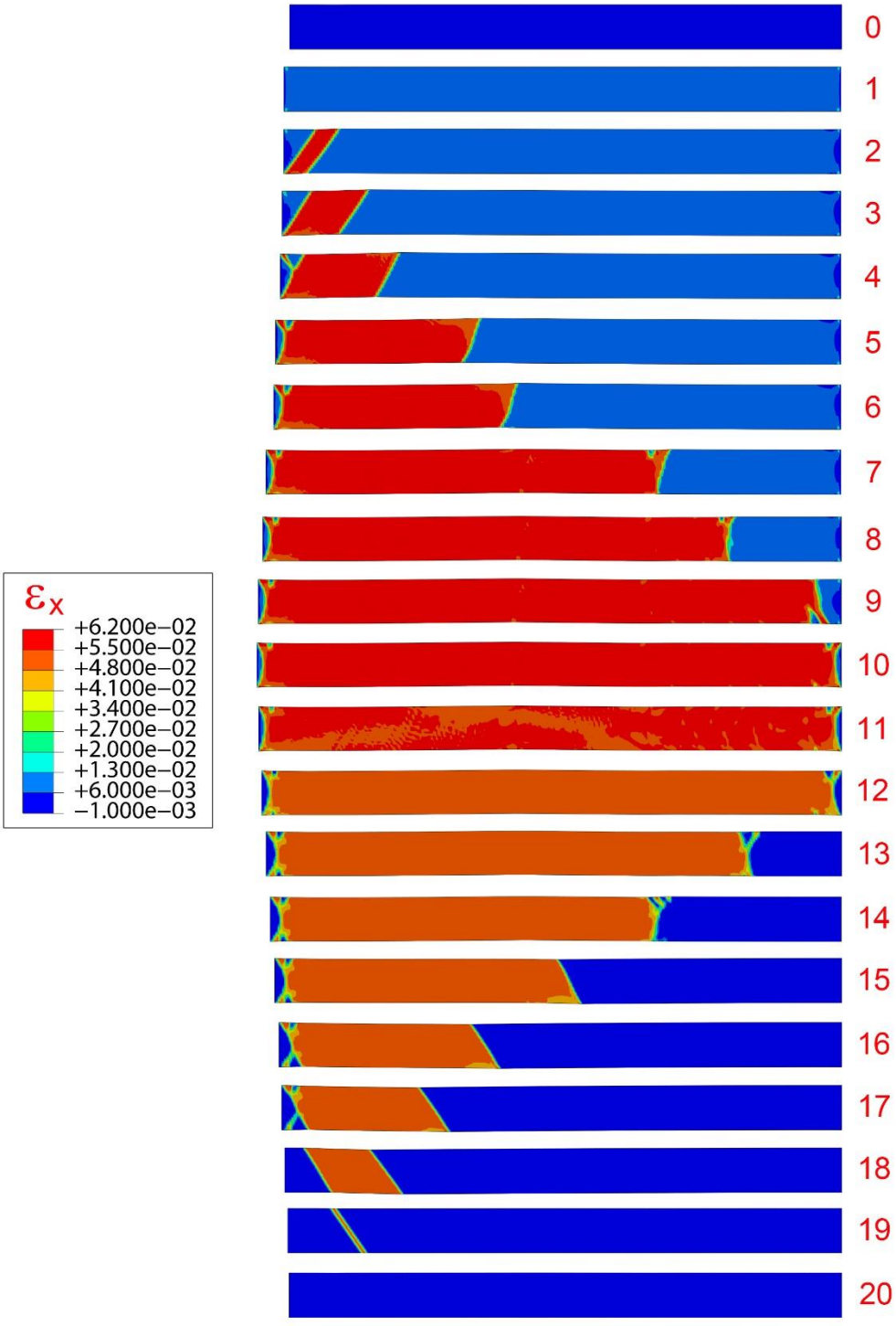

Fig. 4.22 Sequence of strip deformed configurations calculated using the +1 tensile stress-strain response in Fig. 4.20a.

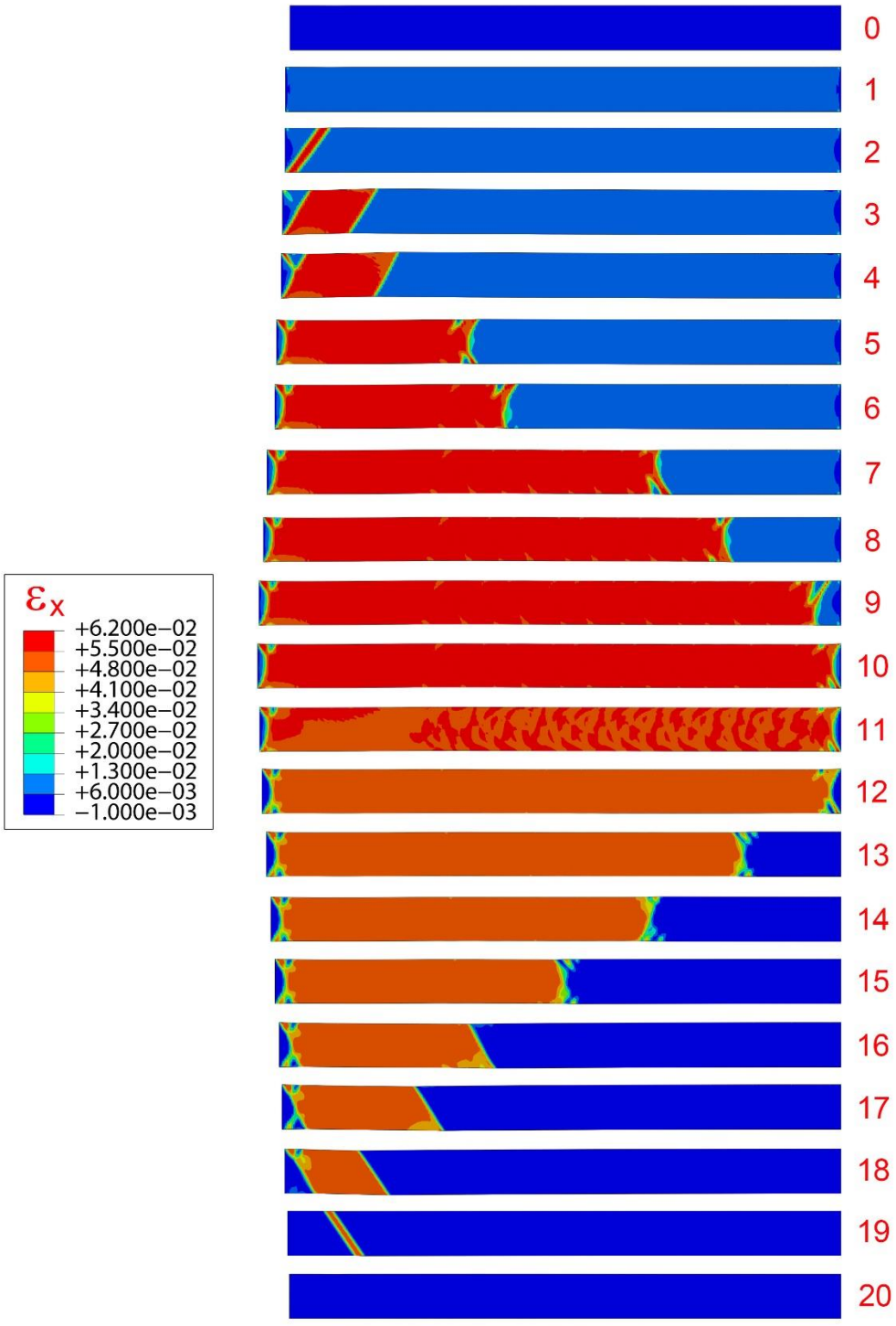

Fig. 4.23 Sequence of strip deformed configurations calculated using the -1 tensile stress-strain response in Fig. 4.20a.

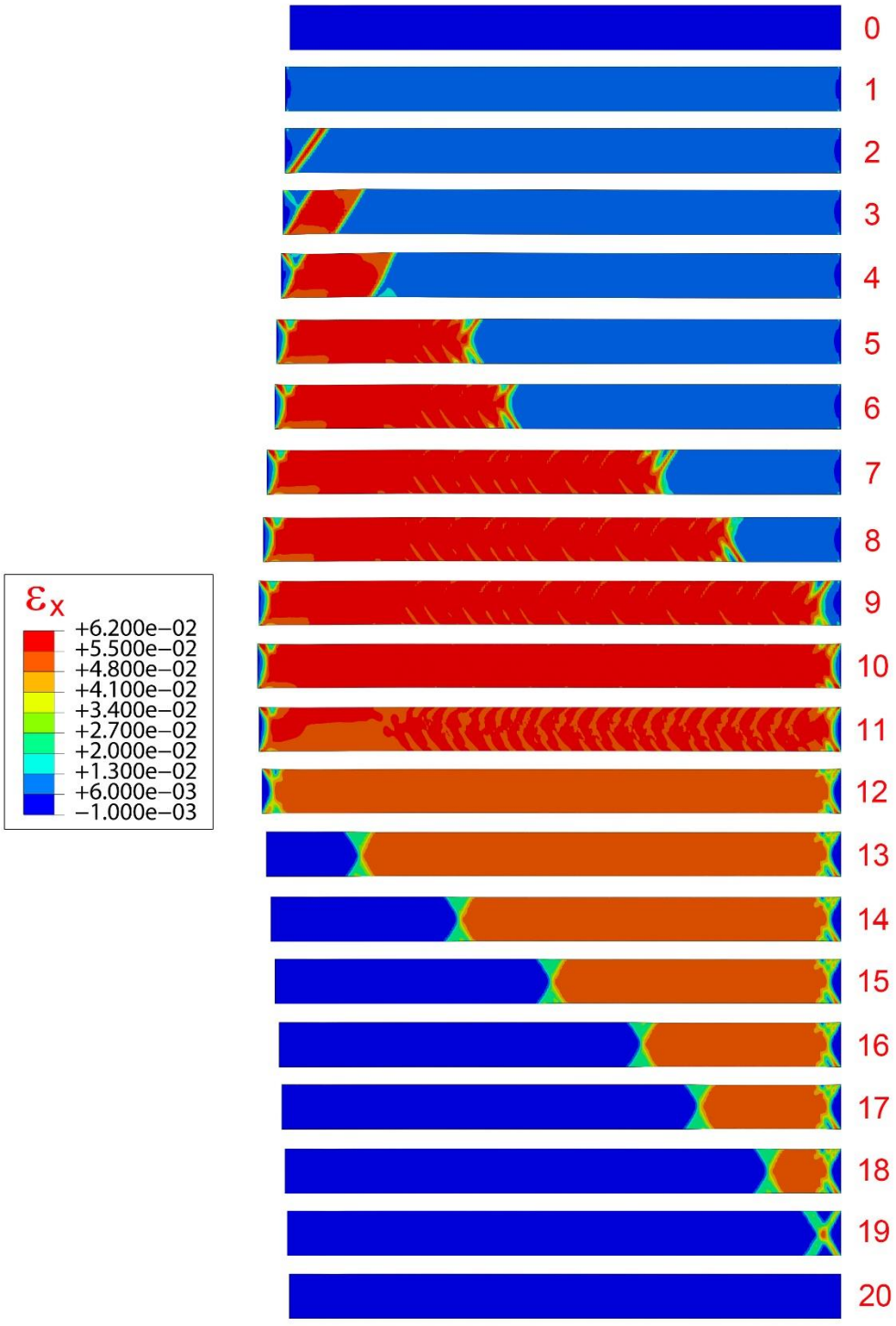

Fig. 4.24 Sequence of strip deformed configurations calculated using the -2 tensile stress-strain response in Fig. 4.20a.

Chapter 5: UNIAXIAL TENSION OF NiTi TUBES

5.1 INTRODUCTION

The constitutive model framework presented in Chapter 2 has achieved success in reproducing the buckling and recovery of NiTi tubes under primarily compressive stress states and the propagation of phase transformation fronts in NiTi strips under tension. In this chapter, the model is utilized to study the experiment on a NiTi tube under uniaxial tension. As was the case for the strip studied in Chapter 4, this problem also involves a primarily tensile stress state, but it has been shown to develop significantly different patterns because of constraints imposed by the tubular geometry. The results of a uniaxial tension experiment on a NiTi tube reported in Bechle and Kyriakides [2016a] are reviewed first. The calibration of the constitutive model and the finite element adopted follows. The main part of the chapter is dedicated to the results of the numerical simulation of the experiment. The chapter finishes with results of a sensitivity study of the solution to several problem parameters.

5.2 EXPERIMENT

Bechle and Kyriakides [2016a] (hitherto referred to as BK16a) used a unique testing facility involving combined axial load and internal pressure to record the response of NiTi tubes loaded along radial stress paths in the axial-hoop stress space. The tubes, with a diameter of 6.35 mm, wall thickness of 0.25 mm and an A_f = 12ºC, were tested at 23 ºC under isothermal conditions. The specimens were clamped at the ends using special locking assemblies leaving a test section of 50 mm (see Figs. 1 and 2 of BK16a). Each specimen was loaded until the completion of the transformation of martensite and unloaded along the same stress path. Stereo digital image correlation was used for full-

field monitoring of the evolution of transformation-induced deformation. The recorded nominal axial stress-mean strain response under pure axial tension is shown in Fig. 5.1 and a corresponding sequence of 20 DIC images of axial strain in Fig. 5.2. (The DIC field of view–FOV– covers approximately 38 mm of the length and one third of the circumference; $\bar{\varepsilon}_x$ is the spatial average of the axial strain over the FOV.)

The $\sigma_x - \bar{\varepsilon}_x$ response exhibits the usual hysteretic behavior of an isothermal pseudoelastic tensile response consisting of: (a) an initial stiff branch when the initial austenitic phase deforms elastically; (b) it is followed by a stress-plateau during which transformation to martensite takes place resulting in a macroscopic strain of about 7%; (c) a second stiff branch develops as the martensite loads and then unloads elastically; (d) a second stress plateau is traced as unloading progresses during which martensite transforms back to austenite. The response is completed by elastic unloading of austenite, closing the hysteresis and returning the material to its undeformed state. The images in Fig. 5.2 clearly demonstrate that both the forward and reverse transformations that take place in the course of the upper and lower stress plateaus result in highly inhomogeneous deformations. In other words, the response is similar to that reported for a NiTi strip (Jiang et al., 2017a), but the phase transformation deformation patterns are different, because of the constraints imposed in each case by the geometry of the specimen.

As in the strip, transformation initiated from the inherent stress concentrations at the clamped ends, however here they are in the form of two helical higher deformation band-like patterns with pointed tips (image ②). The two helixes have an initial inclination of about 55^o to the axis of the tube but follow opposite directions. They both grow in length while their back ends broaden forming helical patterns of increasing width around the tube surface (images ③ and ④). The deformations within the bands reach strain levels close to 7% while the strain in the rest of the specimen remains at 0.82%. As the

top and bottom of the specimen transforms the top reverts to a multi-helical front (images ⑤ to ⑧) presumably to reduce bending of the specimen. The two fronts coalesce just after image ⑨ producing a small stress valley. The entire specimen is now in the martensitic phase and the stress takes an upswing. Image ⑩ shows the FOV to be uniformly deformed.

On unloading from ⑩ the specimen deforms homogeneously up to point ⑫ when transformation back to austenite initiates at the lower end. A multi-helical front develops (image ⑬) and propagates upwards. The austenitic phase is at a strain of about 0.47% whereas the martensitic phase is at 5.9%, each corresponding to the ends of the lower stress plateau. Close to image ⑭, a new multi-helical front initiates at the top of the FOV but with the opposite chirality (see ⑮). In images ⑯ to ⑱ the two fronts propagate towards each other and eventually coalesce producing a small stress peak. The specimen is now back to the austenitic phase (image ⑳), which unloads elastically along the trajectory of initial loading.

In summary, whereas in the strip the initiation and propagation of the alternate phase involved either a single or two inclined fronts, the tube transformation took place through either helical bands or straighter multi-pronged fronts. In both cases the fronts were along one of the two characteristics of Hill of about $\pm 55^{o}$.

5.3 Constitutive Model Calibration

The finite element simulations on the tension test of the NiTi tube described in Section 5.2 adopts the constitutive model framework presented in Chapter 2. As illustrated in the experimental results in Figs. 5.1 and 5.2, transformation under tensile stress-states results in unstable material behavior, which is modeled by introducing

softening branches in up-down-up loading and unloading stress-strain responses (see Jiang et al. [2017a, 2017b]). The two up-down-up responses are calibrated to the measured response in Fig. 5.1 using Eq (2.27) with the following guidelines and assumptions:

- The elastic modulus, E, and Poisson's ratio, ν, of the two phases are assumed to be the same and are assigned the measured values reported for austenite in Appendix C of BK16a.
- The softening modulus of the A→M transformation is similar to that determined in Hallai and Kyriakides [2013] for a NiTi strip with similar properties to those of the present tubes using a sandwich experiment (see also Xiao et al. [2016], Zhu et al. [2016]). This modulus is also adopted for the reverse transformation.
- The two negative slopes are placed at stress levels that correspond approximately to the Maxwell stresses, but the exact positions are determined for best match between the predicted and measured stress plateaus.
- The size of the transformation surface, σ_{ot}, is chosen to correspond to the stress difference between the measured loading and unloading stress plateaus shown in Fig. 5.1.
- The stable and unstable branches are connected by functions that provide algebraic convenience.
- The compressive response included in the model is based on the compressive stress-strain response of the tube analyzed in Jiang et al. [2016b].

With these assumptions, the derivatives of the back stress potentials y_c^t and y_t^t take the following form:

$$\frac{d\psi^t}{d\varepsilon_e^t} = h_0\varepsilon_e^t + (h_1 - h_0)\left[\varepsilon_e^t - \frac{1}{b}(1 - e^{-b\varepsilon_e^t})\right]$$
$$+ (h_2 - h_1)\begin{cases} 0 & \varepsilon_e^t \le \varepsilon_1 \\ (\varepsilon_2 - \varepsilon_1)(2.5\zeta^4 - 3\zeta^5 + \zeta^6), & \varepsilon_1 \le \varepsilon_e^t \le \varepsilon_2 \\ (\varepsilon_2 - \varepsilon_1)/2 + (\varepsilon_e^t - \varepsilon_2) & \varepsilon_2 \le \varepsilon_e^t. \end{cases} \tag{5.1}$$

with $\zeta = (\varepsilon_e^t - \varepsilon_1)/(\varepsilon_2 - \varepsilon_1)$. The values of the parameters $\{b, h_0, h_1, h_2, \varepsilon_1, \varepsilon_2\}$ are listed in Table 5.1. The constant a in the function f in Eq. (2.23b) is assigned the value of 0.953344, which leads to $f(1) = 0.62$.

The resultant stress-strain response is plotted in Fig. 5.3a together with the measured stress-average elongation response. The loading part of the response is in good agreement with the measured response. Since the elastic modulus of the two phases was assumed to be the same, the initial unloading of the martensitic phase deviates somewhat from the experimental results. Figure 5.3b shows the corresponding tensile and compressive back stress responses.

Table 5.1 Model parameters for tensile and compressive responses

Model	E GPa	n	σ_o MPa	b	h_o GPa	h_1 GPa	h_2 GPa	ε_1 (%)	ε_2 (%)
Comp.	66.3	0.425	110.3	2500	1534	2.775	613.6	3.1	3.3
Tens.	66.3	0.425	110.3	2500	1844	-9.458	41.42	3.1	3.3

5.4 FINITE ELEMENT MODEL

The constitutive model is implemented as a UMAT in a finite element model of a NiTi tube under tension. The model, shown in Fig. 5.4, has the same dimensions of the tube used in the experiment reported in Section 5.2: $\{L \times D \times t\} = \{50 \times 6.32 \times 0.27\}$ mm.

The structure is meshed using ABAQUS's 3-D incompatible elements C3D8I that accommodate strain jumps inside the elements (see Jiang et al. [2017a], Hallai and Kyriakides [2013], and references thereof). In order to avoid any directional bias, the meshes adopted are uniform with nearly cubical elements. The mesh used to generate the main results that follow has 2 elements through the thickness, 144 around the circumference and 376 along the length for a total of 108,288 elements.

In the experiments, steel plugs were inserted into the ends of the tube while the outside surface was clamped using a special axisymmetric locking assembly (see Fig. 2 BK16a). The clamping results in a stress concentration that initiated localized phase transformation during loading. This complex boundary condition is difficult to reproduce numerically, so instead no circumferential constraint was used in the model in which the axial displacement of the nodes at $x=0$ are fixed, and the average displacements of these nodes in the other two directions are made zero (to remove rigid body motion). At $x=L$ the axial displacement of the nodes, δ, is prescribed and the other two degrees of freedom of these nodes are free. Under these conditions, material instability is initiated from a small local thickness reduction introduced on the surface of the tube as shown in Fig. 5.4. The imperfection is generated by reducing the thickness by $0.02t$ over an area of $t\times t$ with $t/2$ transition zones all around. It is located a distance t from the end at $x=L$.

5.5 Numerical Results

The results of the numerical simulation of the experiment outlined in Section 5.2 are presented in Figs. 5.5-5.12. Figure 5.5 shows the calculated average nominal axial stress-elongation response $(\sigma_x - \delta/L)$ together with the experimental one. A sequence

of corresponding deformed configurations with color contours of axial strain superimposed (x-y plane) are shown in Fig. 5.6. As in other structures, the inhomogeneous deformation that develops causes some out of plane deformations, which are resisted to some degree by the imposed end constraints resulting in the build-up of moments. The moments M_y and M_z that develop at $x = L$ are plotted against the applied axial elongation in Fig. 5.7. Figure 5.8 plots the average lateral displacement in the z-direction of the right end versus the elongation.

The stress rises along the prescribed tensile stress-strain response with the specimen deforming uniformly. At 546 MPa, just before the 551 MPa stress maximum of the prescribed up-down-up response, the stress drops sharply down to 469 MPa, signaling the initiation of localized deformation in the specimen. The "jump" fashion of this drop is caused by unloading in the rest of the specimen. Tracking the actual unloading trajectory requires a path-following incrementation scheme, which, for simplicity, is not opted for here since the jump does not affect the events that follow (see Appendix A of Jiang et al. [2017a]). The initiation of localization is depicted in Fig. 5.10, which shows a sequence of expanded images, a-h, of the right end of the specimen. For clarity, three views of each image are shown, with 0^o representing the top view of the specimen (positive x-y plane), 180^o representing the opposite side (negative x-y plane), and the 90^o views being along the negative x-z plane. The location of each set of images is marked with a bullet on the zoomed in stress-elongation response shown in Fig. 5.9.

Image a shows localized deformation in the form of two narrow inclined bands that have initiated from the imperfection. The bands are initially oriented towards the free end from where they reflect inwards forming two helixes that circle the specimen meeting on the back at a distance of about D from $x = L$. The bands are oriented at $\pm 55^o$ to the axis of the tube. The axial strain in the bands is approximately 6.7% and outside

them 1.06%–they respectively correspond to the strains at the end and beginning of the upper stress plateau. As the end elongation increases, the band broadens by initially growing mainly toward the left (images b and c). This unsymmetrical deformation distorts the tube locally. The distortion is resisted by the imposed planar constraint on the right end but also displaces the end laterally (the average of the lateral displacement is plotted in Fig.5.8) both of which lead to the build-up of moment M_y observed in Fig. 5.7a between points ② and ③. As the inclined band broadens, in an effort to relieve this moment, a new pair of weak inclined bands develops at the crest of the forward end of the deformed zone, first seen in image c. In image d, the band continues to grow toward the left but now also towards the right end while simultaneously the two narrow bands at its crest have strengthened becoming distinct finger-like features each along the two Hill characteristics. The breakup of the forward front into spiral prongs at the top (0^o) continues in image e, and similar patterns are seen to start developing in the island of undeformed material on the bottom side (180^o) on the right. In image f, the prongs on the forward front have increased to two pairs of three oriented in opposite directions. This image also corresponds to point ④ in Fig. 5.7a where M_y has gone past its maximum value and is starting to decrease. This drop in moment is related to the symmetry of the multi-prong front about the *x*-*z* plane, and to the continued erasure of the undeformed island on the back of the right end. In image g the number of prongs of the forward front has increased to 8, the right end is almost all completely consumed by the higher strain, and consequently the moment has decreased significantly. In image h, the number of prongs has increased to ten, five on either side, the deformation on the right has been completed, and the moment has decreased to a local minimum. Throughout these events the average axial stress has dropped gradually to a value of 457 MPa.

Beyond point h, the front propagates to the left via two pairs of five-prong fronts until point ⑧ is reached near the end of the upper stress plateau. The two sides of the front are essentially symmetric about the *x*-*z* plane and propagate approximately along the generator that passes through the initial imperfection. As new prongs initiate, the stress fluctuates slightly about an average value of 455 MPa. Figure 5.11 shows three expanded views of the front corresponding to point ⑥. Two sets of five bands initiate from the top (0^o) with each set spiraling around the half circumference (90^o) but with opposite chirality. They meet at the bottom (180^o) forming the pattern shown in the figure. The bands have narrow tips but widen behind it. The strain inside the bands is approximately 6.8%, which corresponds to the value at the end of the upper stress plateau in Fig. 5.5. The strain across the boundaries of the bands transitions from the low to the high deformation states across approximately one element. The overall width of the multi-pronged front along the axis is about 0.58*D*. Differences between the top and bottom of the front cause a small local kink to the tube in the *x*-*z* plane. Because of this kink, the point of application of the net axial force on the right is displaced in the *z*-direction causing a moment in the plane. This explains why the minimum moment, which occurs when the ten-pronged front first develops in image h, is not zero. Furthermore, as the front propagates to the left, the kink moves with it further displacing the point of action of the axial force on the right resulting in the linear increase in M_y with δ observed in Fig. 5.7a. By contrast, because of the symmetry of the front in the *x*-*y* plane, M_z is seen to hover around zero level for the duration of the forward transformation (① to ⑨).

By image ⑧ at the end of the plateau, a small island of undeformed material remains on the left end. Its erasure is accompanied by a small drop in stress that is caused by the front encountering the free end. Some small islands of low deformation observed in image ⑨ remain and the associated local distortion causes the sharp change in

moment observed in Fig. 5.7a. Further elongation requires an increase in the applied force. The higher axial stress deforms most of the remaining pockets of low deformation, and returns the specimen to essentially uniform deformation (image ⑩).

On unloading from ⑩, the specimen initially deforms uniformly and M_y returns to zero. At a stress of about 162 MPa (point ⑪) the lower softening branch of the stress-strain response triggers localized deformation. Localization is initiated once again from the right end, but this time from a site nearly diametrically opposite to the location of the imperfection. This is a site that was last to transform on the right end during the forward initiation of localization (see 180° images f-h in Fig. 5.10). The unloading leaves behind some small islands of somewhat lower strain (e.g., see image ⑪), which are favored as initiation sites during the reverse transformation. In Fig. 5.12, which shows expanded the right end of image ⑫, two helical bands have initiated from such a site at $x = L$. They are oriented at ±55° to the axis of the tube. One of the bands has propagated down the length of the tube while the second has been arrested. The initiation results in a "jump" increase in the stress to 235 MPa. The axial strain inside the bands is about 0.44% and outside it about 5.6%, both corresponding to the values at the two ends of the lower plateau.

Images ⑬ and ⑭ show the helical band propagating toward the left while simultaneously broadening. In the course of this propagation the axial stress remains essentially unchanged but both M_y and M_z are seen to oscillate about zero but 90° out of phase. Between images ⑬ and ⑭, the tip of the helical band has reached the left end and subsequently the band broadens. At some stage, the second band on the right, hitherto dormant, starts to grow, intersects with the existing one causing erasure of the higher deformation on the right end (image ⑮). This results in a disturbance in the stress in Fig. 5.5 and new oscillations in the two moments in Fig. 5.7. By image ⑯, about 75% of the tube is back to a strain of 0.44% and the axial stress is back to its plateau value.

The higher strain in the remainder of the specimen is removed through a multi-prong front that is observed forming in image ⑮ and fully developed in image ⑰. The erasure of the final island of higher strain on the left leads to a small increase in stress as the front encounters the free end. The specimen subsequently unloads to zero stress along the initial stiff slope deforming homogeneously.

5.6 PARAMETRIC STUDY

As was shown in Chapter 4, solutions such as the present one can be influenced by various parameters of the problem. Presented below are the results of a limited parametric study performed.

5.6.1 Mesh Sensitivity of the Solutions

The softening branches in the tensile up-down-up stress strain response used imply some degree of mesh sensitivity of the solutions. As in the other problems considered in this dissertation, the uniform mesh shown in Fig. 5.4 was selected fine enough to reproduce the finer features of the deformation patterns that develop. The present version of the constitutive model is rate independent which precludes the usual regularization by the addition of a mild rate dependence to the constitutive model (Needleman [1988]). Consequently, sensitivity of the solution presented in Section 5.4 to the mesh density is investigated by considering finer meshes with 3 and 4 (N_t) elements through the thickness (N_t). This increases the total number of elements to 365,472 and 866,304 respectively with corresponding dramatic increases in the computational cost.

Figure 5.13 shows the nominal axial stress-normalized elongation responses of the NiTi tube calculated using the meshes with $N_t = 3$ and 4, together with the case using $N_t = 2$ presented in Section 5.5. Clearly, the predicted hysteretic response of the tube is

essentially unaffected by the mesh density, with the exception of some small differences in the value of average strain at which the stress disturbances in the lower plateaus take place. Figures 5.14 and 5.15 show sequences of deformed configuration of the tube superimposed with color contours of axial strain calculated by N_t = 3 and 4, respectively. Both cases reproduce the initial localization of deformation into two narrow bands along the two Hill characteristics from the imperfection. The bands subsequently evolve into a multi-pronged front that propagates towards the left until the whole tube has transformed. The reverse transformation leads to inhomogeneous deformation in the form of a spiral band that widens as it traverses the length of the tube. Although the plane of symmetry for the front in the N_t = 3 and N_t = 4 cases tends to rotate slightly during propagation, overall the main patterns predicted are insensitive to the mesh density.

5.6.2 Effect of Imperfection

The geometry of the imperfection used to initiate localization was found to influence the front patterns that develop. In the case of the results presented in Section 5.5, localization initiated from a small thickness reduction introduced close to one end of the specimen as shown in Fig. 5.4. Results from two additional imperfections will be shown here. The first case involves the addition of an identical thickness imperfection diametrically opposite to the original one. Figure 5.16 shows the calculated stress-elongation response using this imperfection (blue), which is nearly coincident to the one calculated using the single imperfection. The resultant deformation patterns, however, shown in Figs. 5.17-18, are significantly different. Here, each imperfection site activates a pair of inclined bands of localized deformation oriented along the two characteristics. Thus, the phase transformation front that develops past image ④ is doubly symmetric. This symmetry maintained until the end of the upper stress plateau in image ⑨. The front

develops two pairs of multi-pronged fronts on each in the *x*-*y* and *x*-*z* planes, as shown in the expanded views of the front along four orthogonal orientations (corresponds to image ⑥ in Fig. 5.18). Furthermore, during unloading localization initiated on the right end and propagated via a multi-pronged front that was symmetry only about the *x*-*y* plane as shown in the expanded view of image ⑮ in Fig. 5.18.

The second case introduces an axisymmetric groove imperfection with the same $0.02t$ depth and the same width at the same distance to the right end as the local imperfection in Fig. 5.4. The predicted response of the tube (drawn in green in Fig. 5.16) is quite similar to the one calculated using the local imperfection. Figure 5.19 shows a sequence of deformed configurations corresponding to the groove imperfection. The front associated with forward transformation now consists of four sets of prongs arranged around the circumference at 90^o intervals as depicted in the expanded views of Fig. 5.20. This pattern with four planes of symmetry prevails until about 40% along the length of the tube has deformed to the high strain. It then gives way first to a pattern with two planes of symmetry and later to another pattern with only one plane of symmetry. Upon unloading, a multi-pronged front with one plane of symmetry similar to image ⑮ shown in Fig. 5.18 develops which propagates from left to right.

5.6.3 Effect of Softening Modulus

The softening slopes adopted in the tensile stress-strain response shown in Fig. 5.3a are equal to that measured in the sandwich experiment of Hallai and Kyriakides [2013]. To study the effect of the softening slope on the numerical solution, we vary the slope of the softening branches as shown in Fig. 5.21a. The response designated as "+1" has softening slopes that are 65% larger than that in the base case ("0") and the slopes of the one marked "-1" are 33% smaller than those of case "0".

The resultant stress-elongation responses are compared in Fig 5.21b. They trace plateaus with the same stress levels, but the stress peak during loading increases and the valley during unloading decreases as the softening slopes increase. This of course is a direct consequence of the changes in the stress peaks/valleys of the up-down-up response as the softening slopes are altered.

The deformation patterns are also affected by the softening slopes. For case +1, shown in Fig. 5.22, the deformation front during loading is symmetric about the *x-z* plane but the number of prongs decreases to 8 (see the expanded views in Fig. 5.23), compared to 10 for the "0" case. In addition, this front with mainly one single plane of symmetry tends to rotate as it propagates towards the left and periodically became somewhat unsymmetric, as shown in images ⑤-⑧. The deformation patterns in the tube during unloading are similar to those of the "0" case.

For case -1, the single plane of symmetry front during loading becomes more stable (see Fig. 5.24), but the number of prongs in the front increases to 14 as shown in the expanded views in Fig. 5.25. The localized deformation associated with the lower stress plateau initiates from the right end but evolves to a multi-prong front which is symmetric about the *x-z* plane.

5.7 SUMMARY

Experimental results from a tensile test on a pseudoelastic NiTi tube display the usual closed stress-elongation hysteresis to strains of nearly 7% with an upper and a lower stress plateau associated with the reversible transformations between the *A* phase and the *M* phase. Transformation induced deformation localizes into either helical bands

or multi-pronged fronts due to the tubular geometry. The localization patterns propagate in the specimen during the two stress plateaus.

The constitutive model presented in Chapter 2 is used in a FE model to simulate the tube tension experiment. The constitutive model is calibrated to both the compressive and tensile responses of the material. Similar to the modeling of the strip in Chapter 4, unstable material behavior is modeled by introducing softening that spans the two stress plateaus recorded in the structural response. The tube geometry in the model is the same as that in the experiment but instead of being clamped, the ends are left free. The model is discretized with solid incompatible elements into a mesh that is fine enough to reproduce the finer features of the localization patterns that develop. A small thickness imperfection is introduced close to one of the free ends of the tube to initiate localization.

Under displacement control loading, the simulation reproduces the hysteretic stress-elongation response with the correct levels and extents of the two stress plateaus. The calculated response exhibits the usual stress peak associated with the initiation of the forward transformation and the stress valley at the initiation of the reverse transformation. Localization initiates from the imperfection via two narrow bands along the $\pm 55^{o}$ characteristics. The bands grow and evolve into a symmetric ten-pronged front, which propagates and deforms the specimen to the nearly 7% strain of forward transformation. The front propagates until most of the tube material transforms and the upper stress plateau terminates. Unloading initially is homogeneous until the stress drops to the level of the lower plateau. The deformation then localizes to a single helical band of lower strain, which broadens as it propagates along the length of the tube.

As was the case for the strip, the model reproduces the main features of the experimental response but with some differences in the localization patterns. A parametric study indicates that for the tube, the localization patterns are influenced by the

type and location of the imperfection used to initiate instability, by the boundary conditions and to some degree by the strength of the softening modulus adopted.

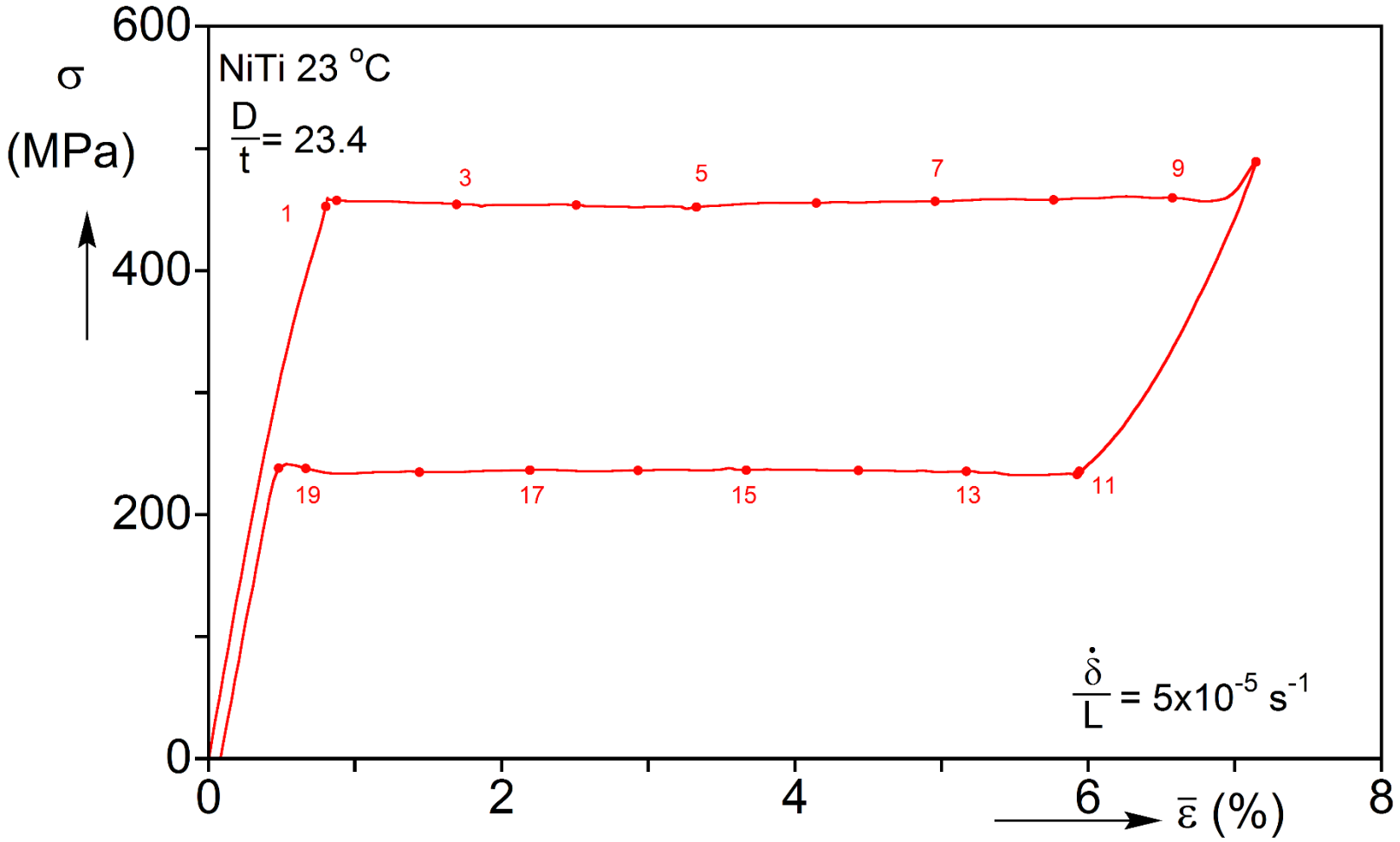

Fig. 5.1 Axial stress-average strain recorded in an isothermal uniaxial tension test on a NiTi tube at 23 ºC.

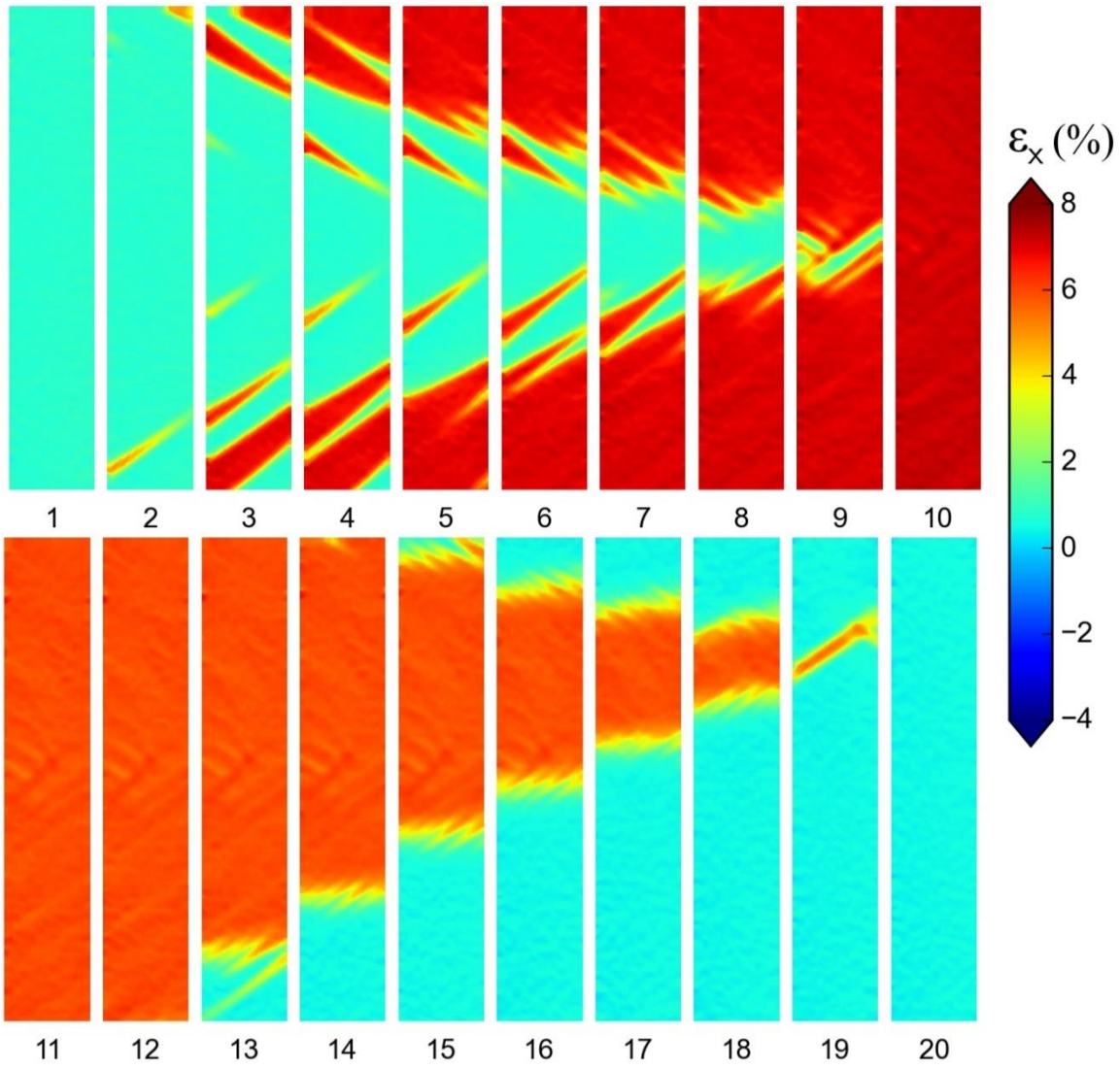

Fig. 5.2 Sequence of axial strain contours from DIC corresponding to the numbered bullets marked on the tensile response in Fig. 5.1.

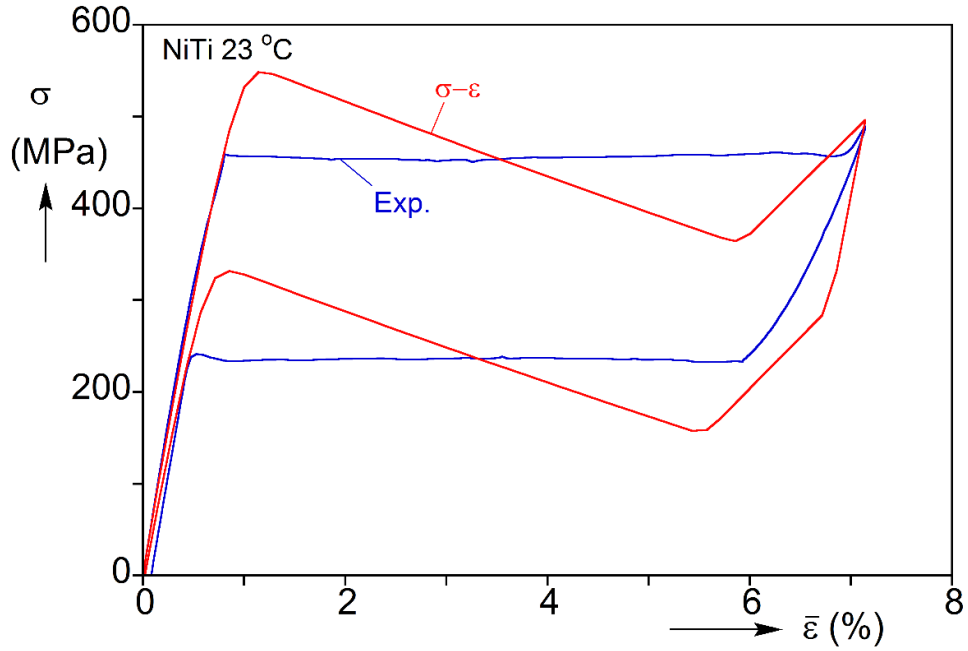

(a)

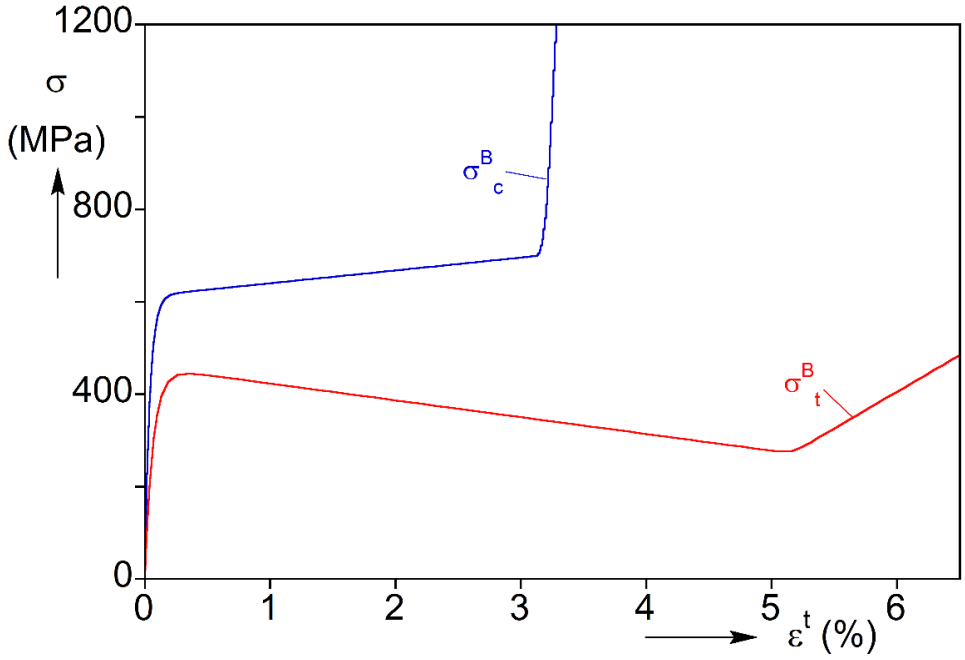

(b)

Fig. 5.3 (a) The assumed softening tensile stress-strain response (red) together with the measured structural response of the tube. (b) The back stress-transformation strain responses for tension and compression used in the model.

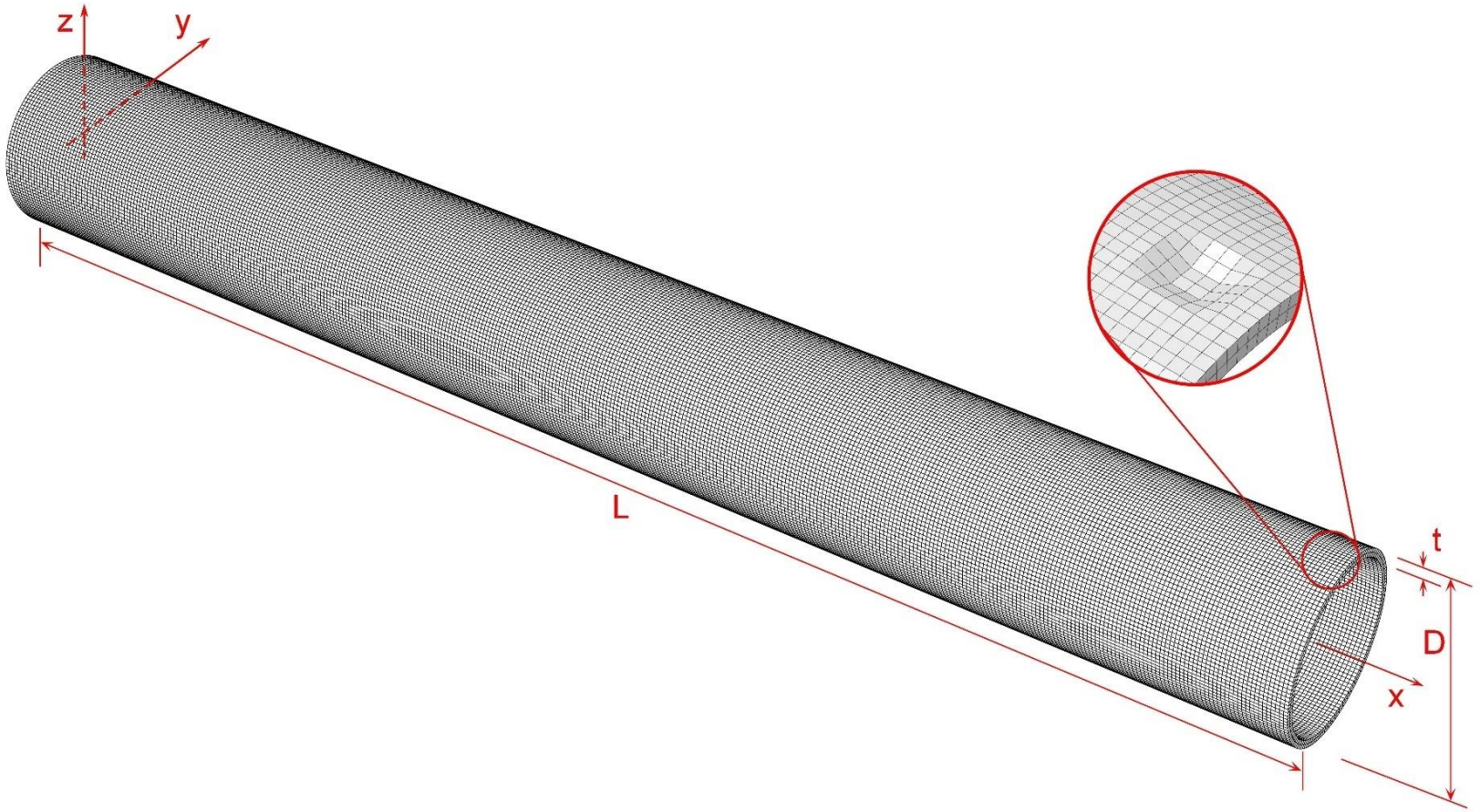

Fig. 5.4 Geometry of the model tube and the finite element mesh used.

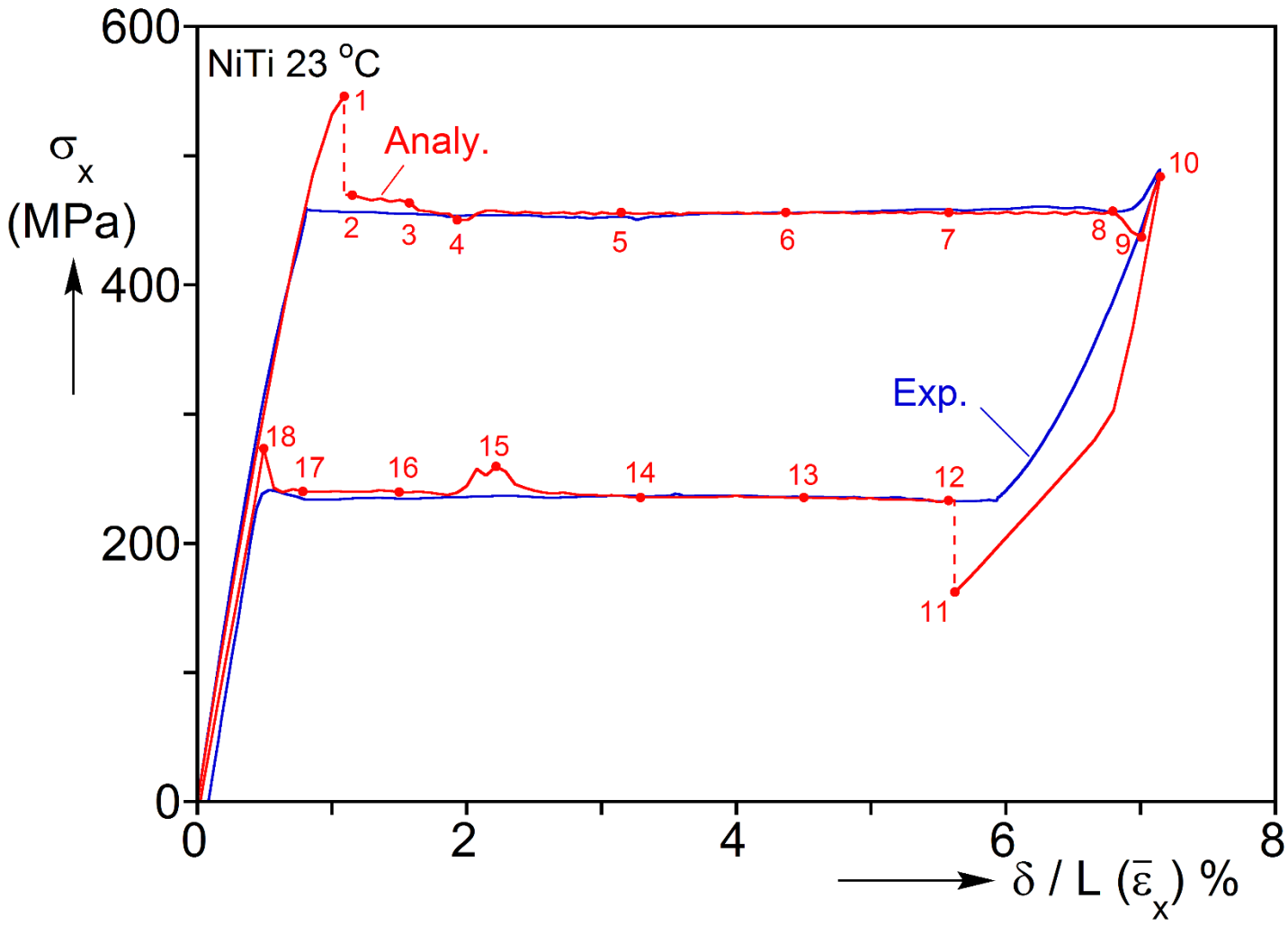

Fig. 5.5 The calculated average stress-elongation response of the NiTi tube together with the measured one .

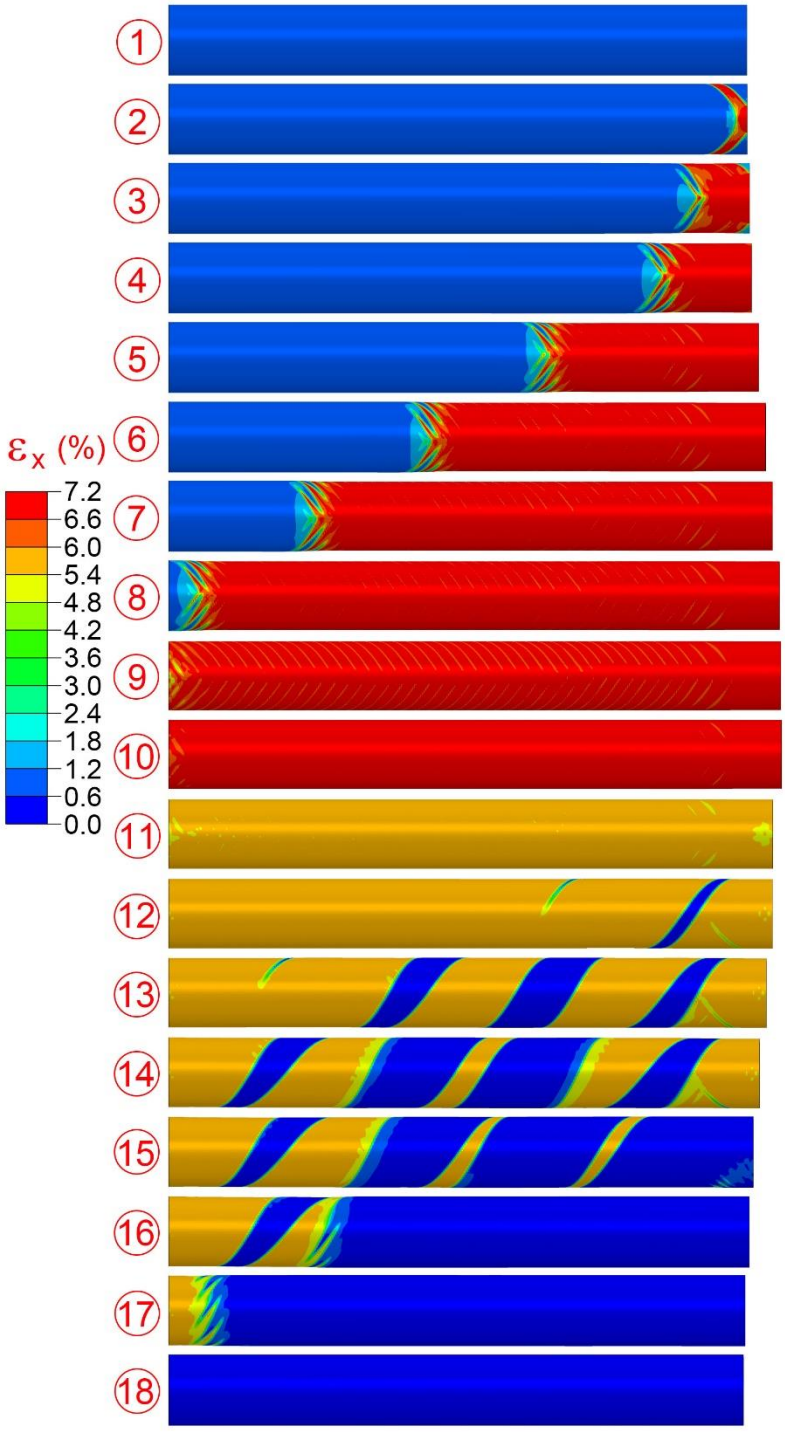

Fig. 5.6 Sequence of calculated deformed configurations with axial strain contours superimposed (*x*-*y* plane), corresponding to the numbered bullets on the response in Fig. 5.5.

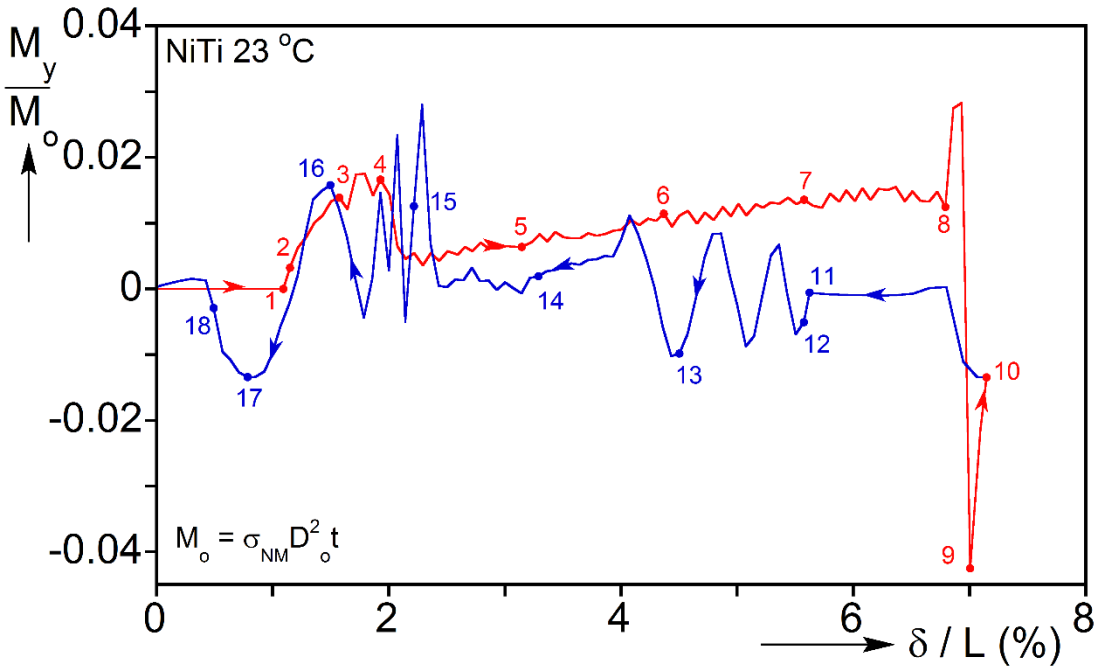

(a)

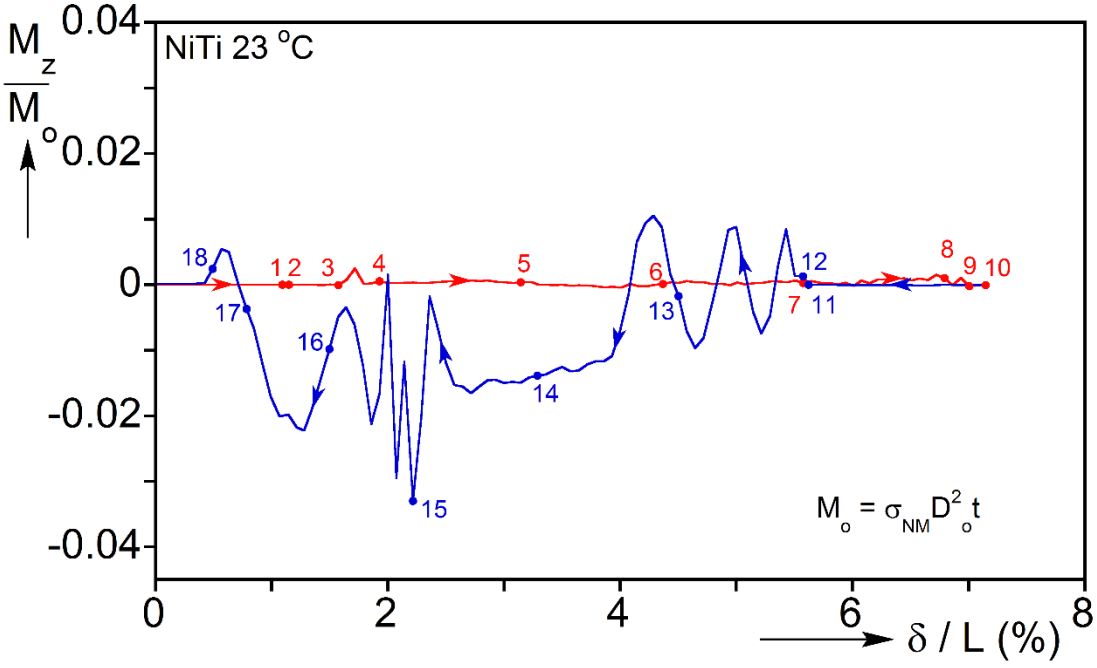

(b)

Fig. 5.7 Moments induced by the inhomogeneous deformation at the end of the tube vs. the applied end-displacement: (a) M_y and (b) M_z.

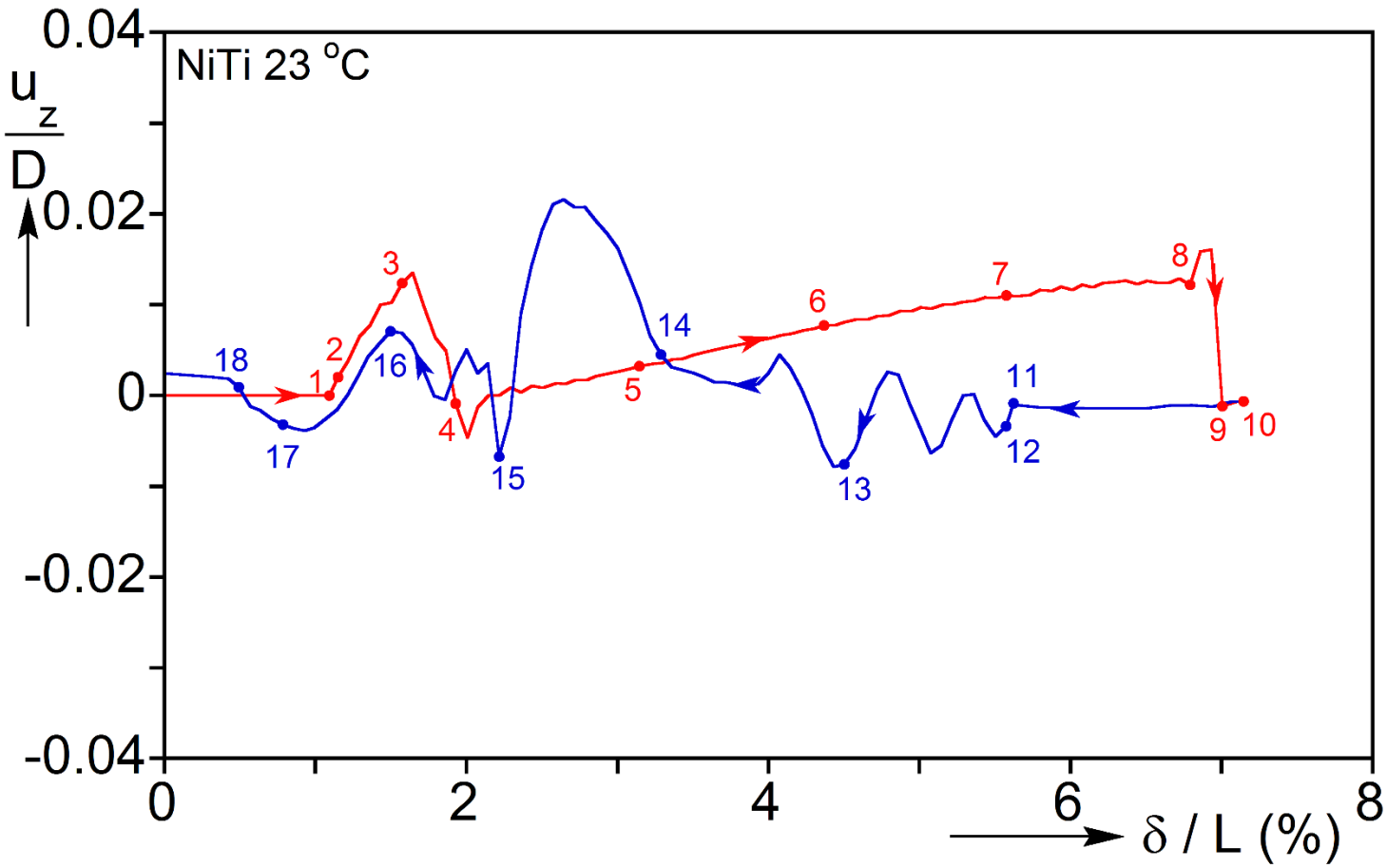

Fig. 5.8 Average lateral displacement on the right end in *z*-direction versus elongation.

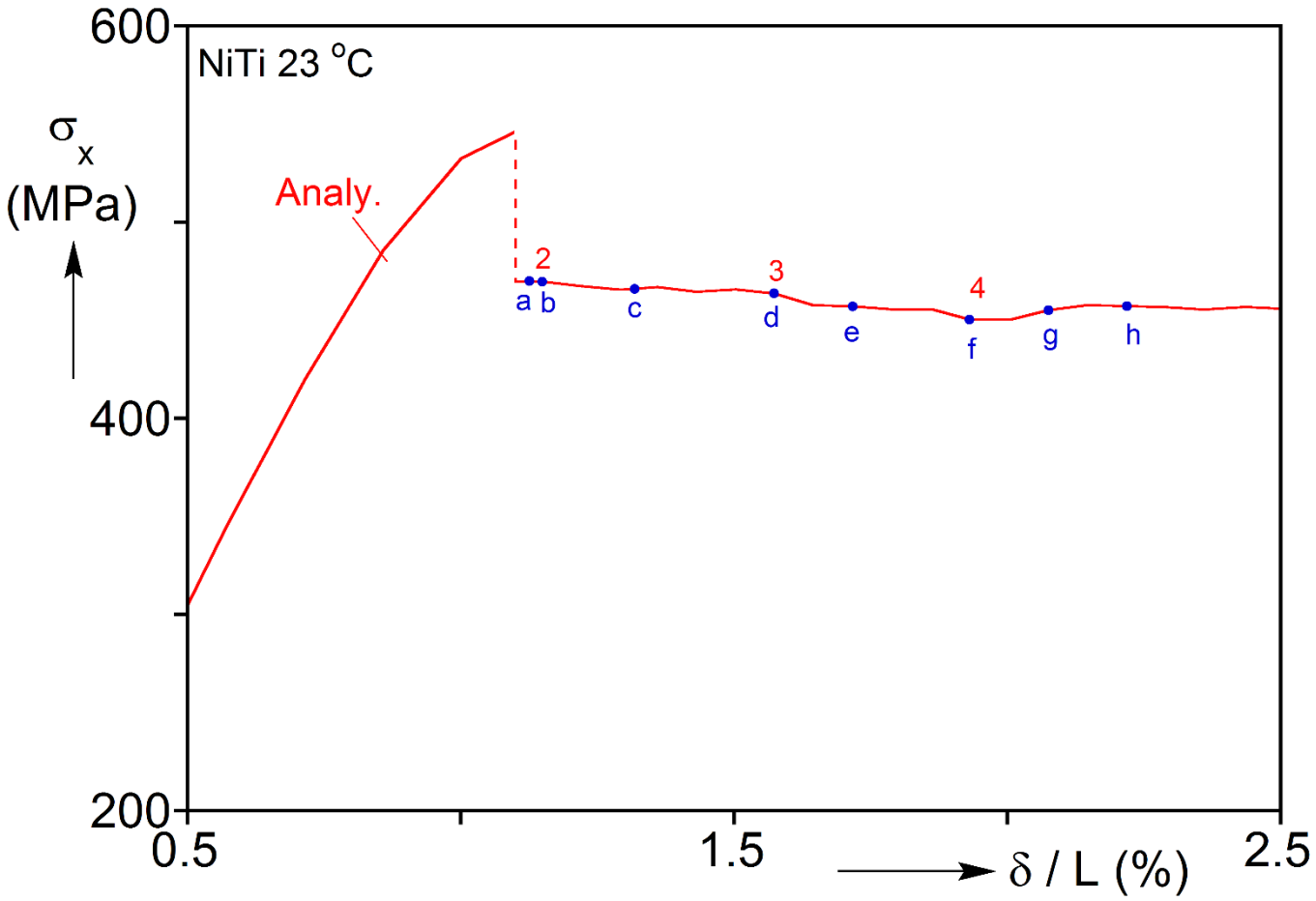

Fig. 5.9 Zoomed in average axial stress-elongation response during the initiation of the localization.

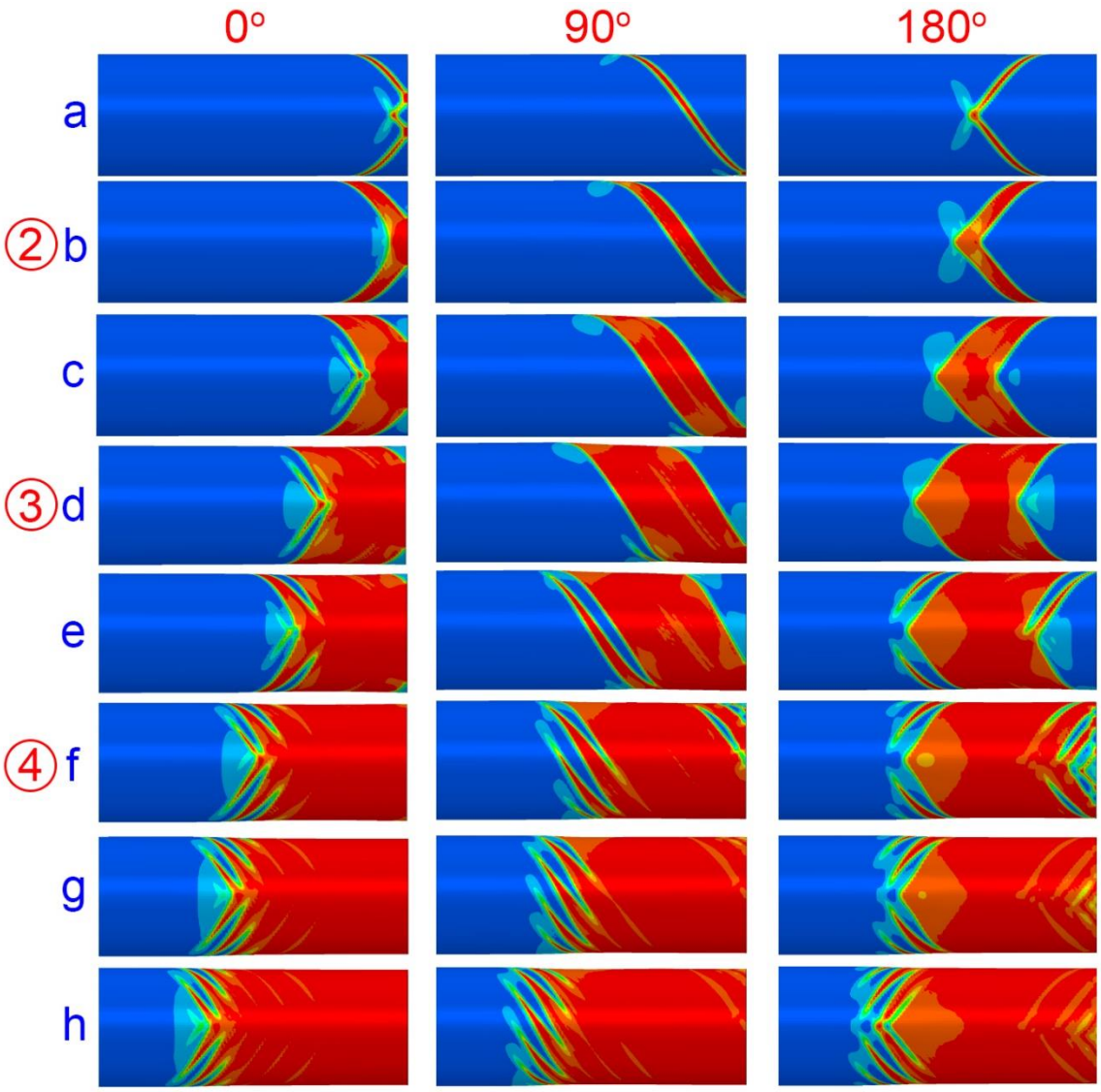

Fig. 5.10 Expanded sets of images of the right end with axial strain contours superimposed that show details of the initiation of localized deformation from the geometric imperfection.

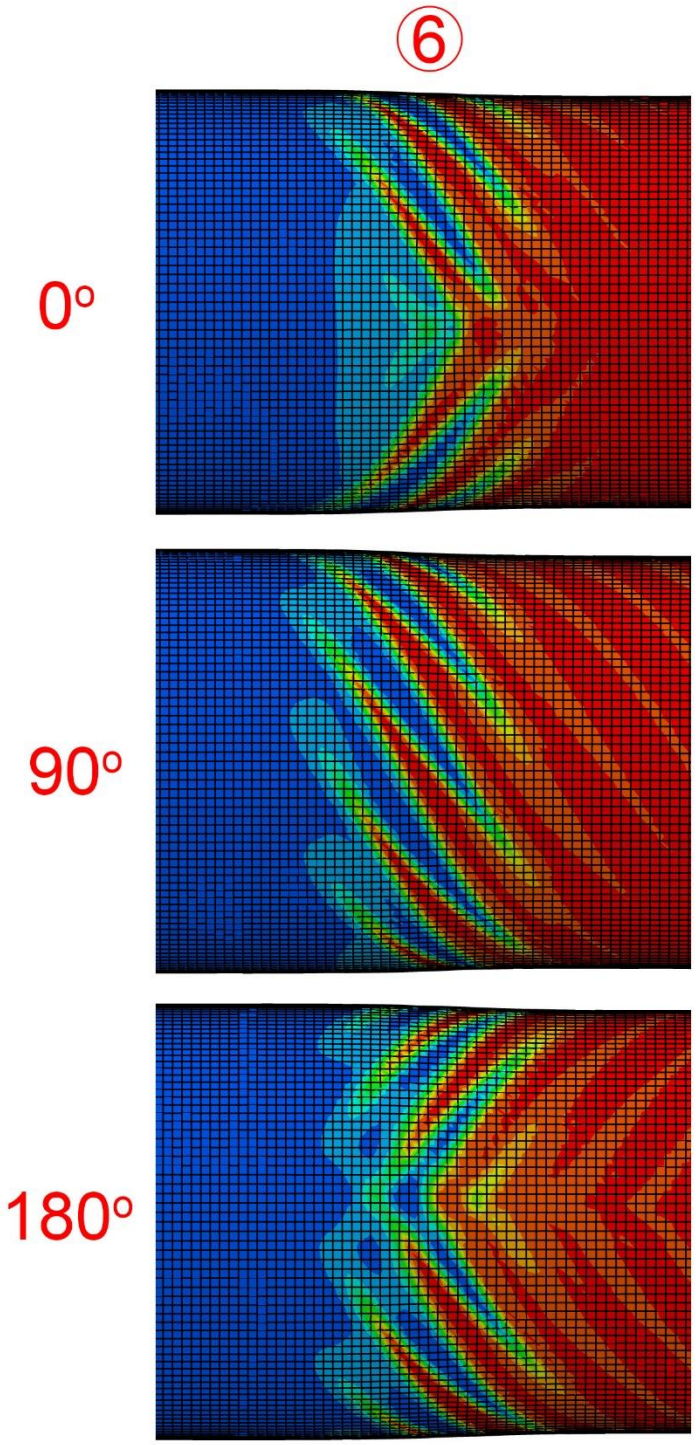

Fig. 5.11 Expanded views of the multi-prong front during steady state propagation (image ⑥).

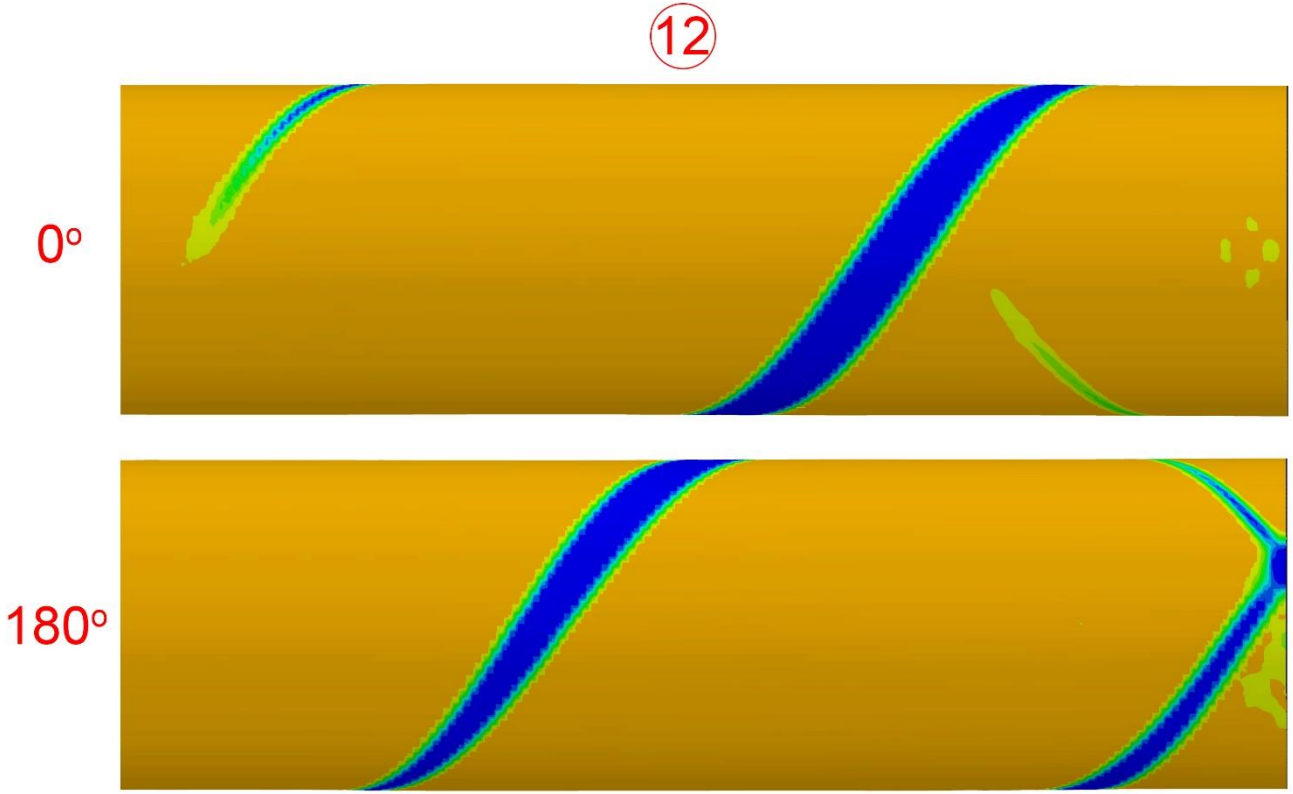

Fig. 5.12 Expanded views of image ⑫ showing the initiation of a lower strain helical band from the right end of the tube during unloading.

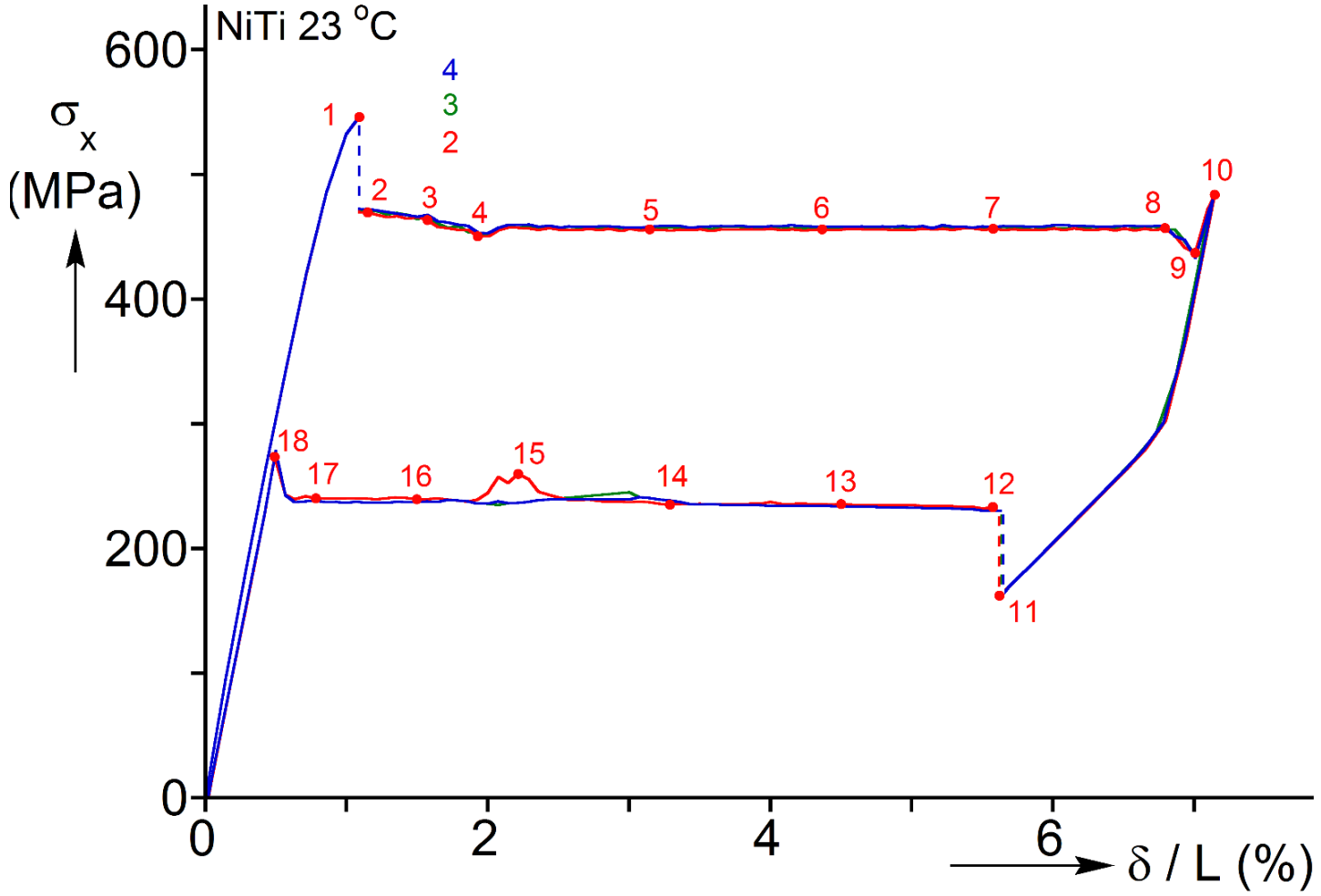

Fig. 5.13 Axial stress-elongation responses using the meshes with N_t =2, 3 and 4.

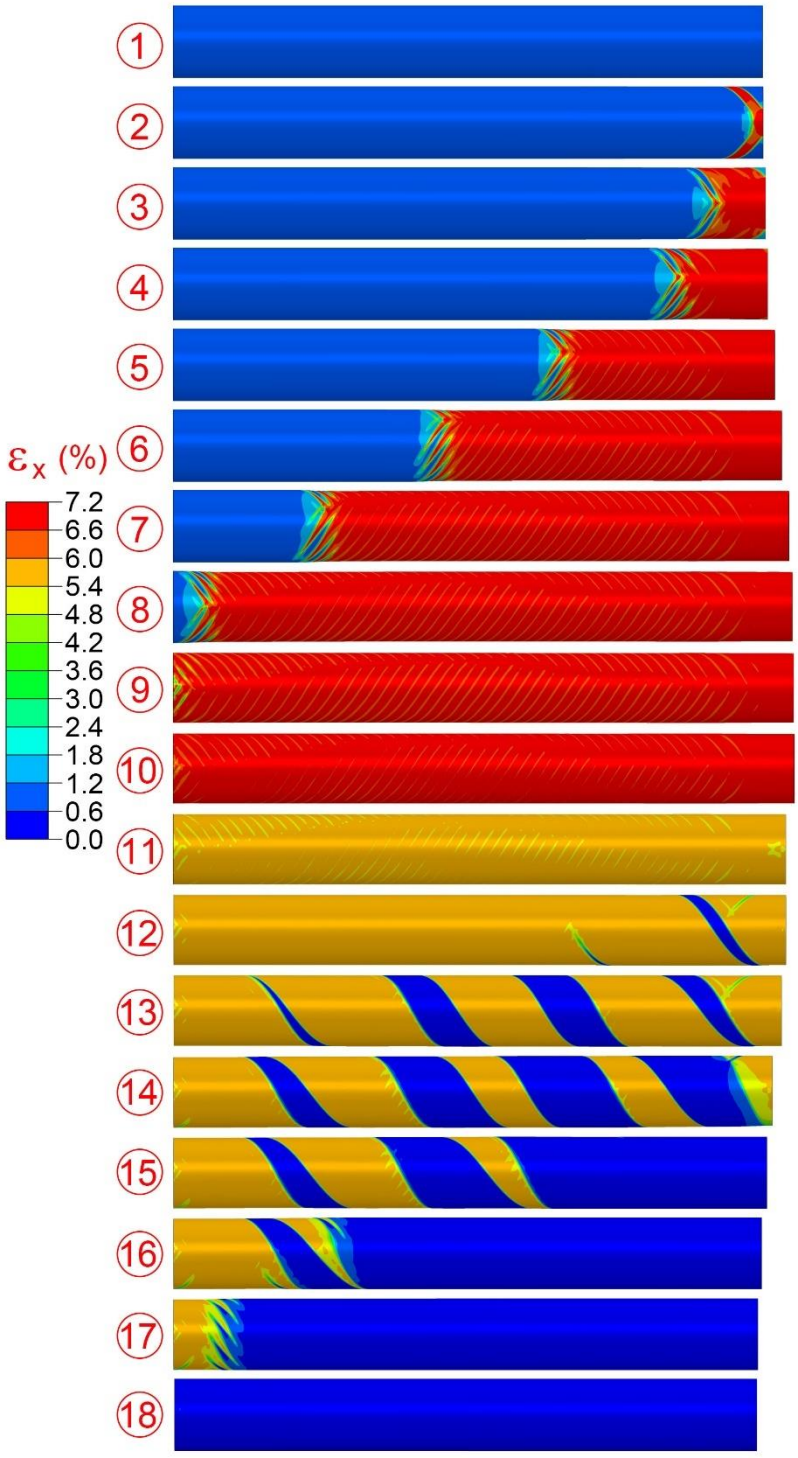

Fig. 5.14 Sequence of deformed configurations with axial strain contours superimposed (*x*-*y* plane) calculated using the mesh $N_t = 3$.

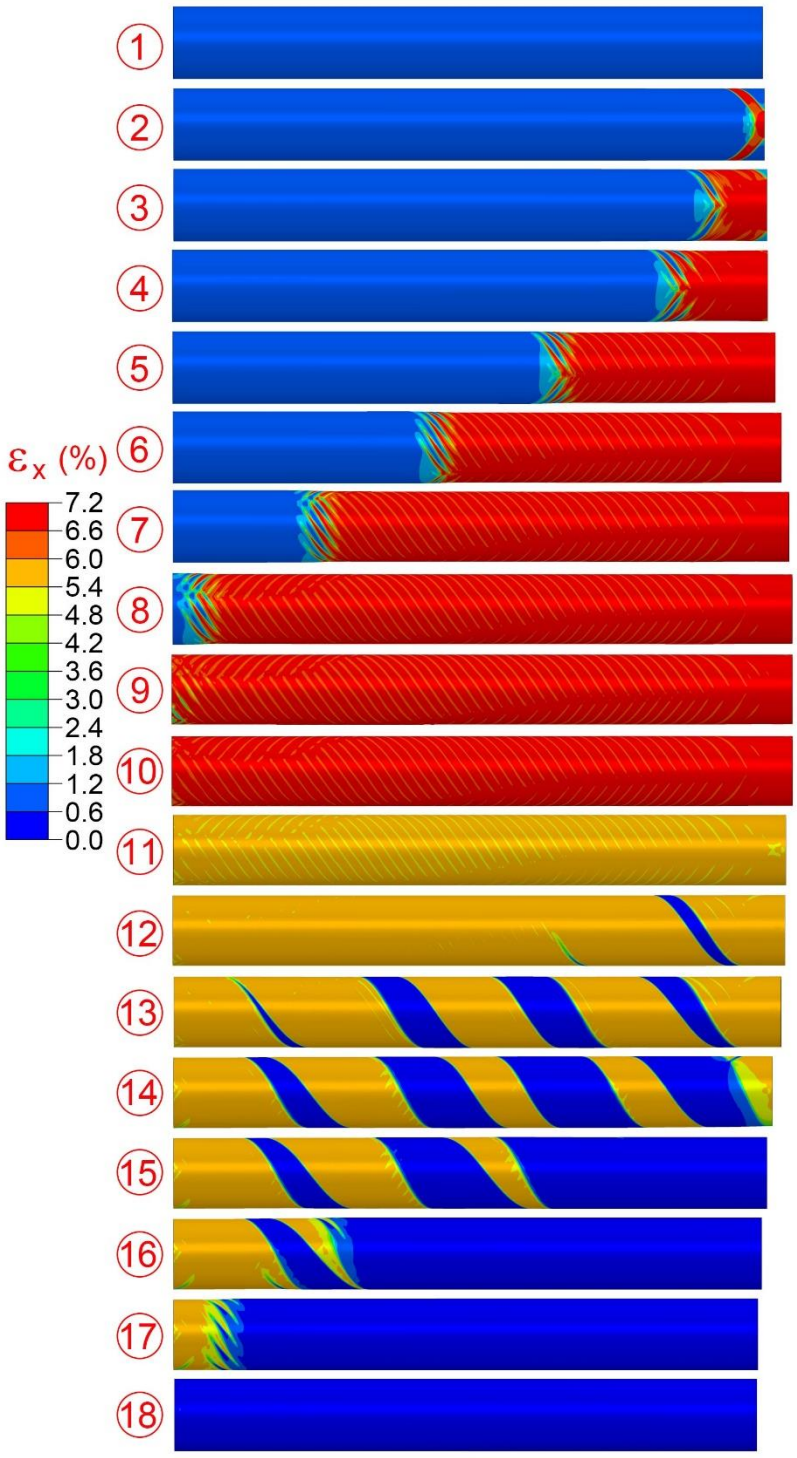

Fig. 5.15 Sequence of deformed configurations with axial strain contours superimposed (x-y plane) calculated using the mesh $N_t = 4$.

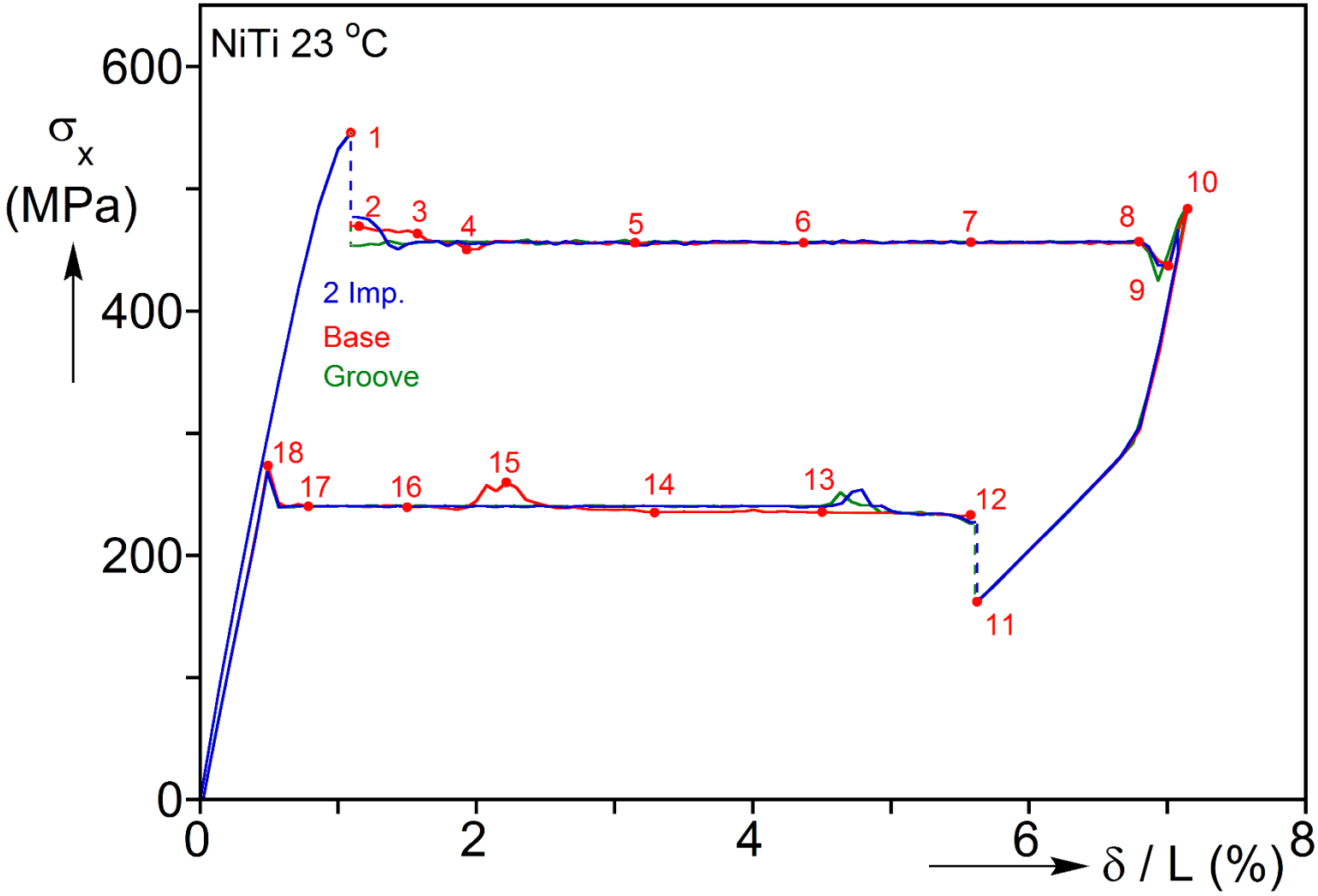

Fig. 5.16 Axial stress-elongation responses calculated using the three types of imperfections.

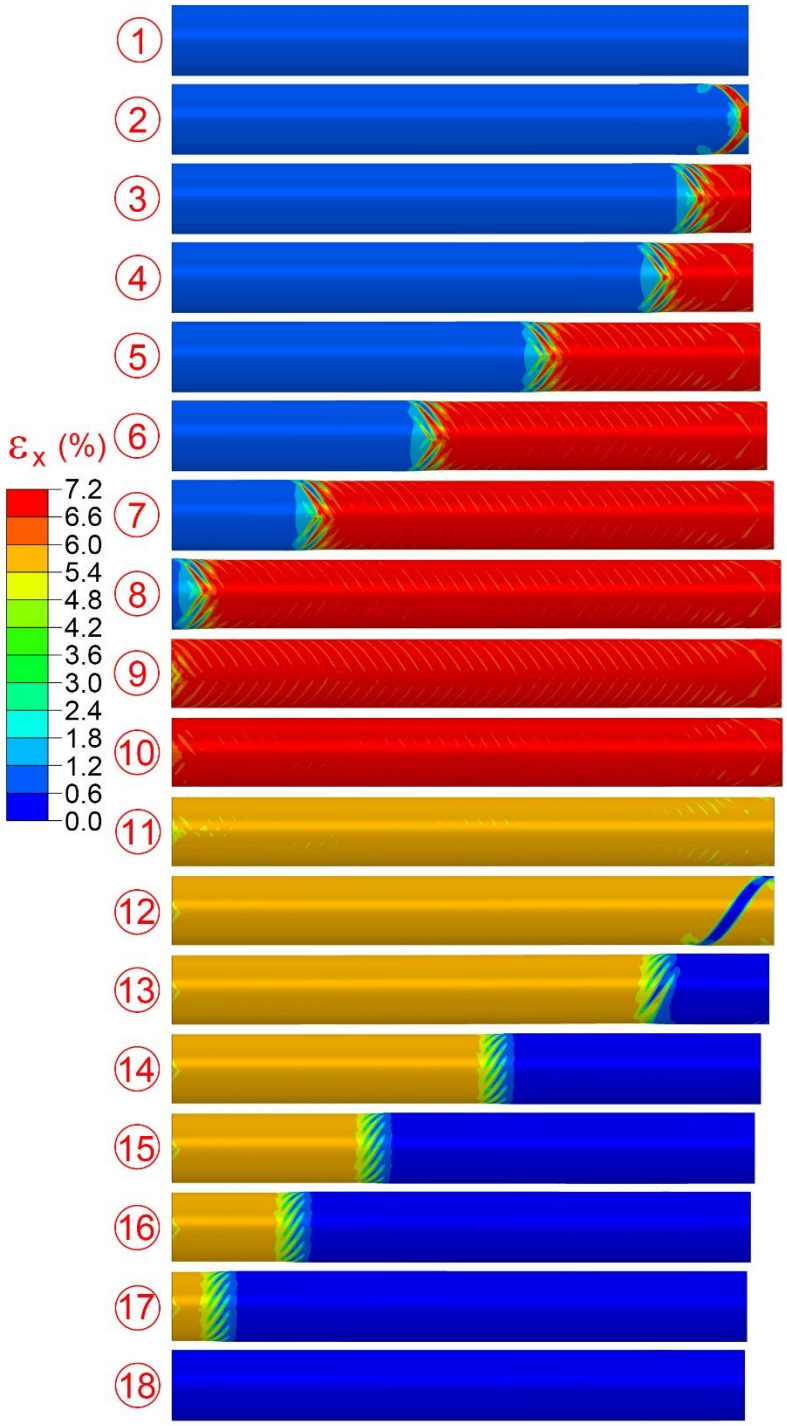

Fig. 5.17 Sequence of calculated deformed configurations with axial strain contours superimposed using the FE model with an additional identical thickness imperfection on the diametrically opposite side to the one in Fig. 5.4.

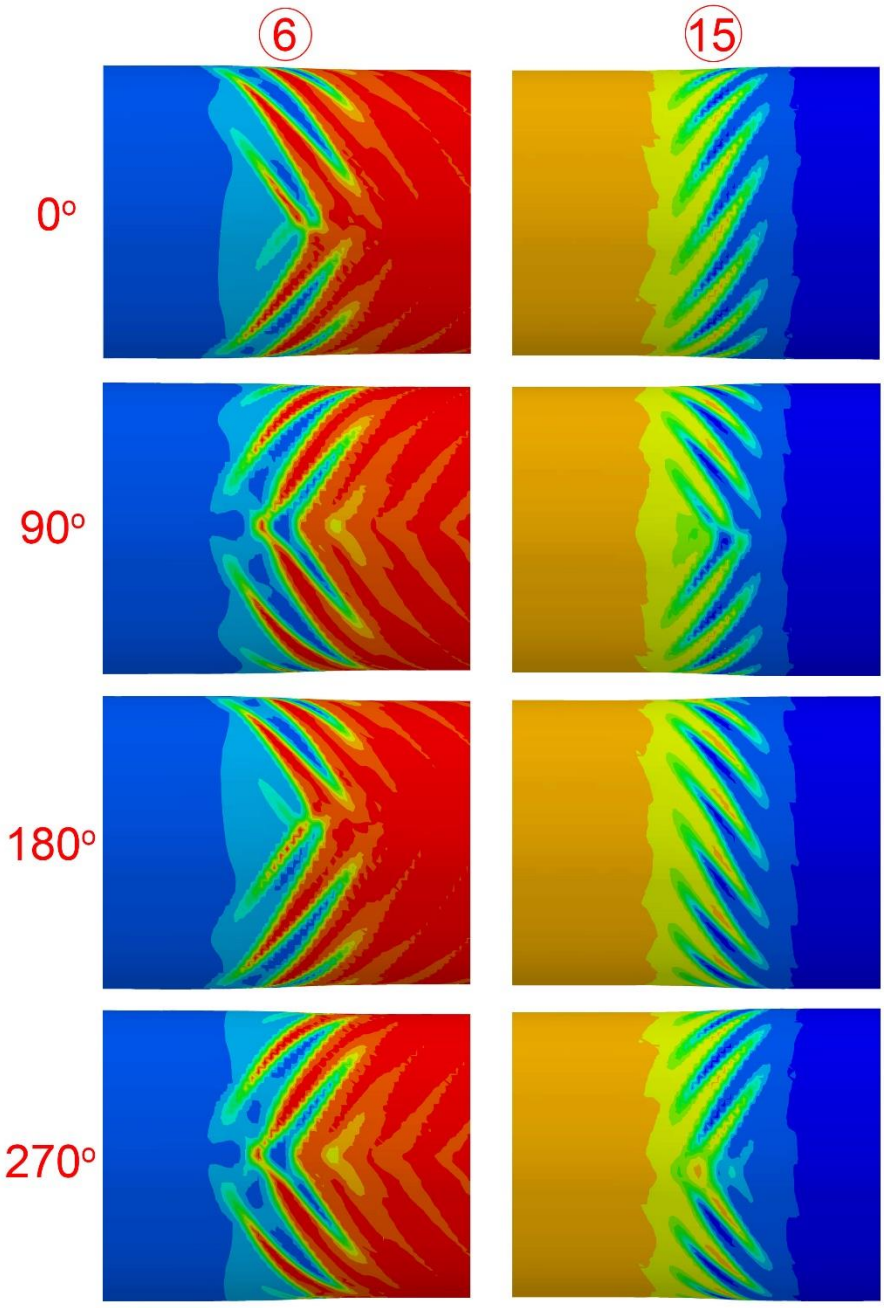

Fig. 5.18 Expanded views of the propagating front in images ⑥ and ⑮ in Fig. 5.16.

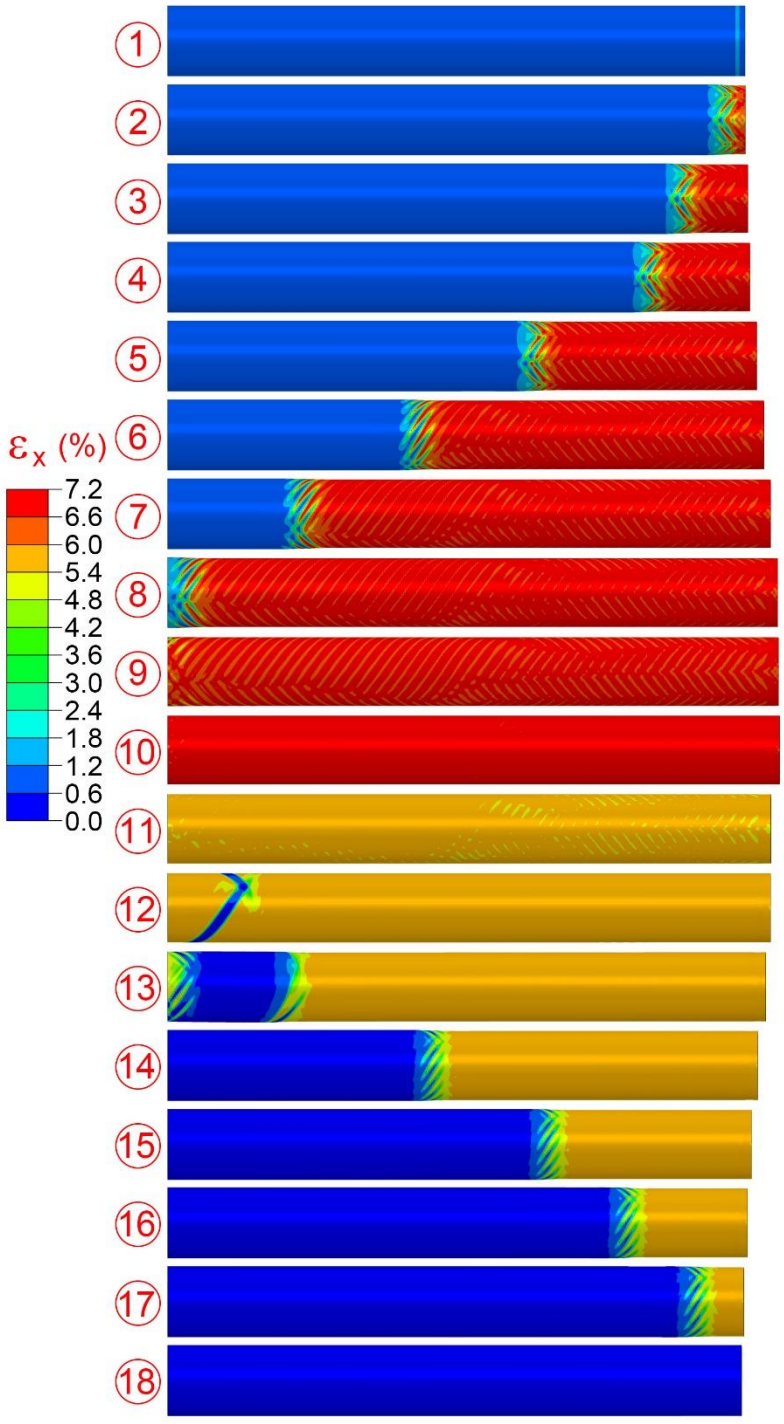

Fig. 5.19 Sequence of calculated deformed configurations with axial strain contours superimposed using the FE model with an axisymmetric groove thickness imperfection at the same location with the local imperfection in Fig. 5.4.

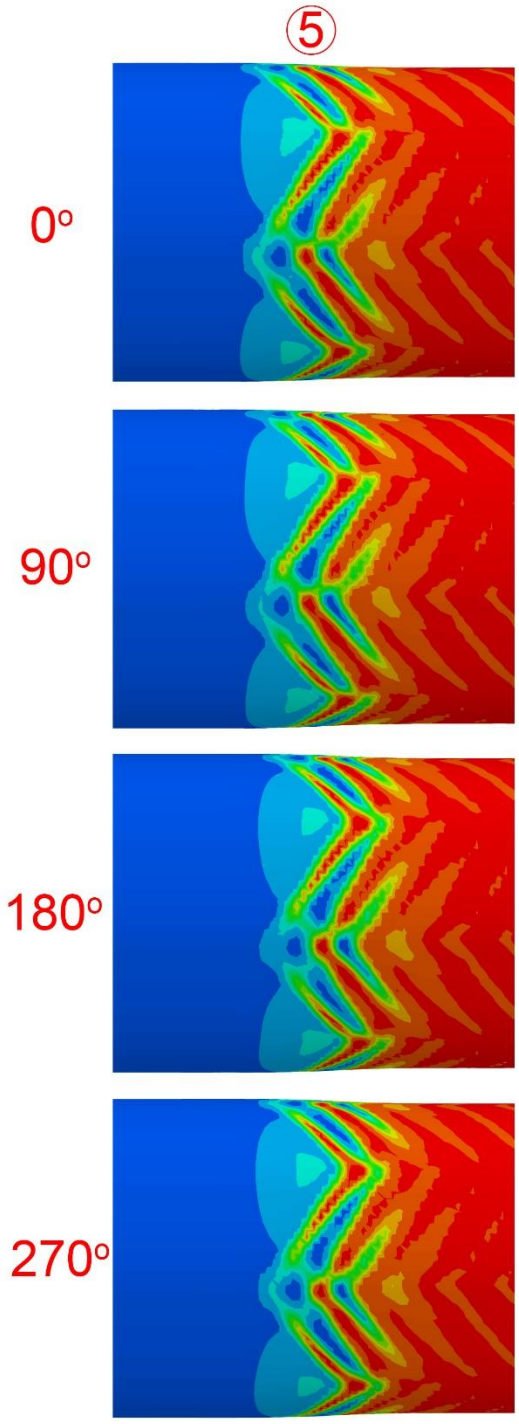

Fig. 5.20 Expanded views of the propagating front in images ⑤ in Fig. 5.19.

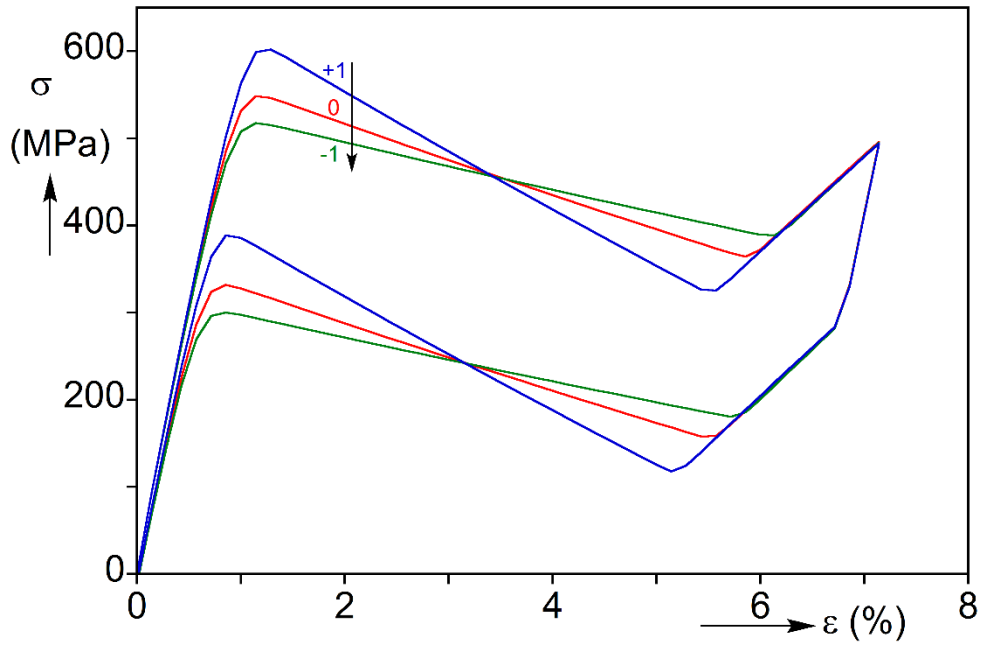

(a)

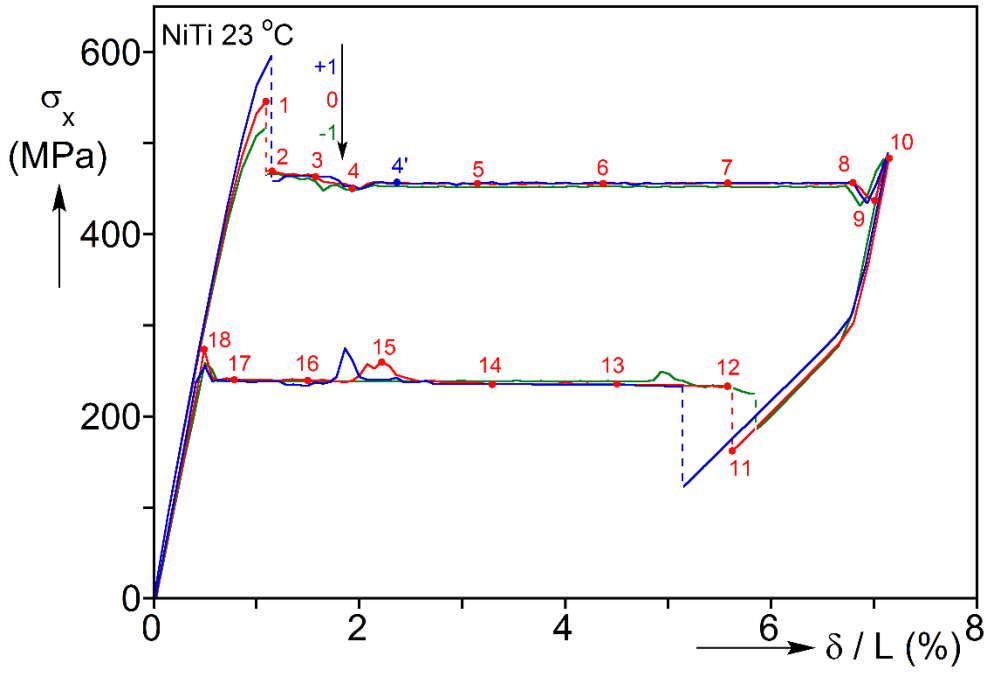

(b)

Fig. 5.21 (a) Tensile stress-strain responses with different softening slopes ("0" corresponds to the values in the base case simulation-Fig. 5.3a). (b) Axial stress-elongation responses calculated using the three different sets of softening slopes

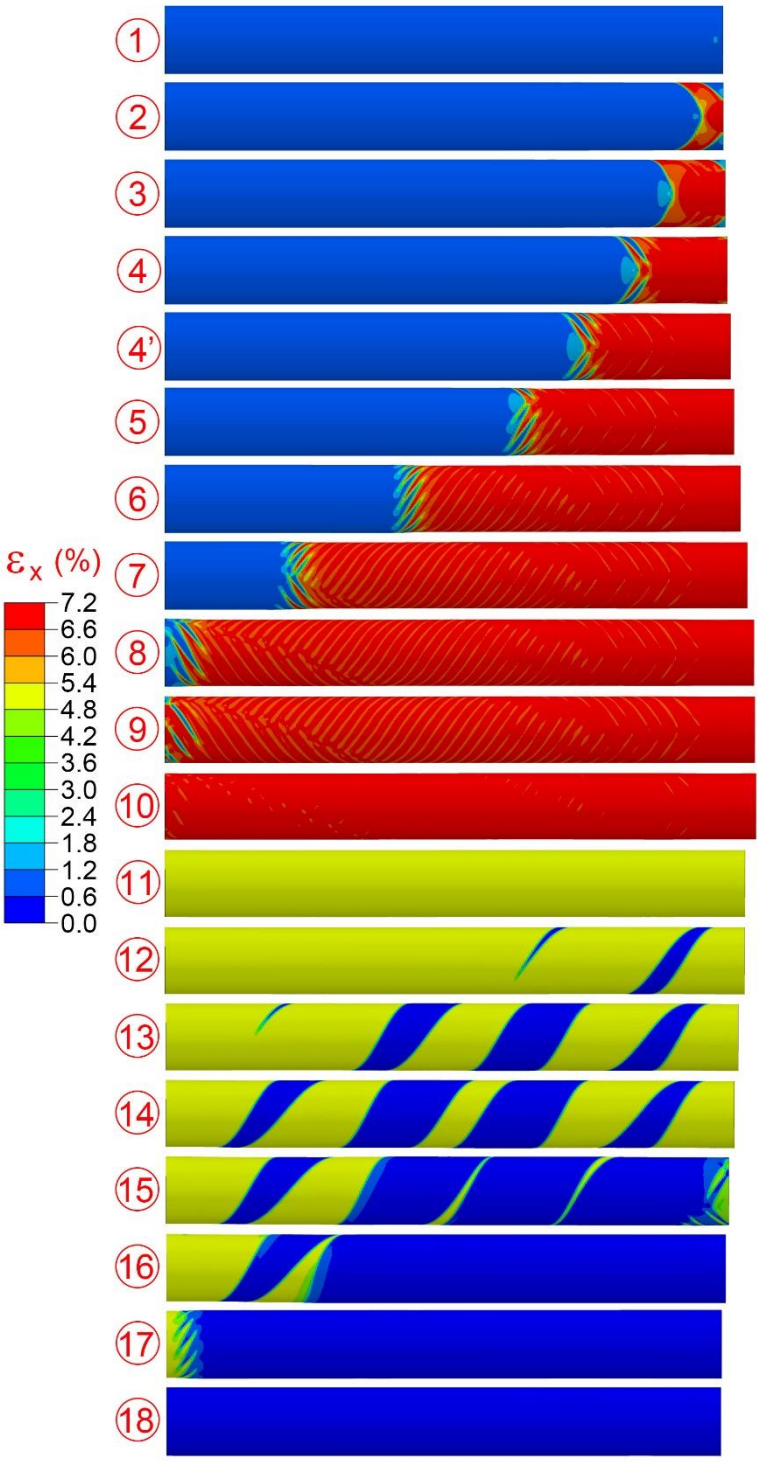

Fig. 5.22 Sequence of calculated deformed configurations using the +1 softening slopes in Fig. 5.21a, correspond to the stress-elongation response in Fig. 5.21b.

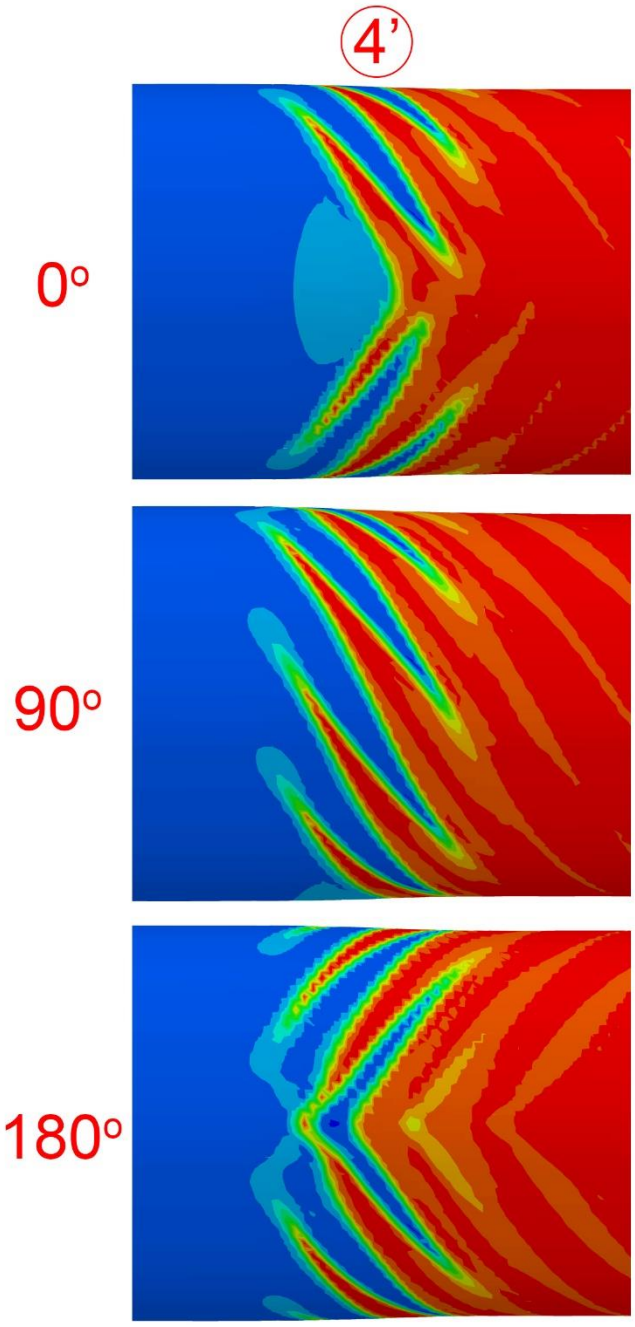

Fig. 5.23 Expanded views of the propagating front using the +1 softening slopes in image ④ in Fig. 5.22.

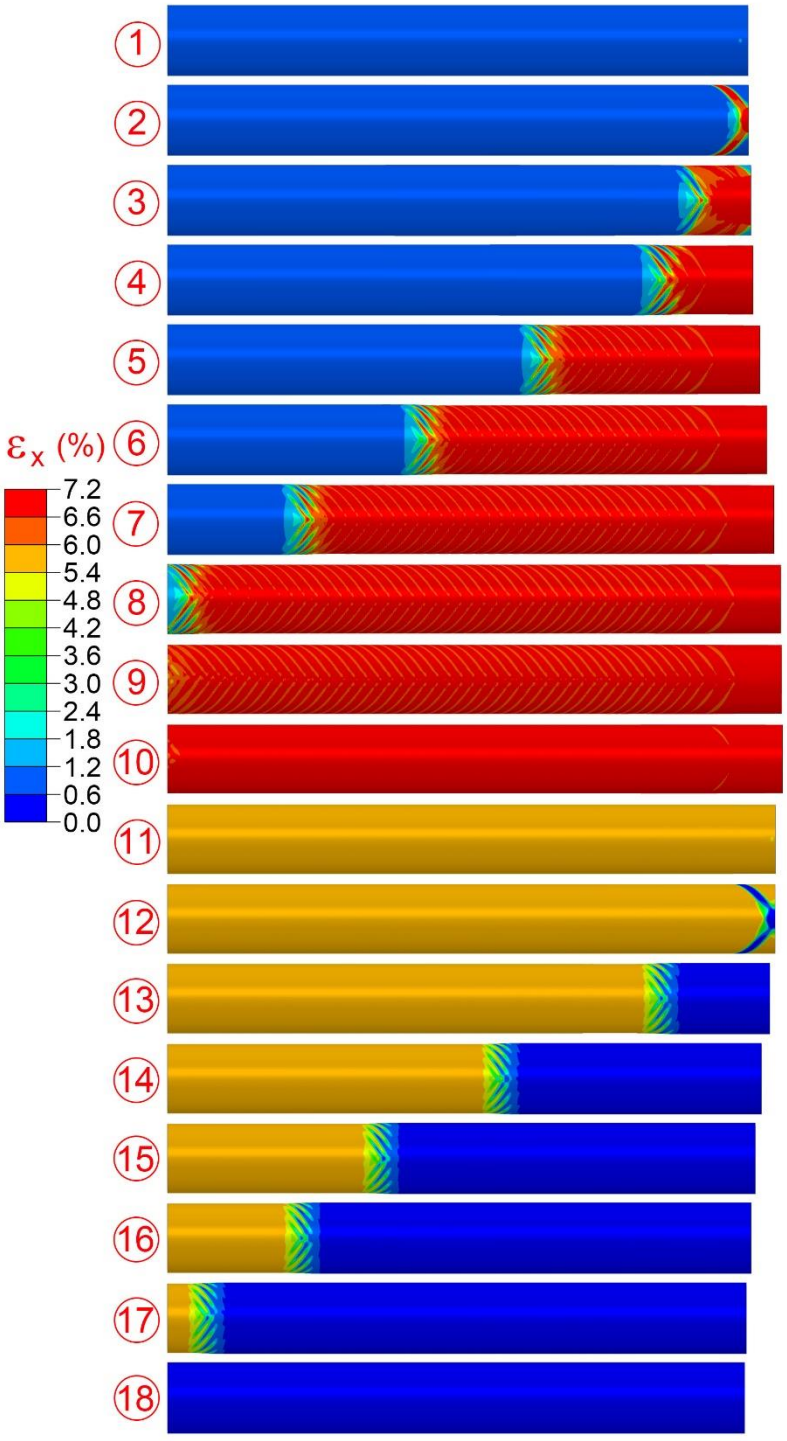

Fig. 5.24 Sequence of calculated deformed configurations using the -1 softening slopes in Fig. 5.21a, correspond to the stress-elongation response in Fig. 5.21b.

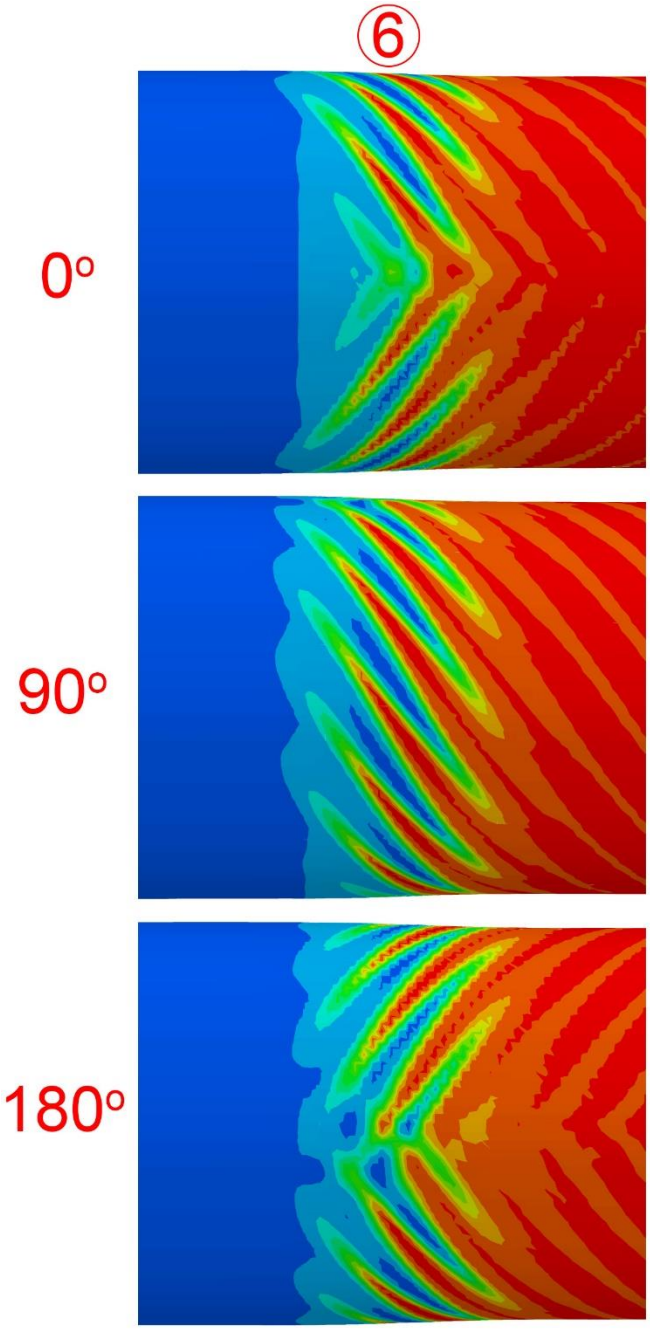

Fig. 5.25 Expanded views of the propagating front using the -1 softening slopes in image ⑥ in Fig. 5.24.

Chapter 6: PURE BENDING OF NiTi TUBES

6.1 INTRODUCTION

In previous chapters, the constitutive model framework was used to numerically simulate the nonlinear response of NiTi structures under either primarily compressive (Chapter 3) or primarily tensile (Chapters 4 and 5) states. This chapter presents the results of a study on the pure bending of NiTi tubes, in which the structure undergoes tension and compression simultaneously. Figure 1.3 shows the uniaxial tensile and compressive responses of the NiTi tubes used in the bending experiments. Both responses trace closed hysteretic characteristic of pseudoelastic NiTi behavior but also exhibit significant tension/compression asymmetry that includes stable compressive hysteresis and a tensile one with an upper and a lower stress plateaus and associated inhomogeneous deformations.

In the bending experiments on NiTi tubes of Bechle and Kyriakides [2014], it was demonstrated that this asymmetric material behavior plays a significant role in the complex bending response observed. It is thus expected that to correctly reproduce this behavior the constitutive model must be capable of capturing the asymmetric behavior of the material. These demands require the use of the most complete version of the constitutive model presented in Chapter 2.

In this chapter, select results of bending experiments on NiTi from Bechle and Kyriakides [2014] and tubes are first outlined. This is followed by the calibration of the constitutive model and the description of the finite element model used to simulate the experiments. Results from FE simulations are then presented and analyzed in detail and the chapter finishes with results from a sensitivity study of the solution.

6.2 EXPERIMENT

Bechle and Kyriakides [2014] used a miniature pure bending device to conduct a series of bending experiments on NiTi tubes with a diameter of about 5.1 mm and a wall thickness of 0.625 mm (see Section 3 of reference). The tubular stock was nearly equiatomic NiTi with A_s = -15 ºC and A_f = 21 ºC, supplied by Memry. Figure 6.1 shows the normalized moment-end rotation response $(M / M_o - \bar{\theta} / L\kappa_o)$ recorded in an isothermal bending experiment at 23 ºC. The normalizing parameters are as follows: $M_o = \sigma_{PM} D_o^2 t$, $\kappa_o = 2\varepsilon_o / D$, $D_o = D - t$, where σ_{PM} is the average stress of the upper plateau in tension, and ε_o is the strain at the onset of martensite transformation in the same response. The main parameters of the tube tested are listed in Table 6.1.

Table 6.1 Main parameters of the tube used in the bending experiments

T ºC	D mm	t mm	$2L$ mm	σ_{PM} MPa	ε_o %
23	5.11	0.625	76.7	381	0.827

Figure 6.2 shows sets of full-field images of the deforming tube during loading (① -⑩) and unloading (⑪-⑳). Initially, the material is in the *A* phase, the response is stiff, and the tube bends with a uniform curvature (image ①). When the bending stress reaches the transformation stress martensite nucleates (②), the moment starts to trace a ragged plateau that hovers at about $1.2M_o$ while the curvature localizes on the left as seen in images ③-⑤. Two curvatures start to co-exist; most of the tube is bent to a curvature that approximately corresponds to that at the beginning of the moment plateau $(\sim 1.5\kappa_o)$, while the transformed zone is bent to a significantly larger curvature $(\sim 7\kappa_o)$ (see also plots of tube slope distributions along the length in Fig. 17 of Bechle and Kyriakides [2014]). In images ④ and ⑤, the high curvature spreads towards the center of the specimen, and in image ⑥ a second zone of high curvature develops on the right. In images ⑦ and ⑧ the two high curvature zones propagate inwards until the whole length

has been so deformed in ⑨. Most of the material at the upper and lower sides has now transformed to martensite and the moment takes an upswing.

The specimen unloads with gradually decreasing stiffness and uniform curvature (images ⑪-⑬). In the neighborhood of image ⑭, the stiffness is down to very low values an indication that transformation back to austenite has commenced. Austenite nucleates in the middle of the specimen and results in a lower local curvature that can be seen in image ⑮. Continued unloading causes outward spreading of the lower curvature zone as illustrated in images ⑯ and ⑰ with the smaller curvature being at about $1.29\kappa_o$ and the larger at $5.2\kappa_o$. As this takes place, the moment stays at about $0.59M_o$. By image ⑳ the specimen unloads with uniform curvature eventually producing a fully closed hysteresis. (For a more complete expose of the events during this bending experiments see the movie in Appendix C of Bechle and Kyriakides [2014].)

Shattering of a fine oxide layer left on the tubes by the processing indicated that transformation resulted in the formation of diamond shaped deformation patterns on the tensioned side of the high-curvature zones (see Fig. 13 of Bechle and Kyriakides [2014] and Nacker [2009]). The evolution of such patterns was later captured in similar bending experiments using digital image correlation (DIC). Figure 6.3 shows a sequence of deformed images from such a bending experiment where images ①-⑧ are from loading and ⑨-⑯ from unloading (from Jiang et al., 2017b). Localization starts again on the left with the appearance of a diamond shaped pattern of high strain. As the high curvature spreads to the right, additional diamonds form progressively next to it. Between images ③ and ④ a second transformation front initiates on the right end of the specimen causing again localization in curvature and diamond patterns. In images ⑤ and ⑥, the high curvature propagates inwards leaving an untransformed low curvature section in the middle of the specimen. The middle section is then transformed by the propagation of the

high curvature from both sides until in image ⑧ the whole specimen has been consumed by the high curvature and localized deformation patterns covering the whole extrado. By contrast, the compressed side appears nearly uniformly deformed (similar patterns have been reported in Reedlunn et al. [2014]).

Unloading leads to the gradual erasure of the diamond patterns, starting in the middle of the bent specimen and the right end (images ⑩ and ⑪). In other words, in this case the transformation back to austenite does not follow the reverse order of the forward transformation. Subsequent to image ⑫, the erasure of the patterns is rather irregular. In image ⑯ two small islands of high deformation remain and the specimen has essentially returned to uniform curvature.

6.3 Constitutive Model Calibration

The constitutive model uses the framework outlined in Chapter 2 (see also Jiang et al. [2016b] and Jiang and Landis [2016]). Here we list the key points of its custom calibration to the needs of the tube bending problem using the material properties of the tubes used in the bending experiments.

a. The elastic modulus, E, and Poisson's ratio, ν, of both phases are assigned the constant values listed in Table 6.2 (the small difference between the tensile and compressive moduli reported in Bechle and Kyriakides [2014], and those between the moduli of A and M are neglected).
b. The sizes of the transformation surfaces in compression, σ_{oc}, and tension, σ_{ot}, are determined from the widths of the corresponding hystereses in Fig. 1.3 and are given in Table 6.2.

c. The function ψ_c^t in Eq. (2.27) is chosen for an optimal fitting of the shape of the compressive response in Fig. 1.3 using the following expression:

$$\frac{d\psi_c^t}{d\varepsilon_e^t} = h_0\varepsilon_e^t + (h_1 - h_0)\left[\varepsilon_e^t - \frac{1}{b}(1 - e^{-b\varepsilon_e^t})\right]$$
$$+ (h_2 - h_1)\begin{cases} 0 & 0 \le \varepsilon_e^t \le \varepsilon_1 \\ (\varepsilon_2 - \varepsilon_1)(\zeta^3/4 + \zeta^2/8), & \varepsilon_1 \le \varepsilon_e^t \le \varepsilon_2 \\ 3(\varepsilon_2 - \varepsilon_1)/8 + (\varepsilon_e^t - \varepsilon_2) & \varepsilon_2 \le \varepsilon_e^t \end{cases} \qquad (6.1)$$
$$\text{with} \quad \zeta = (\varepsilon_e^t - \varepsilon_1)/(\varepsilon_2 - \varepsilon_1)$$

where $\{b, h_0, h_1, h_2, \varepsilon_1, \varepsilon_2\}$ are fitting parameters listed in Table 6.2. The resultant back stress-transformation strain responses are plotted in Fig. 6.4a and the complete fit of the hysteretic stress-strain responses are compared to the experimental one in Fig. 6.4b. The agreement between measured and fitted results is quite good. As mentioned in Chapter 2, the tensile potential y_t^t should be as close to the compressive one y_c^t as possible to avoid potential numerical difficulties in FE simulations.

d. The unstable behavior in tension is modeled by adopting an up-down-up stress-strain response in the spirit of Ericksen [1975] and Abeyaratne and Knowles [2006] and previous work on Lüders banding. The construction of the up-down-up response is based on the measured hysteresis in Fig. 1.3 and is generated using expression (6.1). The softening modulus associated with the $A \rightarrow M$ transformation is assigned the value extracted from the sandwich experiment on NiTi strips reported in Hallai and Kyriakides [2013] (governed by h_1). The $M \rightarrow A$ transformation was assumed to have the same softening modulus as the forward transformation. The two negative slopes are placed at stress levels that bring the corresponding Maxwell stresses close to those of the two stress plateaus. The two negative slopes are connected to the stable

branches smoothly by appropriate choices of the fitting parameters (Table 6.2). For simplicity, the elastic modulus of martensite is assumed to be the same as that of austenite. Consequently, the initial unloading slope of martensite is seen in Fig. 6.4b to be higher than that of the experiment. Furthermore, the connection to the lower softening branch is similar to the transition from softening to hardening in the forward transformation. The resultant back stress-transformation strain response is seen in Fig. 6.4a to exhibit the expected up-down-up trajectory. The complete stress-strain response is compared to the experimental hysteresis in Fig. 6.4b. The stable branches follow the corresponding measured ones well while the two negative branches are parallel.

f. For numerical expedience, the change in size of the transformation surface σ_o between compression and tension is smoothened by making the transition a function of J'_3 as follows:

$$\sigma_o = \begin{cases} \sigma_{oc} & \eta < 0 \\ \sigma_{oc} + (\sigma_{ot} - \sigma_{oc})(10\eta^3 - 15\eta^4 + 6\eta^5), & 0 \le \eta \le 1 \\ \sigma_{oc} & 1 < \eta \end{cases} \tag{6.2}$$

with $\eta = (J'_3 + 0.01) / 0.0098$.

g. The constant a in the function f in Eq. (2.23b) is assigned the value of 0.9808, which leads to $f(1) = 0.578$.

Table 6.2 Model parameters for tensile and compressive responses

Model	E GPa	n	s_o MPa	b	h_o GPa	h_1 GPa	h_2 GPa	e_1 (%)	e_2 (%)
Comp.	66.3	0.425	120.7	2500	1179	2.775	117.9	2.8	3.4
Tens.	66.3	0.425	110.3	2500	1706	-12.34	91.96	2.8	3.4

6.4 STRUCTURAL MODEL

As in Hallai and Kyriakides [2011b] and preceding publications on bending of tubes, rather than simulating the present pure bending experiment exactly, we adopt the somewhat idealized domain shown in Fig. 6.5. We consider a section of tube of diameter D, wall thickness t and length $2L$ under pure bending where the variables correspond to those of the tubes used in the experiments listed in Table 6.1. We assume symmetry about the mid-span, the $y-z$ plane, and about the plane of bending x-z; therefore, consideration of only one-quarter of the tube suffices. In the experiments, the ends of the tubes were inserted into larger diameter tight fitting thick-walled tubes that engaged the four bearings through which the end couples were applied (see Fig. 9 in Bechle and Kyriakides, 2014). This arrangement resulted in stress concentrations at the ends of the NiTi tubes that were sufficient to initiate phase transformation at the ends. In the present idealized setting, in order to have a consistent evolution of events, geometric imperfections in the form of two small thickness reductions are introduced at the x-z plane of symmetry a distance D from the mid-span as shown in the inset in Fig. 6.5. In most cases presented, the thickness is reduced by $0.05t$, on diametrically opposite sides of the tube, over an area of $t \times t$ with $t/2$ transition zones all around.

Anticipating again the need to accommodate inhomogeneous deformations with jumps in strain on the order of 6-8%, the structure is discretized with incompatible elements C3D8I within the ABAQUS finite element package (e.g., see Aguirre *et al.* [2004], Hallai and Kyriakides [2011b, 2013], Liu et al. [2015] for bending, Shaw and Kyriakides [1998], Kyriakides and Miller [2000], Jiang et al. [2016c] for tension). These are linear elements enhanced to allow the deformation gradient inside the element to vary while the displacement field maintains continuity (see Wilson et al. [1973], Ortiz et al. [1987], Nacar et al. [1989], Simo and Armero [1992]).

A uniform mesh with cubical elements is adopted to reduce any directional bias. The mesh used in the model that generates the main results presented in the following section has 4 elements through the thickness, 52 along the half circumference and 250 along the half length for a total of 52000 elements.

Following our previous works on bending, the tube is bent by prescribing the angle of rotation at $x = L$ (q_L). This end is constrained to remain plane while the cross section is free to deform by imposing the following multi-point constraint:

$$\tan q_L = \frac{x_{ref} - x_i}{z_{ref} - z_i}, \tag{6.3}$$

where (x_i, z_i) are the coordinates of the ith node in this plane and (x_{ref}, z_{ref}) are those of a reference node (e.g., the bottom node). The moment is calculated at the plane of symmetry $(x = 0)$ from:

$$M = 2\sum_{i=1}^{N} z_i F_i, \tag{6.4}$$

where F_i is the axial force acting on the ith node of the cross section and z_i is its distance from the axis of the tube.

6.5 Numerical Results

6.5.1 Simulation of a NiTi Tube Bending Experiment

The bending experiment in Bechle and Kyriakides [2014] is simulated using the FE model mesh and imperfection parameters outlined in Section 6.4 and the constitutive model as calibrated in Section 6.3. Figure 6.6 shows the calculated moment-end rotation $(M / M_o - q_L / Lk_o)$ response together with the experimental one (Fig. 11 in Ref.) and the same normalizing variables as those used in the experiment in Section 6.2. Figure 6.7 shows a sequence of 20 deformed configurations of the quarter of the tube analyzed

corresponding to the numbered bullets marked on the response. The superimposed color contours correspond to the axial strain. The loading branch of the calculated $\overline{M} - \bar{\theta}_L$ response is seen to follow the experimental one quite well; i.e., the slope of the initial linear stiff branch is reproduced, the moment knee that represents the onset of transformation is captured, and the level and extent of the moment plateau that follows agree with the measurements. (The calculated moment plateau extends somewhat further than in the experiment but at these higher curvatures the level of confidence in the experimental measurements is reduced.) As was the case in the experiment, bending induces localized deformation, one effect of which is localization of curvature. This effect is best illustrated in the plots of the local slope, $q(s)$, versus the natural measure of distance along generators, *s*, in Fig. 6.8 ($q(s)$ is the average of the slopes of the top and bottom generators). Figure 6.8a shows the slope along the length for the loading configurations in Fig. 6.7 and Fig. 6.8b for the unloading configurations.

Interestingly, neither the calculated nor the measured response exhibits the moment peak that usually accompanies the initiation of localization. Such initiation peaks were, for example, recorded in most moment-end rotation responses of tubes with Lüders bands reported in Hallai and Kyriakides [2011a, 2011b] (e.g., see Fig. 14 of 2011a and Fig. 3 of 2011b). Configuration ①, which precedes the moment knee, shows the model to be bending uniformly reflected by its constant slope in Fig. 6.8a. Localized deformation in the form of a pair of higher strain bands are seen in configuration ②, which is just past the moment knee. The bands initiated from the imperfection on the tensioned side of the tube and are approximately at $\pm 54^o$ to the axial direction, which is very close to the characteristics of Hill [1952]. Simultaneously, the compressed side remains essentially uniformly strained. Further bending, rather than causing a spreading of deformation from

these two bands, results in the progressive initiation of three additional X-shaped band pairs that can be seen in image ③.

6.5.2 Initiation of Localization Bands

Figures 6.9 and 6.10 show in more detail the progressive initiation of the four X-shaped localization bands. Figure 6.9 shows an expanded view of the part of the moment-end rotation response that includes the neighborhood of points ①, ②, and ③. Figure 6.10 shows a set of images of the tensioned side of the tube that correspond to the bullets identified by Latin letters on the expanded response. Here, half of the model tube has been assembled for clarity and is viewed down from the top. The first X-shaped bands initiate from the site of the imperfection just prior to image **a**. Their initiation is accompanied by a small drop in the moment. Despite the bands being initially rather "weak", the localization penetrates the thickness of the tube, as is required for compatibility. In image **b**, the bands have broadened, lengthened and the intensity of the strain has increased. In image **c**, they are fully developed reaching strain levels of about 6.8% on their centerlines and covering approximately an angular span of about 120°. In the process the moment recovers somewhat, and this enables the initiation of a second similar band a distance 1.77D further down the length, as shown in image **d**. Once more, the initiation of the bands is accompanied by a small drop in the moment. In images **e** and **f** these bands in turn broaden and strengthen. The moment has again recovered somewhat, and soon after image **f** the third pair of bands initiate at a site 2.24D down the length as shown in image **g**. The pattern of band strengthening and broadening repeats and image **h** shows the initiation of the fourth band a distance 1.60D from the third accompanied, once more, with a similar small drop in moment. The four pairs of bands are reflected as small disturbances in the otherwise nearly linear slope for configuration

③ in Fig. 6.8a. These will remain in the slope plots until they are erased by the formation of the diamond deformation patterns, discussion of which follows.

Past experience with propagating instabilities has taught that localization at multiple sites before the instability starts spreading is highly unusual. So we investigated if the location, amplitude, and type of imperfection used to trigger the localization played any role in this behavior (e.g., see Section 6.6.4). Furthermore, any influence from the mesh density and the loading increments was also examined (see Section 6.6.1). The multiple nucleations were found to persist for all variations and combinations of the parameters considered, but the location of the nucleation sites was found to vary. This and their rather random spacing indicate that the locations of the nucleation sites are governed more by numerical noise rather than any physical problem variable.

Since the absence of an initiation moment peak and the persistence of multiple initiation peaks were also observed in the SMA tube bending experiments, it appears that the moment plateau caused by the onset of transformation represents a critical state for the structure. This facilitates the initiation of localization at multiple sites rather than the expected propagation of the instability. It appears that the stable material behavior on the compressed side, and the higher transformation stress in compression play a stabilizing role that results in this behavior.

6.5.3 Propagation of Localization

Soon after point ③ the moment increases somewhat enabling deformation on the tensioned side of the tube to start localizing in a more systematic manner. Additional inclined bands of higher strain initiate from the site of the first X-shaped localization propagating progressively first towards the $x = 0$ plane of symmetry with the moment dropping slightly as this takes place. By point ④, the bands have coalesced into the first

diamond shaped pattern that can be seen in the corresponding image in Fig. 6.7. The strain inside the diamond is nearly uniform at about 6.8% whereas the strain on the compressed side is smaller and only mildly nonlinear across the depth. This concentration of high tensile strain on the top results in a local increase in curvature in the tube that is clearly reflected in the change in slope $q(s)$ for ④ in Fig. 6.8a, while the slope in the rest of the tube remains essentially unchanged.

An additional effect of the diamond deformation pattern is that the tube undergoes a local change in shape with the top and bottom thirds of the circumference flattening somewhat as shown in Fig. 6.11. This causes a change in the diameter in the plane of bending, DD/D, that is plotted for each configuration against the natural coordinate s in Fig. 6.12. (This cross sectional deformation is akin to bending induced ovalization reported for thinner-walled tubes with Lüders bands–Aguirre and Kyriakides [2004], Kyriakides et al. [2008], Hallai and Kyriakides [2011a, 2011b], Liu et al. [2015]–however, because of the relatively large thickness of the present tube, the cross sectional deformation is mainly in the form of flattening of the tensioned side with minimal change in diameter in the x-y plane.) Interestingly, the initiation of each of the four X-shaped localization patterns has introduced a small disturbance in $\Delta D/D$ that can be seen in image ③ in Fig. 6.12a. These will remain until the progressive formation of diamonds overwhelms them.

Once the first diamond shaped deformation pattern is fully developed, new X-shaped bands with a rightward orientation start emanating from the site of the first one. As the bands develop, the moment drops slightly but recovers as the formation of the second diamond pattern is completed as seen in image ⑤. The higher curvature regime now covers the tube section that encompasses both diamond patterns (Fig. 6.8a) and so does the cross sectional flattening (Fig. 6.12a).

Because of the proximity of the second X-shaped localization bands, formation of the third diamond involves left oriented bands that emanate from it and rightward oriented bands that initiate from the edge of the second diamond. The third diamond can be seen fully developed in image ⑥ by which point right looking bands are seen to emanate from its right edge that eventually form the fourth diamond. The progressive formation of diamonds continues with the fifth diamond being influenced by its proximity to the third initial X-shaped bands that is observed in image ⑦. Image ⑧ shows the sixth diamond being formed by bands that initiate from the right edge of the fifth. It becomes fully developed in image ⑨ together with the seventh diamond whose development was influenced by the proximity of the fourth pair of initial X-shaped bands.

The progressive propagation of higher strain patterns on the tensioned side is completed in image ⑩ with the formation of an eighth diamond. The corresponding slope plot indicates that the whole length of the tube has acquired the high curvature. The eight major moment undulations in the response in Fig. 6.6 correspond to the completion of a diamond–hill– and the initiation of a new one–valley. Figure 6.8 shows the high curvature regime covering more of the length of the beam with each additional configuration. At the same time, the near parallelity of the $q(s)$ trajectories corresponding to the relatively undeformed sections indicates that the local curvature remains constant until the section transforms. The average value of the larger curvature regime is $7.38k_o$ and the average value of the small curvature is $2.35k_o$. The $\Delta D/D - s$ plots show the propagation of cross sectional deformation from left to right that accompanies the patterned propagation of localization. The average value of $\Delta D/D$ is approximately 2% with each peak corresponding to the center of each diamond shaped deformation pattern.

The tube is bent somewhat further to point ⑪, which leads to an upswing in the moment and a uniform increase in curvature and in the change in diameter (see corresponding $q(s)$ and $DD/D(s)$ plots). Unloading takes place by incrementally decreasing q_L resulting in a nonlinear decrease in the moment (Fig. 6.6). The diamond deformation patterns retain their shape (image ⑫) until point ⑬ but they undergo some reduction in the local strain. Reverse "transformation" commences just before point ⑬ when part of the 8th diamond is erased causing a small undulation in the local moment. The moment achieves a local minimum at ⑬ when the erasure of the 7th diamond starts. Once this diamond is completely removed, just before image ⑭, the moment increases somewhat to a local peak. Further reduction in q_L results in the erasure of the remainder of diamond 8 with a second moment peak developing when this is completed. Diamond 5 is removed next (in progress in image ⑮) with the moment reaching another moment peak when it is completed. The moment drops slightly once more causing the gradual erasure of diamond 6 (in progress in image ⑯) and increases when this is completed. The next diamond erased is the one next to the $x = 0$ plane of symmetry accompanied by one more undulation in the moment (removed by image ⑰). This is followed by diamond 3 (image ⑱), diamond 2 (image ⑲), with diamond 4 being erased last (image ⑳). In other words, the removal of the diamond patterns does not follow the order in which they were generated during loading. The removal of each diamond is accompanied by a change in the local curvature and a reduction in the local cross sectional flattening. The local curvature reduces to $0.701\,k_o$ and the DD/D to nearly zero. The disorderly erasure of the diamonds is reflected in the unloading configuration slope trajectories in Fig. 6.8b and in the change in diameter plots in Fig. 6.12b. Beyond point ⑳ the beam unloads elastically to the undeformed configuration.

6.5.4 Formation of a Diamond Deformation Pattern

In this section, we examine the formation of the diamond deformation patterns in more detail by considering the formation of the second diamond from the $x = 0$ plane of symmetry in Fig. 6.7. A sequence of fourteen deformed configurations of the model have been extracted from the solution and are shown truncated in Fig. 6.13 with contours of axial strain superimposed. The corresponding moment-end rotation values are marked on the expanded section of the response in Fig. 6.14. In addition to the overall strain contours, the strains and stresses that develop across section A of the tube, identified in Fig. 6.13, have been plotted in Figs. 15/16 and for section B in Figs. 17/18.

In image 1 of Fig. 6.13, the formation of the first diamond next to the $x = 0$ plane of symmetry has been completed (configuration ④ in Fig. 6.7). Section A senses the presence of the right facing prong of the original X-shaped localization bands, and this is reflected in the waviness of the strain in the upper half. The lower half has a nearly linear strain distribution and smaller values of strain. In contrast, the strain profile at B is smoother than that at A. Observe that at both sections, because of the material asymmetry, the location of zero strain is significantly below the mid-surface. The tensile stress at A traces a wavy plateau, an indication that some localization has commenced. Transformation has begun on the compressed side also, but this side is free of any localization. The tensile stress at section B shows that transformation has also commenced here as the initial stress maximum in the response (Fig. 6.4) has been surpassed; but overall, the stress is smoother than at section A. The compressive stress distribution is similar to that at A. Both stress profiles demonstrate the strong tension/compression asymmetry.

In image 2 in Fig. 6.13, a second band initiates from the edge of the first diamond. This causes a sharp local increase in the tensile strain at A and a corresponding local drop

in the stress. The tensile strain and stress at B remain unaffected. In image 3, both bands broaden and lengthen and a second local increase in the tensile strain has developed at A while the stress develops a second dip. The compressive stress at A adjusts so that zero net axial force is satisfied for the section. The strain and stress profiles at B remain relatively unaffected.

In image 4 in Fig. 6.13, the two deformation prongs broaden and lengthen and a third one appears above the other two. Localization is sensed at the top of section A and a third dip has developed in the tensile stress. The top two bands have gotten closer to section B causing some undulations in the tensile strain and stress. In images 5 and 6, the three bands mainly broaden with limited growth in length. The top band is now closer to section B and this is reflected in a local increase in the tensile strain and some change in the local stress.

In images 7 and 8 the three bands mainly broaden. In fact their tips appear to be lining up along an alternate direction characteristic. The strain in the lower tension part of A grows further while the tensile stress appears to settle to an undulating plateau. The compressive strain has also gradually grown with each increase in q_L while the compressive stress experiences relatively small adjustments required for the overall equilibrium of the section. The tensile strain and stress at B is increasingly more affected by the top band.

In images 9 and 10 in Fig. 6.13, the three bands have broadened forming essentially a new triangular zone of high strain. The right edge of the triangle has moved to the right aligning its edge with an alternate characteristic. By image 11 the triangle is nearly isosceles and the apex is well below the mid-surface at about the same level as that of the first diamond. The upper part of the tensile strain at A has reached an undulating plateau that does not change after image 9 and the same is true for the stress. The top

part of section B is experiencing an increasingly higher local strain with corresponding undulations in the tensile stress. A new localization band initiates from the upper corner of the second diamond, which is seen to lengthen and strengthen in image 12. By image 13, it has joined with the second initial X-shaped localization pattern. In images 13 and 14 localization at section B is completed and the strain and stress profiles do not change any further. The new diamond has a length $\lambda = 0.93D$ and a depth $h = 0.56D$ (both values are somewhat smaller than the average values reported earlier).

Why Transformation Zones are Diamond Shaped?

A puzzling question is why the transformation-induced deformation is organized in adjacent diamonds. To answer this question, we idealize the deformed tube to consist of a periodic pattern of diamond-shaped zones of uniform strain on the tensioned side as shown in the schematic in Fig. 6.19. A characteristic section consists of a diamond shaped zone of length λ and depth h that has transformed to a uniform strain of e_t, the transformation strain in tension. The compressed side, drawn in blue color, is also transformed but the strain is nearly linearly varying across the depth. The complement of the tube section remains untransformed with a linearly varying strain across the depth.

Consider a fiber a distance z from the apex of the triangular high strain zone. The orange section of the fiber with a length of z/h is strained to e_t. The yellow complements of the fiber with total length of $(1-z/h)/$ have a strain of approximately $e_1 z/h_1$ (h_1 is the distance of the "neutral" axis from the top). Thus, the average strain of this fiber is approximately given by:

$$\bar{\varepsilon}(\zeta) \approx \left[\varepsilon_t \frac{\zeta}{h}\lambda + \varepsilon_1 \frac{\zeta}{h_1}\left(1-\frac{\zeta}{h}\right)\lambda\right] \Big/ \lambda = \frac{\zeta}{h}\left[\varepsilon_t + \varepsilon_1 \frac{h}{h_1}\left(1-\frac{\zeta}{h}\right)\right] \qquad (6.5)$$

Since the transformation in tension leads to a jump in strain of $(e_t - e_1)$, by limiting it to such diamond-shaped zones enables the tube to deform to uniform curvature that is

implied by the nearly linear average strain across the depth. The curvature of such a partially transformed section can be expected to be

$$\kappa_t \approx \varepsilon_t / h. \tag{6.6}$$

6.6 Parametric Studies

6.6.1 Mesh Sensitivity of the Solution

The softening introduced in the tensile stress-strain response implies some degree of mesh sensitivity of the solution. As in previous studies, our approach has been to choose a uniform mesh that is fine enough to reproduce the finer features of the localized deformation observed in the experiments. Once this is decided, the addition of mild rate dependence to the constitutive model can regularize the solution removing the sensitivity to the mesh (Needleman [1988]). The alternative approach is to introduce higher order gradients in the formulation with an intrinsic length scale. To date, this length parameter is chosen for best performance of the model—e.g., see He and Sun [2010], Duval et al. [2011] for SMA applications, Maziere et al. [2016] for Lüders banding. The phenomenological constitutive model adopted for pseudoelastic NiTi here is rate independent and, consequently, the mesh sensitivity of the tube pure bending solution presented in the previous section must be examined. We have thus simulated the experiment using two additional mesh densities in which the number of cubical shaped elements through the thickness, N_t, is 3 and 5. This respectively changes the number of elements around the circumference to 40 and 64 and to a total number of elements of 22,080 and 97,920.

The solutions from the two new meshes are very similar to the one depicted in Figs. 6.6 and 6.7 for N_t = 4 and so will be discussed here only in brief. Figure 6.20 compares the three moment-end rotation responses where they are seen to be essentially

identical for loading. The lower plateaus are similar but with some differences in the positions of the moment undulations. The deformed configurations corresponding to the numbered bullets on the response for N_t of 3 and 5 appear in Figs. 6.21 and 6.22. Overall, the number and geometry of the diamond patterns formed are essentially identical in the three solutions. The sequence of diamond formation is the same for loading, but the order in which they are erased during unloading is somewhat different. This difference is also responsible for the observed difference in the rotation position of the moment undulations on the unloading plateau. We remind the reader that reverse transformation tends to localize at sites with lower stress. The mesh can introduce small differences in the stress distribution along the length resulting in the observed difference in the order of erasure of the diamonds.

As was the case in previous studies in which partially unstable constitutive models were adopted (e.g., Shaw and Kyriakides [1998], Kyriakides and Miller [2000], Jiang et al. [2016c]), the main effect of the size of the mesh is observed in the size of the transition zone separating the highly deformed and the relatively undeformed zones. This affects most prominently the finger like bands and the edges of the diamond patterns. This effect is illustrated in Fig. 6.23a, which presents expanded views of the LHS end of configuration ④ containing the first diamond formed. The transition zones in each solution are observed to occupy approximately two elements and, consequently, these zones become narrower as the mesh size decreases. This effect is examined in more detail in Fig. 6.23b in which the axial strain along the section of the deformed generator drawn in yellow in the three configurations is plotted along the length. The strain gradients along this line are seen to become somewhat sharper as N_t increases. However, the width of this transition zone does not affect the other features of the solution when the mesh is fine enough to capture the main features of localized deformation.

6.6.2 Symmetric Material Model

As pointed out in the introduction, the localized deformation associated with Lüders banding is macroscopically similar to localized deformation exhibited by pseudoelastic NiTi in tension being considered here (e.g., Hallai and Kyriakides, 2013). Indeed, this macroscopic similarity in material behavior leads to localization and subsequent propagation of curvature in both steel and NiTi tubes under bending, at least during loading. At the same time, the present results point to significant differences between the two sets of moment-rotation responses. The most obvious difference is the reversibility of stress-induced phase transformations in NiTi that results in full recovery of bending deformations on unloading. Other differences include the tension/compression asymmetry of NiTi vs. the symmetric behavior of Lüders banding, and the significantly larger transformation strain of NiTi in tension (~7%) than the Lüders strain (typically 2-3%). These differences in the material behavior lead to some disparities in the tube bending behavior mentioned in Section 6.5.

In order to assess the effect of the tension/compression asymmetry on these differences, we use the same tube geometry and FE model to evaluate the bending response of a tube that has the same unstable material response in tension and compression. In other words, the distinction between tension and compression is removed, the weight function $\xi = 0$ in Eq. (2.22), and the back stress-transformation strain response becomes that of tension shown in Fig. 6.4a with softening. This makes the bending response for loading similar to those of tubes with Lüders bands in Hallai and Kyriakides [2011b] but with a significantly larger "plateau strain." In the absence of the stabilizing effect of the hardening material response in compression from the solution, the structure becomes more sensitive to imperfections, so the depth of the two local thickness imperfections is reduced to $0.01t$ (see Fig. 6.5).

The moment-end rotation response produced using the symmetric material model is shown in Fig. 6.24 and Fig. 6.25 shows a sequence of corresponding deformed configurations (M and q_L are normalized by the same tensile material variables as in the previous Sections). Overall, the tube response is similar to that of the asymmetric material model exhibiting a closed hysteresis with an upper and a lower undulating moment plateau during which diamond shaped localization patterns progressively develop during loading and are erased during unloading. The main characteristics of this solution can be summarized as follows:

a. The response exhibits a local moment maximum associated with the onset of localization and a local moment minimum at the onset of reverse "transformation" of unloading. Such local moment maxima are commonly observed in bending of tubes with Lüders bands but are absent in the present NiTi responses because of the stabilizing effect of the material hardening in compression (see Fig. 6.6).

b. Localization initiates at the imperfections at the top and bottom and takes the form of two X-shaped narrow bands. Spurious nucleations at other sites like those in Fig. 8 do not develop here.

c. Progressive development of diamond-shaped localization patterns takes place next on both the tensioned and compressed sides. Diamonds first consume the section to the left of the imperfections, and subsequently propagate to the right until the whole length is consumed.

d. Eventually eleven diamonds form both on the top and bottom of the tube, as well as a half diamond at the plane of symmetry and another at the rotated end. The average length of the tension diamonds $\lambda = 0.675D$ and their depth $h = 0.46D$ (the λ values on the compressed side are somewhat smaller because of the differences in arc length induced by bending). Both values are significantly smaller than the dimensions

of the tension diamonds in Fig. 6.7. The axial strains in the diamonds are approximately 6.8%, however the outer fibers are at somewhat higher values. The compressive patterns mirror the tensile ones, but on the tensile side the patterns are somewhat irregular while being more triangular on the compressed side.

e. Similar to Fig. 6.8, curvature localizes to a value of $10.65k_o$ in the section of the tube consumed by diamonds, a value significantly larger than the corresponding one for the asymmetric material. Concurrently, the unaffected section remains at $1.69k_o$. The high value of localized curvature indicates that the outer fibers of the cross section are at stress levels corresponding to the stiff *M*-phase branch of the material response in Fig. 6.4b.

f. The material softening induced more severe flattening of the cross section, which now appears more like Brazier [1927] ovalization.

g. Both moment plateaus are lower than the corresponding levels in Fig. 6.6. Each moment undulation again corresponds to the initiation and completion of localization in a tension/compression pair of diamonds. The upper plateau terminates into a local valley formed when localization reaches the free end. The lower plateau terminates into a local moment peak associated with the erasure of the final islands of local deformation at the plane of symmetry.

6.6.3 Effect of Softening Modulus

The softening slope adopted in the tensile response in the calculations thus far, is based on the one measured in the sandwich tensile test performed by Hallai and Kyriakides [2013]. Here we vary the slope of the negative branches, keeping other characteristics of the up-down-up responses the same and examine the effect on the bending response. In these calculations, the compressive stress-strain response is kept the

same as in Fig. 6.4. The tensile stress-strain responses considered are shown in Fig. 6.26a. The response used thus far is designated as 0 and the ones with stronger and weaker softening are designated as +1 and -1 respectively.

Figure 6.26b shows the moment-end rotation responses calculated for each of the three softening moduli, using the mesh of the base case (Fig. 6.5). The calculated sets of deformed configurations for the +1 and -1 materials are shown in Figs. 6.27 and 6.28. (The images correspond to approximately the same normalized rotations as those of the bullets on response 0 in Fig. 6.26b). The following observations can be made by comparing the three sets of results.

a. The moment-end rotation responses exhibit similar stiffnesses during the stable branches and the same levels and extents of the upper and lower moment plateaus. As the magnitude of the softening modulus in the tensile response increases, the moment plateaus develop more pronounced undulations corresponding to the initiation and completion of diamond patterns.

b. All three cases progressively develop diamond deformation patterns that propagate as the moment plateaus are traced. Curvature localizes to about the same curvature in the diamond affected zones. However, stronger softening makes the diamonds more pronounced and weaker softening more diffuse with less regular geometry. Furthermore, because of the construction of the up-down-up responses (Fig. 6.26a) the diamond strain reduces somewhat as the softening slope decreases.

c. The order of diamond formation and localization is affected by the strength of the softening and differs in the three cases. Consequently, the location of moment undulations varies also. The order of diamond erasure is different than the order they were formed and different in the three cases. This results in differences in the locations of the corresponding moment undulations in the lower plateau.

Overall, the strength of the instabilities dictated by the slope of the softening of the tensile response adopted have only modest influence on the moment-rotation response but affect the localized pattern formation on the tensioned side of the bent tube. Clearly methods for measuring these slopes would be most helpful.

6.6.4 Effect of Imperfection

Several different imperfections for initiating transformation were considered in this study. The one found to be most effective involved local thickness reduction of the type shown in Fig. 6.5. However, the location of such imperfections was found to influence the evolution and distribution of localization patterns that developed, while at the same time, the influence on the moment-end rotation response is minimal. Figures 6.29-6.33 demonstrate the effect of the location of the thickness imperfection.

Figure 6.29 shows a sequence of deformed configurations calculated with one thickness reduction on the top side at $x = D$. As expected, the localization initiates at the imperfection in the form of X-shaped bands, followed by the initiation of three additional such bands as shown in image 3. These are again followed by the progressive development of diamond shaped patterns. However, the first diamond initiates from the second X-shaped pattern (image 4), in other words away from the location of the imperfection. Consequently, subsequent diamond patterns first propagate from the middle to the left (images 5-7). A new nucleation site then develops at the 3rd X-shaped pattern, which results in diamonds propagating towards the right end (images 8 and 9). Also, sharp triangular zones of localized deformation develop among the diamonds, leading to saw tooth-like patterns seen in images 10 and 11.

Figure 6.30 shows the sequence of deformed configurations calculated with a single thickness imperfection on the compressed side at $x = D$. This imperfection does

not influence the nucleation events. Again, four X-shaped bands initiate but at what appear to be random sites (image 3). The first diamond pattern initiates away from the imperfection site (image 4) and this leads again to a similar disorderly propagation of diamonds to that seen in Fig. 6.29 (images 5-10).

Figures 6.31 shows calculated deformed configurations for a model with two thickness imperfections on diametrically opposite sides at $x = 0$. In this case, the first X-shaped band initiates at the imperfection (image 2), followed by three other X-shaped bands (image 3). However, as shown in image 4, the first diamond shaped pattern of localized deformation grows from the right-oriented prong of the second X-shaped band. Thereafter, diamond patterns propagate towards the left (images 5 and 6). In image 6, another diamond develops from the third X-shaped band and spreads first to the left (images 7 and 8), and then to the right (images 9 and 10) until the transformation has covered the tensioned side of the tube.

In the deformed configurations shown in Fig. 6.32, the tube has two small thickness imperfections on diametrically opposite sides at $x = 2D$. The first X-shaped band initiates on the tensioned side at the imperfection (image 2). Another three X-shaped bands form progressively as shown in image 3. However, the localization of deformation initiates as a triangular zone of relatively high strain close to the right end, followed by another triangle that develops at the left end, i.e. the plane of symmetry (image 4). Thereafter, four diamond shaped patterns develop progressively starting from the imperfection and propagate to the right (images 5-8). Saw tooth like patterns of high deformation cover the remaining sections of the tube (images 9-11).

In the fifth case studied, two thickness imperfections are placed diametrically opposites at $x = L$. The first X-shaped band initiates from the imperfection (Fig. 6.33, image 2), followed sequentially by three additional X-shaped bands (image 3). The first

diamond shaped pattern of localized deformation develops from the left-oriented prong of the third X-shaped band and propagates towards the right end (images 4-6). Another nucleation of diamond shaped pattern starts from the second X-shaped band (image 7) and is followed by the development of saw tooth patterns between this diamond and the one that developed initially (image 8). The remaining part of the loading process is associated with the propagation of the diamond that initiates in image 7 to the left (images 9-10).

Clearly, localization nucleates in the form of multiple X-shaped bands for all five models considered in this section. The location of the imperfection did not play a decisive role in their initiation indicating that their location is governed more by numerical noise rather than any physical problem variable. The diamond bands that follow usually initiated from one of the X-shaped bands but their subsequent evolution did not follow any predictable order. We can thus conclude that the problem is rather insensitive to imperfections. Placing the thickness imperfection at $x = D$ was chosen for the base case solution because it resulted in progressive development of diamond patterns that start from the mid-span and propagate toward the rotated end of the model.

6.7 SUMMARY

In pure bending experiments on pseudoelastic NiTi tubes, the asymmetry between tensile and compressive responses manifests as localized curvature that tends to spread at nearly constant moment, with the tensioned side of the high curvature section developing diamond-shaped patterns of martensite. Unloading leads also to two curvature regimes, the progressive erasure of the diamond patterns, and the moment tracing a lower plateau.

The material reverts to austenite, the hysteresis closes, and the tube returns to its undeformed configuration.

The constitutive model framework presented in Chapter 2 is implemented in a FE model to simulate the pure bending experiment of a NiTi tube. The constitutive model is calibrated to the measured uniaxial tensile and compressive responses of the material. To represent the unstable behavior, softening is introduced over the extents of the two stress plateaus in the tensile response at approximately the Maxwell stress levels. A uniform mesh consisting of cubical 3-D solid incompatible elements is chosen with a mesh density for good reproduction of the finer features of the deformation patterns observed in the experiment. The localization of deformation is initiated by a pair of local thickness imperfections on diametrically opposite sides.

The numerical simulation reproduces the major features of the experimental results including: the overall moment-end rotation response; the correct levels and extents of the moment plateaus; the values of the two curvature regimes during loading and unloading; and the progressive initiation of higher strain diamond patterns on the tensioned side and the nearly homogeneous deformation on the compressed side. The geometry of the calculated diamond patterns is somewhat more regular than those of the experiment, but their lengths and depths agree well with the average values of the ones recorded in the experiment. The axial strain inside the diamonds reaches the value at which phase transformation completes in tension, while the strain outside the diamonds is at levels that correspond to those of the austenitic phase. The following observations can be made from the solution:

- A new diamond initiates from a previously transformed site, and takes the form of X-shaped narrow bands along the two characteristics of Hill. The bands lengthen and broaden until a diamond pattern is filled in.

- The high strain diamond patterns separated by lower strain domains result in a nearly linear distribution of average strain along tube fibers on the tensioned side; this enables the affected section of the tube to develop uniform, beam-like, curvature.
- On the compressed side the deformation is smaller and homogeneous.
- Sensitivity studies demonstrated that the hardening behavior in compression has a stabilizing effect on the structure. Initiation moment peaks and valleys common in bending of tubes with symmetric material behavior (e.g., Lüders banding) are absent. This makes nucleation of transformation easier and results in more random nucleation sites.
- A mesh sensitivity study demonstrated that the mesh density does not influence the overall structural response or the pattern formation. Its main effect is in the width of the transition zones separating the higher and lower strain domains at the edges of diamond patterns.
- The strength of the instabilities, dictated by the slope of the softening in the tensile response, have only modest influence on the moment-rotation response. They do however affect the localized pattern formation on the tensioned side of the bent tube.

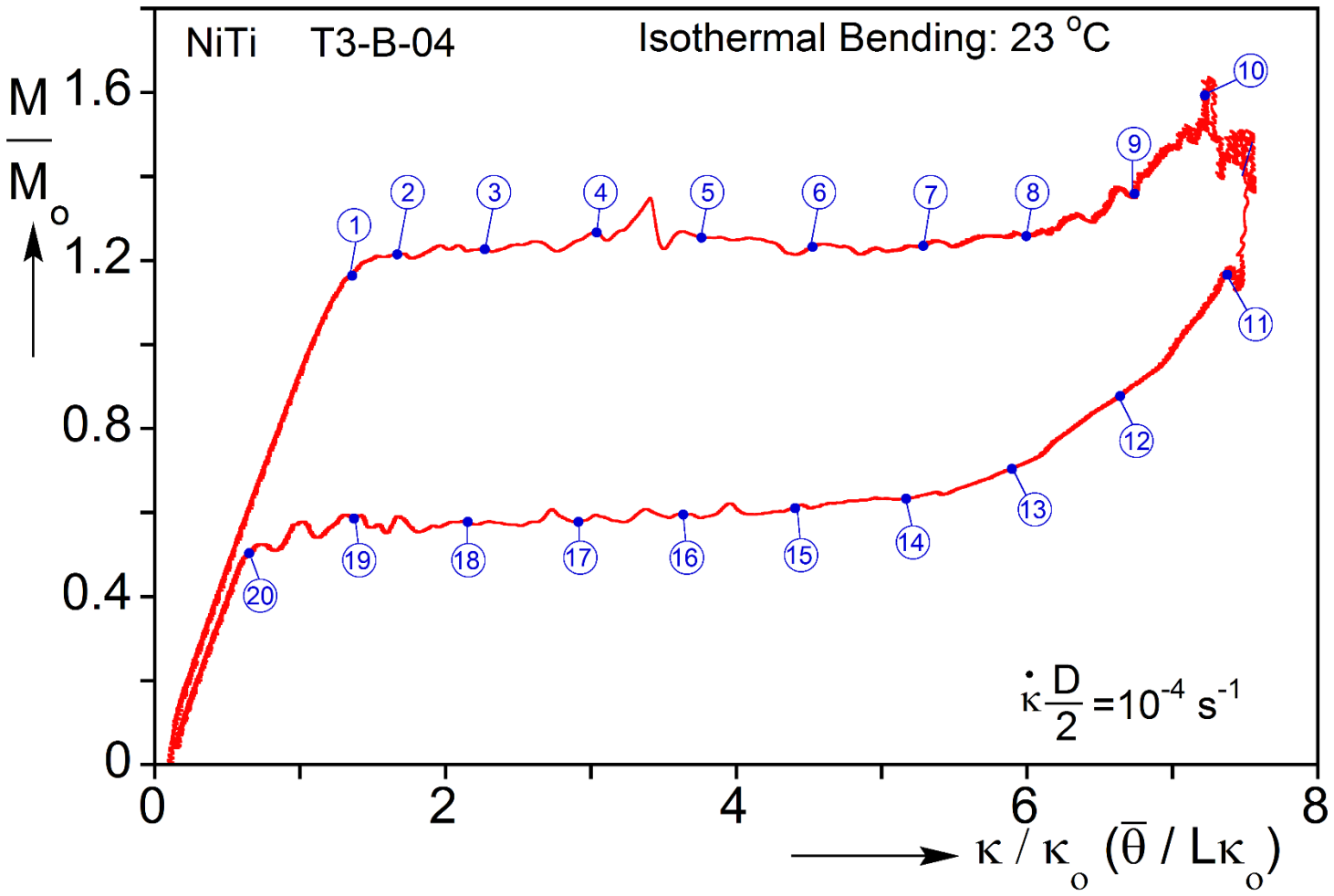

Fig. 6.1 The moment-end rotation response from an isothermal bending experiment on a NiTi tube (from Bechle and Kyriakides [2014]).

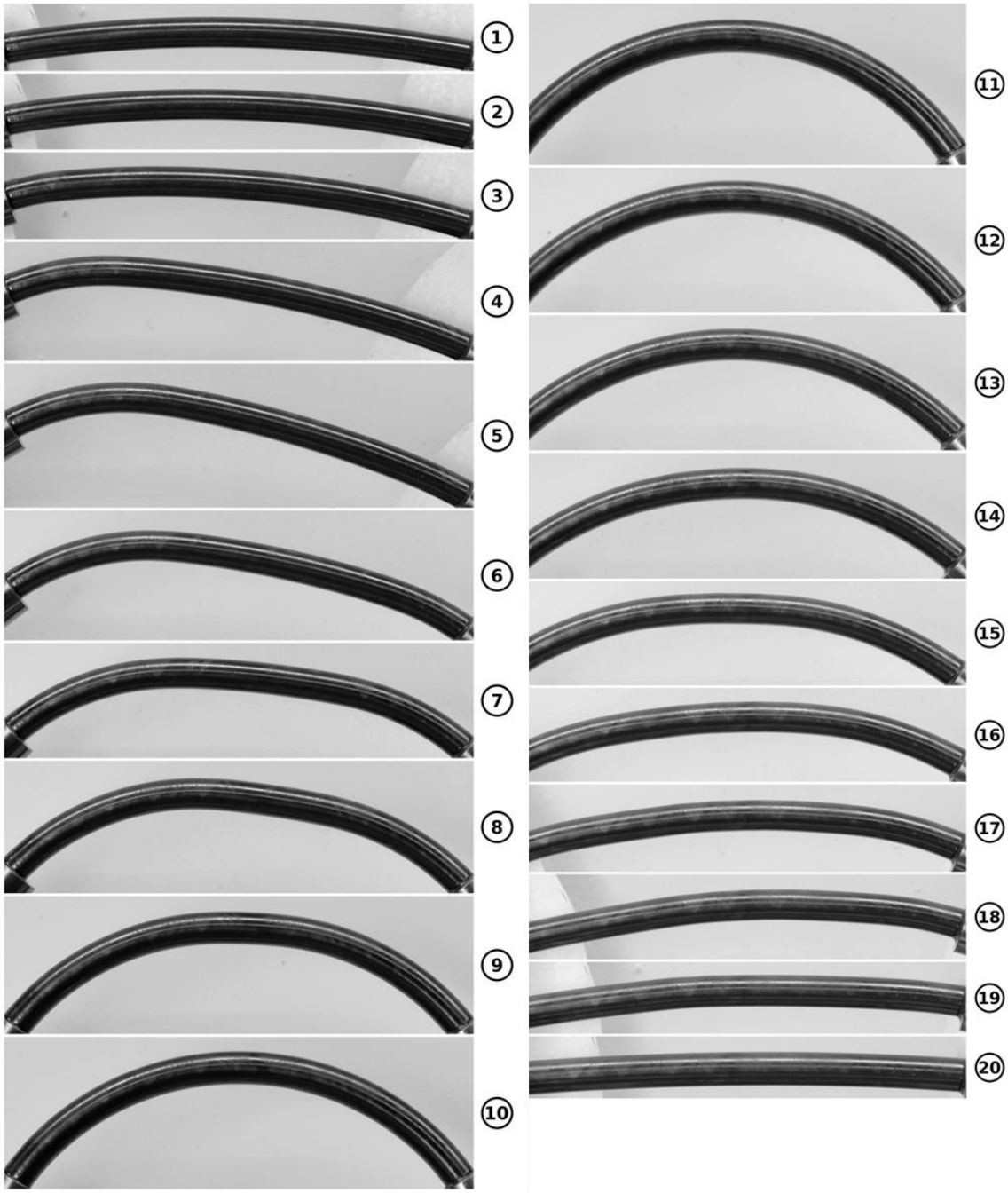

Fig. 6.2 Set of tube bending configurations corresponding to the numbered bullets marked on the response in Fig. 6.1 (from Bechle and Kyriakides [2014]).

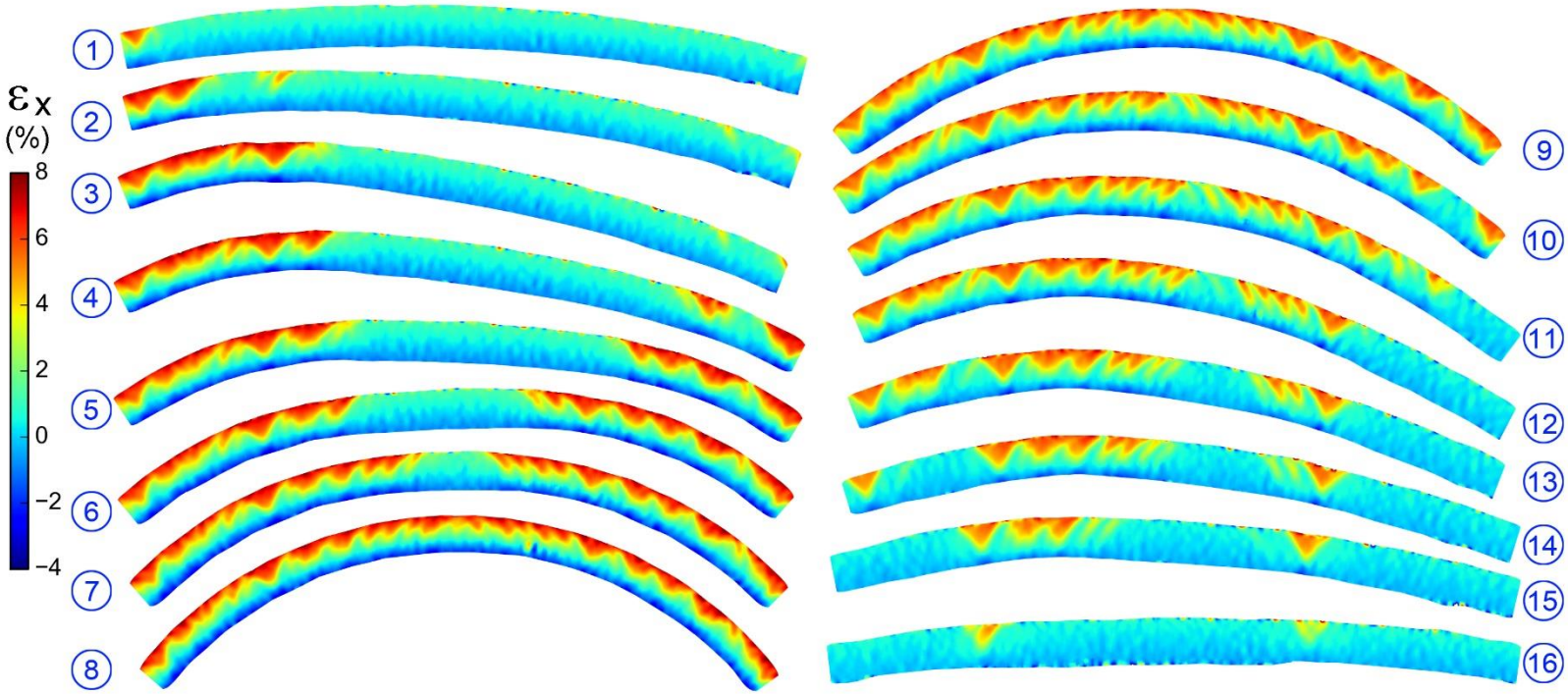

Fig. 6.3 Deformed configurations with DIC strain contours superimposed showing evolution of deformation patterns in a bending experiment on a NiTi tube during loading (images ①-⑧) and unloading (images ⑨-⑯).

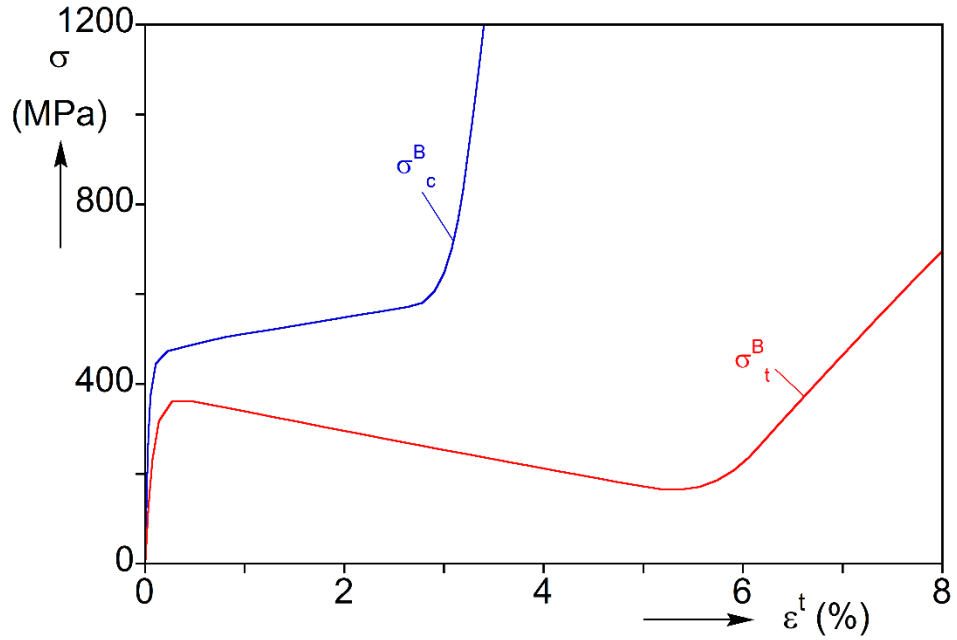

(a)

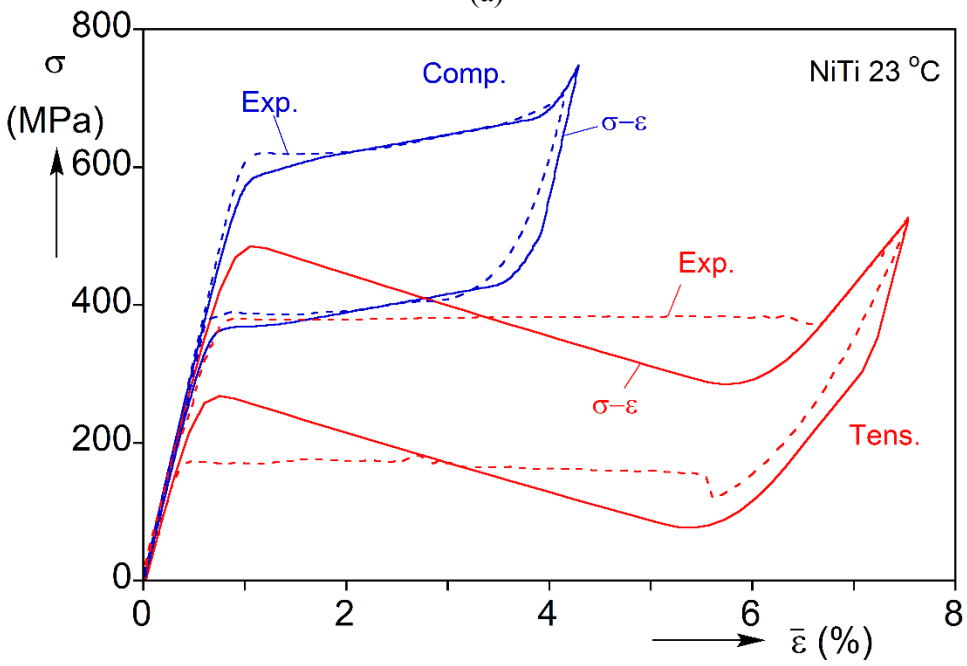

(b)

Fig. 6.4 (a) The back stress-transformation strain responses for tension and compression used in the model. (b) The resultant tensile and compressive stress-strain responses together with the measured ones.

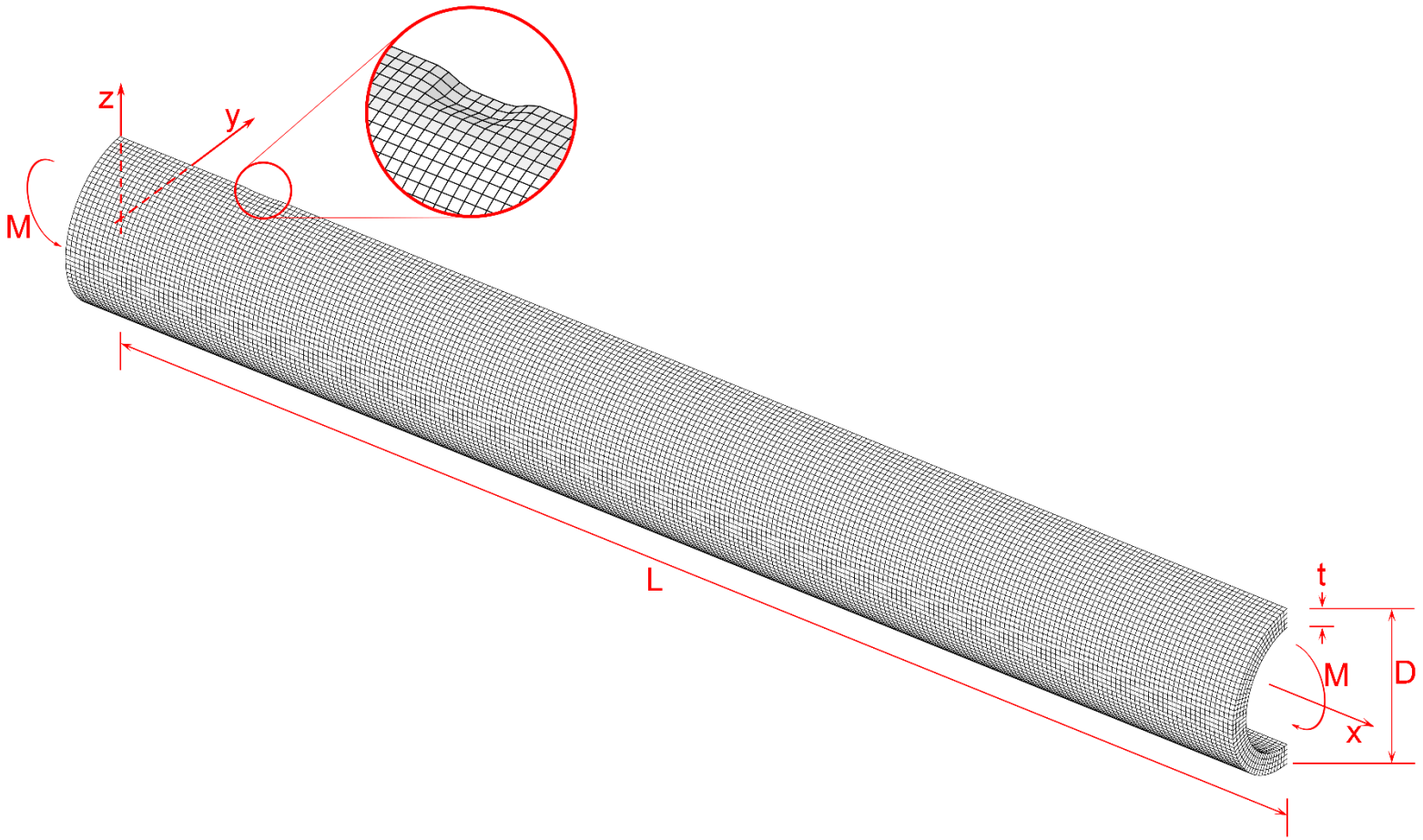

Fig. 6.5 Geometry of the model used in the analysis and the finite element mesh.

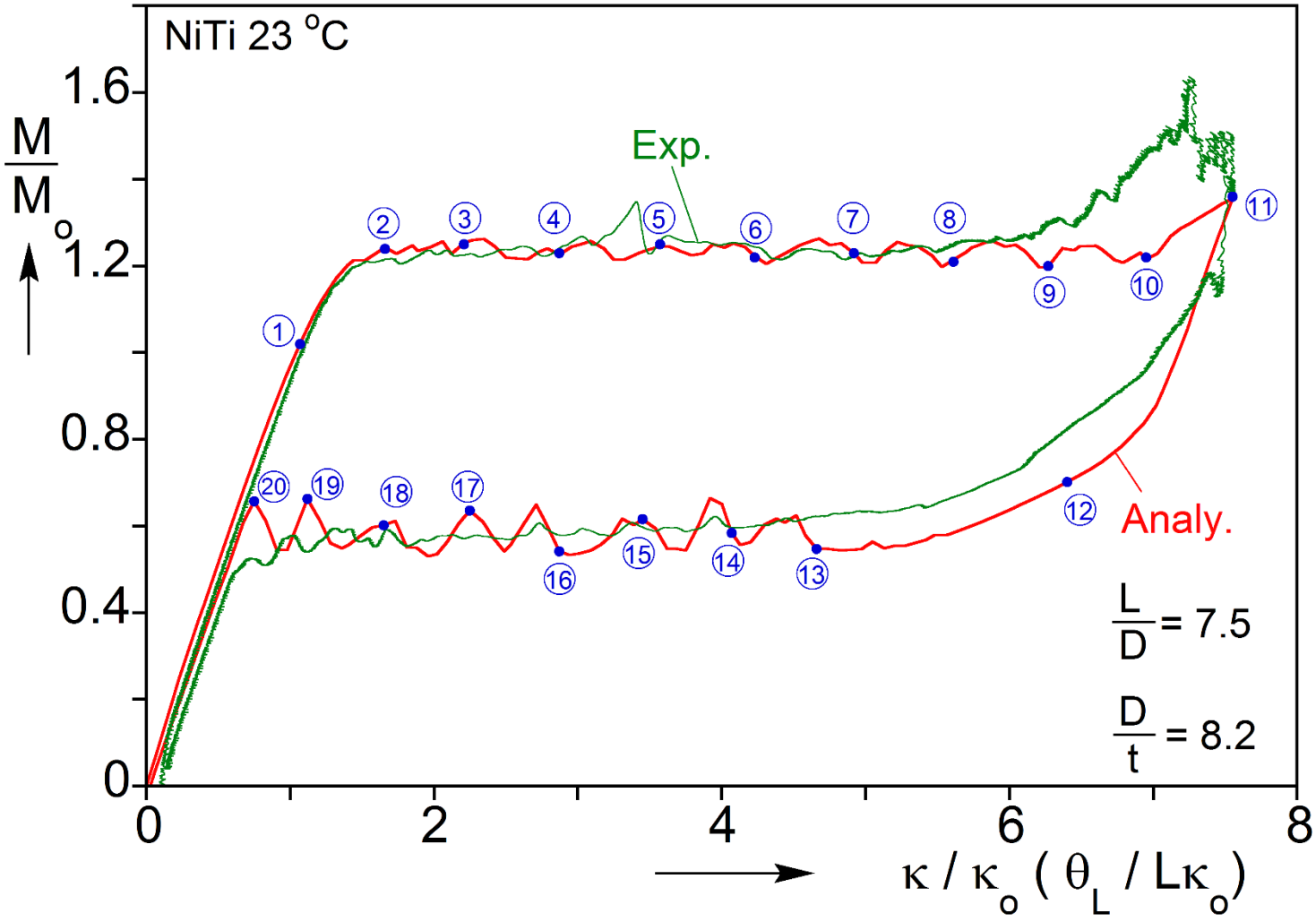

Fig. 6.6 Comparison of calculated and measured moment-end rotation responses for a NiTi tube.

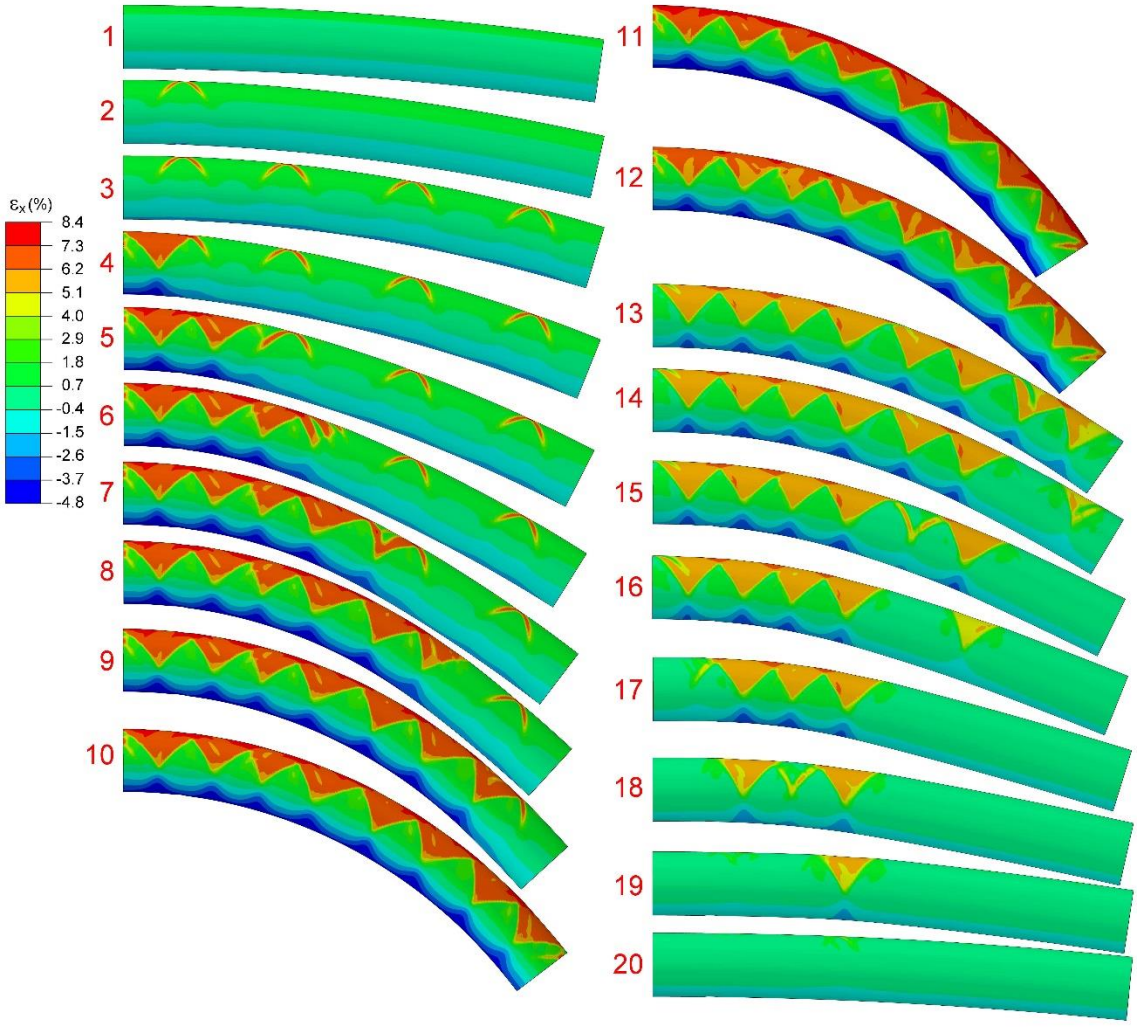

Fig. 6.7 Sequence of calculated tube deformed configurations with axial strain contours superimposed corresponding to the numbered bullets on the response in Fig. 6.6.

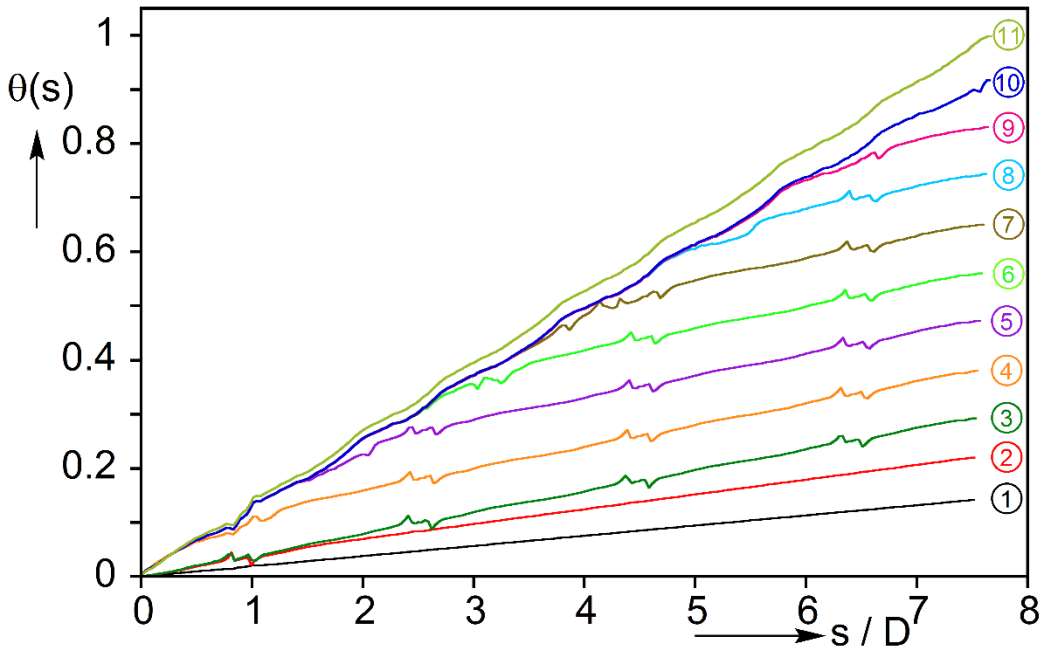

(a)

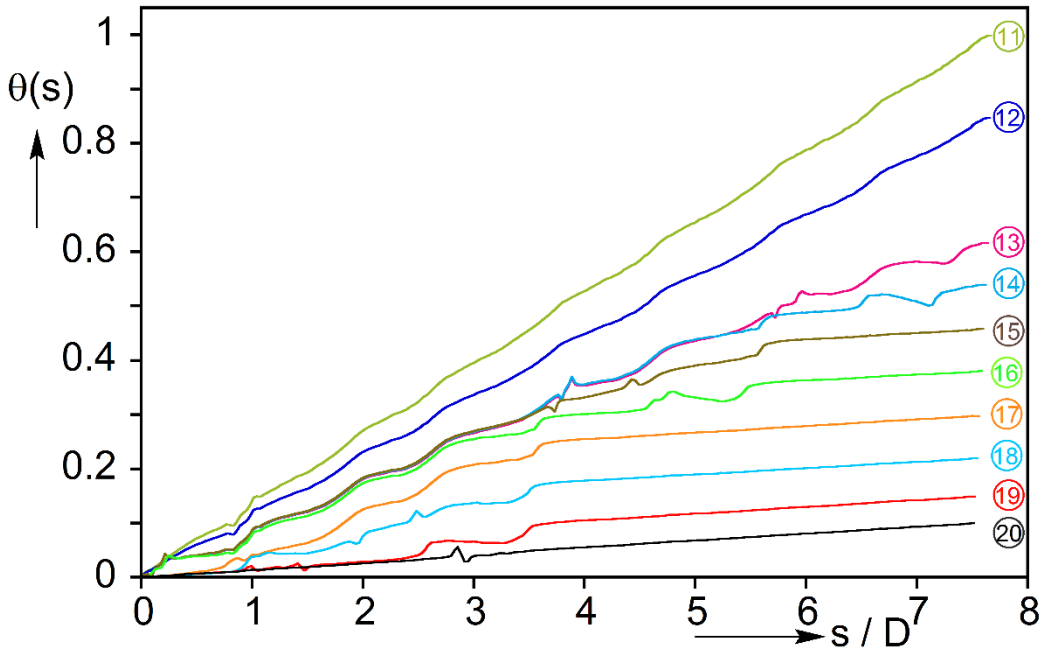

(b)

Fig. 6.8 Calculated tube slope along the length, $q(s)$, corresponding to the images in Fig. 6.7 for (a) loading and (b) unloading.

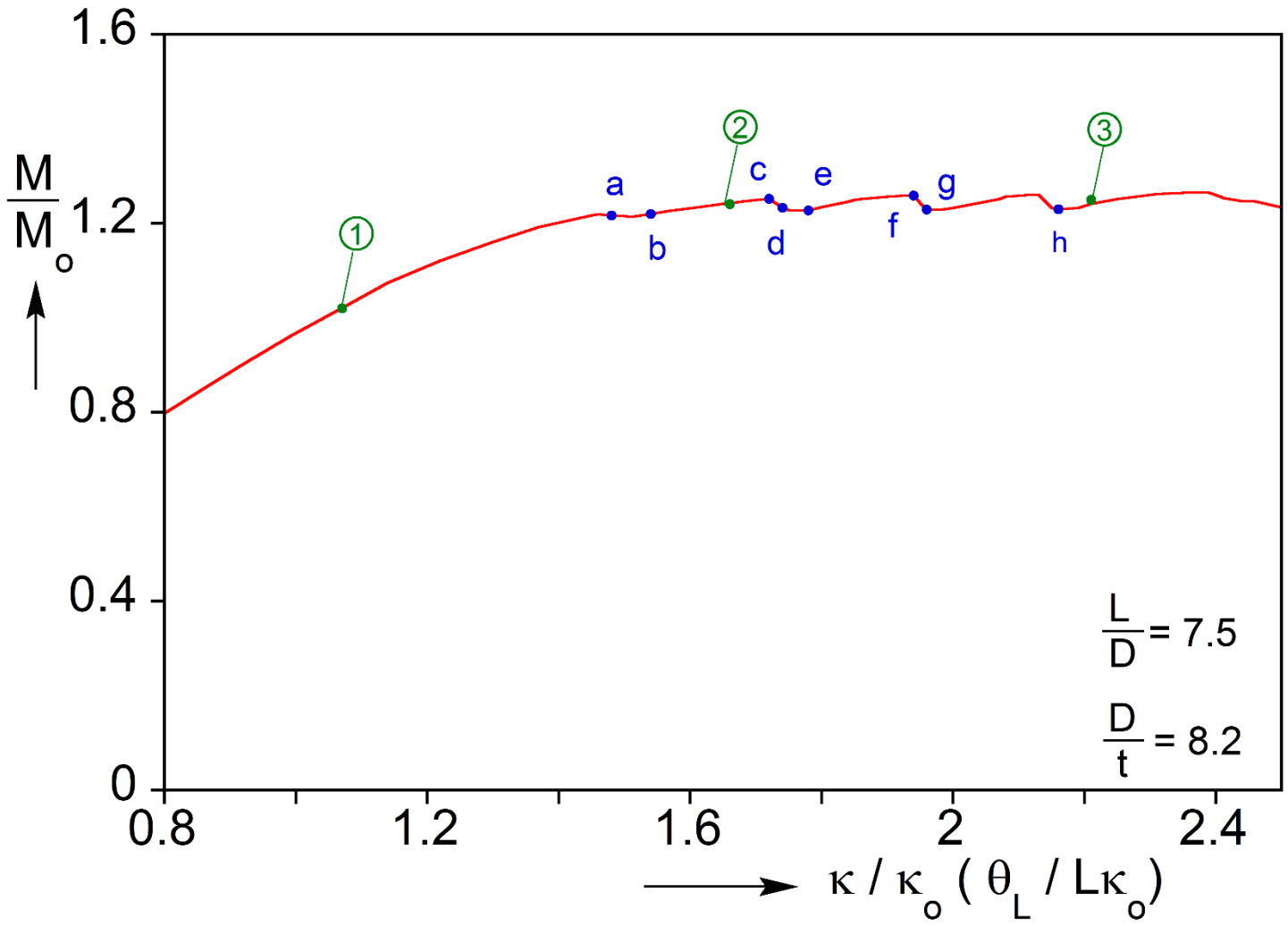

Fig. 6.9 Expanded view of the moment-rotation response that is relevant to the X-shaped localization bands.

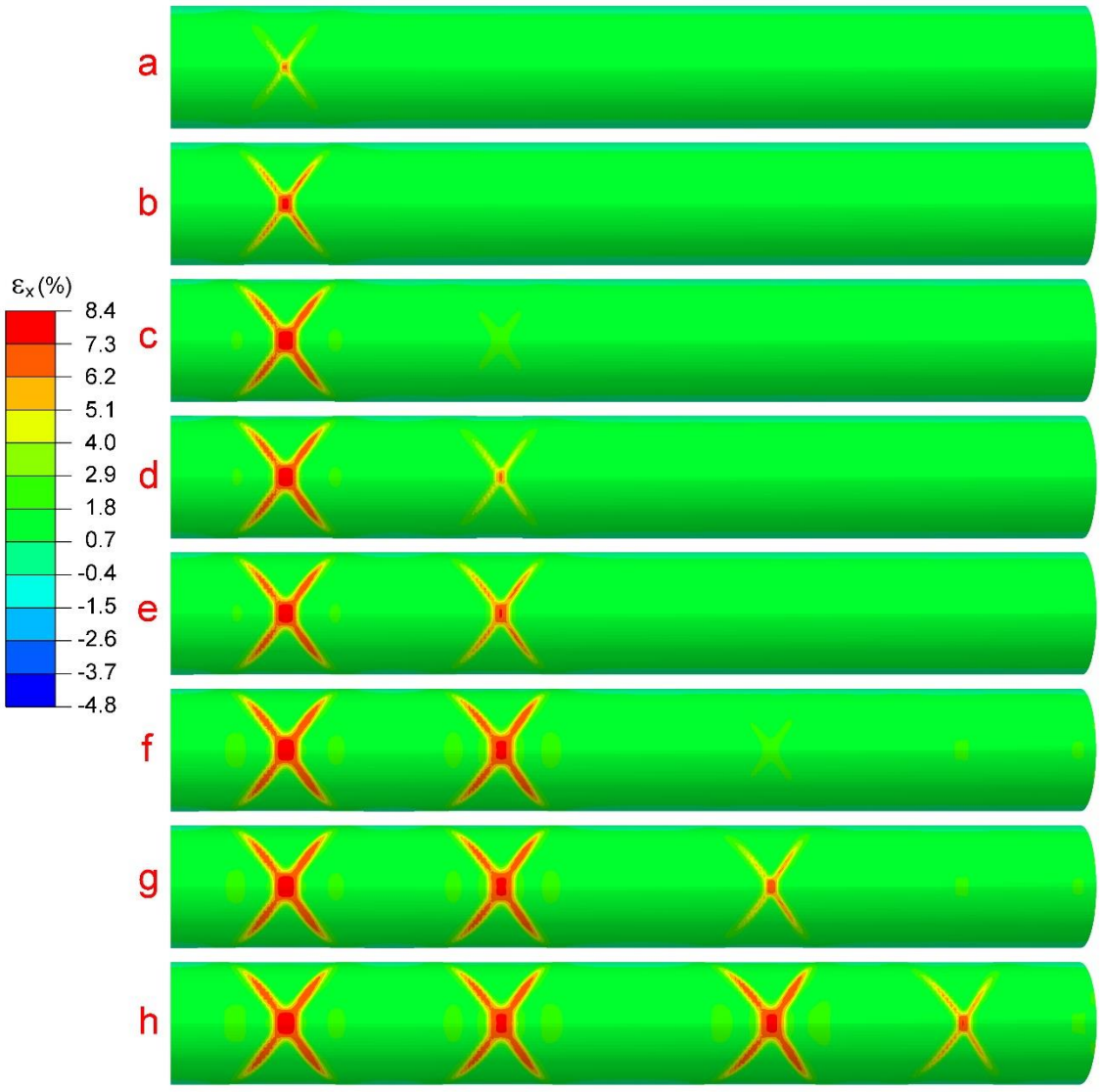

Fig. 6.10 Top views of the model tube showing the progressive nucleation and evolution of X-shaped bands.

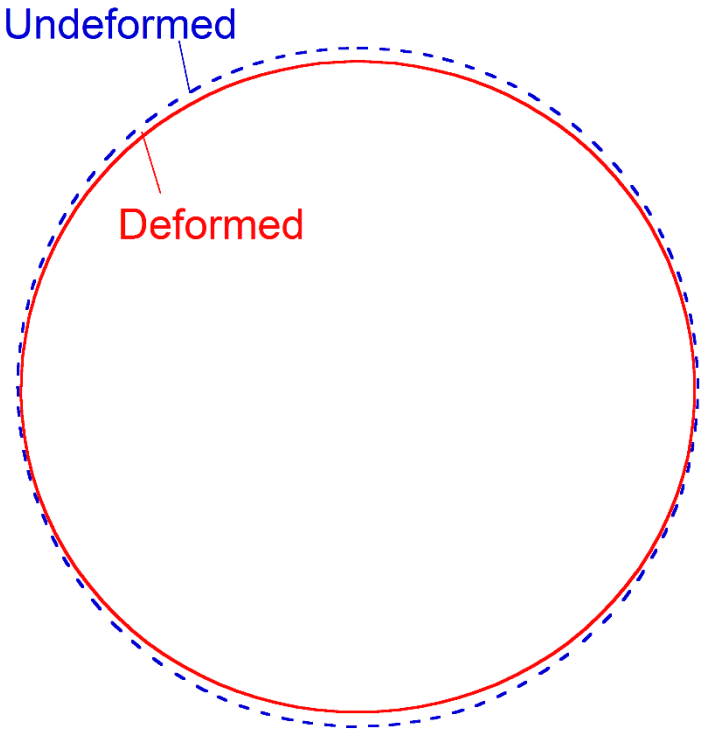

Fig. 6.11 Deformed outer surface of the tube showing the cross sectional distortion induced by transformation across the third diamond (radial displacement amplified x2).

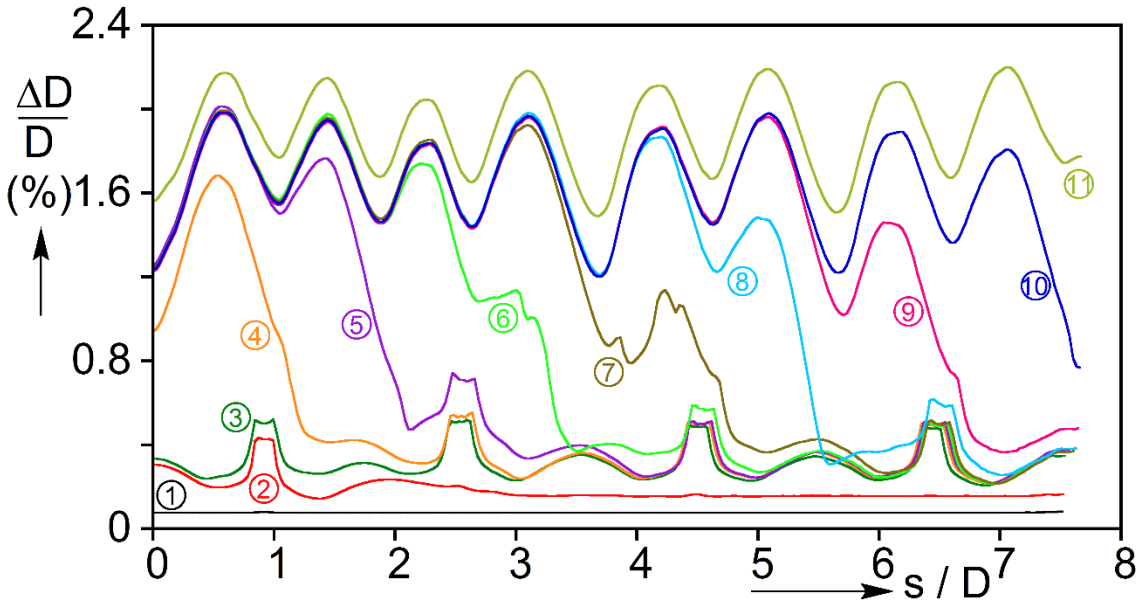

(a)

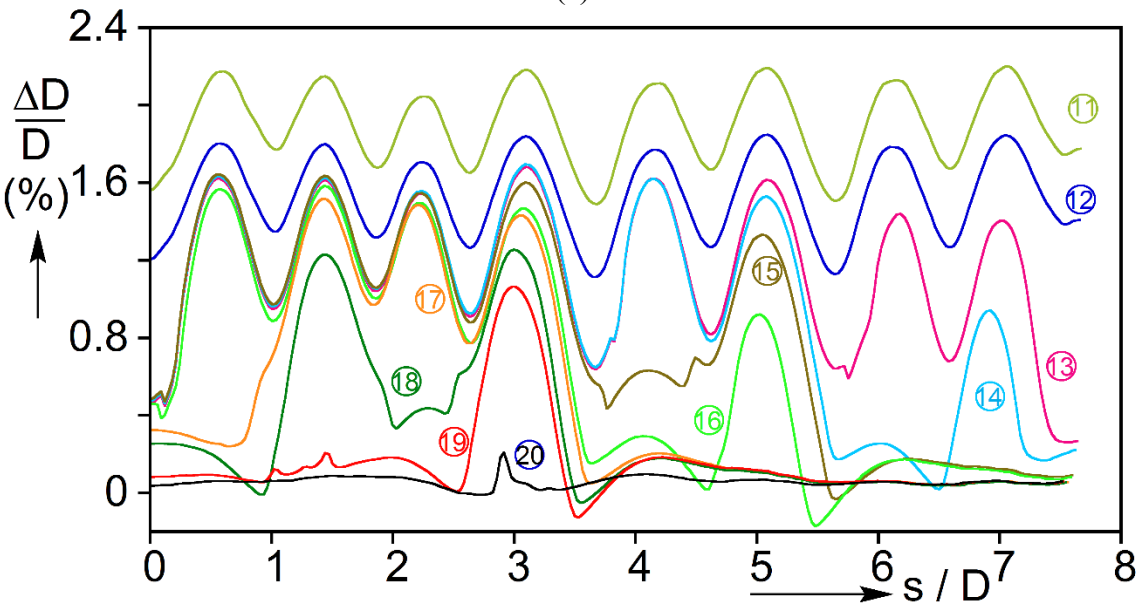

(b)

Fig. 6.12 Change in diameter in the plane of bending along the length, $DD / D(s)$, corresponding to the images in Fig. 6.7 for (a) loading and (b) unloading.

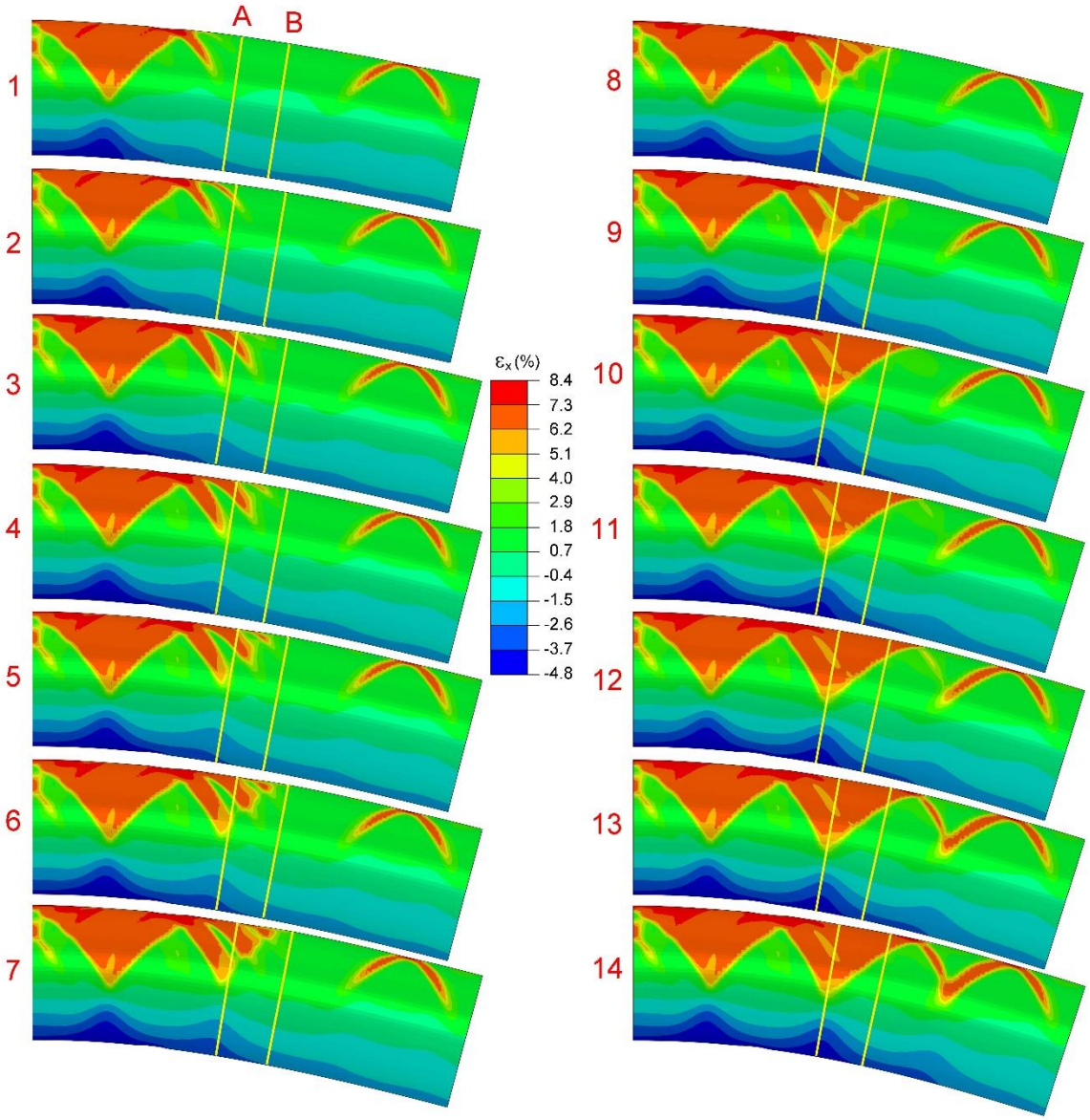

Fig. 6.13 Deformed configurations of part of the model tube showing the development of the second diamond.

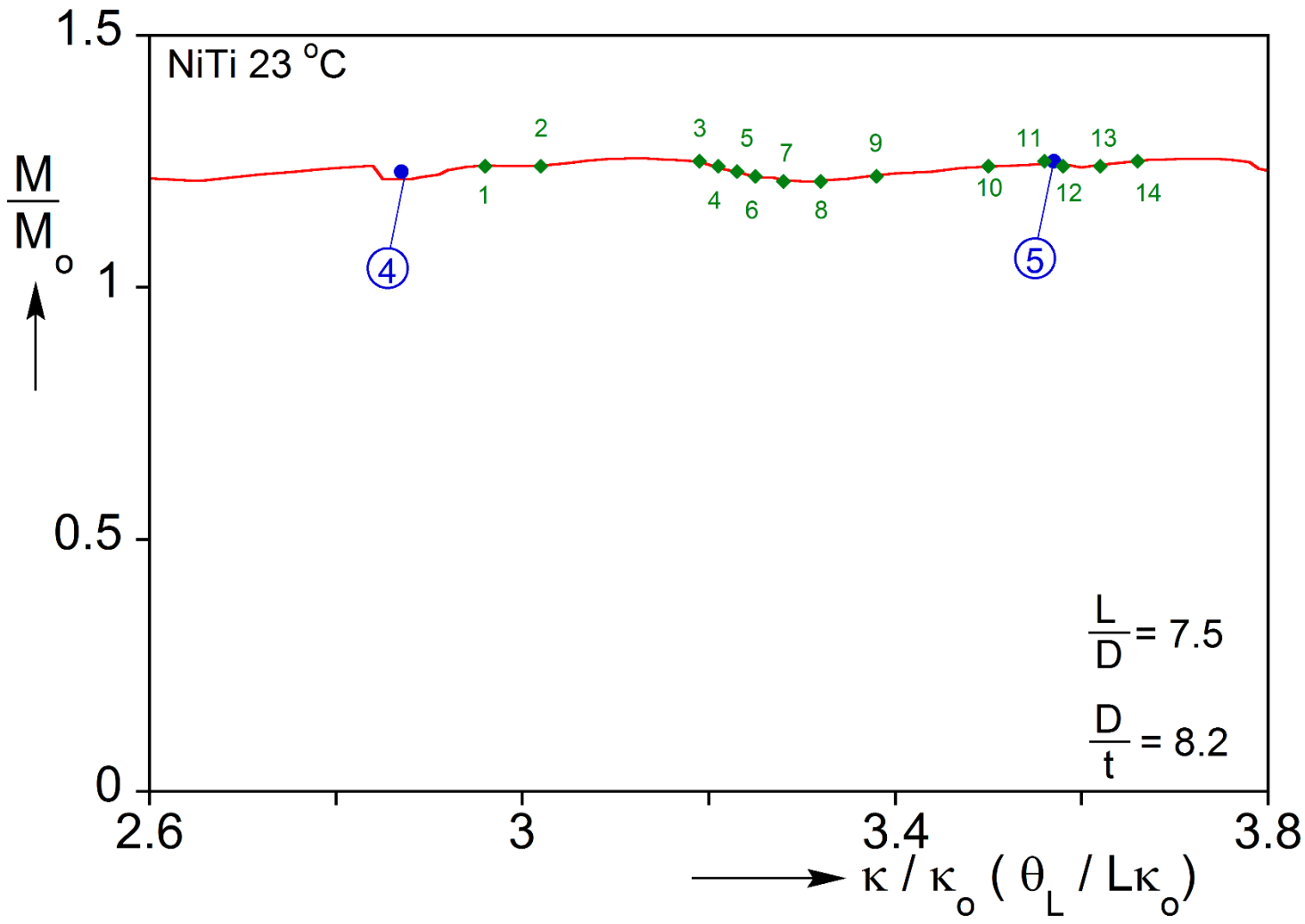

Fig. 6.14 Locations of the images in Fig. 6.13 on a zoomed in section of the moment-end rotation response.

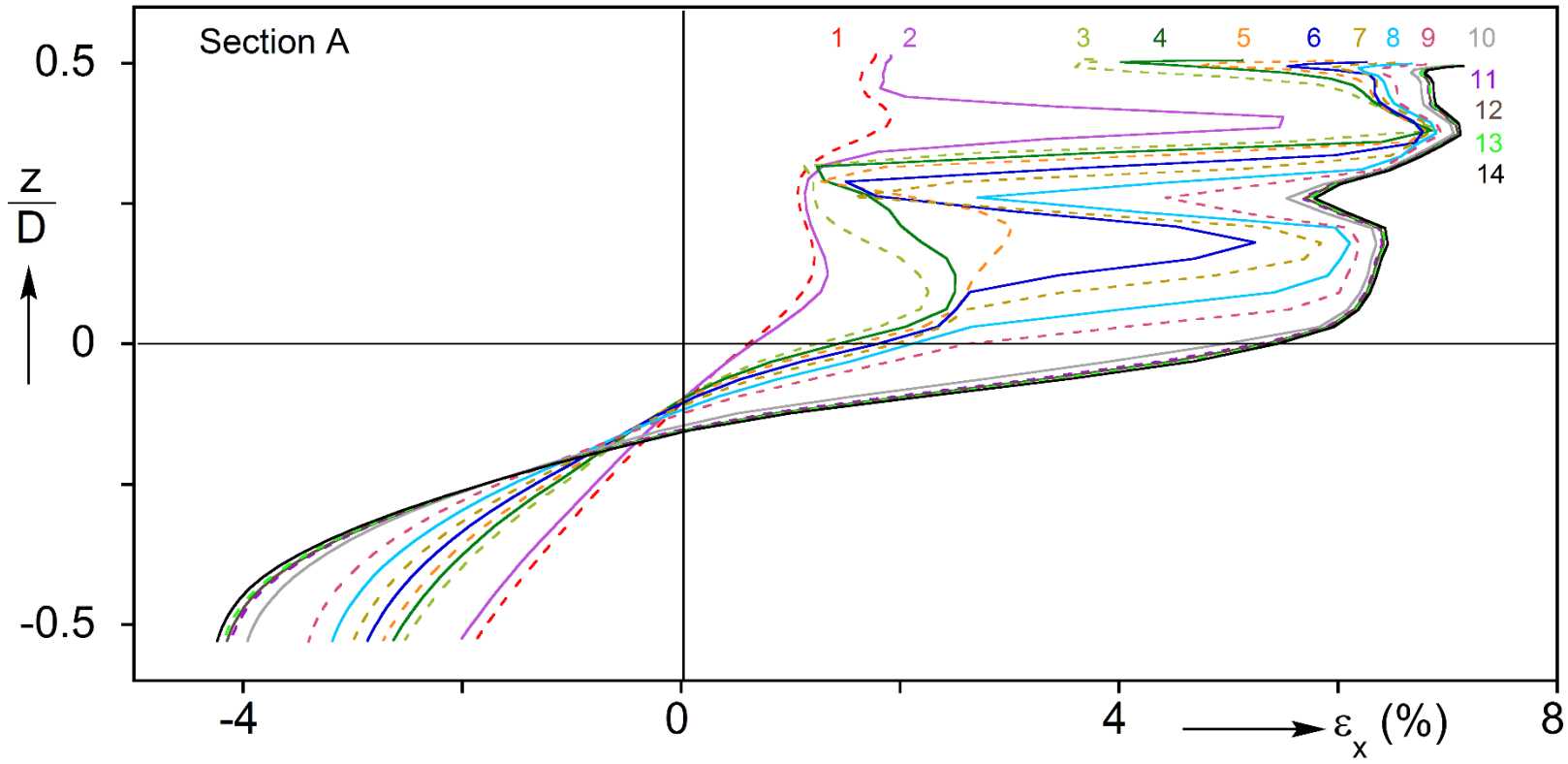

Fig. 6.15 Strains across section A corresponding to the fourteen images in Fig. 6.13 and 6.14.

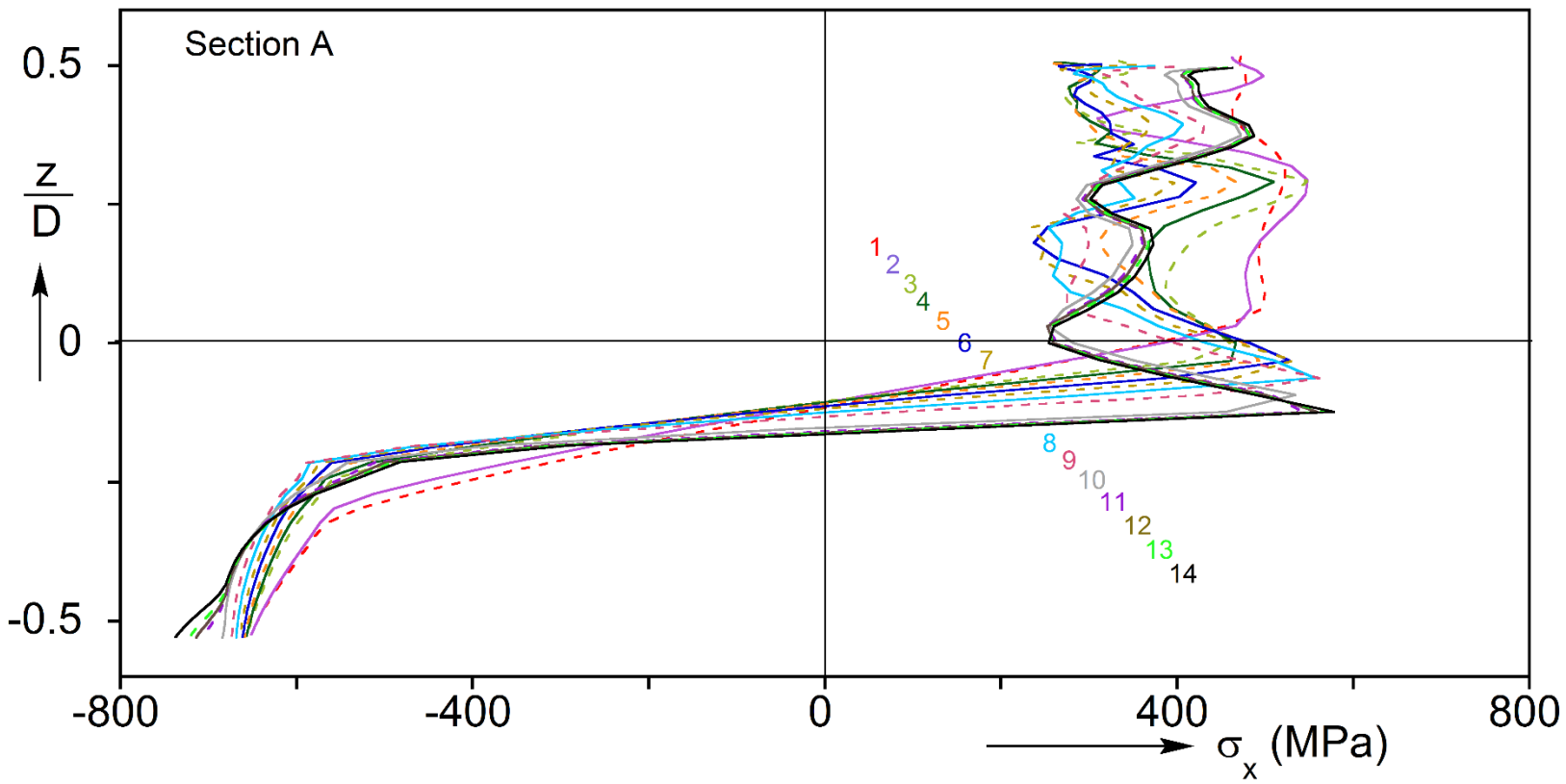

Fig. 6.16 Stresses across section A corresponding to the fourteen images in Fig. 6.13 and 6.14.

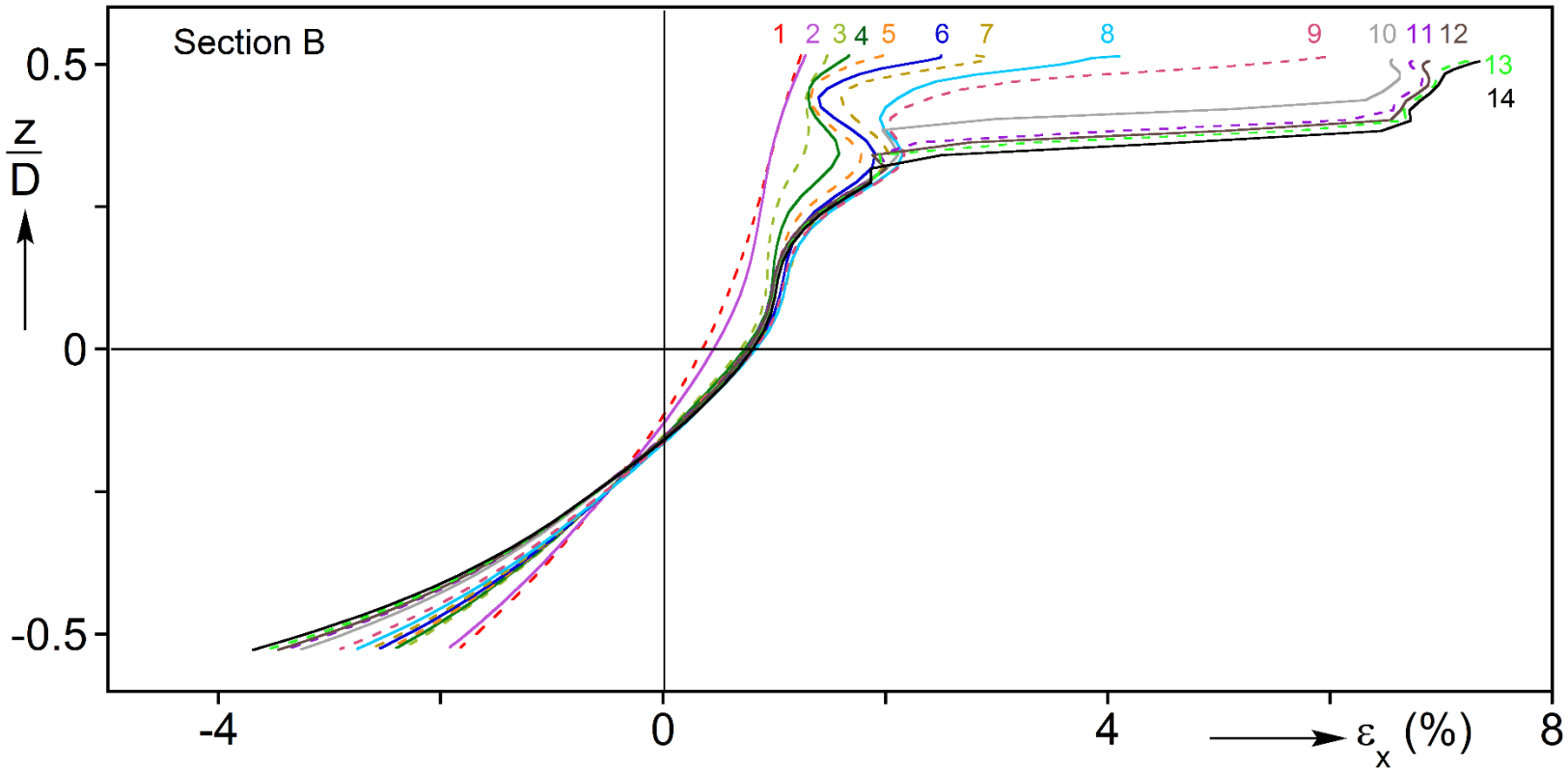

Fig. 6.17 Strains across section B corresponding to the fourteen images in Fig. 6.13 and 6.14.

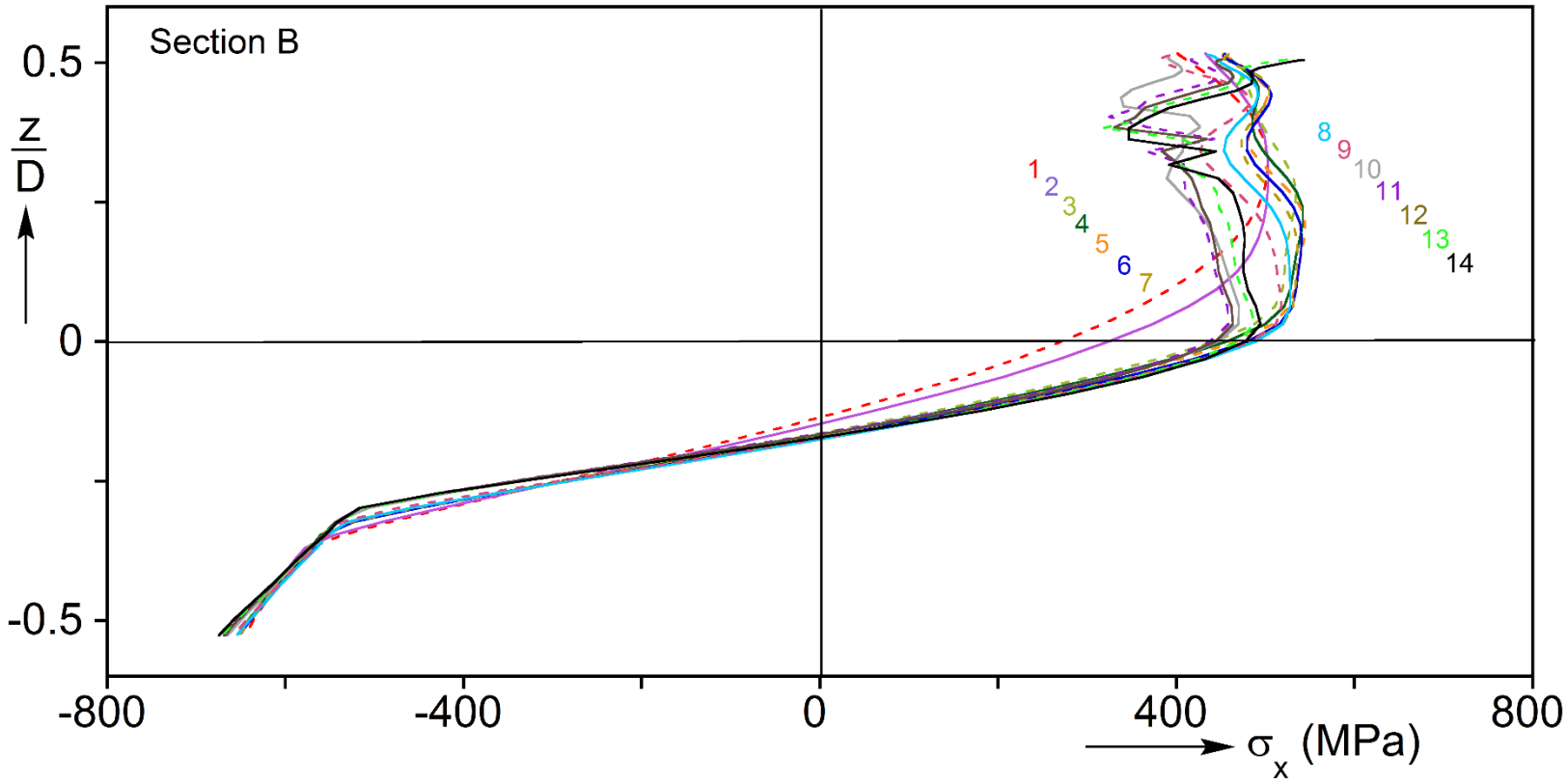

Fig. 6.18 Stresses across section B corresponding to the fourteen images in Fig. 6.13 and 6.14.

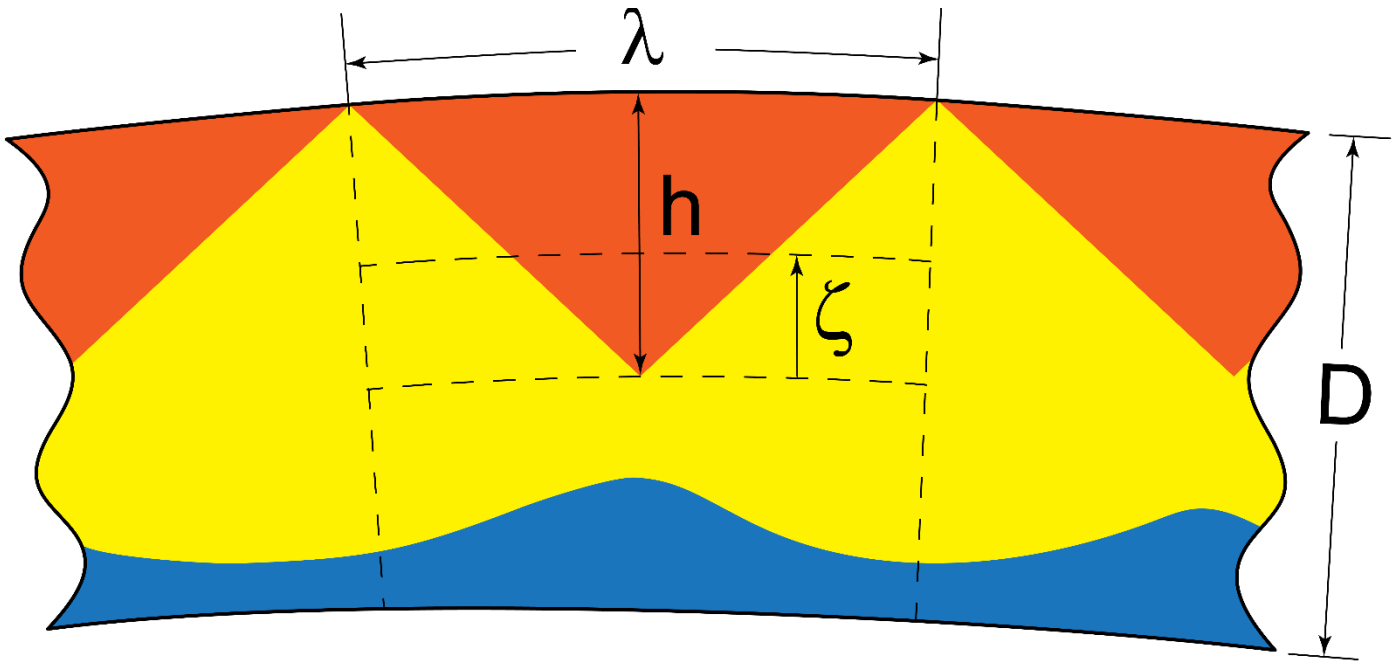

Fig. 6.19 Idealized periodic diamond cell.

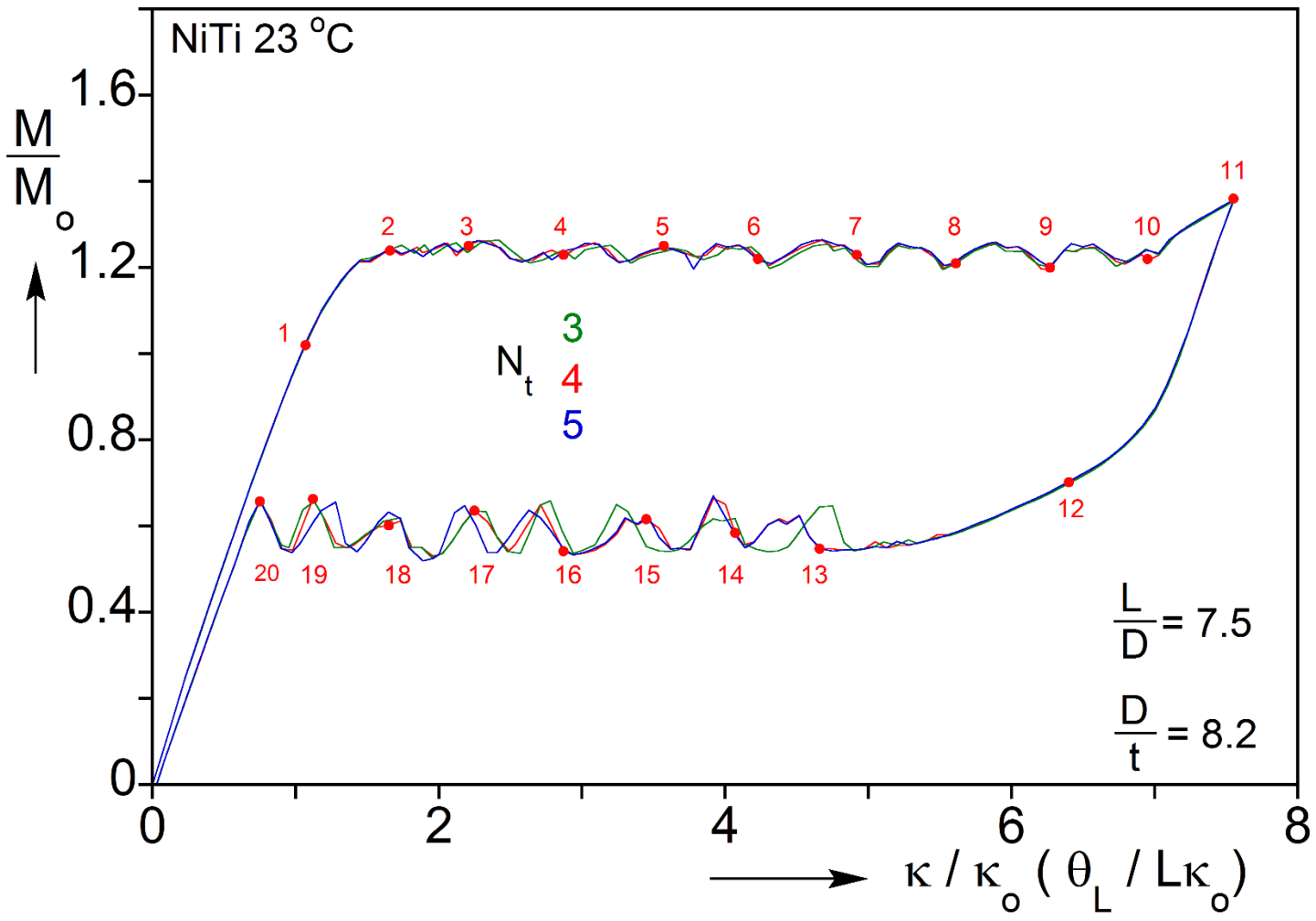

Fig. 6.20 Comparison of moment-end rotation responses calculated for three different mesh densities.

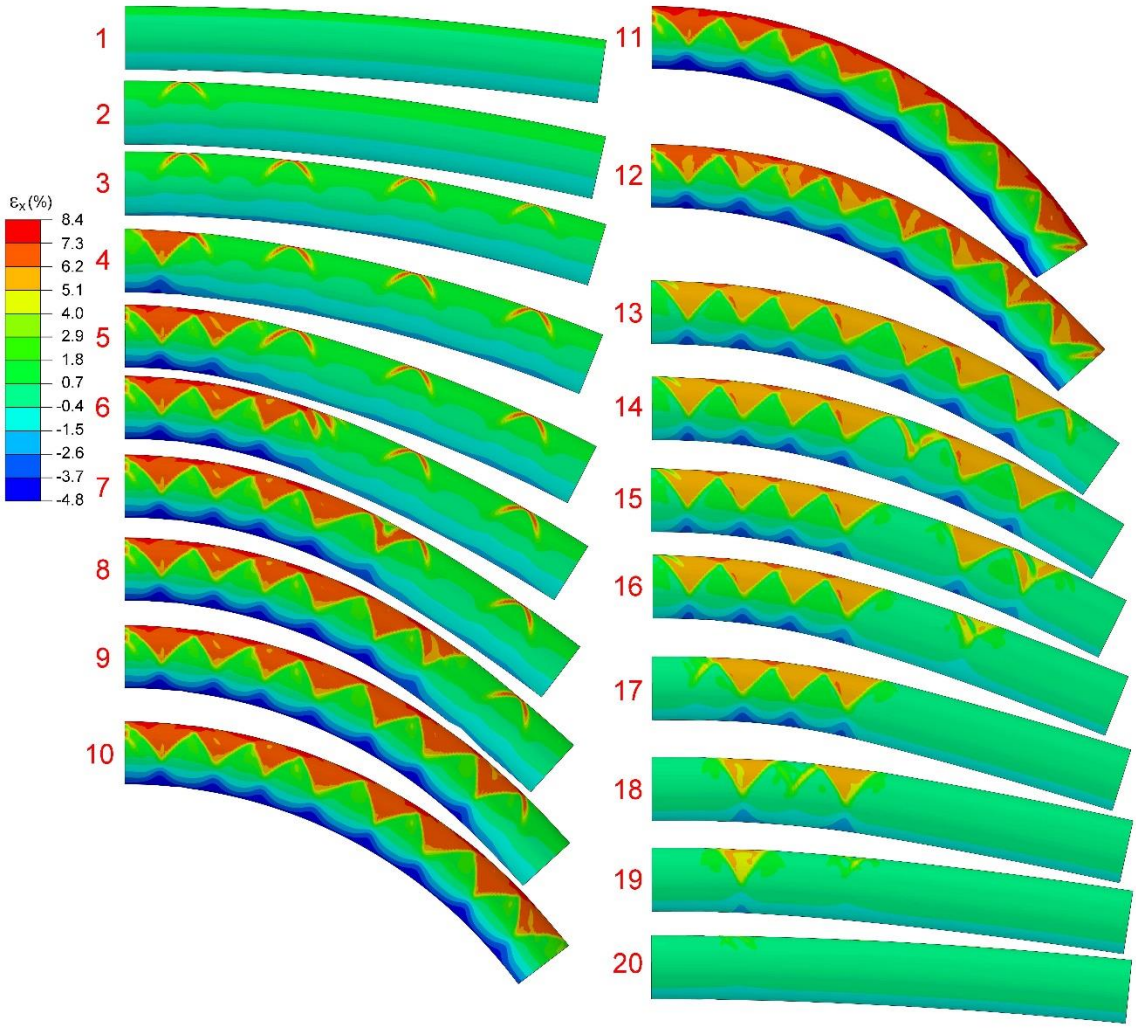

Fig. 6.21 Calculated sequence of tube deformed configurations for a finite element mesh with $N_t = 3$; corresponds to moment-end rotation response in Fig. 6.20.

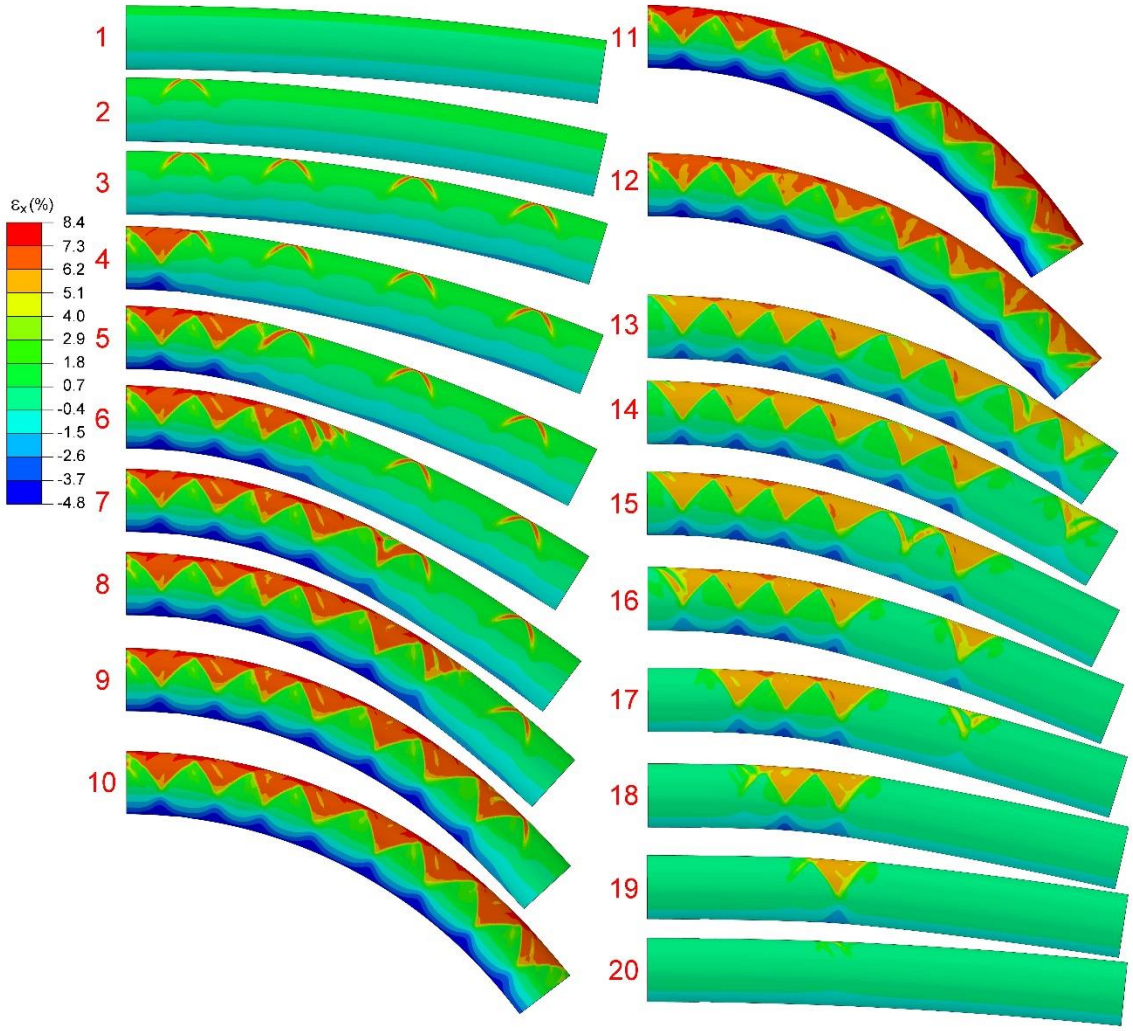

Fig. 6.22 Calculated sequence of tube deformed configurations for a finite element mesh with $N_t = 5$; corresponds to moment-end rotation response in Fig. 6.20.

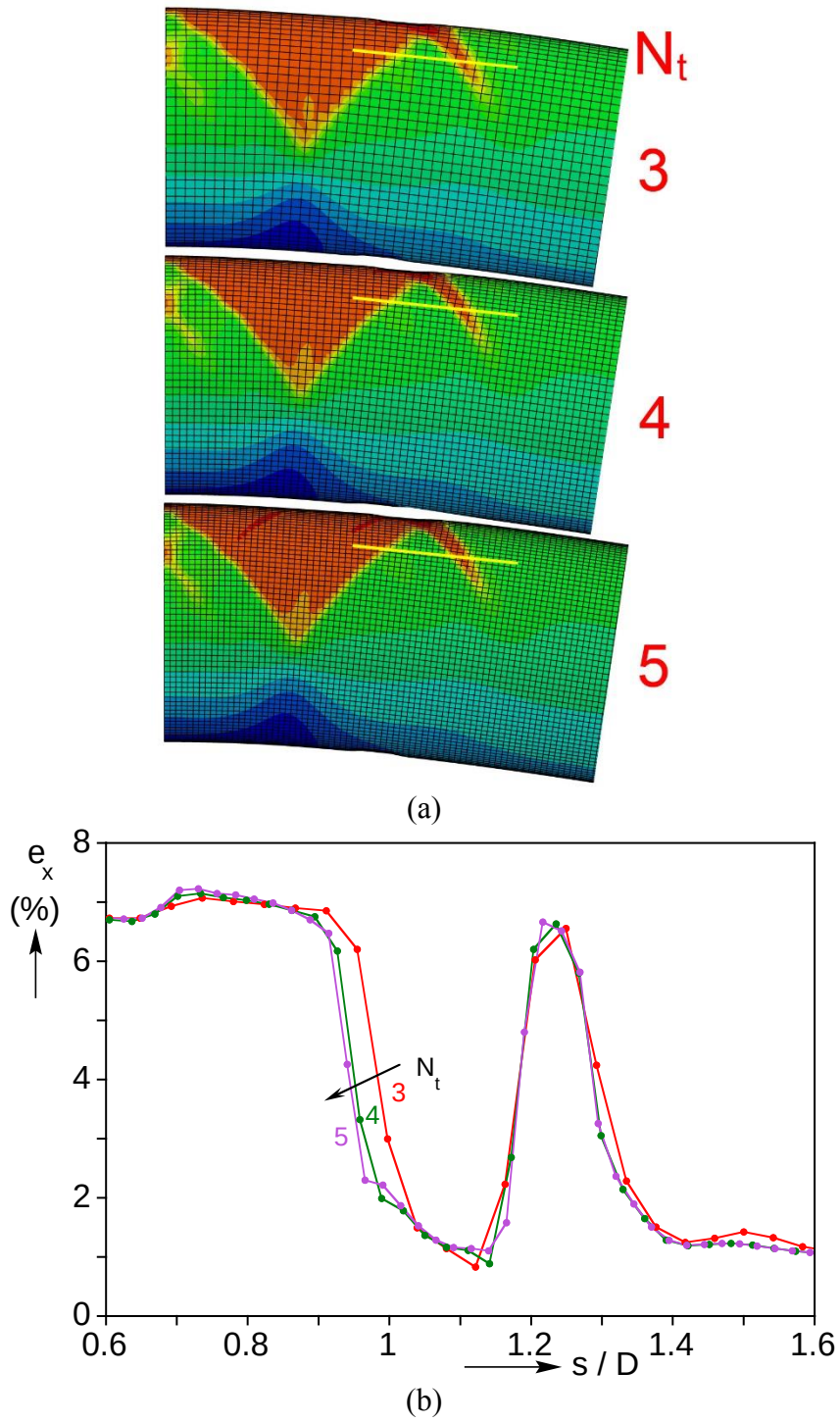

Fig. 6.23 (a) Comparison of expanded views of the first diamond deformation pattern for FE meshes with $N_t = 3$, 4 and 5. (b) The axial strain profiles along the deformed fiber drawn yellow in the images in (a) corresponding to the three meshes.

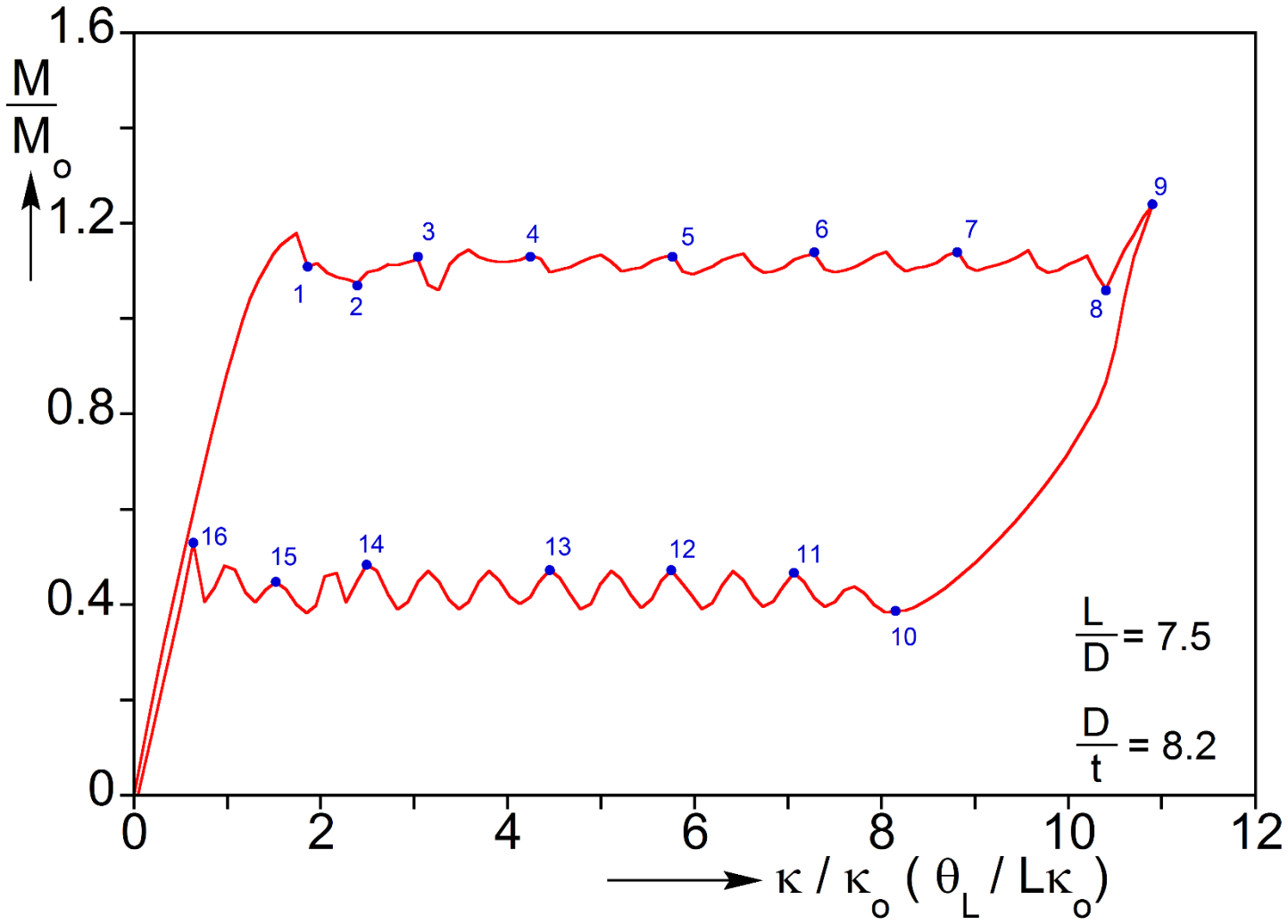

Fig. 6.24 Moment-end rotation response produced by the unstable symmetric constitutive model.

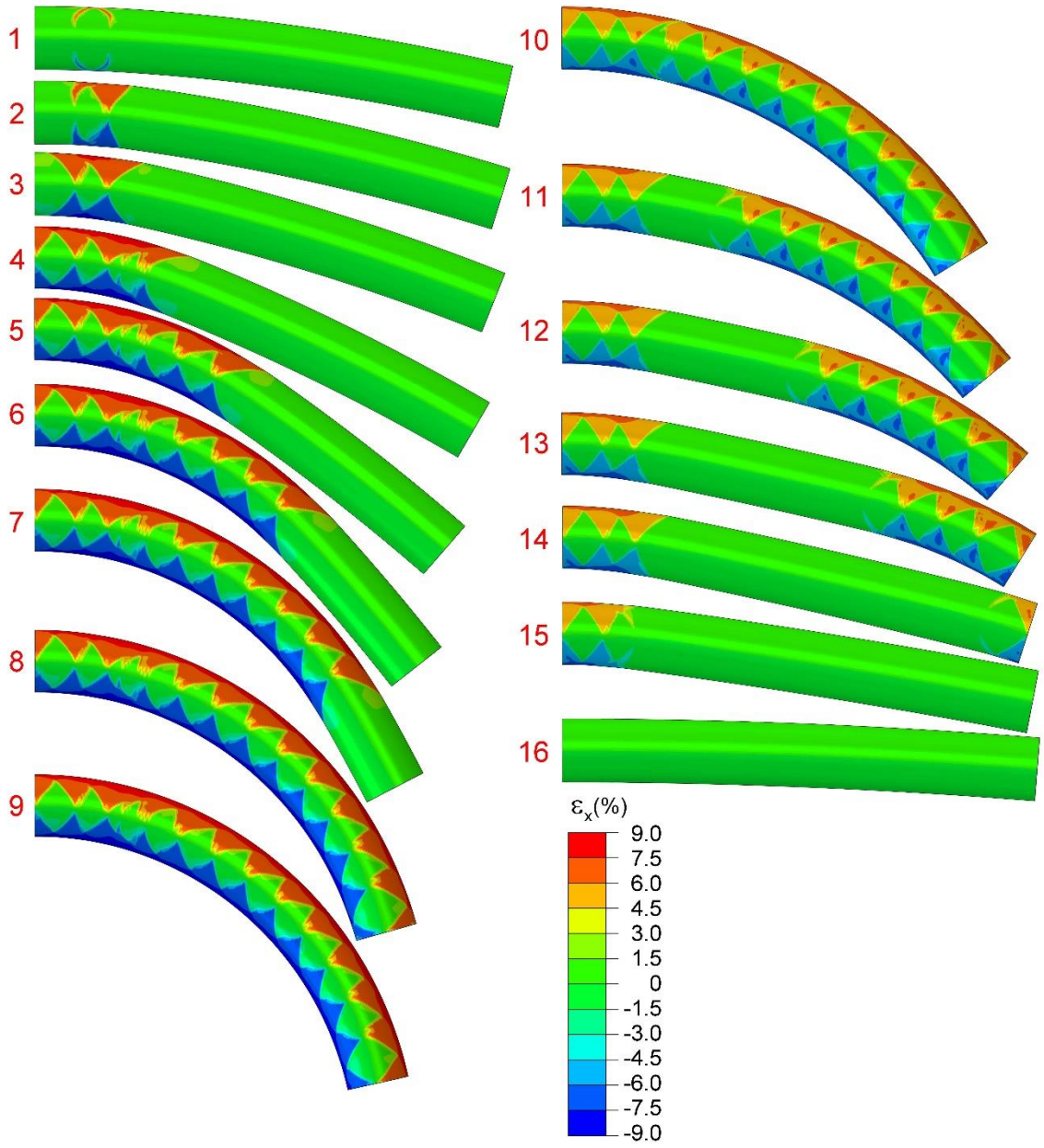

Fig. 6.25 Sequence of calculated tube deformed configurations with axial strain contours superimposed corresponding to numbered bullets on the response in Fig. 6.24.

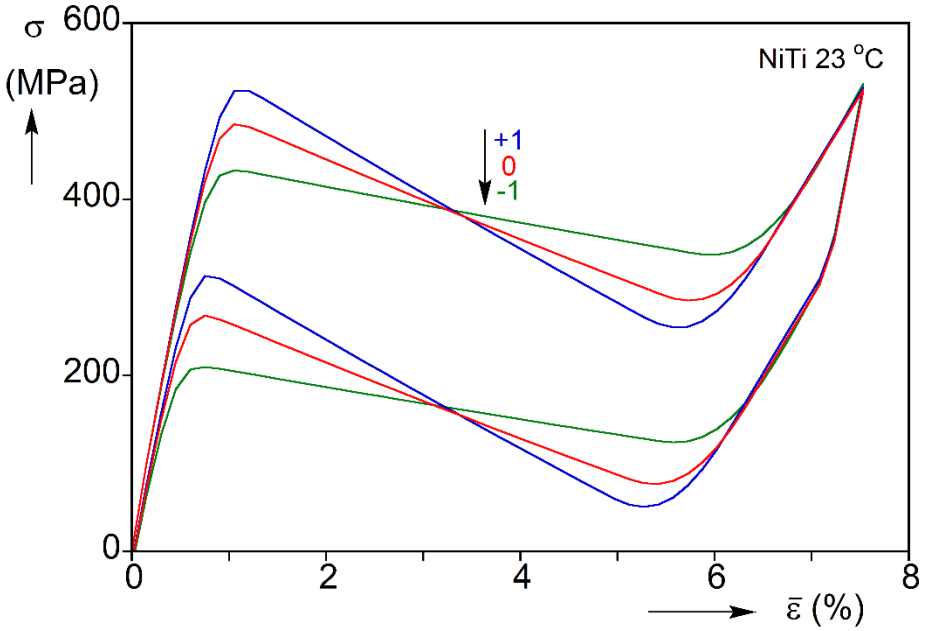

(a)

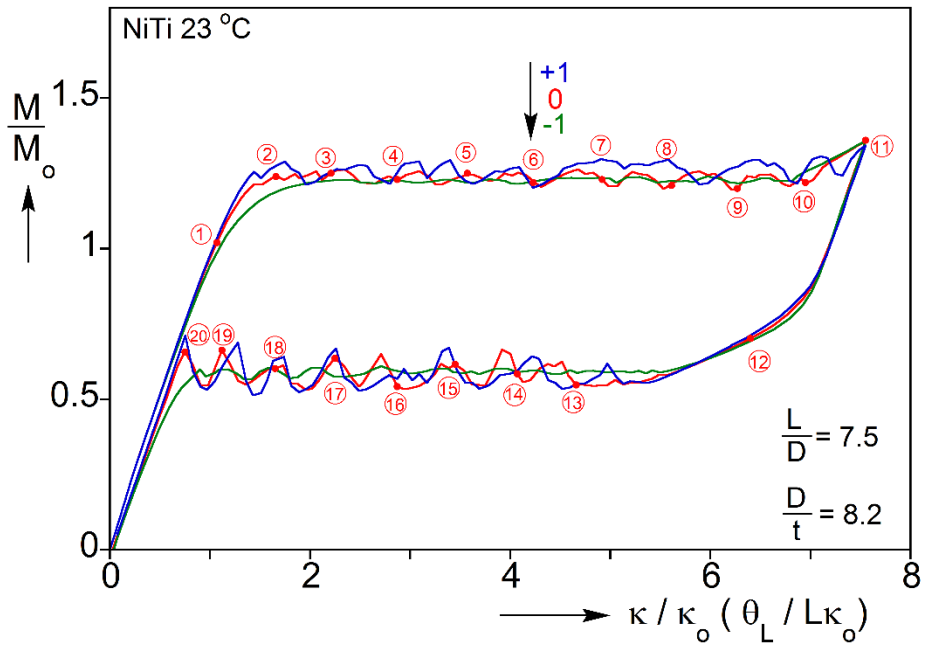

(b)

Fig. 6.26 (a) Tensile stress-strain responses with different softening slopes ("0" corresponds to the values used in the base case simulations—Fig. 6.4b). (b) Moment-end rotation responses produced using the three different sets of softening slopes.

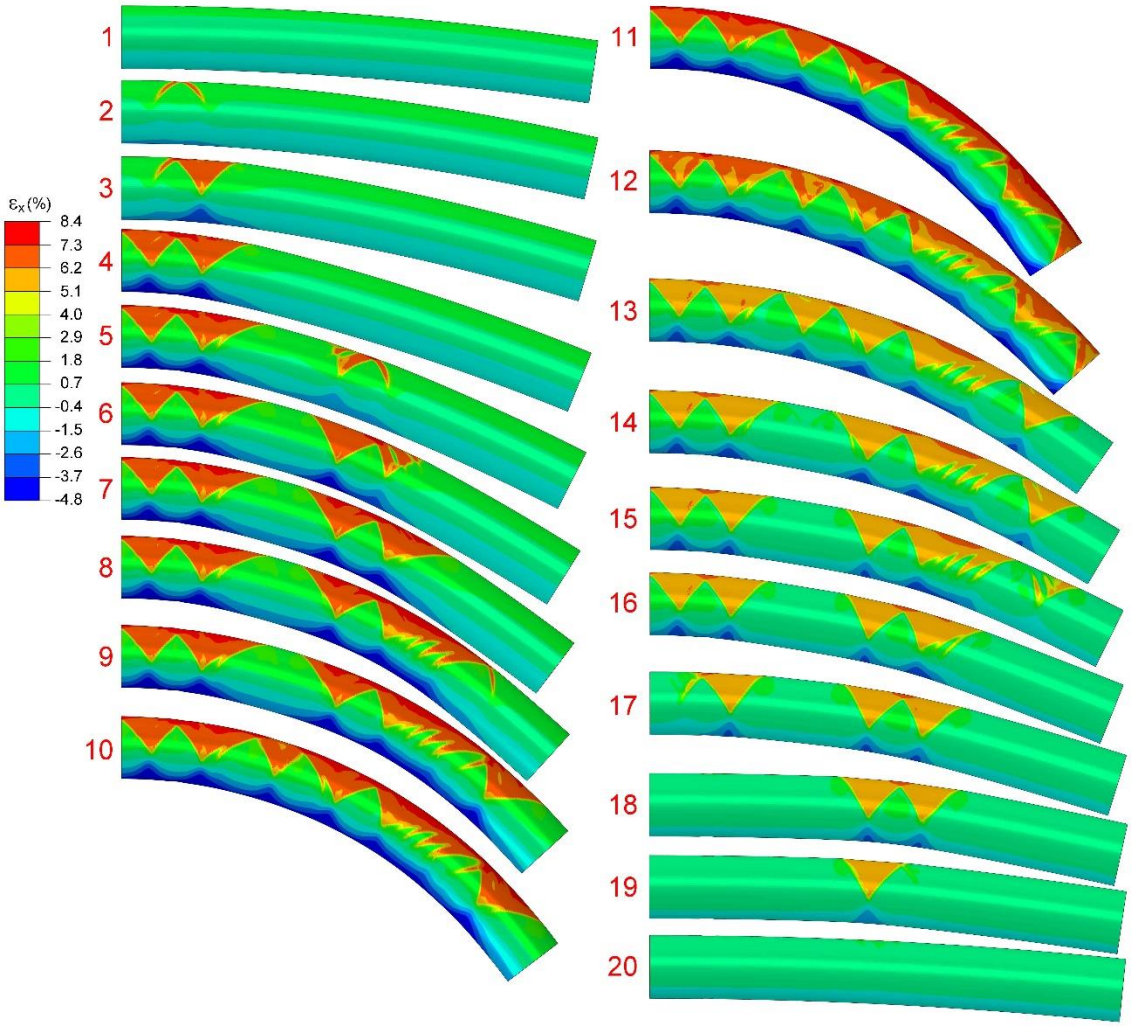

Fig. 6.27 Calculated sequence of tube deformed configurations using the +1 softening slopes in Fig. 6.26a; corresponds to moment-end rotation response in Fig. 6.26b.

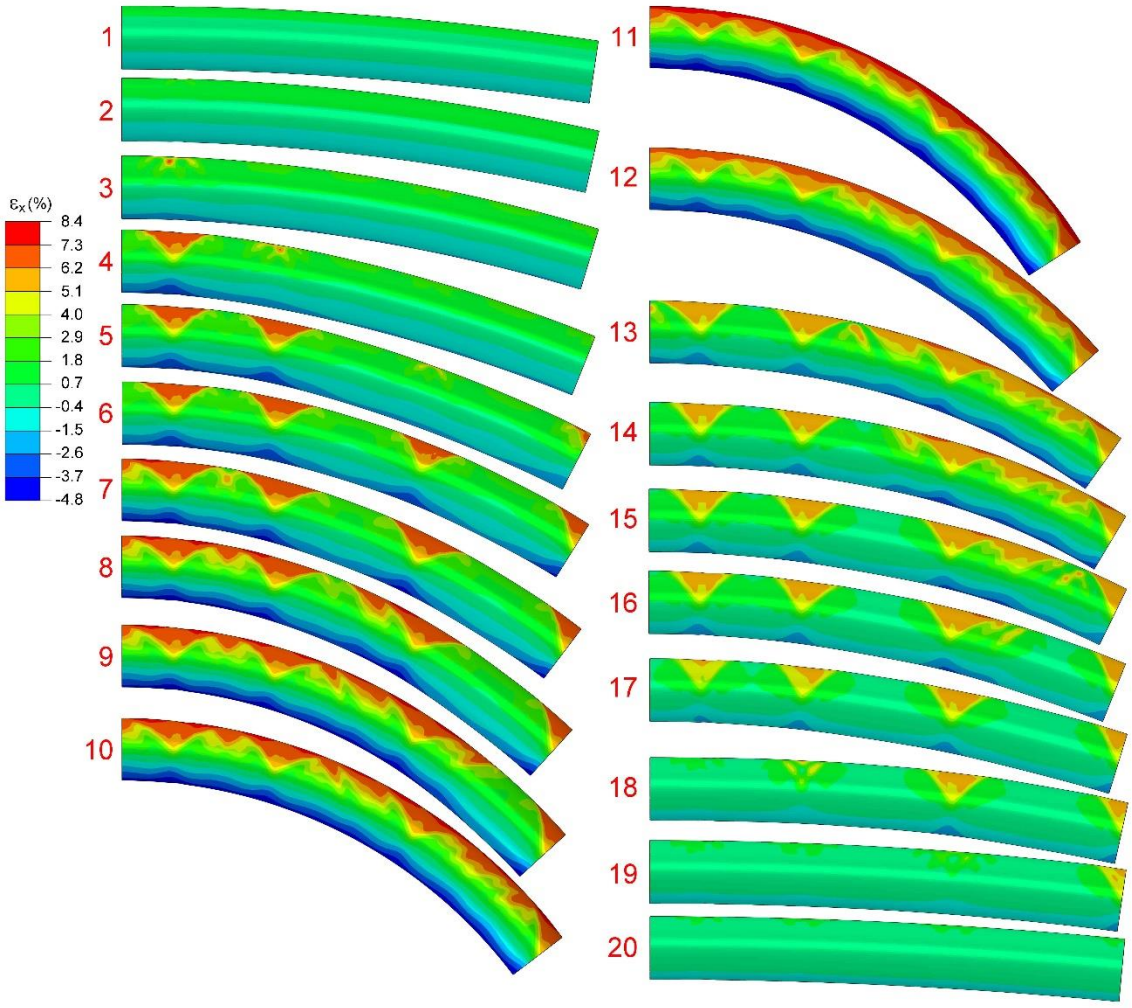

Fig. 6.28 Calculated sequence of tube deformed configurations using the -1 softening slopes in Fig. 6.26a; corresponds to moment-end rotation response in Fig. 6.26b.

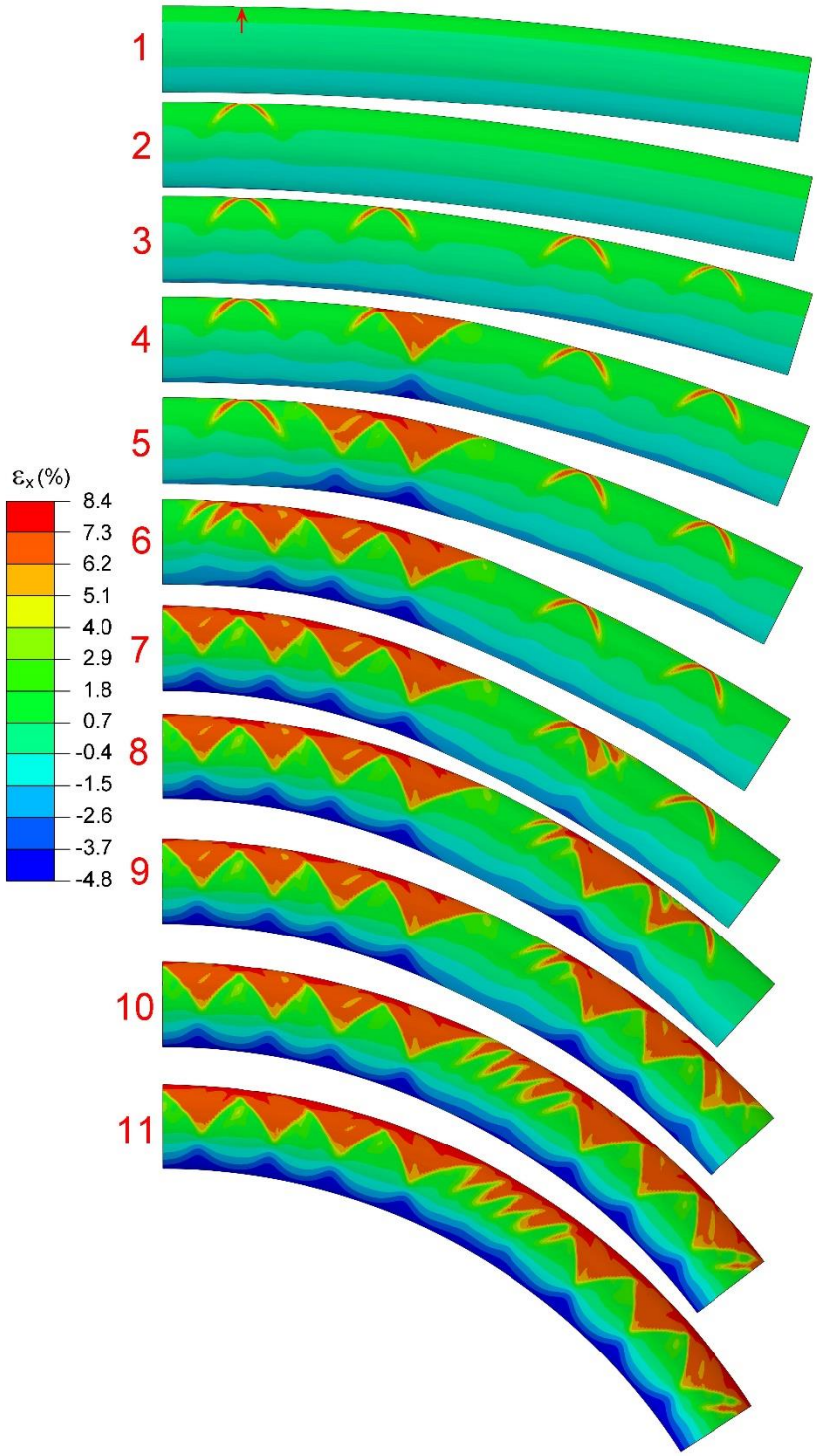

Fig. 6.29 Calculated sequence of tube deformed configurations with a thickness imperfection (marked by the red arrow in image 1) on the tensioned side at $x = D$.

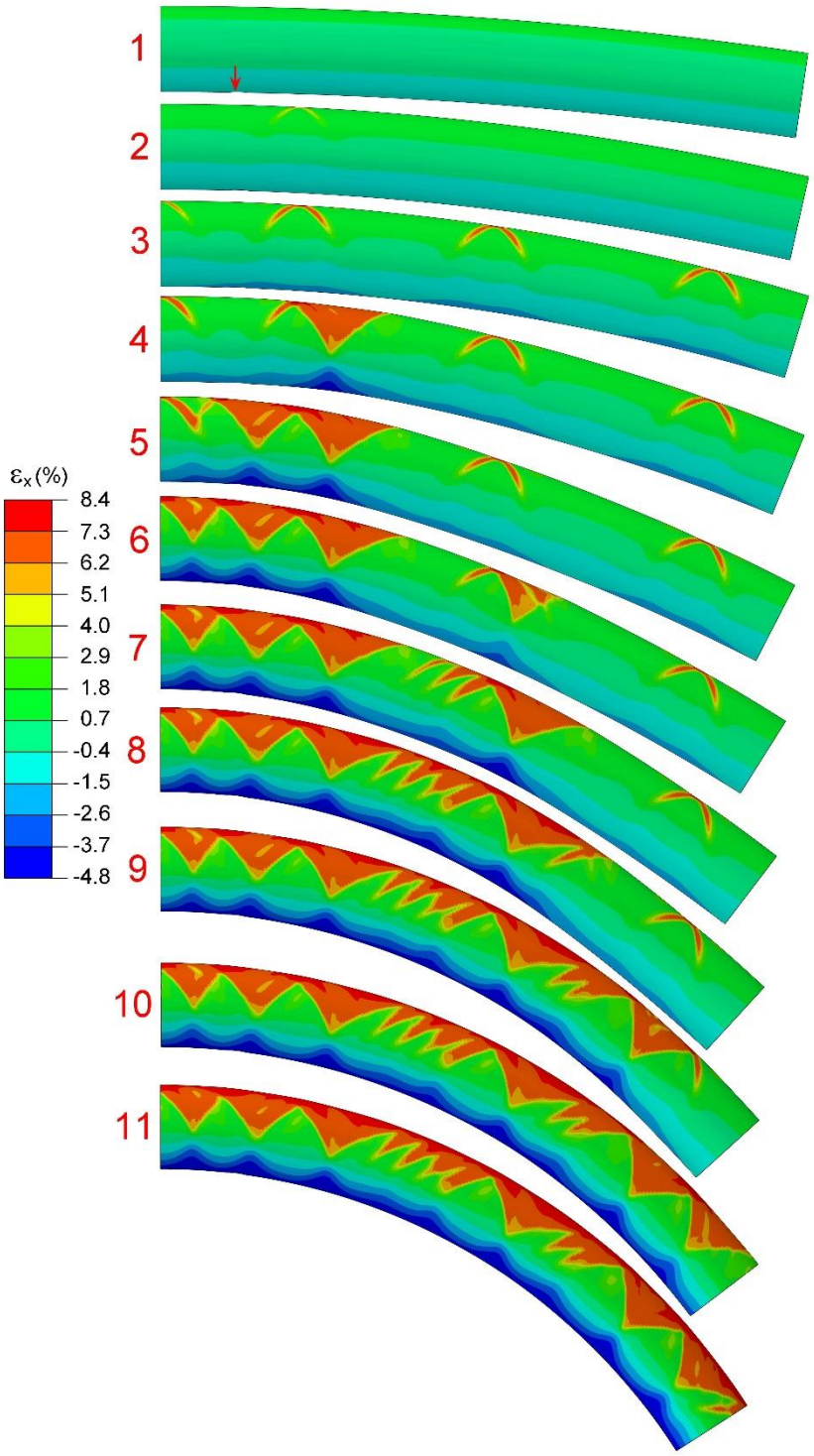

Fig. 6.30 Calculated sequence of deformed configurations with a thickness imperfection (marked by the red arrow in image 1) on the compressed side at $x = D$.

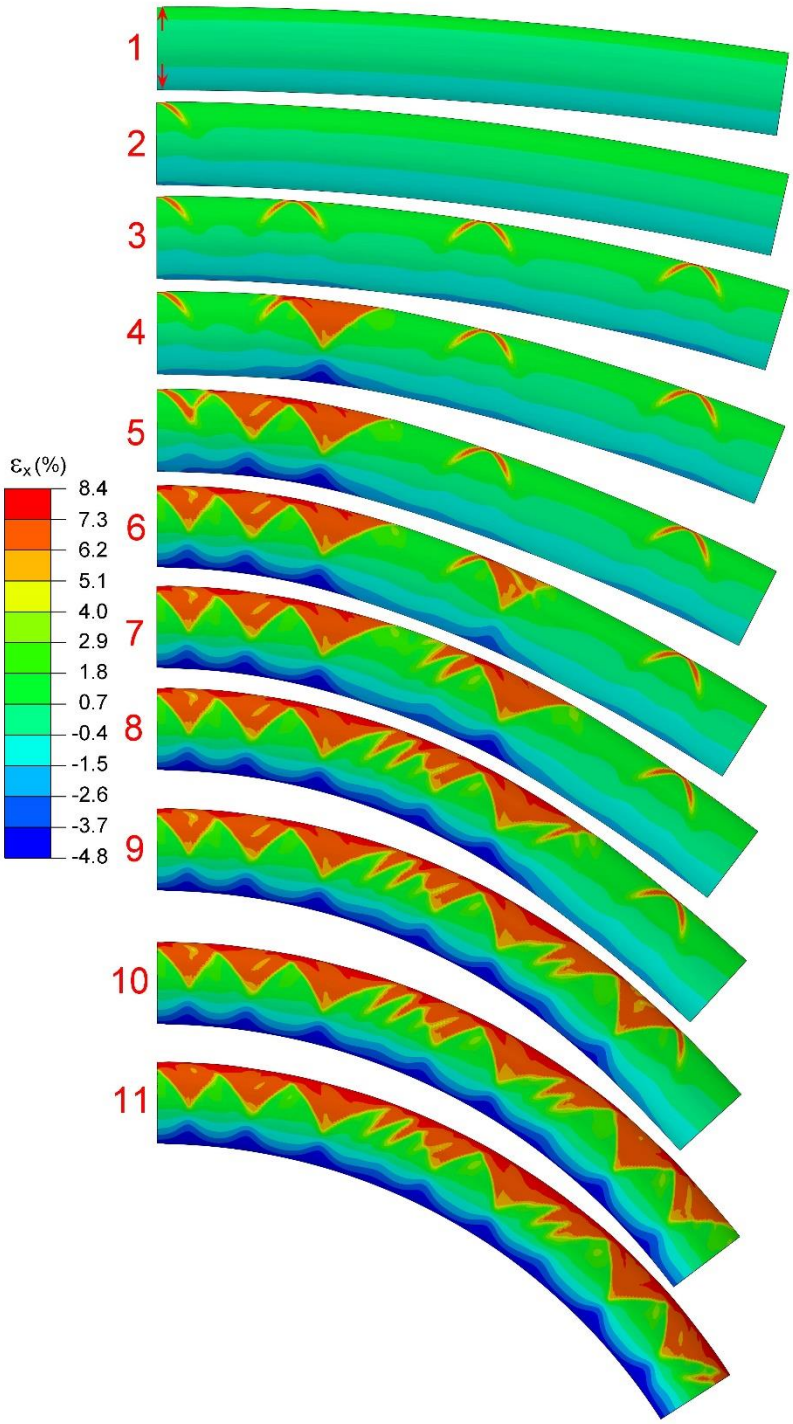

Fig. 6.31 Calculated sequence of tube deformed configurations with two thickness imperfections (marked by the red arrows in image 1) on diametrically opposite sides at $x = 0$.

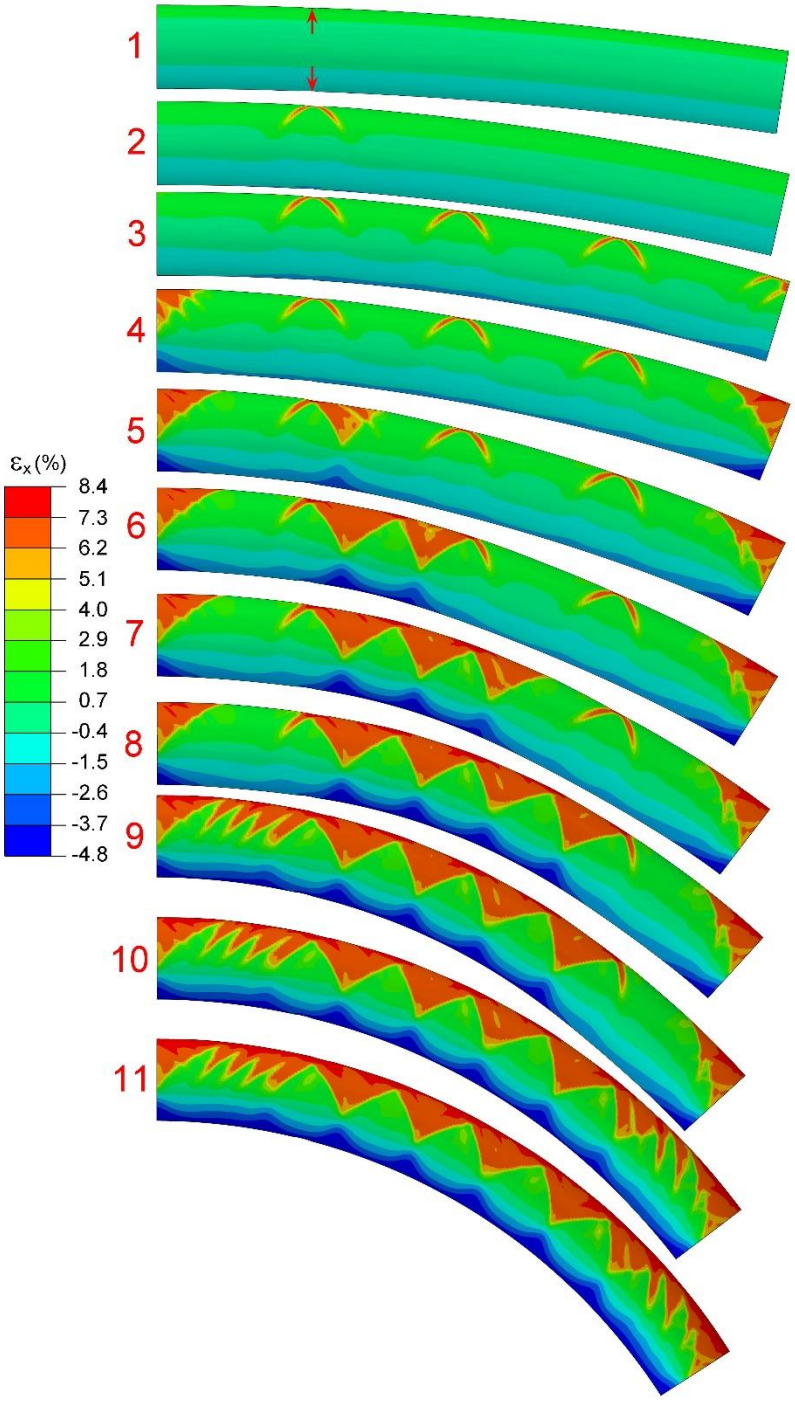

Fig. 6.32 Calculated sequence of tube deformed configurations with two thickness imperfections (marked by the red arrows in image 1) on diametrically opposite sides at $x = 2D$.

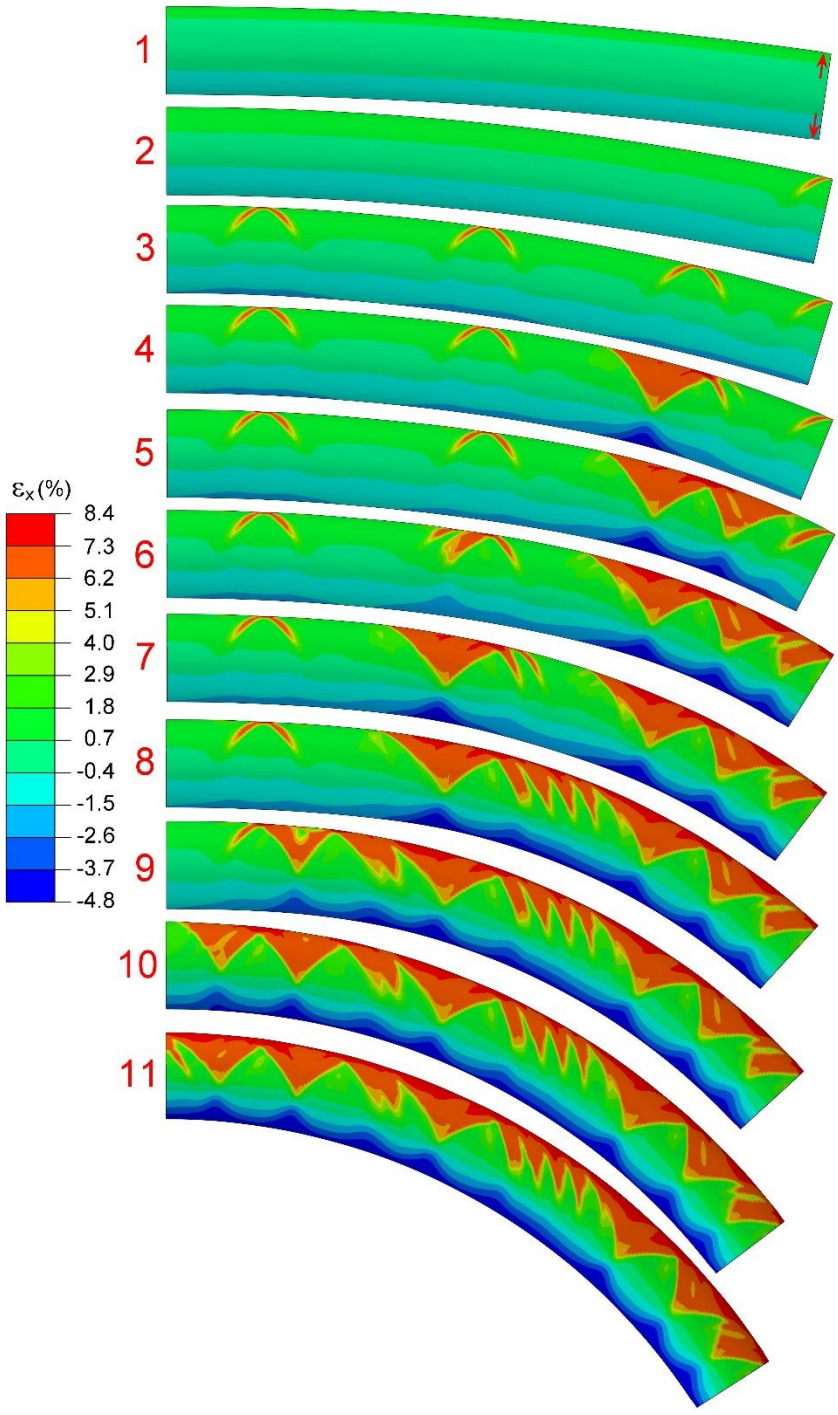

Fig. 6.33 Calculated sequence of tube deformed configurations with two thickness imperfections (marked by the red arrows in image 1) on diametrically opposite sides at $x = L$.

Chapter 7: CONCLUSIONS

Nearly equiatomic NiTi exhibits the unique properties of shape memory and pseudoelasticity, which derive from the diffusionless transformations between the austenitic and martensitic phases. In the pseudoelastic temperature regime, nearly equiatomic NiTi can deform to strains of the order of several percent and fully recover upon unloading. Processing induced texture and possibly other factors cause significant tension/compression asymmetry. For the materials analyzed in this study, transformation under compression initiates at nearly double the stress level as that in tension and results in approximately only half the transformation strain. Furthermore, under tension transformation results in highly inhomogeneous deformation whereas under compression the material transforms with nearly homogeneous deformation. These material nonlinearities have been shown to interact with structural nonlinearities with intriguing consequences. The thrust of the research included in this dissertation involved: first the development of a constitutive modeling framework that can capture the complex pseudoelastic behavior of NiTi; and second, use suitably calibrated versions of the constitutive model to simulate nonlinearities of simple structures under tension, compression and bending.

The constitutive modeling framework developed is based on J_2-type kinematic hardening, in which the back stress is defined as the derivative of a weighted mix of two potentials. The weighting allows the two potentials to be independently calibrated to the tensile and compressive material responses. For each of the structural problems studied, constitutive model, suitably calibrated, is implemented as a user defined subroutine UMAT in a finite element model of the structure.

The model was first used in Chapter 3 to analyze the buckling and recovery of a NiTi tube under compression. Transformation first leads to axisymmetric wrinkling, followed by collapse by progressive development of mode-3 buckling lobes. The buckling recovers on unloading. The FE model for this problem is discretized using quadratic reduced-integration solid elements. A small geometric imperfection with an axisymmetric component and a non-axisymmetric one is introduced to trigger the structural instability. The needs of this problem lead to progressive extensions of the constitutive model to first include plastic deformations at the completion of martensitic transformation and subsequently the addition of the tension/compression asymmetry including the unstable/stable material behaviors. The extended constitutive model lead to the successful reproduction of the hysteretic stress-displacement response and other characteristics of the tube buckling and recovery. The study shows that the inclusion of the asymmetry plays a major role in making the calculated response more realistic and the addition of plasticity further improves the predictions.

Two NiTi structures under primarily tensile stress states were examined next: a tension test on thin strip (Chapter 4) and a second one on a tube (Chapter 5). The tests were performed at room temperature where the material is pseudoelastic. Both structures exhibit closed hysteretic force-elongation responses with the characteristic upper stress plateau associated with the transformation from austenite to martensite during loading, and a lower plateau with the reverse during unloading. In both cases, the unstable material behavior was modeled by introducing softening that spans the two stress plateaus.

In the strip, as the stress plateaus are traced, the deformation localizes into inclined bands that which propagate until the whole specimen is transformed. The FE model for the strip has a mesh of cubical incompatible elements to accommodate the

strain jumps. The localization initiates from a local imperfection on one side of the strip. The simulation reproduces the hysteresis with the two stress plateaus of the correct levels and extents, as well as the banded localization of deformation. The tube behavior is similar but the cylindrical geometry imposes multi-helical patterns of localization. Similar cubical incompatible elements were used to mesh the tube. A small initial thickness imperfection was used to initiate localized deformation. The FE analysis reproduces the closed hysteresis and the initiation and propagation of multi-helical localization patterns. In both problems, the fronts separating the two deformation regimes were shown to be influenced by the problem boundary conditions, by the nature of the initiation imperfection adopted and to some degree by the strength of softening.

The last structure analyzed using the constitutive model is a NiTi tube under bending (Chapter 6). This structure is under tension and compression simultaneously, which places additional challenges into the constitutive model. The tube is again meshed with cubical incompatible elements while localization is initiated by small thickness imperfections. The simulation captures the major features of the experimental results: the hysteretic moment-end rotation response; the correct levels and extents of the moment plateaus; the localization of curvature during loading and unloading; and the progressive initiation of higher strain diamond patterns on the tensioned side and the nearly homogeneous deformation on the compressive side.

In all three structures analyzed, tension played a significant role, and localized deformation consistently initiated from the imperfection along the Hill characteristics. Subsequently localized deformation evolved into patterns specific to the problem because of the constraints imposed by the geometry of the structure.

Recommendations for Furtherer Work

The present constitutive model is isothermal. Since the transformation of SMAs is well documented to be strongly dependent on temperature, the model should be extended to include this dependence (e.g., Shaw and Kyriakides [1995]; Bechle and Kyriakides [2014]). Such an extension will also enable the proper modeling of the thermomechanical interactions, resulting from the latent heat of transformation. A first step in this direction might be to make the back stress temperature dependent.

Although the constitutive model developed has been used in fully 3-D calculations of the four structures analyzed, the model has not been fully evaluated in stress states that deviates significantly from uniaxial stress states. Efforts are ongoing to evaluate the model in the range of biaxial stress states studied experimentally in Bechle and Kyriakides [2016a]. Such a comparison could identify strengths and weakness of the constitutive model and facilitate more representative forms of the back stress.

Appendices

APPENDIX A: REDUCTION OF THE CONSTITUTIVE MODEL TO UNIAXIAL SETTING

The following derivatives are required in (2.25):

$$\frac{\partial J'_2}{\partial \varepsilon^t_{ij}} = \frac{2}{3}\frac{e^t_{ij}}{J'_2}, \tag{A.1}$$

$$\frac{\partial J'_3}{\partial \varepsilon^t_{ij}} = \frac{4}{3J'^2_3}(e^t_{ik}e^t_{kj} - \frac{J'^2_2}{2}\delta_{ij}), \tag{A.2}$$

$$\frac{\partial J_r}{\partial \varepsilon^t_{ij}} = \frac{4}{3J'_2\ J'^2_3}(e^t_{ik}e^t_{kj} - \frac{J'^2_2}{2}\delta_{ij}) - \frac{2J'_3}{3J'^3_2}e^t_{ij}, \tag{A.3}$$

$$\frac{\partial \varepsilon^t_e}{\partial \varepsilon^t_{ij}} = (f - J_r f')\frac{2e^t_{ij}}{3J'_2} + \frac{4f'}{3J'^2_3}(e^t_{ik}e^t_{kj} - \frac{J'^2_2}{2}\delta_{ij}). \tag{A.4}$$

Then, specializing these to uniaxial setting: $\{\varepsilon_{11}, \varepsilon_{22}, \varepsilon_{33}\}^t = \varepsilon^t_{11}\{1, -1/2, -1/2\}$ and

$$J'_2 = \left|\varepsilon^t_{11ct}\right|,\ J'_3 = \varepsilon^t_{11ct},\ J_r = \mathrm{sgn}(\varepsilon^t_{11ct}),\ \varepsilon^t_e = \left|\varepsilon^t_{11ct}\right| f(\mathrm{sgn}\ \varepsilon^t_{11ct}). \tag{A.5}$$

(A.5) in turn lead to

$$\frac{\partial J_r}{\partial \varepsilon^t_{11}} = 0, \tag{A.6}$$

$$\frac{\partial \varepsilon^t_e}{\partial \varepsilon^t_{11t}} = \frac{2}{3}f(1),\quad \frac{\partial \varepsilon^t_e}{\partial \varepsilon^t_{11c}} = -\frac{2}{3}f(-1). \tag{A.7}$$

APPENDIX B: CYLINDRICAL SHELL INELASTIC BIFURCATION BUCKLING UNDER AXIAL COMPRESSION

The first buckling mode of thicker shells that buckle in the plastic range is associated with the periodic axisymmetric buckling model of Lee [1962] and Batternman [1965] with wavelength 2λ given by:

$$\tilde{w} = a\cos\frac{\pi x}{\lambda} \quad \text{and} \quad \tilde{u} = b\sin\frac{\pi x}{\lambda}. \tag{B.1}$$

The corresponding critical stress and half wavelength are

$$\sigma_C = \left[\frac{C_{11}C_{22} - C_{12}^2}{3}\right]^{1/2}\left(\frac{t}{R}\right), \quad \lambda_C = \pi\left[\frac{C_{11}^2}{12\left(C_{11}C_{22} - C_{12}^2\right)}\right]^{1/4}(Rt)^{1/2}, \tag{B.2}$$

where $R = (D-t)/2$ and $[C_{\alpha\beta}]$ are the instantaneous incremental elasto-plastic moduli of the material. These are customarily the incremental deformation theory moduli based on the current state of stress (see related results in Bardi and Kyriakides [2006], Kyriakides *et al*. [2005], Kyriakides and Corona [2007]).

The geometrically perfect NiTi shell considered here is under a uniaxial state of stress until it bifurcates into the wrinkled mode. The nonlinearity in the material response is due to phase transformation and for a compressive stress state is represented by the uniaxial stress-strain response developed in Section 3.4 (prior to the saturation of martensitic transformation)

$$\varepsilon = \frac{\sigma}{E} + \varepsilon^t, \quad \sigma = \sigma_o + h_0\varepsilon^t + (h_1 - h_0)\left[\varepsilon^t - \frac{1}{b}(1 - \mathrm{e}^{-b\varepsilon^t})\right], \tag{B.3}$$

where ε^t is the transformation strain, σ_o is the size of the transformation surface, and the remaining material constants take the values given in Table 3.3. These produce the initial stress-strain response shown in Fig. B.1. The calculated critical state is marked on the response with "↓" and is represented by the following values:

$\{\sigma, \varepsilon, \lambda\}_C = \{731.5\ \text{MPa}, 1.37\%, 0.274\ D\}$.

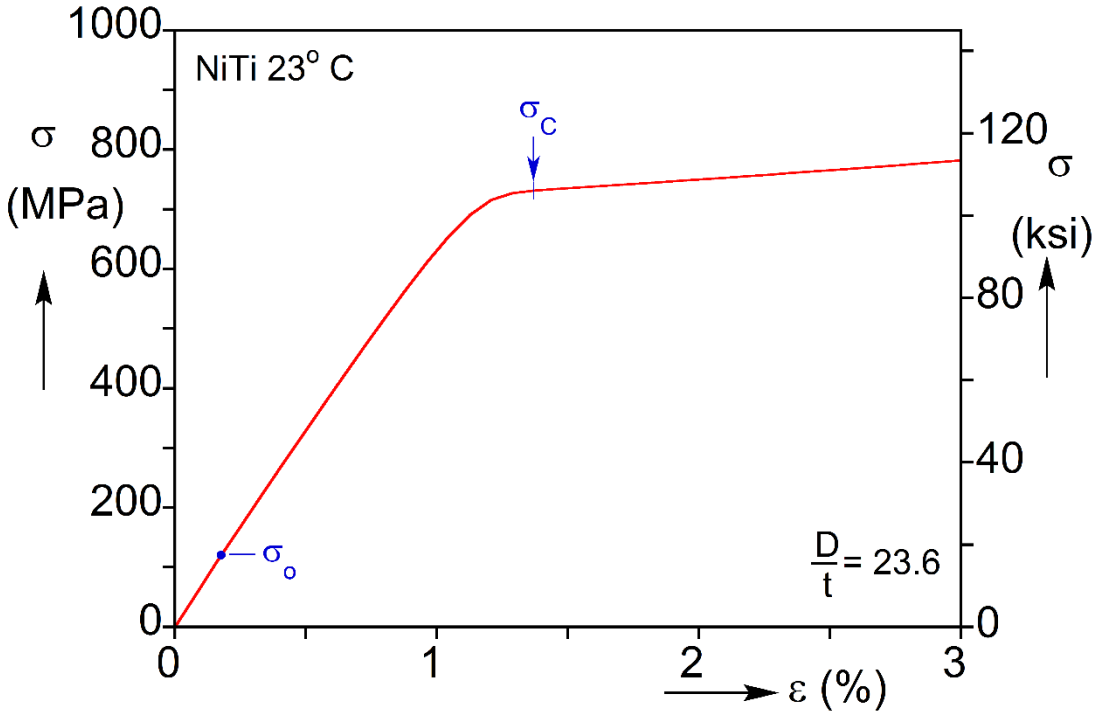

Fig. B.1 Compressive material response adopted and the predicted bifurcation point into the wrinkle mode.

APPENDIX C: EFFECT OF LOADING SCHEME ON INITIAL LOAD DROP OF THE NITI STRIP UNDER UNIAXIAL TENSION

In the numerical simulation of the strip tension tests presented in Chapter 4, localized deformation initiates as a narrow, inclined band of higher deformation. It causes a drop in load that leads to some unloading in the rest of the strip. For the particular length of strip analyzed, the unloading is large enough that it cannot be handled by the displacement controlled loading scheme adopted. A more rigorous arc length incrementation scheme based on Riks' method shows the response to unload along a path that is to the left of the vertical as depicted in Fig. C.1. Thus, the vertical part of the solution in Fig. 4.7a constitutes a "jump." This particular aspect of the response is not of interest in the rest of the study and thus for simplicity the solutions shown are based on a displacement controlled loading.

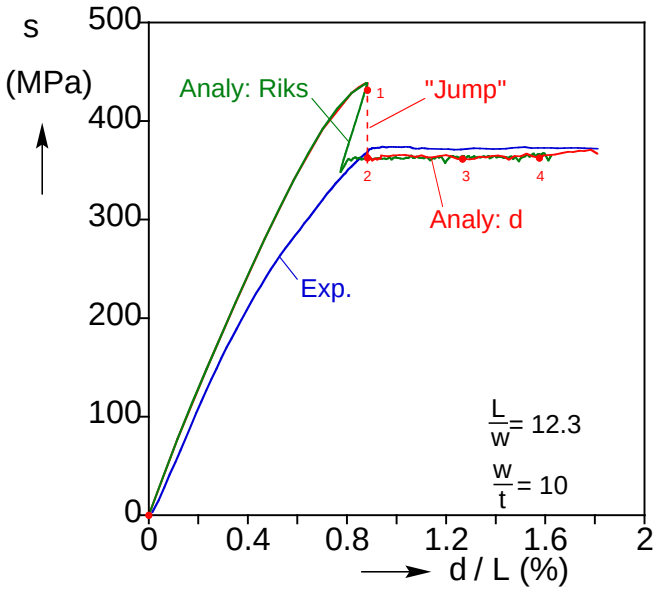

Fig. C.1 Initial parts of the stress-deformation response calculated using "displacement controlled" loading and the Riks arc length incrementation method.

References

Abeyaratne, R., Knowles, J.K. (1993). A continuum model of a thermoelastic solid capable of undergoing phase transitions. *J. Mech. Phys. Solids* **41**, 541-571.

Abeyaratne, R., Knowles, J.K. (2006). Evolution of phase transitions: A continuum theory. Cambridge University Press, New York.

Aguirre, F., Kyriakides, S., Yun, H.D. (2004). Bending of steel tubes with Lüders bands. *Int. J. Plast.* **20**, 1199-1225.

Ahmadian, H., Ardakani, S.H., Mohammadi, S. (2015). Strain-rate sensitivity of unstable localized phase transformation phenomenon in shape memory alloys using a non-local model. *Int. J. Solids Struct.* **63**, 167-183.

Andreasen, G.F., Hilleman, T.B. (1971). An evaluation of 55 cobalt substituted nitinol wire for use in orthodontics. *Journal of the American Dental Association* **82**, 1373–1375.

Arghavani, J., Auricchio, F., Naghdabadi, R., Reali, A., Sohrabpour, S. (2010). A 3-D phenomenological constitutive model for shape memrory alloys under multiaxial loadings. *Int. J. Plast.* **26**, 976-991.

Asgarian, B., Moradi, S. (2011). Seismic response of steel braced frames with shape memory alloy braces. *J. Constructional Steel Research* **67**, 65-74.

Auricchio, F., Taylor, R.L. (1997). Shape-memory alloys: modelling and numerical simulations of the finite-strain superelastic behavior. *Comput. Method Appl. Mech. Engrg.* **143**, 175-194.

Auricchio, F., Taylor, R.L., Lubliner, J. (1997). Shape-memory alloys: macromodelling and numerical simulations of the superelastic behavior. *Comput. Method Appl. Mech. Engrg.* **146**, 281-312.

Auricchio, F., Petrini, L. (2004). A three-dimensional model describing stress-temperature induced solid phase transformations: solution algorithm and boundary value problems. *Int. J. Num. Meth. Eng.* **61**, 807-836.

Badnava, H., Kadkhodaei M., Mashayekhi, M. (2015). Modeling of unstable behaviors of shape memory alloys during localization and propagation of phase transformation using a gradient-enhanced model. *J. Intell. Mater. Syst. Struct.* **26**, 2531-2546.

Batterman, S.C. (1965). Plastic buckling of axially compressed cylindrical shells. *AIAA J.* **3**, 316-325.

Bardi, F.C., Kyriakides, S. (2006). Plastic buckling of circular tubes under axial compression. Part I Experiments. *Int. J. Mech. Sci.* **48**, 830-841.

Bardi, F.C., Kyriakides, S., Yun, H.D. (2006). Plastic buckling of circular tubes under axial compression. Part II Analysis. *Int. J. Mech. Sci.* **48**, 842-854.

Bechle, N.J., Kyriakides, S. (2014). Localization in NiTi tubes under bending. *Int'l J. Solids Struct.* **51**, 967-980.

Bechle, N.J., Kyriakides, S. (2016a). Evolution of localization in pseudoelastic NiTi tubes under biaxial stress states. *Int'l J. Plasticity* **82**, 1-31.

Bechle, N.J., Kyriakides, S. (2016b). Evolution of phase transformation fronts and associated thermal effects in a NiTi tube under a biaxial stress state. *Extreme Mechanics Letters* **8**, 55-63.

Bechle, N.J. (2016). Evolution of localization in NiTi shape memory alloys and its effect on structures. PhD Dissertation, Engineering Mechanics, Univ. Texas at Austin.

Bhattacharya, K. (2003). Microstructure of martensite: why it forms and how it gives rise to the shape-memory effect. Oxford University Press, Oxford.

Bijlaard, P.P. (1940). Theory of local plastic deformation. Publication of the International Association of Bridge and Structural Engineers **6**, 27-44.

Brazier, L.G. (1927). On the flexure of thin cylindrical shells and other thin sections. *Proc. Royal Soc. London A* **116**, 104-114.

Butler, J.F. (1962). Lüders front propagation in low-carbon steels. J. Mech. Physics of Solid 10, 313-334.

Calkins, F.T., Mabe, J.H., Butler, G.W. (2006). Boeing's variable geometry chevron: morphing aerospace structures for jet noise reduction. Proc. SPIE, Smart Structures and Materials: Industrial and Commercial Applications of Smart Structures Technologies, 6171, 277-786.

Carpenter, B., Lyons, J. (2001). EO-1 technology validation report: lightweight flexible solar array experiment. *Tech. Rep.*, NASA Godard Space Flight Center, Greenbelt, MD (8 August 2001).

Cazacu, O., Plunkett, B., Barlat, F. (2006). Orthotropic yield criterion for hexagonal closed packed metals. *Int. J. Plast.* **22**, 1171-1194.

Christ, D., Reese, S. (2009). A finite element model for shape memory alloys considering thermomechanical couplings at large strains. *Int. J. Solids Struct.* **46**, 3694-3709.

Corona, E., Shaw, J.A., Iadicola, M.A. (2002). Buckling of steel bars with Lüders bands. *Int'l J. Solids Struct.* **39**, 3313-3336.

Cui, J., Wu, Y., Muehlbauer, J., Hwang, Y., Radermacher, R., Fackler, S., Wuttig, M., Takeuchi, I. (2012). Demonstration of high efficiency elastocaloric colling with large ΔT using NiTi wires. *Appl. Phys. Lett.* **101**, 073904.

Dolce, M., Cardone, D., Marnetto, R. (2000). Implementation and testing of passive control devices based on shape-memory alloys. *Earthquake Engineering and Structural Dynamics* **29**, 945-968.

Dolce, M., Cardone, D. (2001). Mechanical behavior of shape memory alloys for seismic applications. 2: austenite NiTi wires subjected to tension. *Int. J. Mech. Sci.* **43**, 2657-2677.

Duval, A., Haboussi, M., Ben Zineb, T. (2011). Modelling of localization and propagation of phase transformation in superelastic SMA by a gradient nonlocal approach. *Int'l J. Solids Struct.* **48**, 1879-1893.

Ericksen, J.L. (1975). Equilibrium of bars. *J. Elasticity* **5**, 191-201.

Feng, P., Sun, Q.P. (2006). Experimental investigation on macroscopic domain formation and evolution in polycrystalline NiTi microtubing under mechanical force. *J. Mech. Phys. Solids* **54**, 1568-1603.

Gall, K., Sehitoglu, H., Chumlyakov, Y.I. & Kireeva, I.V. (1999). Tension-compression asymmetry of the stress-strain response in aged single crystals and polycrystalline NiTi. *Acta Mater.* **47**, 1203-1217.

Gall, K., Sehitoglu, H. (1999). The role of texture in tension-compression asymmetry in polycrystalline NiTi. *Int'l J. Plast.* **15**, 69-92.

Godard, O., Lagoudas, M., Lagoudas, D.C. (2003). Design of space systems using shape memory alloys. *Proc. of SPIE*, Smart Structures and Materials, **5056**, 545–558.

Hallai, J.F., Kyriakides, S. (2011a). On the effect of Lüders bands on the bending of steel tubes: Part I experiments. *Int'l J. Solids & Structures* **48**, 3275-3284.

Hallai, J.F., Kyriakides, S. (2011b). On the effect of Lüders bands on the bending of steel tubes: Part II analysis. *Int'l J. Solids & Structures* **48**, 3285-3294.

Hallai, J.F., Kyriakides, S. (2013). Underlying material response for Lüders-like instabilities. *Int'l J. Plasticity* **47**, 1-12.

Hartl, D.J., Lagoudas, D.C. (2009). Constitutive modeling and structural analysis considering simultaneous phase transformation and plastic yield in shape memory alloys. *Smart Mater. Struct.* **18**, 104017.

He, Y.J., Sun, Q.P. (2010). Macroscopic equilibrium domain structure and geometric compatibility in elastic phase transition of thin plates. *Int'l J. Mech. Sci*. **52**, 198-211.

Hill, R. (1952). On discontinuous plastic states, with special reference to localized necking in thin sheets. *J. Mech. Phys. Solids* **1**, 19–30.

Huang, X., Ackland, G.J., Rabe, K.M. (2003). Crystal structures and shape-memory behavior of NiTi. *Nature Materials* **2**, 307-311.

Jacobus, K., Sehitoglu, H. and Balzer, M. (1996). Effect of stress state on the stress-induced martensitic transformation of polycrystalline Ni-Ti Alloy. *Metallu. Mater. Trans. A* **27,** 3066-3073.

Jiang, D., Bechle, N.J., Landis, C.M., Kyriakides, S. (2016a). Buckling and recovery of NiTi tubes under axial compression. *Int'l J. Solids & Structures* **80**, 52-63.

Jiang, D., Landis, C.M., Kyriakides, S. (2016b). Effects of tension/compression asymmetry on the buckling and recovery of NiTi tubes under axial compression. *Int'l J. Solids Struct.* **100-101**, 41-53.

Jiang, D., Landis, C.M. (2016). A constitutive model for isothermal pseudoelasticity coupled with plasticity. *Shape Memory and Superelasticity* **2**, 360-370.

Jiang, D., Kyriakides, S., Landis, C.M., Kazinakis, K. (2017a). Modeling of propagation of phase transformation fronts in NiTi under uniaxial tension. *Euro. J. Mech. A/Solids* **64**, 131-142.

Jiang, D., Kyriakides, S., Bechle, N.J., Landis, C.M. (2017b). Bending of pseudoelastic NiTi tubes. *Int'l J. Solids Struct.* (submitted).

Johnson, A. (1992). Non-explosive separation device. *U.S. Patent* 5, 119, 555 (June 1992).

Karamooz Ravari, M. R., Kadkhodaei, M., Ghaei, A. (2015). A microplane constitutive model for shape memory alloys considering tension-compression asymmetry. *Smart Mater. Struct.* **24**, 075016.

Kauffman, G.B., Mayo, I. (1997). The story of nitinol: the serendipitous discovery of the memory metal and its applications. *The Chemical Educator* **2**, 1-21.

Kyriakides, S., Miller, J.E. (2000). On the propagation of Lüders bands in steel strips. *ASME J. Appl. Mech.* **67**, 645-654.

Kyriakides, S., Bardi, F.C., Paquette, J.A. (2005). Wrinkling of circular tubes under axial compression: Effect of anisotropy. *ASME J. Appl. Mech.* **72**, 301-305.

Kyriakides, S., Corona, E. (2007). Mechanics of Offshore Pipelines: Vol. 1 Buckling and Collapse. Elsevier, Oxford, UK.

Kyriakides, S., Ok, A. and Corona, E. (2008). Localization and propagation of curvature under pure bending in steel tubes with Lüders bands. *Int'l J. Solids Struct.* **45**, 3074-3087.

Landis, C.M. (2003a). On the strain saturation conditions for polycrystalline ferroelastic materials. *ASME J. Appl. Mech.* **70**, 470-478.

Landis, C.M. (2003b). On the fracture toughness of ferroelastic materials. *J Mech. Phys. Solids* **51**, 1347-1369.

Lee, L.H.N. (1962). Inelastic buckling of initially imperfect cylindrical shells subject to axial compression. *J. Aeronaut. Sci.* **29**, 87-95.

Leon Baldelli, A.A., Maurini, C., Pham, K. (2015). A gradient approach for the macroscopic modeling of superelasticity in softening shape memory alloys. *Int'l J. Solids Struct.* **52**, 45-55.

Levitas, V.I., Ozsoy, I.B. (2009). Micromechanical modeling of stress-induced phase transformations. Part 2. Computational algorithms and examples. *Int'l J. Plasticity* **25,** 546-583.

Lexcellent, C., Vivet, A., Bouvet, C., Calloch, S., Blanc, P. (2002). Experimental and numerical determinations of the initial surface of hpase transformation under biaxial loading in some polycrystalline shape-memory alloys. *J. Mech. Phys. Solids* **50**, 2717-2735.

Li, Z.Q., Sun, Q.P. (2002). The initiation and growth of macroscopic martensite band in nano-grained NiTi microtube under tension. *Int'l J. Plast.* **18**, 1481-1498.

Ling, H.C., Kaplow, R. (1980). Stress-induced shape changes and shape memory in the R and martensite transformations in equiatomic NiTi. *Metallurgical Transactions A* **12**, 2101–2111.

Liu, Y., Kyriakides, S. and Hallai, J.F. (2015). Reeling of pipe with Lüders bands. *Int'l J. Solids Structures* **72**, 11-25.

Lomer, w.M. (1952). The yield phenomenon in polycrystalline mild steel. *J. Mech. Phys. Solids* **1**, 64-73.

Lubliner. J., Auricchio. F. (1996). Generalized plasticity and shape memory alloys. *Int. J. Solids Struct.* **33**, 991-1003.

Mani, R., Lagoudas, D.C., Rediniotis, O.K. (2003). MEMS based active skin for turbulent drag reduction. *Proc. SPIE, Smart Structures and Materials*, **5056**, 9–20.

Mao, S.C., Luo, J.F., Zhang, Z., Wu, M.H., Liu, Y., Han, X.D. (2010). EBSD studies of the stress-induced B2-B19' martensitic transformation in NiTi tubes under uniaxial tension and compression. *Acta Materialia* **58**, 3357-3366.

Maziere, M., Luis, C., Marais, A., Forest, S., Gasperini, M. (2017). Experimental and numerical analysis of the Lüders phenomenon in simple shear. *Int'l J. Solids Struct.* **106-107**, 305-314

Michailidis, P.A., Triantafyllidis, N., Shaw, J.A., Grummon, D.S. (2009). Superelasticity and stability of a shape memory alloys hexagonal honeycomb under in-plane compression. *Int. J. Solids Struct.* **46**, 2724-2738.

Miyazaki, S., Imai, T., Otsuka, K., Suzuki, Y. (1981). Lüders-like deformation observed in the transformation pseudoelasticity of a Ti–Ni alloy. *Scr. Metall.* **15**, 853–856.

Moya, X., Kar-Narayan, S., Mathur, N.D. (2014). Caloric materials near ferroic phase transitions. *Nature Materials* **13**, 439-450.

Nacar, A., Needleman, A. and Ortiz, M. (1989). A finite element method for analyzing localization in rate dependent solids at finite strains. *Comp. Methods Appl. Mech. Eng*. **73**, 235–258.

Nacker, J. C. (2009). The evolution of phase transformations in pseudoelastic NiTi tubes under pure bending. MS Thesis, Engineering Mechanics, Univ. Texas at Austin.

Needleman, A. (1988). Material rate dependence and mesh sensitivity in localization problems. *Comp. Methods Appl. Mech. Eng.* **67,** 69-85.

Nemat-Nasser, S., Choi, J.Y., Isaacs, J.B., Lischer, D.W. (2006). Quasi-static and dynamic buckling of thin cylindrical shape-memory shells. *ASME J. Applied Mech.* **73**, 825-833.

Orgeas, L., Favier, D. (1998). Stress-induced martensitic transformation of a NiTi alloy in isothermal shear, tension and compression. *Acta Mater.* **46**, 5579-5591.

Ortiz, M., Leroy, Y. and Needleman, A. (1987). A finite element method for localized failure analysis. *Comp. Methods Appl. Mech. Eng*. **61**, 189–214.

Otsuka, K., Sawamura, T., Shimizu, K. (1971). Crystal structure and internal defects of equiatomic TiNi martensite. *Phys. Stat. Sol*. **5**, 457-470.

Ozsoy, I.B., Babacan, N. (2016). Finite element simulations of microstructure evolution in stress-induced martensitic transformations. *Int'l J. Solids Struct.* **81**, 361-372.

Perkins, J. (1981). Shape memory behavior and thermoelastic martensitic transformations. *Mater. Sci. Eng.* **51**, 181-192.

Petrini, L., Migliavacca, F. (2011). Biomedical applications of shape memory alloys. *J. Metall.* **2011**, 501483.

Philip, T.V., Beck, P.A. (1957). CsCl-type ordered structures in binary alloys of transition elements. *Trans. AIME J. Metals* **209**, 1269-1271.

Popov, P., Lagoudas, D.C. (2007). A 3-D constitutive model for shape memory alloys incorporating pseudoelasticity and detwinning of self-accommodated martensite. *Int. J. Plast.* **23**, 1679-1720.

Qidwai, M.A., Lagoudas, D.C. (2000). On thermomechanics and transformation surfaces of polycrystalline NiTi shape memory alloy material. *Int. J. Plast.* **16**, 1309-1343.

Rahman, M.A., Qiu, J., Tani, J. (2001). Buckling and postbuckling characteristics of the superelastic SMA columns. *Int. J. Solids Struct.* **38**, 9253-9265.

Raniecki, B., Lexcellent, C. (1998). Thermodynamics of isotropic pseudoelasticity in shape memory alloys. *Euro. J. Mech. A/Solids* **17**, 185–205.

Reedlunn, B., Churchill, C.B., Nelson, E.E., Shaw, J.A., Daly, S.H. (2014). Tension, compression, and bending of superelastic shape memory tubes. *J. Mech. Phys. Solids* **63**, 506-537.

Sedlak, P., Frost, M., Benešova, B., Ben Zineb, T., Šittner, P. (2012). Thermomechanical model for NiTi-based shape memory alloys including R-phase and material anisotropy under multi-axial loadings. *Int'l J. Plast.* **39**, 132-151.

Shabalovskaya, S. (1995). Biological aspects of TiNi alloys surfaces. *Journal de Physique IV* **5**, 1199–1204.

Sharabash, A.M., Andrawes, B.O. (2009). Application of shape memory alloy dampers in the seismic control of cable-stayed bridges. *Engineering Structures* **31**, 607-616.

Shaw, J.A., Kyriakides, S. (1995). Thermomechanical aspects of NiTi. *J. Mech. Phys. Solids* **43**, 1243-1281.

Shaw, J.A., Kyriakides, S. (1997). On the nucleation and propagation of phase transformation fronts in a NiTi alloy. *Acta Materialia* **45**, 683-700.

Shaw, J.A., Kyriakides, S. (1998). Initiation and propagation of localized deformation in elasto-plastic strips under uniaxial tension. *Int. J. Plast.* **13**, 837-871.

Shaw, J.A. (2000). Simulations of localized thermo–mechanical behavior in a NiTi shape memory alloy. *Int'l J. Plasticity* **16**, 541–562.

Simo, J.C. and Armero, F. (1992). Geometrically non-linear enhanced strain mixed methods and the method of incompatible modes. *Int'l J. Numer. Methods Eng.* **33**, 1413–1449.

Speck, K., Fraker, A. (1980). Anodic polarization behavior of Ti-Ni and Ti-6Al-4V in simulated physiological solutions. *J. Dent. Res.* **59**, 1590–1595.

Strelec, J. K., Lagoudas, D. C., Khan, M. A., Yen, J. (2003). Design and implementation of a shape memory alloy actuated reconfigurable wing. *J. Intell. Mater. Systems & Struct.* **14**, 257-273.

Sun, Q.P., Li, Z.Q. (2002). Phase transformation in superelastic NiTi polycrystalline micro-tubes under tension and torsion-from localization to homogeneous deformation. *Int. J. Solids Struct.* **39**, 3797-3809.

Tang, Z. and Li, D. (2012). Quasi-static axial buckling behavior of NiTi thin-walled cylindrical shells. Thin Walled Structures **51**, 130-138.

Van Humbeeck, J. (1999). Non-medical applications of shape memory alloys. *Mat'l Sci & Eng.* **A273-275**, 134-148.

Vacher, P., Lexcellent, C. (1992). Study of the pseudoelastic behavior of polycrystalline shape memory alloys by resistivity measurements and acoustic emission. In: Jono, M. (Ed.), Mechanical Behavior of Materials- VI, **3**, pp. 231-236.

Wagner, M.F.-X, Windl, W. (2008). Lattice stability, elastic constants and macroscopic moduli of NiTi martensites from first principles. *Acta Materialia* **56**, 6232-6245.

Wang, F.E., Buehler, W.J., Pickart, S.J. (1965). Crystal structure and a unique 'martensitic' transition of TiNi. *J. Appl. Phys.* **36**, 3232-3239.

Wasilewski, R.J. (1971). The effects of applied stress on the martensitic transformation in NiTi. *Metall. Trans.* **2**, 2973-2981.

Wilson, E.L., Taylor, R.L., Doherty, W.P., Ghaboussi, J. (1973). Incompatible displacement models. In: Fenves, S.J. et al. (Eds.), *Numerical and Computer Models in Structural Mechanics*. Academic Press, New York.

Xiao, Y., Zeng, P., Lei, L. (2016). Experimental investigation on the mechanical instability of superelastic NiTi shape memory alloy. *J. Mater. Eng. Perform.* **25**, 3551-3557.

Zhang, X.H., Feng, P., He, Y.J., Yu, T.X., Sun, Q.P. (2010). Experimental study on rate dependence of macroscopic domain and stress hysteresis in NiTi shape memory alloy strips. *Int'l J. Mech. Sci*. **52**, 1660-1670.

Zhu, P., Feng, P., Sun, Q.-P., Wang, J., Dai, H.-H. (2016). Determining the up-down-up response through tension tests of a pre-twisted shape memory alloy tube. *Int'l J. Plast*. **85**, 52-76.

Vita

Dongjie Jiang entered Tsinghua University in August 2005 as an undergraduate student and obtained his B.E. degree on Engineering Mechanics and Aerospace Engineering in 2009 with the honor "Excellent Graduate." Two years later, he received his M.E. degree on Engineering Mechanics from the same university. Since August 2011, he has been studying in the University of Texas at Austin in pursuit of a Ph.D. degree in Engineering Mechanics.

Permanent email: jiangdj@utexas.edu

This dissertation was typed by the author.